The Impact of Flow on the Nuclear Translocation of NF-κB

Daniel C. Baeriswyl

Supervised by:

Professor Yiannis Ventikos

and

Professor Rob Krams

This thesis is submitted in partial fulfilment

of the requirements for the degree of

Doctor of Philosophy

of

University College London

Department of Mechanical Engineering

University College London

July 2017

Abstract

In this dissertation, the impact of flow on the nuclear translocation of NF-κB in vascular endothelial cells was investigated. NF-κB is a key promoter of inflammatory responses and its mis-regulation is related to the development of vascular diseases. The aim was to establish a link between hemodynamic forces and NF-κB to gain insight in cardiovascular disease mechanisms such as aneurysms.

Human umbilical vein endothelial cells (HUVEC) were transfected with two plasmids: H2B-mCherry and GFP-RelA. The nuclear translocation of NF-κB within the transfected primary cells was verified with TNF-α stimulation and compared to immunohistochemistry of TNF-α stimulated non-transfected cells.

In the first part of the thesis, transfected HUVECs were exposed to different flow environments, including uniform low shear stress, uniform high shear stress and a shear stress gradient, and imaged live for 6 hours. Computer vision techniques were applied to track each individual cell and each nuclear NF-κB concentration was evaluated as a function of time. In each experiment, more than 1000 single cells were tracked and analysed.

TNF-α stimulation caused a synchronised population response with a nuclear NF-κB peak at 30 minutes. The population mean of cells under static conditions remained constant, while spontaneous nuclear translocation of NF-κB in individual cells was observed. Uniform low shear stress stimulation increased translocating activity after 5 hours of flow. Alternatively, uniform high shear stress promoted increased nuclear translocation, directly after onset of flow and after 5 hours. Small differences of

nuclear translocation of NF-κB at different shear stress magnitudes within a shear stress gradient were observed. The percentage of cells experiencing early nuclear translocation increased with increased shear stress. It is believed that high shear stress induces nuclear translocation early, while for low shear stresses, responses are delayed.

In the second part of the thesis, a numerical model was developed to predict cell population responses of the NF-κB pathway. The model is deterministic but includes extrinsic noise to mimic stimulus dependent cell-to-cell variability. Population responses to different TNF-α concentrations were predicted in close agreement with live-cell measurements. The model was extended with a shear dependent activation module to predict small variabilities observed in nuclear translocation of NF-κB under different shear conditions. The close agreement between nuclear translocation of NF-κB in a shear stress gradient and the measurements allowed prediction of inflammatory responses in different flow environments such as a backward facing step channel.

This work provides a first insight in the temporal dynamics of nuclear translocation of NF-κB in a large population of endothelial cells exposed to different flow environments. Although the effects were much weaker than with TNF-α stimulation, differences between static and flow conditions were observed, which indicate that hemodynamic forces affect intracellular signalling.

Statement of Originality

I hereby declare that this dissertation is my own work and all materials presented reflect the true content.

Any contribution made by others is explicitly acknowledged.

I also declare that the intellectual content of this dissertation is the product of my own work.

Daniel Claude Baersiwyl

July 2017

Acknowledgements

First, I would like to thank Prof. Yiannis Ventikos for accepting me as a Ph.D. student and for the tremendous support and supervision I received during the years of my Ph.D.

Second, I am very thankful to Prof. Rob Krams for allowing me to perform experiments in his laboratory and to be part of his research group. I am very thankful for the extensive training I have received in experimental methods of molecular bioengineering.

Third, I am very thankful to Ioanna Prionisti for helping in the laboratory with the immunohistochemistry experiments during her master's thesis. It was an intense period with many experiments.

I would like to thank my mother Regula and her husband Walter, my father Claude and his life partner Elisabeth, my brother Michael and his wife Claudia and their beautiful daughter Seraphina, my sister Sarah and her husband Hannes, for all their support over the years.

Lastly, I am thankful to many colleagues with whom I have discussed research, solved problems and enjoyed the Ph.D life. I hope I have not forgotten anyone. I would like to thank: Mireya Ferrandis Martinez for her love and care, Dr. John Vardakis, Dr. Jeremy Nahon, Dr. Qicheng Meng, Dr. Bingyue Song, Dr. Stefan Van Duivenboden, Dr. Hugo Santana Pereira, Prof. Ryan Pedrigi, Dr. Mean Ghim, Dr. Syed Bin Omar, Dr. Michael Bloesch, Dr. Muge Sarper, Dr. Eleni Bazigou, Dr. Ivan Stojanovic, Dr. Adrian Victor Matei, Dr. Nikos Bempedelis, Dr. Tom Peach, Dr.

Grigoris Tsolkas, Miten Patel, Dr. Luca Annecchino, Dr. Weilin Zeng and Dr. Tania Rodin.

Contents

List of Figures

List of Tables

Acronyms

Ca^{2+}: Calcium Ion

Cl^{-}: Chloride Ion

K^{+}: Potassium Ion

Na^{+}: Sodium Ion

α: Womersley Number

3T3: Fibroblast cell line

AKT: Protein kinase B

AP-1: Activator protein 1

BAECs: Bovine Aorta Endothelial Cells

Bcl-3: Chronic Lymphatic Leukemia Protein

BR3: tumor necrosis factor receptor superfamily member 13C

c-Rel: proto-oncogene c-Rel

CAMs: Cell adhesion molecules

CAV-1: Caveolin-1

Cbl: Casitas B-lineage Lymphoma

CD40: Cluster of differentiation 40

CFD: Computational Fluid Dynamics

CO2: Carbon dioxide

CRISPR-Cas: Clustered Regularly Interspaced Short Palindromic Repeats - CRISPR-associated

DMEM: Dulbecco's Modified Eagle's Medium

DNA: deoxyribonucleic acid

ESL: E-selectin

EC: Endothelial Cells

ECM: Extracellular Matrix

eNOS: Endothelial Nitric oxide synthases

Erk: Extracellular signal–regulated kinases

FAK: Focal adhesion kinase

Flk-1 or VEGFR-2: Kinase insert domain receptor

GAG: Glycosaminoglycans

GF-Rs: cell surface receptors

GFP-p65: green fluorescent protein tagged NF-κB p65 subunit

mDIa: Diaphanous-related formin-1

GFP: green fluorescent protein

GPCR: G-protein-coupled receptors

GTP: Guanosine-5'-triphosphate

H2B: histone proteins

HUVECs: Human Umbilical Vein Endothelial Cells

ICAM-1: Intercellular Adhesion Molecule 1

IgG: Immunoglobulin G

IHC: Immunohistochemistry

IKK: IκB kinase

IKKα: IκB kinase alpha

IKKβ: IκB kinase beta

IKKγ: IκB kinase gamma

IL-1β: Interleukin 1 beta

IκBNS: nuclear factor of kappa light polypeptide gene enhancer in B-cells inhibitor, NS

IκBα: nuclear factor of kappa light polypeptide gene enhancer in B-cells inhibitor, alpha

IκBβ: nuclear factor of kappa light polypeptide gene enhancer in B-cells inhibitor, beta

IκBε: nuclear factor of kappa light polypeptide gene enhancer in B-cells inhibitor, epsilon

IκBζ: nuclear factor of kappa light polypeptide gene enhancer in B-cells inhibitor, zeta

JNK: c-Jun N-terminal kinases

KLF-2: Krüppel-like Factor 2

LB medium: Lysogeny broth medium

LED: Light Emitting Diode

LPS: Lipopolysaccharides

LTβR: Lymphotoxin beta receptor

MAPK: mitogen-activated protein kinase

MCP-1: Monocyte chemoattractant protein 1

MEFcells: Mouse Embryonic Fibroblasts cells

MMP-9: Matrix metallopeptidase 9

MMPs: Matrix metalloproteinases

MRI: Magnetic Resonance Imaging

NADPH: Nicotinamide adenine dinucleotide phosphate

NF-κB: Nuclear factor kappa-light-chain-enhancer of activated B cells

NF-κB2: nuclear factor NF-kappa-B p100 subunit

NIK: NF-kappa-B-inducing kinase

NO: Nitric oxide

FRET: Fluorescence resonance energy transfer

O2-: Superoxide

p-IKKα/β: Phosphorylated IκB kinase alpha and beta

p100: nuclear factor NF-kappa-B p100 subunit

p105: nuclear factor NF-kappa-B p105 subunit

p50-p65: p50 and p65 NF-κB heterodimer

p50: nuclear factor NF-kappa-B p50 subunit

p52: nuclear factor NF-kappa-B p52 subunit

P65: nuclear factor NF-kappa-B p65 subunit, different name for p65

PBS: Phosphate Buffered Saline PDGF-B: Platelet-derived growth factor subunit B

PECAM-1: Platelet endothelial cell adhesion molecule

pEGF: Precursor Epidermal Growth Factor

Pen Strep: Penicillin Streptomycin

PI3K: Phosphatidylinositol-4,5-bisphosphate 3-kinase

PIV: Particle Image Velocimetry

PKD1: Polycystin-1

PMDS: Polydimethylsiloxane

Ras: a protein superfamily of small GTPases

RCF: Relative centrifugal forc

Re: Reynolds Number

RelA: nuclear factor NF-kappa-B p65 subunit

RelB: Transcription factor RelB

Relish: nuclear factor NF-kappa-B subunit

RHR: Rel homology region

ROCK: Rho-associated protein kinase

RTK: Receptor tyrosine kinases

SEM: Scanning electron microscope

Src: Proto-oncogene tyrosine-protein kinase

SSRE: Selective Serotonin Reuptake Enhancer

TIMP-1: Tissue Inhibitor of Metalloproteinases-1

TLR/IL-1: Toll-like receptors

TNF-α: tumor necrosis factor alpha

TNFR: tumor necrosis factor receptor

TRIF: TIR-domain-containing adapter-inducing interferon-β

USPIO: Ultrasmall Superparamagnetic Iron

VE-cadehrin: Vascular endothelial cadherin)

VEGFA: Vascular endothelial growth factor A

VEGFC: Vascular endothelial growth factor C

VEGFD: Vascular endothelial growth factor D

VEGFR-2: Vascular endothelial growth factor receptor 2

VSMC: Vascular smooth muscle cell

Nomenclature

Chapter 2, 3 and 4:

d_h: Hydraulic diameter of gradient channel [m]

$\frac{GFP-RelA(t)}{GFP-RelA(t^*)}$**:** Mean pixel intensity of nuclear GFP-RelA normalised by earliest time point [-]

h_1: Gradient channel narrow height [m]

h_2: Gradient channel tall height [m]

$I^*[-]$**:** Ratio of immunohistochemistry intensity of cytoplasm and nucleus [-]

$I_{Control}$: IHC mean pixel intensity of cells under static conditions

$I_{Experiment}$: IHC mean pixel intensity of experiment

I_n^M**:** Mean pixel intensity normalised by time average [-]

I_n^{MAX}**:** Mean pixel intensity normalised by maximum intensity [-]

I_n^{STD}**:** Mean pixel intensity standardised [-]

I_n^T**:** Mean pixel intensity normalised by earliest time point [-]

$I_n(t)$**:** mean pixel intensity [-]

$O_i(t)$**:** Pulse

$P_n(t)$**:** number of pixel per nuclei [-]

$Q_{i,n}(t)$**:** nuclear GFP-RelA intensity [-]

$r_i(t)$**:** number of activated receptors

T_{end}: Latest common time point [s]

T_{max}: Length of pulse

T_{Start}: Earliest common time point [s]

λ_i**:** stoichiometric coefficient

μ_n**:** $\langle I_n(t) \rangle$

σ_n**:** Standard deviation of $I_n(t)$

d: Squared Euclidean distance

$GFP-RelA_n^*(t)$**:** Mean pixel intensity of nuclear GFP-RelA normalised by time average [-]

L: Length of gradient channel [m]

p**:** pressure [Pa]

Q: Flow rate [mL/s]

Re**:** Reynolds number [-]

U**:** Velocity [m/s]

w: Gradient channel width [m]

z: Gradient channel length variable [m]

μ**:** Dynamic viscosity [kg/s m]

ρ**:** density [kg/m^3]

τ**:** Shear stress [Pa]

Chapter 5:

$\vec{u}$: $\begin{pmatrix} u \\ v \\ w \end{pmatrix}$

∇: $\left(\frac{\partial}{\partial x}, \frac{\partial}{\partial x}, \frac{\partial}{\partial x}\right)$

p: Pressure [Pa]

Re: Reynolds number [-]

μ: Dynamic viscosity [kg/s m]

ρ: Density [kg^3/m^3]

Chapter 6:

a_1: Association rate of nuclear IκBα and nuclear NF-κB [1/sM]

a_2: Active IKK and IκBα binding rate [1/sM]

$a_3(t)$: Binding rate of active IKK and IκBαNFκB [1/sM]

A_{max}: Total number of initial activated cells [-]

B_{max}: Total number of early activated cells [-]

c_1: A20 mRNA production rate dependent on nuclear NF-κB [1/s]

c_{1a}: IκBα mRNA production due to nuclear NF-κB [1/s]

c_2: A20 mRNA production constant [M/s]

c_{2a}: Constant IκBα mRNA production [M/s]

c_4: A20 production rate [1/s]

c_{4a}: IκBα production rate from IκBα mRNA [1/s]

c_{6a}: Disassosication rate of IκBα and NF-κB [1/s]

C_{max}: Total number of mid activatied cells [-]

D_{max}: Total number of late activated cells [-]

E_t: Total Enzyme [M]

i_1: Nuclear import rate of NF-κB [1/s]

i_{1a}: Nuclear import of unbound IκBα [1/s]

k_1: IKK activation rate [1/s]

k_2: Inactivation rate of IKK due to binding with A20 [1/sM]

k_3: Inactivation rate of IKK [1/s]

k_{deg}: Neutral IKK degradation rate [M/s]

K_M: Michaelis constant [M]

k_{prod}: Neutral IKK production rate [M/s]

k_v: Cytoplasmic to nucleus ratio [-]

$P_i(t)$: Gaussian normal distribution

$r_i(t)$: Number of activated receptors [-]

R_{max}: Number of total inactive cells [-]

t_2: Binding rate of active IKK and IκBαNFκB [1/s]

T_{Delay}: Initial delay time constant [s]

T_{SDecay}: Slow natural decay time constant [s]

X_i: Inititally activated receptors [-]

λ_i: stoichiometric coefficient **[-]**

$\mu_A(t)$**:** Number of shear stress dependent initial activated cells [-]

$\mu_B(t)$**:** Number of shear stress dependent early activated cells [-]

$\mu_C(t)$: Number of shear stress dependent mid activated cells [-]

$\mu_D(t)$: Number of shear stress dependent late activated cells [-]

$\mu_R(t)$**:** Number of shear stress dependent inactive cells [-]

S: Substance [M/s]

v: Reaction rate [M/s]

α: TNF-α stimulation constant [-]

ξ_B**:** Random time constant of early activated cells [s]

ξ_C: Random time constant of mid activated cells [s]

ξ_D: Random time constant of late activated cells [s]

$\phi_i(t)$: Activation scale [-]

ω_{Delay}: Initial delay random constant [-]

ω_L: Random walk number $\in \{-1,0,1\}$

$A20_{mRNA}$: A20 mRNA [M]

$A20(t)$: A20 [M]

E: Enzyme [M]

E: Total number of cells of a population [-]

$e1a$: Nuclear export rate of IκBα [1/s]

$e2a$: Nuclear export rate of nuclear IκBαNFκB complex [1/s]

$I\kappa B\alpha_{Cyto}(t)$: Total cytoplasmic IκBα concentration [M]

$I\kappa B\alpha_{mRNA}(t)$: IκBα mRNA [M]

$I\kappa B\alpha_n(t)$: Unbound nuclear IκBα [M]

$I\kappa B\alpha NF\kappa B_n(t)$: Nuclear IκBαNFκB complex [M]

$I\kappa B\alpha NF\kappa B(t)$: Cytoplasmic IκBαNFκB complex [M]

$IKK_a(t)$: Activated IKK [M]

$IKK_a I\kappa B\alpha(t)$: Active IKK and IκBα complex [M]

$IKK_a I\kappa B\alpha NF\kappa B(t)$: Active IKK and IκBαNFκB complex [M]

$IKK_{Activated}(t)$: Total activated IKK concentration [M]

$IKK_i(t)$: Inactive IKK [M]

$IKK_n(t)$: Neutral state of IKK [M]

$I\kappa B\alpha(t)$: Unbound IκBα [M]

M: Total number of receptors of a cell [-]

$NF\kappa B_{Nuc}(t)$: Total nuclear NF-κB concentration normalised by time average [-]

$NF\kappa B(t)_n$: Nuclear NF-κB [M]

$NF\kappa B(t)$: Cytoplasmic NF-κB [M]

β: TNF-α stimulation constant [-]

γ: TNF-α stimulation constant [-]

$\mu(t)$: Time dependent stimulus intensity

σ: Standard deviation

1. Motivation and Introduction

Summary: *This chapter introduces the reader to the main scientific question approached in this dissertation. First, the whole thesis layout is discussed for orientation. This is followed by general considerations and a clear definition of the aim of this work. Then a broad literature review is presented, which covers topics including the cardiovascular system, mechanotransduction, gene expression and its relationship to disturbed flows, aneurysms and the role of inflammation, biology of NF-κB, temporal dynamics of NF-κB, activation of NF-κB by shear stress, techniques in live-cell imaging and in-vitro shear stress devices.*

1.1. Overview

This dissertation is structured into eight chapters. In chapter 1, the motivation for this work and a broad literature review are presented. Previous studies about nuclear translocation of NF-κB are summarised to inform the reader regarding the current state of knowledge about the pivotal transcription factor NF-κB and its role in cardiovascular diseases.

The experimental investigation of NF-κB in human umbilical vein endothelial cells (HUVECs) is presented in chapters 2, 3 and 4. In chapter 2, the experimental methods applied are described in detail. The experimental methods range from tissue culture, synthetic biology, live-cell imaging techniques, single cell tracking algorithms and data analysis of single cells. In chapter 3, experimental results are depicted regarding the nuclear translocation of NF-κB in HUVECs, stimulated with TNF-α, investigated with immunohistochemistry and live-cell imaging. In chapter 4, experimental results are presented for the nuclear translocation of NF-κB in HUVECs exposed to uniform low and high shear stress, and a shear stress gradient investigated with immunohistochemistry and live-cell imaging.

The flow characteristics of a gradient channel, specifically devised and prototyped for this study, and of a backward facing step channel were investigated using computational fluid dynamics in chapter 5. The numerical approach to predict NF-κB in a cell population when stimulated with TNF-α or flow is shown in chapter 6. First, the cell population model based on individual cell activation is described in detail. Second, the population model was exemplified when stimulated with different TNF-α concentrations. Third, based on experimental observations in this study, the cell population model was extended to account for shear dependent activation. The shear induced NF-κB pathway model was applied to predict the NF-κB pathway in different flow environments.

In Chapter 7, the key findings of the dissertation are discussed, as well as limitations and further work suggestions. Chapter 8 presents an overall conclusion.

1.2. Aim of the thesis

The aim of this work was to provide an insight into the nuclear translocation of NF-κB on a single cell level in vascular endothelial cells. The main goal was to understand the temporal dynamics of the nuclear translocation of NF-κB to different shear forces. NF-κB is the pivotal transcription factor of the immune system. Understanding the temporal dynamics of nuclear NF-κB concentrations in response to different shear forces would define a link between hemodynamics and immune responses within the vasculature.

As indicated in this work, many steps of verification had to be undertaken to discover a link. A system had to be developed that allowed measuring live nuclear translocation of NF-κB in endothelial cells. This was achieved by inserting GFP tagged

NF-κB into primary human umbilical vein endothelial cells (HUVECs). The modified cells were tested and verified for nuclear translocation to a known stimulus such as TNF-α. The verified cells were then exposed to different flow environments such as uniform low and high shear stress and a shear stress gradient. It will be shown throughout the dissertation that single cell dynamics of nuclear NF-κB are highly heterogeneous under static conditions and can be synchronised with high TNF-α dose. The aim was to understand if flow as a stimulus per se, can strongly influence the nuclear translocation of NF-κB of such a heterogeneous system. It will be demonstrated throughout the dissertation that flow has only a weak effect on the nuclear translocation of NF-κB and provides moderate improvement to the synchronisation of a population's heterogeneity.

1.3. The cardiovascular system

Evolutionary-wise, a convection-based circulation system is needed, as simple diffusion is not sufficient to supply a complex multicellular organism such as the human body with the required nutrients and oxygen for its metabolic needs. The cardiovascular systems primary role is to distribute gases and molecules for nutrition, growth and repair. Secondarily, it circulates hormones and neurotransmitters for chemical signaling, it dissipates heat and maintains the immune system with inflammatory and defence responses.

The circulation system consists of three fundamental organs. The heart that is the pump, the blood that is the medium and the vessels serving as pipes. The heart consists of two pumps, the left and right ventricles. The left ventricle supplies the systemic circulation and the right the pulmonary circulation. The two circuits operate

in serial mode and require good timing. Deoxygenated blood flows from the right ventricle into the pulmonary circulation, where it is oxygenated by the lungs. The oxygenated blood flows into the left ventricle where it is pumped to the tissues of the body. Tissue extracts oxygen from the blood and it returns deoxygenated blood via the veins back into the right ventricle, where the cycle commences again. The circulation process is shown diagrammatically in Figure 1 [1, 2].

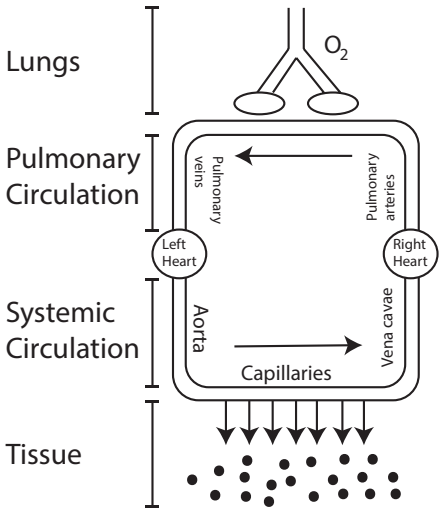

Figure 1: The human circulation with the pulmonary circuit to load and the systemic circuit to supply oxygen.

1.4. Hemodynamics

Blood flow is driven by a pressure gradient along the circulation system. Ejected from the left ventricle, the aortic blood pressure is roughly 100 mmHg above atmospheric pressure. Whereas, the pressure in the veins is close to atmospheric pressure. This significant pressure difference enables flow from arteries to veins. The heart's periodic ejection of blood is called systole, and the rest phase is defined as diastole. This pulsatile arterial pressure is characterised by the heartbeat frequency.

The blood is a composition of plasma (a pale-white watery solution), cells (erythrocytes and leukocytes) and platelets (thrombocytes). Its viscosity is defined as

shear thinning non-Newtonian, but its exact shearing behaviour is still controversial. In general, hemodynamics is unsteady, the fluid is non-Newtonian and the walls are elastic. Therefore the physical nature of blood flow corresponds to a very complex system [1, 2].

1.5. Anatomy of the vasculature

Blood is pumped into the aorta from the left ventricle. The aorta has multiple conduit arteries that supply different parts of the body. These arteries branch repeatedly until they form very small arteries (diameter of 0.1-0.5cm).

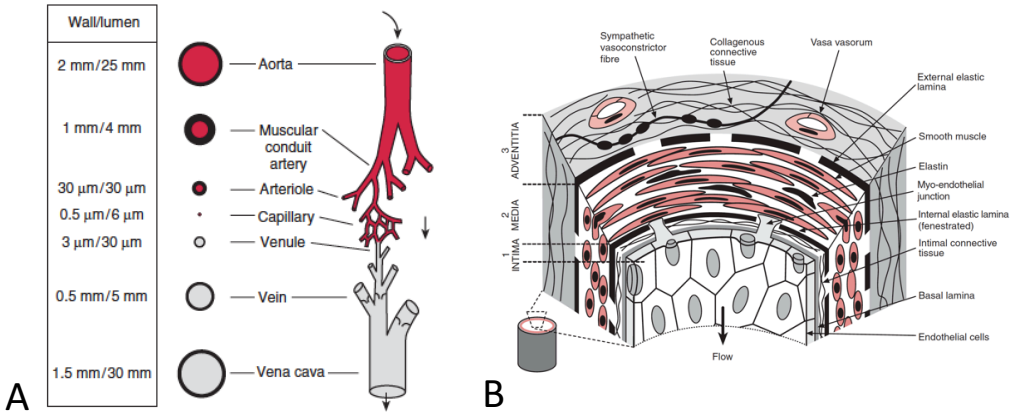

Figure 2: A: An overview of blood vessel sizes [1]. B: A schematic description of the structure of a blood vessel [1].

The small arteries branch into smaller vessels named arterioles. Subsequently, arterioles subdivide into capillaries. Capillaries then merge into venules that further merge into small and large veins (Figure 2.A).

The vascular wall consists of three layers (Figure 2.B), except for capillaries. The first layer, the intima, is a layer of bedded endothelial cells on a thin layer of connective tissue. The endothelial cells are in direct contact with the blood. Therefore, they are the main barrier for plasma and blood cells. The second layer, the media, is to assure contractile capacity and mechanical strength. It is made of smooth muscle cells

arranged in a matrix of elastin and collagen fibres. The outer layer, the adventitia, consists of connective tissue with no specific outline [1].

1.6. Inflammation

Inflammation is a reaction caused by harmful stimuli and conditions likened to injuries and infections. It involves the delivery of blood components to the site of infection or injury. Inflammation is categorised into two types: acute and chronic inflammation. Acute inflammation is triggered for example by blood infection or a cut, and is well understood. Alternatively, chronic inflammation due to chronic infections and autoimmune diseases is only partially understood. Furthermore, the mechanisms of systemic chronic inflammatory conditions found in type-2 diabetes and cardiovascular diseases are barely known [3].

A brief description of acute inflammation is as follows. Acute inflammatory response caused by infection or tissue injury initates delivery of blood components (plasma and leukocytes) to the local injury or infection. Recognition of infection is triggered by tissue-resident macrophages and mast cells. This causes production of inflammatory mediators such as chemokins, cytokines, vasoactive amines, eicosanoids and products of proteolytic cascades. The purpose and effect of these mediators is to evoke a local inflammatory exudate. Access through the postcapillary venules to the extravascular tissues at the infection is granted to plasma proteins and leukocytes (mainly neutrophils), which in a healthy state are restricted to blood vessels. The endothelium is activated and enables selective extravasation of neutrophils while stopping erythrocytes to exit. At the endothelial surface and the extravascular spaces, selectivity is caused by inducible ligation of endothelical-cell

selectins and chemokine receptors on leukocytes. Once the afflicted tissue site is reached, neutrophils are activated directly by the pathogen or by cytokines secreted by tissue-resident cells. Foreign agents are to be killed by reactive oxygen species (ROS), reactive nitrogen species, proteinase 3, cathepsin G and elastase. No discrimination between microbial and host targets leads to collateral damage to host tissues.

A successful acute inflammatory response is characterised by the elimination of the infectious agents. This is followed by a repair phase lead by tissue-resident and recruited macrophages. Chaing lipid mediators cause the transition from inflammation to resolution, from pro-inflammatory prostaglandis to lipoxins (anti-inflammatory). The recruitment of neutrophils is hindered by lipoxins and the recruitment of monotcytes (remove dead cells and initiate tissue remodelling) is promoted. Additionally, resolvins and protectins (another class of lipid mediators) play an important role in resolution of inflammation and in the initation of tissue repair.

In cases where the acute inflammatory response fails to eliminate the pathogen, the inflammatory process persists and acquires new characteristics. Macrophages replace the neutrophil infiltration and T cells, if infection exists. In cases where this response is still insufficient, a chronic inflammatory state arises. This includes the formation of granulomas and tertiary lymphoid tissue. In cases of persistent pathogens, an autoimmune response or undegradable foreign bodies cause chronic inflammation. In cases of unsuccessful attempts on pathogens or foreign bodies by macrophages, formations of granulomas and layers of macrophages occur on the walls of the infection. In conclusion, mechanisms of infection-induced inflammation

are well understood, while others such as chronic inflammatory states are poorly understood [3].

1.7. Mechanotransduction of vascular endothelial cells

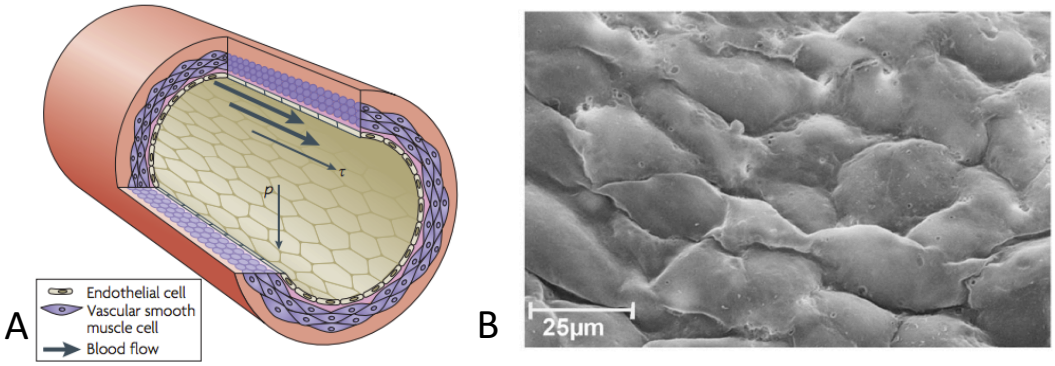

Figure 3: A: The mechanical forces that act on the vessel wall. Shear stress is directed with the blood flow and pressure acts normal to the vessel wall on the vasculature [4]. B: High resolution SEM image of endothelium of a common iliac artery [5]

The cardiovascular system is a well-regulated system that supplies oxygen to tissue at maximum efficiency under varying conditions. Consequently, the vasculature is exposed to mechanical forces such as fluid-derived fluid shear stress and pressure derived strain. These forces play an important role in regulating and stimulating physiological effects (Figure 3). Fluid shear stress (frictional force per unit area) acts tangentially on the endothelial cells. The blood pressure acts normal (*e.g.* perpendicular) to the surface and stretches circumferentially the ECs and smooth muscles cells (intima and media) [4]. An SEM image of an endothelial cell surface is shown in Figure 3.B [5].

ECs and VSMCs both react to mechanical forces to ensure the needs of the surrounding tissue. For example, an increasing shear stress causes NO production in ECs, which contributes to relaxation in smooth muscles. Flow has many effects on

the vasculature such as permeability, extra cellular matrix remodelling, angiogenesis, oxidative stress and - of interest in this work – inflammation and thrombosis [6].

Endothelial cells can transmit mechanical forces into biochemical signals, which then may cause gene expression and protein production. The subsequent expressed genes have functions and can cause pathological changes. This reaction pathway is shown in Figure 4, where fluid shear stress is sensed. Moreover, it activates signaling pathways (consisting of proteins) that affect gene expression, particularly in cell functions.

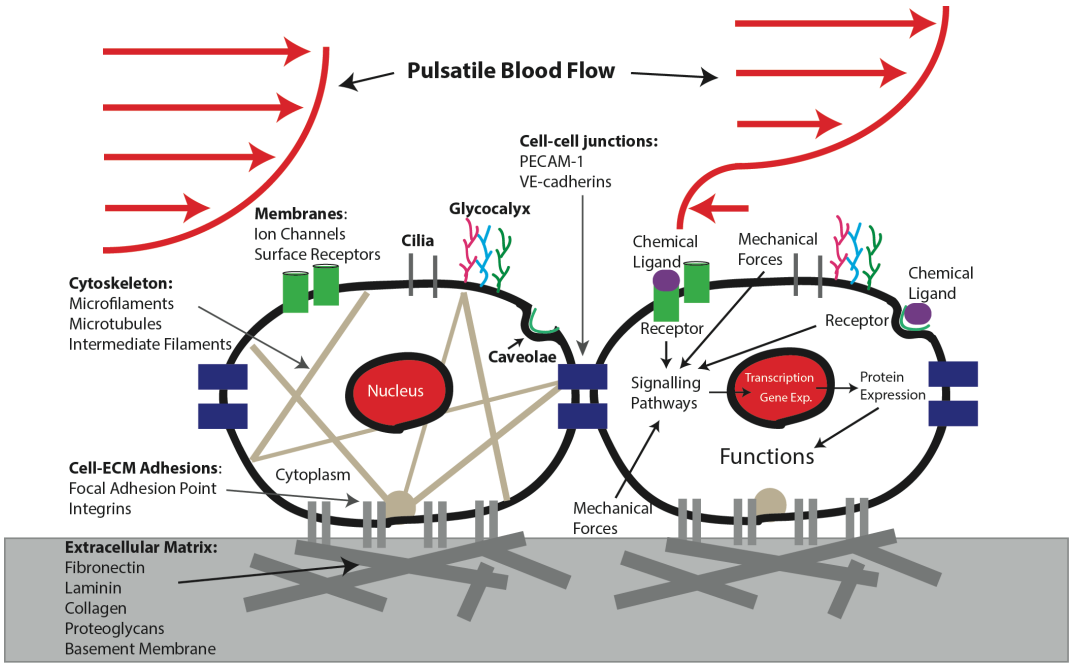

Figure 4: The elements and function of shear sensing endothelial cells. The left cell describes all the mechanotransduction elements, and the right cell shows schematically protein expression due to mechanical stimuli [7, 8].

To sense and transmit shear stress, the endothelial cells possess several sensing elements. These include glycocalyx, cytoskeleton, integrins, cell-to-cell junctions, receptor tyrosine kinase, heterotrimeric G-proteins, primary ciliae, caveolae, and ion channels. The sensing elements are schematically depicted in Figure 4 and are briefly described in the following paragraphs.

Glycocalyx: The luminal surface of an endothelial cell that is in direct contact with blood is coated with glycocalyx. Glycocalyx has a gel-like composition that varies in thickness and composition along the vasculature [9, 10]. The main function of glycocalyx is believed to be sensing of fluid shear stress and its translation into intracellular signaling [7]. The chemical composition of glycocalyx is a complex construct. Glycoproteins and proteoglycans form the main body of the glycocalyx. Negatively charged glycosaminoglycan (GAG) side chains are attached to the protein core of proteoglycans, and other core proteins are extruded from the GAG side chains [11, 12]. The glycoproteins contribute to the coagulation, fibrinolytic and haemostatic systems by serving as adhesions molecules [13]. Glycocalyx is believed to be an important mechanotransductor as its depletion blocks shear-induced NO production [14]. Glycocalyx provides a mesh like framework that is suitable for binding of plasma proteins (blood) and soluble GAGs.

Cytoskeleton: The cytoskeleton consists of microtubules, actin and intermediate filaments that physically connect the different regions of ECs. Mechanical forces are sensed on the apical, basal or lateral domain surfaces of the EC. The cytoskeleton enables communication within the cell by transmitting signals along the different regions [4, 7].

Integrins: Integrins connect intracellular to extracellular structures. They bind the extracellular matrix (ECM) proteins with their respective ectodomain via short cytoplasmic tails to the cytoskeleton [15]. The intracellular bound is dynamic, as the cytoskeleton controls the integrin ectodomain that affects the extracellular matrix. Vice versa, the extracellular matrix influences the shape and composition of the cytoskeleton. Cytoskeletal contraction or extracellular matrix rigidity induces forces

that are transmitted through the integrins across the membrane and initiate biochemical signalling [15]. The integrin bond plays a fundamental role in the cell adhesion of leukocytes and is thus very important for the immune system [16].

Cell-cell junctions: PECAM-1, VE-cadherin and VEGFR-2 have been reported to form a mechanosensory complex that leads to integrin activation and thus plays an evidential role in sensing shear stress. Moreover, a mechanical force applied to PECAM-1 actives Src. In the presence of VE-cadherin, Src activates VEGFR-2 which further activates PI3K and nitric oxide [17, 18].

PECAM-1 is a cell-cell adhesion molecule, a transmembrane immunoglobulin family member. It is largely expressed in endothelial cells and participates in haemophilic adhesion at cell-cell junctions. PECAM-1 is believed to take up an evidential role in mechanotransduction as the cellular connections experience large mechanical forces when exposed to shear stress, which subsequently converts the cell-cell adhesion molecules to a transducer [4, 7]. PECAM tyrosine phosphorylation is enhanced by several mechanical stimuli such as stretching, swelling, and tension. Moreover, it affects the transactivation of VEGFR2, activation of Erk, and the production of NO in response to flow [17].

It has been shown using a FRET-based tension sensor that shear stress increases forces on PECAM-1 [19]. An alternative study has shown that local tension forces on PECAM-1, created using a magnetic field and magnetic beads attached to the PECAM-1 proteins, resulted in the activation of PI3K, integrins and small GTPase RhoA [20]. This demonstrated conversion of a global signalling event in to a mechanical force.

VE-cadherins (or Cadherins 5) control the cohesion and organisation of intercellular junctions and are essential for limiting vascular permeability [17, 21]. Studies have revealed the importance of VE-cadherins in embryonic processes, angiogenesis, vascular maintenance and the repair of vasculature [21]. Moreover, VE-cadherins play an important role in junction mechanotransduction, and there is no clear evidence of direct transduction of shear stress. Direct exposure of force on VE-cadherin did not show pathways stimulation, whereas forces on PECAM-1 did [18, 22]. However, VE-cadherin plays an important role. This is most likely as an adaptor for the association of PECAM-1 and VEGFR2, and the activation of VEGFR2 [17].

Receptor tyrosine kinase: VEGFR-2, also named Flk-1, is a cell-surface receptor for VEGFA, VEGFC and VEGFD. VEGFR-2 plays a crucial role in regulating angiogenesis, vascular development, vascular permeability and embryonic haematopoiesis [23, 24]. A rapid activation of VEGFR-2 in ECs upon exposure to shear stress has been reported to be ligand-independent and thus suggests VEGFR-2 as a key mechanotransductor [25]. Moreover, VEGFR-2 activates pathways of the AKT and MAP kinases [26, 27] and is involved in NO production and activation of Src [22]. In addition, VEGFR-2 activation is compulsory for PI3K activation [18]. The VEGF family consists of two more members, VEGFR1 and VEGFR3. However, their functions have not been associated with shear stress [24].

Heterotrimeric G-proteins: “Heterotrimeric G proteins are molecular switches that turn on intracellular signaling cascades in response to the activation of G-protein-coupled receptors (GPCRs) by an extracellular stimuli [28].” The role of G-proteins as a direct mechanotransductor remains unclear, however there is evidence that flow and increased membrane fluidity activates heterotrimieric G-proteins. Several

studies have suggested that the lipid bilayer membrane itself takes up an important role in mechanochemical signal transduction, as purified teterotrimieric G-proteins activate on exposure to shear stress [29, 30].

Primary cilia: "Primary cilia is a solitary organelle that emanates from the cell surface of most mammalian cell types" [31]. They are maintained and structured by intra-flagella transport molecules, also named as intraflagella transport particles [32]. Evidence obtained in various ways has shown that in vascular endothelial cells, primary cilia's play an important role in sensing and transducing external forces such as fluid shear stress into intracellular signaling and biochemical responses. Experiments with cultured ECs have demonstrated that endothelial cilia cleave PKD1 and induce transient intracellular calcium responses [32]. The induction of Krüppel-Like Factor 2 (KLF-2) has been correlated with endothelial cilia, as non-ciliated cells express significantly less KLF-2 [33]. In addition, a dysfunction of endothelial cilia has been link to atherosclerosis [32, 34, 35].

Caveolae: Caveolae are defined as invaginations of the plasma membrane. These invaginations have a diameter of 60-80nm and are a construct of polymerised caveolins. They comprise of a subset of lipid-raft components such as cholesterol and sphingolipids. Caveolae can occur randomly alone or as a cluster of caveolae intermingled with non-caveolar membrane. Caveolae can lose their identity, with their ability to flatten out into the plasma membrane [36]. Several studies have shown that CAV-1 and caveolae are important factors of the mechanotransduction mechanism of ECs, however their exact function is largely unknown [36]. In cultured ECs, chronic exposure of shear stress increased the surface concentration of CAV-1 and subsequently increased the surface density of caveolae [37, 38]. Further studies

have confirmed these findings and have stated that integrins cause CAV-1 phosphorylation [39]. A study by Yu *et al.*[40] produced more evidence about the role of caveolae in mechanonsensing. In particular, CAV-1-null mice showed dysfunctions in flow dependent remodeling and dilation. Moreover, it has been shown that flow dependent activation eNOS requires CAV-1.

Ion channels: Multimeric proteins (ion channel receptors) form a passageway from one side of a plasma membrane to the other. These passageways - ion channels - open and close in response to chemical, electrical or mechanical stimuli. Ions can move out or in, once the ion channel is open. There exist several types of ion channels that are specific to particular ions [41]. Ion channels that are known to be activated by flow are K^+ channels, Ca^{2+} activated K^+ channels, Cl^- channels, Ca^{2+}channels and Na^+channels [42, 43]. However, the mechanism of activation of ion channels in response to flow remains unknown. Two possibilities have been argued in the literature: A direct activation caused by physical interaction of flow with the channel protein or structure that consequently leads to opening of the gate, and an indirect activation due to binding of ligand to surface receptors or through activation via G-proteins or integrins [42, 44].

1.8. Gene expression in vascular wall in response to external stimuli

Over the last decades, a growing body of evidence has shown that the feedback control of intracellular mechanics and signaling to external stimuli, such as shear stress and chemical compositions, act as maintenance for homeostasis at cellular level [8, 45]. The maintenance mechanism protects normal functioning endothelial cells against pathophysiological changes. Mechanosensing transduces mechanical

force into intracellular signaling pathways that control gene and protein expression in the nuclei that alter the functions of the EC. EC can change in response to mechanical forces with characteristics such as permeability, proliferation, inflammation, vasodilation [8, 45-47]. In Figure 5, an endothelial cell is displayed with its mechanosensors (*i.e.* cell-cell junctions, G protein-coupled receptor (GPCR), receptor tyrosine kinases (RTK), ion channels, integrins, membrane lipids, caveolae and glycocalyx), which can activate intracellular signaling throughout the cytoplasm in response to shear stress.

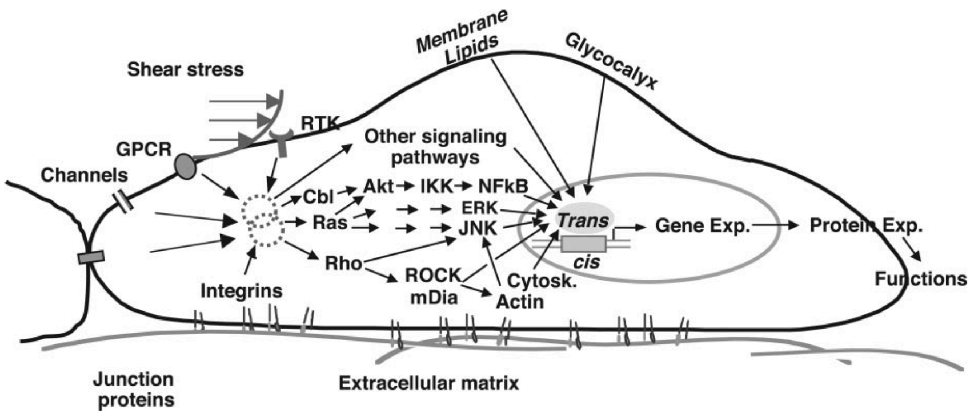

Figure 5: A schematic diagram that shows intracellular signalling triggered by mechanotransducer that cause gene and protein expression with cellular functions [8].

Examples of shear stress induced intracellular signalling in Figure 5 are: Activation of Ras, which induces the MAP kinase pathway (phosphorylation of ERK and JNK) and continually activates - in the nucleus - the transcription factors (AP-1) for gene expression such as MCP-1, small GTPase Rho that activates Rho kinase (ROCK) and mDIa that stimulates actin. In addition, the activation of Cbl, which phosphorylates AKT and triggers the NF-κB nuclear translocation. There are several other signaling pathways that are not displayed in Figure 5. However, Figure 5 does illustrate the

complexity of a vascular endothelial cell system that includes shear stress sensing, signaling pathways, gene expression and modulation of cell function [8].

Another mechanical stimulus is the circumferential stretch. Circumferential stretch is sensed by mechanotransductors and causes intracellular signaling that leads to gene expression and functional adaption of the cell. Lu *et al.* have reviewed the role of shear stress and stretch in vascular mechanobiology [48]. In Figure 6 the influence of wall shear stress and circumferential stretch on intracellular signaling in endothelial cells and smooth muscles cells are shown.

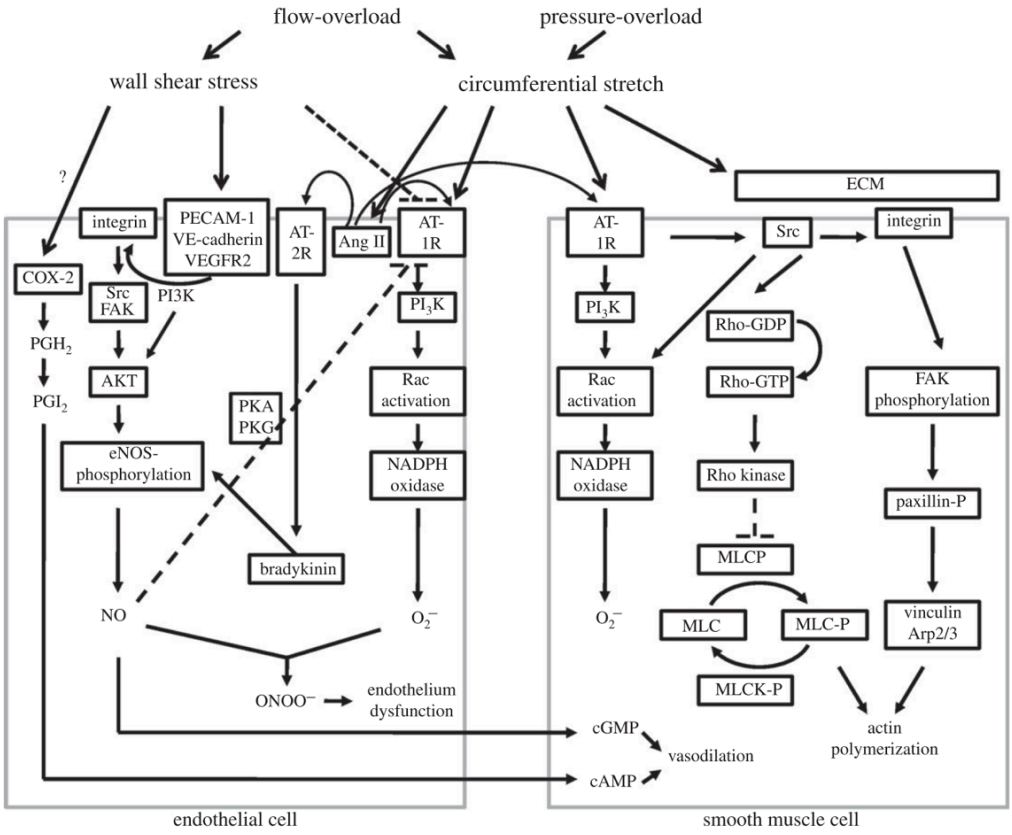

Figure 6: Flow and pressure-overload cause intracellular signaling induced by shear stress and circumferential stretch. Two cell types, endothelial cells and smooth muscle cells, are depicted. While shear stress acts only on the ECs, circumferential stretch is sensed in ECs and smooth muscles cells [48].

Figure 6 presents with the following reactions: the activation of PECAM-1 and integrins by wall shear stress, leading to eNOS phosphorylation. Endothelial nitric

oxide synthase (eNOS) produces nitric oxide (NO). NO is a fundamental molecule for the regulation of homeostasis by modulating vascular dilator tone, local cell growth and protection of the vessel from injurious consequences of platelets and cells circulating in blood [49]. Circumferential stretch activates in endothelial cells NADPH oxidase, which produces superoxide (O2-). Superoxide binds with NO and forms peroxynitrite.

An over-production of Superoxide results in the over-production of peroxynitrite, which reduces vasodilation due to a reduction in NO availability. A reduced vasodilation is characterised as an endothelial dysfunction. Circumferential stretch also activates signaling in the vascular smooth muscle cell via integrins as shown in Figure 6. Such activation causes the production of superoxide and FAK phosphorylation, which cause actin polymerisation in smooth muscle cells [48].

1.9. Pathological changes due to certain hemodynamic characteristics

Healthy vascular endothelial cells respond to mechanical and chemical stimuli to maintain homeostasis. In the case of abnormal physiological conditions - mostly described as flow disturbance or instabilities - endothelial cells can malfunction and may fail to maintain homeostasis. Since the first scientific publication on the topic by Donald L. Fry [50], there has been strong evidence suggesting that high wall shear stress causes endothelial damage and leads to pathological changes. A very substantial volume of research has been conducted to identify specific flow patterns (low or high shear stress and disturbed flow) that lead to endothelial dysfunction [51]. Surprisingly, all theories that link flow patterns to disease development have only partially succeeded and the exact relationship between blood flow and vascular

disease development remains unknown. However, there is general agreement that abnormal flow has a damaging effect on the vasculature. Abnormal flows are flow patterns that are chaotic, periodically unstable or stagnant. In most hemodynamic studies, abnormal flows are defined as a *disturbed* flow. It is important that a clear definition of abnormal flow is provided for either disturbed flow or flow instabilities. A disturbed flow is defined as recirculating, separating or stagnant. Flow instability is defined as a flow that is periodically unstable (beyond the periodicity connected to the physiological pulsatility) and/or chaotic. Flow instabilities develop in the transition from laminar to turbulent flow and increase in number until turbulence has fully developed. The influence of disturbed flow on ECs has been studied extensively [6], whilst little is known on the influence of flow instabilities on the vasculature. Most flow instabilities result in the same effect as disturbed flow, however the difference between a “simple” disturbed flow and a “complex” unstable flow must be distinguished.

To characterise hemodynamics, useful metrics are non-dimensional numbers such as the Reynolds and Womerseley numbers. The Reynolds number is the ratio of inertial forces to viscous forces. It characterises the flow as either laminar (low Re) or turbulent (high Re), and is given as

$$Re = \frac{\rho U L}{\mu} \qquad (1)$$

where ρ is the density of the fluid, U the velocity of the fluid, L the characteristic length of the fluid environment and μ the dynamic viscosity of the fluid.

To describe the pulsatility of fluids, the Womersley number α is used as a non-dimensional expression to compare characteristics of frequency-dependent flows.

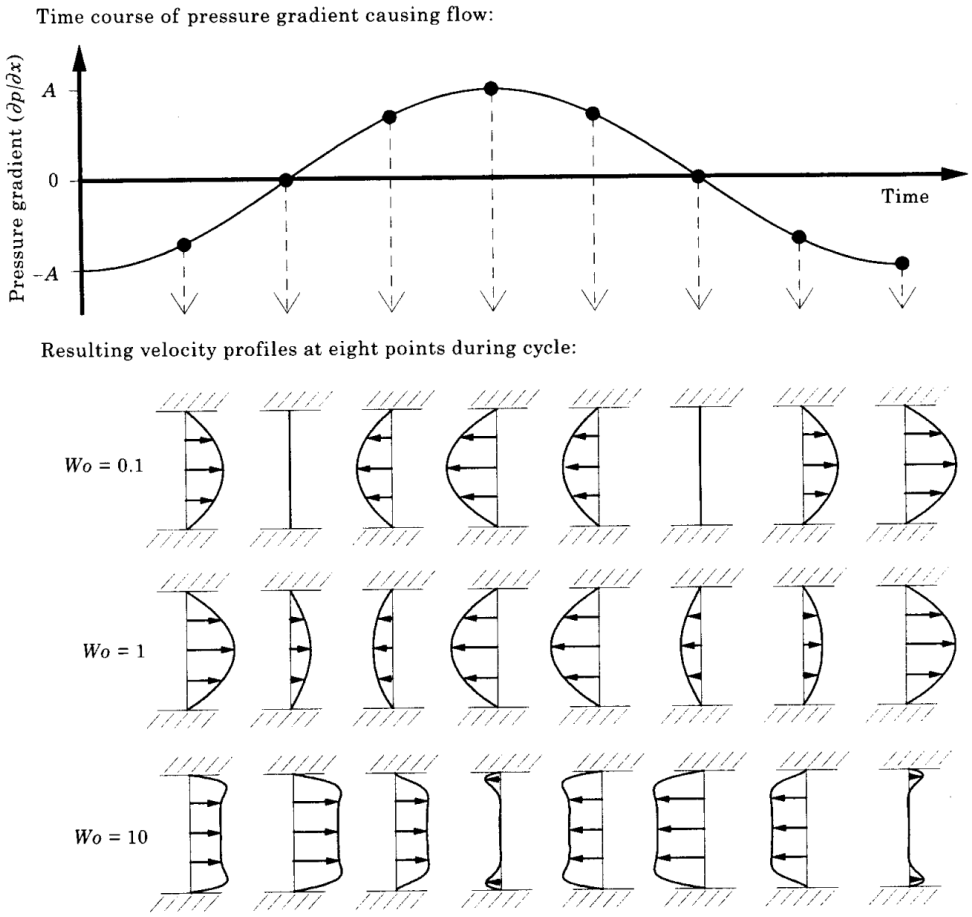

Figure 7: Velocity profiles for three different Womersley numbers (0.1, 1 and 10) at eight time points during sinusoidal pressure gradient cycle [52].

Flows with a low Womersley number (< 1) have a similar velocity profile to Poiseuille flow. At high Womersley numbers (> 10) the velocity profile is deemed as bulk flow and lags from the pressure gradient by 90 degrees. The Womersley number is given as:

$$\alpha = L\sqrt{\frac{\omega\rho}{\mu}} \qquad (2)$$

where ω is the angular frequency [rad/s]. In Figure 7, the velocity profiles for three Womersley numbers (0.1, 1 and 10) at 8 different time points of a sinusoidal pressure wave are depicted [52]. Velocity profiles at low Womersley number (0.1

and 1) are close to a Poiseuille flow profile. A high number causes a bulk like flow circulation at the maximum and minimum of the pressure gradient.

1.10. The effect of disturbed flow on endothelial cells

Disturbed flow is defined as recirculating, separating or stagnant and occurs naturally at arterial bifurcations, curvatures and at the aortic and venous valve sinuses.

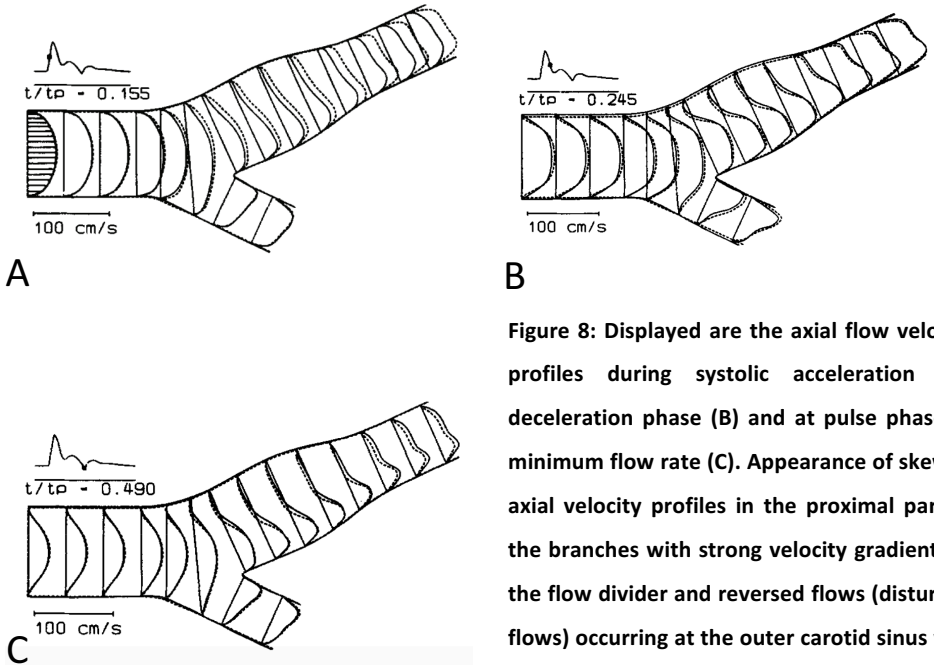

Figure 8: Displayed are the axial flow velocity profiles during systolic acceleration (A), deceleration phase (B) and at pulse phase of minimum flow rate (C). Appearance of skewed axial velocity profiles in the proximal part of the branches with strong velocity gradients at the flow divider and reversed flows (disturbed flows) occurring at the outer carotid sinus wall (systolic flow deceleration and minimum flow rate). [53]

Disturbed flow also occurs in pathophysiological conditions such as atherosclerosis, stenosis and aneurysms, and surgical interventions such as bypass graft surgery or stent deployment [6]. Examples of disturbed flow are shown with a compliant carotid artery bifurcation [53], a pulsatile flow over a modeled stenosis [54], and a cardiac cycle in a human aorta [55] in Figure 8, Figure 10, and Figure 11, respectively.

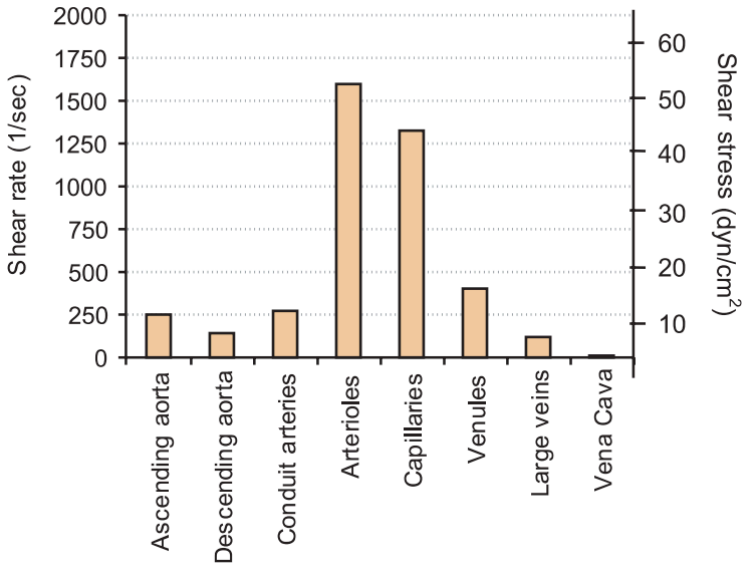

Figure 9: The shear stress magnitudes in different cardiovascular vessels of cat mesentery [196].

Typical shear stress and sheaer rate in different cardiovascular vessels of cat mesentery are depicted in Figure 9 [196]. In addition, the ECs are aligned and elongated in the direction of the flow.

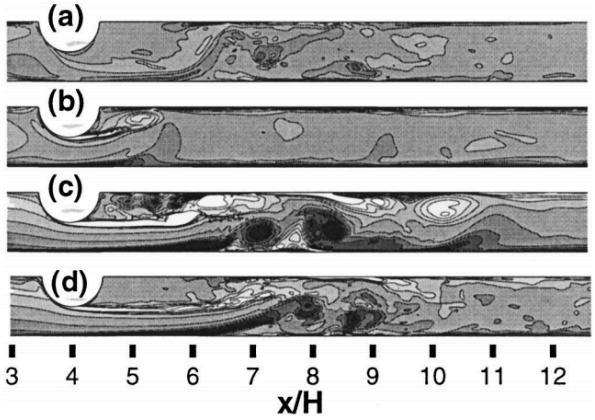

Figure 10: LES simulation of pulsatile flow of Re = 2000 through a modeled arterial stenosis. The counterplots shows clockwise (dark) and counterclockwise (light) vortices at a) t/T=0, b) t/T = 0.25, c) t/T = 0.5 and d) t/T = 0.75. It is obvious that a large flow disturbance with many vortices occurs after a stenosis, and especially in the diastole phase [54].

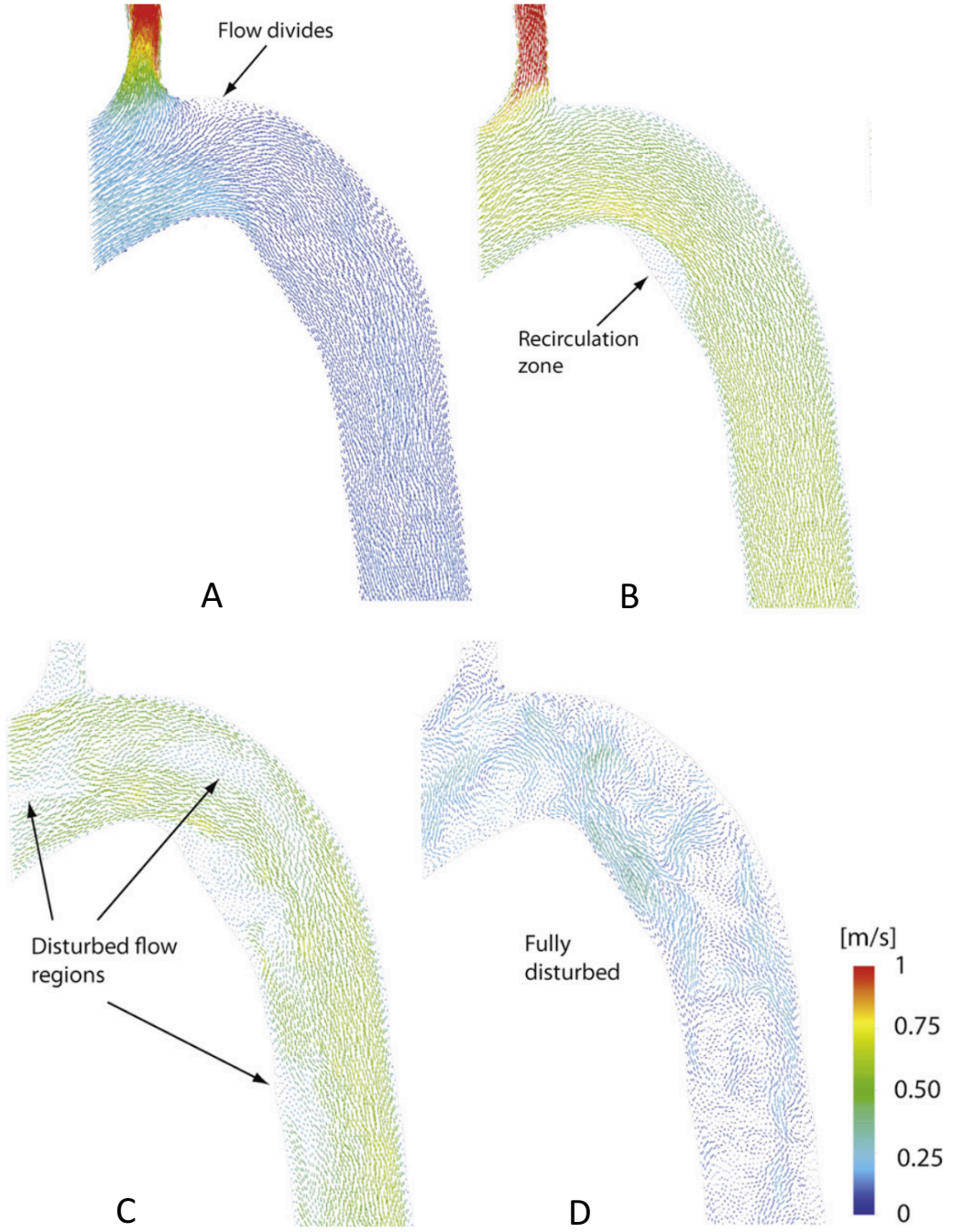

Figure 11: A large-eddy simulation (LES) of a cardiac circle in a human aorta. The flow vectors are shown at max acceleration (A), systole peak (B), max deceleration (C) and end of systole (D). Recirculation zones in the curvature occurs at systole peak, at maximum deceleration the flow breaks up in many disturbed flow regions, and at the end of systole the flow field is fully disturbed with local reversal flows, low velocities and no uniform direction. This unstructured flow remains during the whole diastole [55].

The actin stress fibres are long and organised and the cell-cell junction proteins are evenly distributed. Contrary to this, in regions of disturbed flow ECs reveal a

polygonal shape without orientation. Moreover, short and randomly located actin stress fibres and cell-cell junction proteins are discontinuously distributed [6].

Shear stress that is laminar, in a normal physiological range and definitive in its direction induces the expression of atheroprotective and antithrombogenic genes that maintain the vasculature with their antioxidant, anti-inflammatory, anticoagulant and antiapoptotic functions.

Low and reciprocating shear stress – the characteristic of disturbed flow – may induce gene expression of atherogenic and thrombogenic genes, enhancement of EC proliferation and modulates smooth muscle cells [6].

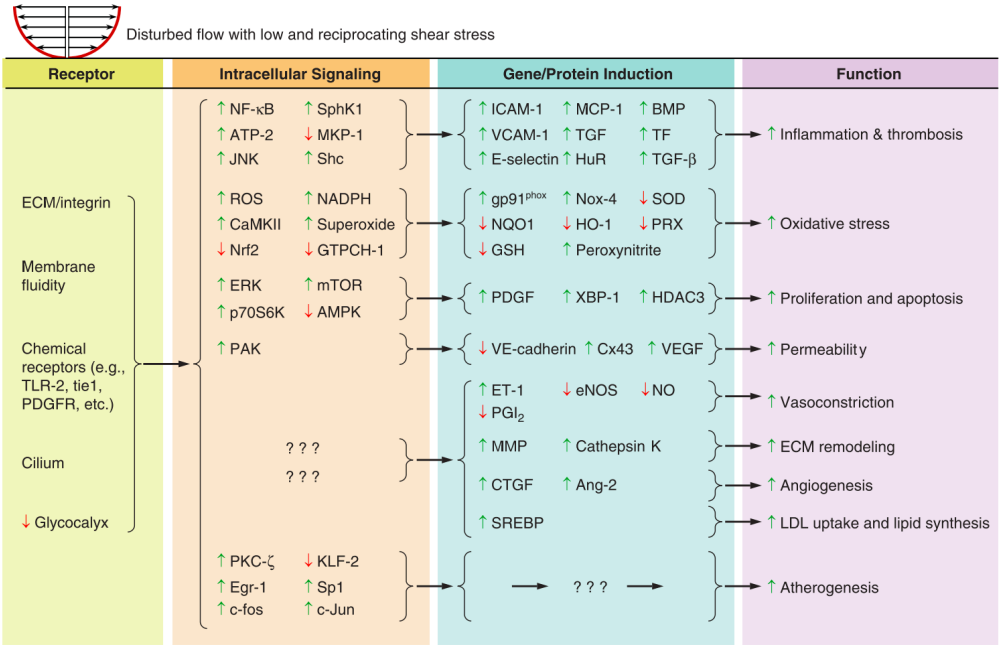

Figure 12: The effect of disturbed flow on intracellular signalling, gene/protein induction and their resulting functions. Arrows describe an increase or decrease in comparison with laminar high shear stress [6].

In Figure 11, a summary is provided regarding the current state of the art in *in-vitro* and *in-vivo* research about the effect of disturbed flow on endothelial cells. The disturbed flow is sensed by the previously described mechanotransducers (Integrins, Glycocalyx Cilia etc.) and causes different intercellular signaling pathways that lead

to gene production and finally to functional changes of the EC. The arrows indicate an increase or decrease in comparison with laminar high shear stress.

For examples, disturbed flow is sensed by the cell-cell junction that causes an up regulation of NF-κB, such an overexpression results in gene expression of CAMs, which enable greater adhesion of leukocytes. Due to disturbed flow an up regulation of NADPH induces the production of peroxynitrite, which leads to oxidative stress.

1.10.1. Importance of inflammation in aneurysms

The nature of cardiovascular diseases development is not fully understood. Diseas such as aneurysms [60] and atheroscleoris are closely linked to inflammation [6]. Here we briefly describe the role of inflammation in aneurysm formation, as an improved understand of the link between shear stress and inflammation might shed new light in the formation of aneurysms.

Cerebral aneurysms are balloon-like invaginations of cerebral arteries that occur in 1-5% of the population [56]. The cause of cerebral aneurysms is associated with disturbed flow conditions, high blood pressure and genetic factors. During growth of aneurysms the vascular tissue undergoes significant pathological changes and remodelling [57].

The most common locations for cerebral aneurysms are illustrated in Figure 13. These include the anterior communicating artery, middle cerebral artery, posterior communicating artery and the basilar tip. Due to the loss of internal elastic lamina and disruption of the media of the cerebral aneurysm wall during growth, the risk of rupture is high and fatal consequences such as ischemic stroke and haemorrhage make cerebral aneurysms a vascular disease with high mortality and morbidity.

Although surgical and minimally invasive interventions are well advanced, the mortality and morbidity are still very high [58].

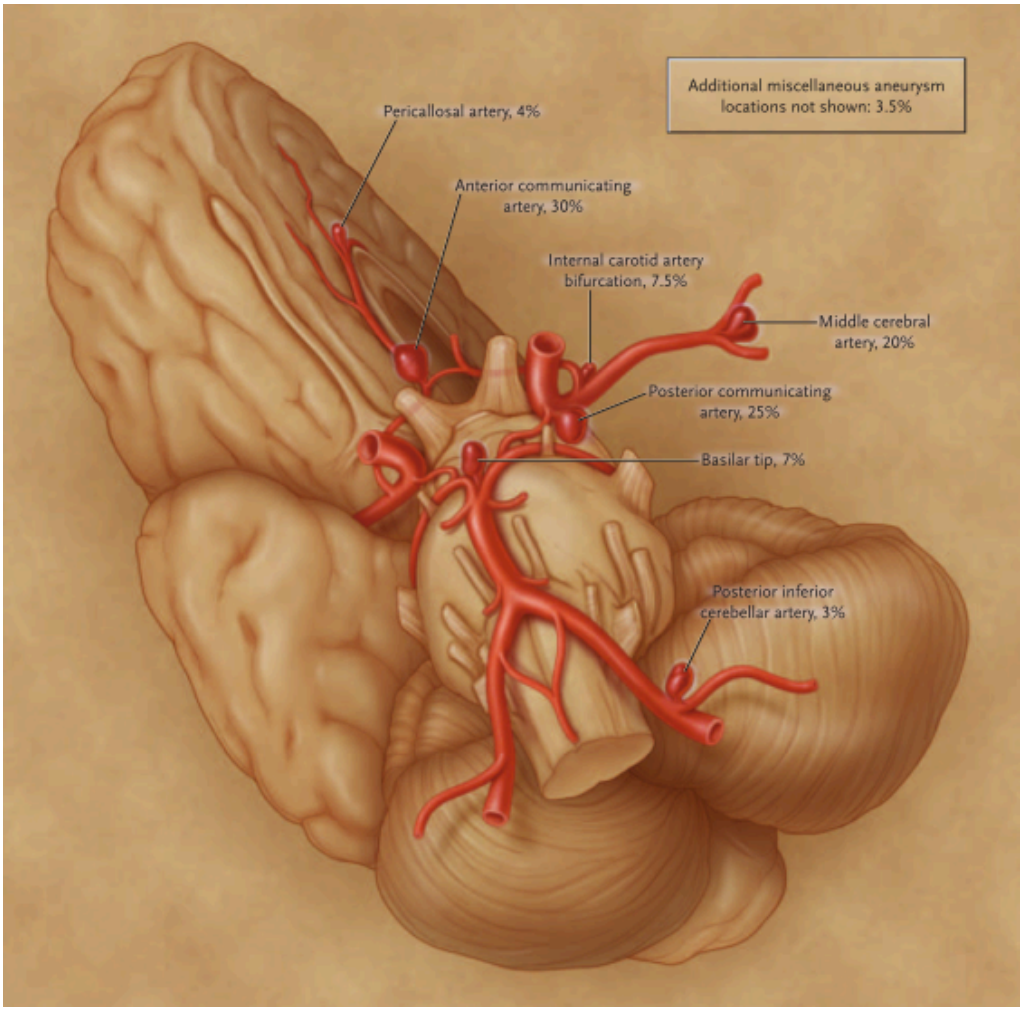

Figure 13: The intracranial vasculature with the most frequent locations of intracranial aneurysm [56].

Current therapeutic approaches are microsurgical clipping and endovascular treatment (stenting or coiling). The latter includes less risk, however intervention and following complications still have a high morbidity. Therefore, the optimal treatment for ruptured and unruptured cerebral aneurysms has not been identified yet [59].

The formation of aneurysms most commonly involves an endothelial dysfunction or injury, elevated inflammatory response, modulation of vascular smooth muscle cells, very substantial extracellular matrix remodelling, and as a result cell death and

vessel wall degeneration [60]. This possible formation pathway is depicted in Figure 14. Shear stress can trigger the initial endothelial dysfunction. Consequently, intracranial aneurysms (IAs) are mostly found at arterial junctions, bifurcations or eccentric vascular curvatures. Shear stress, endothelial dysfunction and inflammation are closely linked. As reviewed later, shear magnitudes can modulate the activation of NF-κB – a key inflammatory promoter – in endothelial cells (See section 1.16) Shear stress can also trigger other gene expressions, including MMPs that cause pathological changes of the vessel wall. In particular, MMP-9 deconstructs the extracellular matrix providing the space for an aneurysm to grow. MMPs are expressed by leukocytes (macrophages and mast cells) and VSMC. Due to inflammatory reactions, leukocyte migration will occur at site and may enhance the expression of MMPs. The overexpression of MMP-1, -2, and -9 in aneurysms has been demonstrated by Takemura *et al.* [61], and its pivotal role in aneurysm formation has been pointed out. Further studies have pointed out the central role of inflammation in the pathogenesis of cerebral aneurysms [59]. They conclude a pathway for cerebral aneurysm growth, and rupture with the following steps. Initial endothelial dysfunction due to hemodynamic forces, inflammatory reaction with macrophage presence, the degradation of extracellular matrix by MMPs and ultimately the degradation can lead to rupture. It has been suggested that investigations of possible drugs targeting inflammatory reactions, which treat aneurysm formation, growth and rupture shoud be carried out [59].

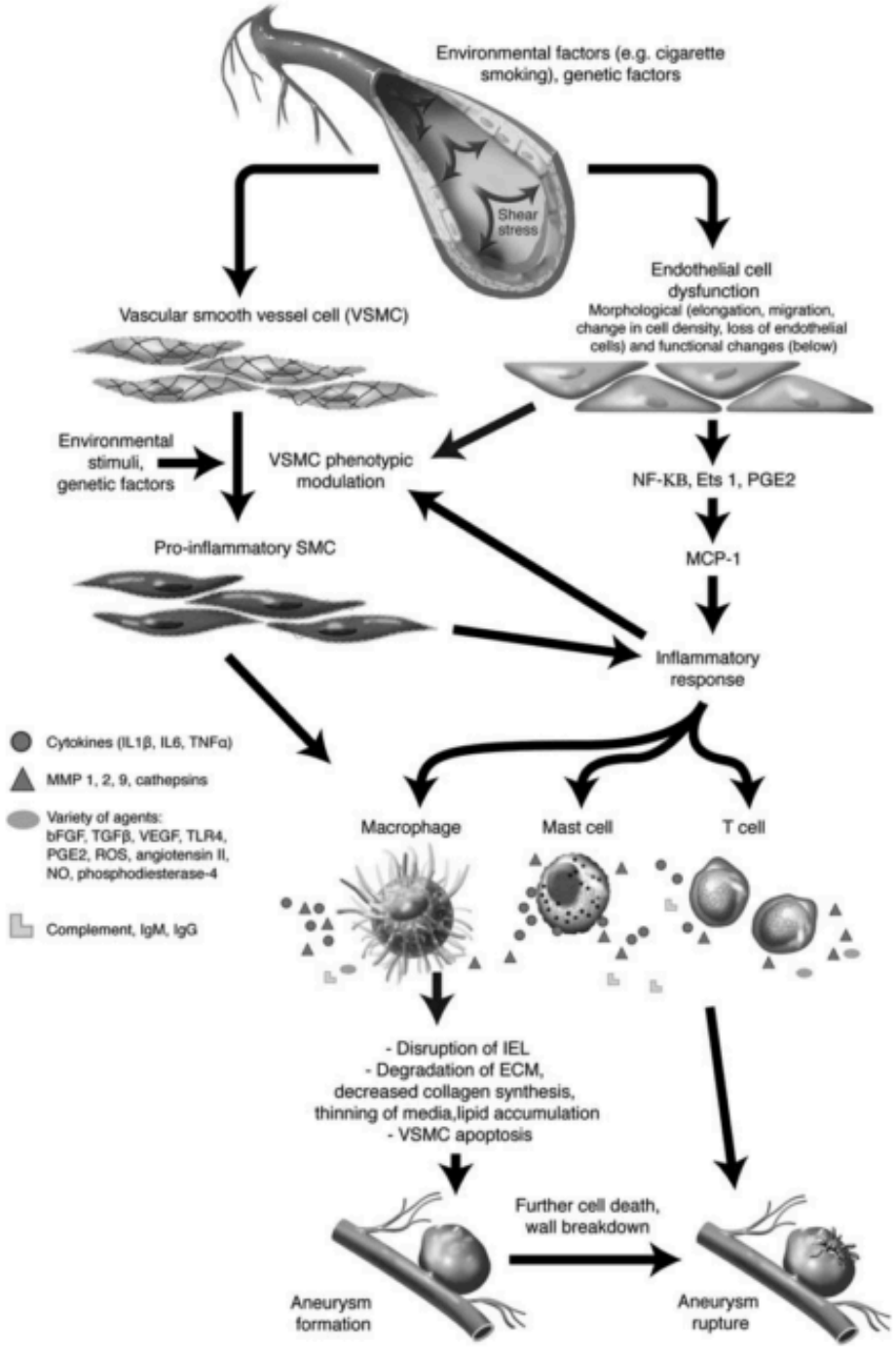

Figure 14: The role of inflammation in the formation of intracranial aneurysms. Abnormal hemodynamic flow pattern trigger endothelial dysfunction that causes an inflammatory response (cytokines release, mediates, leukocyte infiltration) and modulation of VSMC to a pro-inflammatory phenotype. The MMP expression due from macrophages is substantial (due to their high concentration) and therefore IEL is disrupted, ECM remodelled, and finally an aneurysm formed. The ultimate aneurysm rupture is caused by cell death and vessel wall degeneration [60].

In recent years, Ferumoxytol has emerged as a contrast agent in MRI [62]. Ferumoxytol is taken up by macrophages and thus shows inflammatory regions. A

pilot study demonstrated successful MRI imaging of macrophages in aneurysm walls [63]. A further pilot study demonstrated the uptake of ultrasmall superparamagnetic particles (USPIO) of iron oxide in abdominal aortic aneurysms, which identified cellular inflammation. Patients with higher uptake of USPIO had a much higher aneurysm growth rate [64].

1.11. The biology of NF-κB

Nuclear factor of κ light polypeptide gene enhancer in B cells (NF-κB) is a transcription factor that is one of the key inflammatory promoters. NF-κB plays a pivotal role in regulating cell signaling, cell growth, cell survival and apoptosis. Since the first discovery of NF-κB by David Baltimore [65, 66], a greater understanding of the NF-κB complex has been achieved [67]. Cytokines, pathogens, injuries and stresses can activate NF-κB transcription factors. The activation process of NF-κB is well regulated and the wrong regulation of NF-κB is related with chronic inflammation, autoimmune and metabolic diseases, and cancer [68-71]. An overview of NF-κB's pro-inflammatory target genes is shown in Figure 15.

NF-κB protein can be distinguished in to 6 different types: RelA (p65), RelB, c-Rel, p50 (p105 precursor), p52 (p100 precursor), and Relish. Each different NF-κB protein shares a conserved DNA-binding and dimerisation domain termed Rel homology region (RHR), which allows them to homo- or heterodimerise.

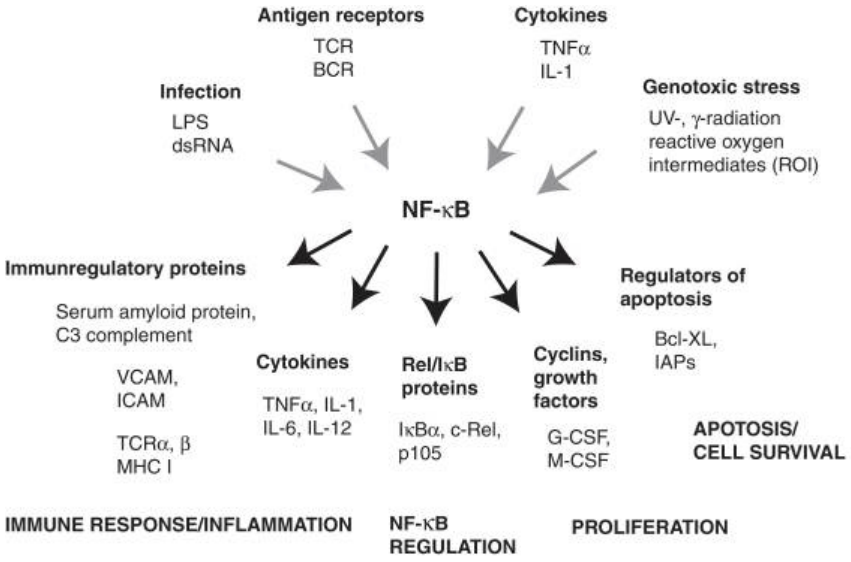

Figure 15: The target genes of NF-κB caused by different stimuli [72].

Aside from pro-inflammatory gene induction, NF-kB also expresses anti-inflammatory genes and induction of leukocyte apotosis during the inflammatory phase. IKKβ has also demonstrated anti-inflammatory effects. A proapoptotic role of NF-kB in neutrophils supports the anti-inflammatory evidence of NF-kB. Anti-inflammatory roles of IKKβ during baterical infections have been reported. IKKβhas been reported to suppress the proinflammatory M1 phenotype and promote anti-inflammatory M2 macrophages production. Furthermore, it has been reported that NF-kB inhibits a pro-inflammatory phenotype of TAM. All the findings are evidence of the anti-inflammatory role of NF-kB to control bactericidal and tumoricidal functions of macrophages. Finally, many gene knockout studies have demonstrated pro- and anti-inflammatory roles of NF-kB proteins [73].

By owning a C-terminal transactivation domain RelA(p65), RelB and c-Rel are able to target gene expression. Moreover, p50 (p105 precursor), p52 (p100 precursor) and Relish own an ankyrin repeat-containing domain at their C terminus, which makes them unable to activate target gene expression as a homodimer [67]. The crystal

structure and ribbon diagram of the p50/p65 heterocomplex bound to DNA is shown in Figure 16.

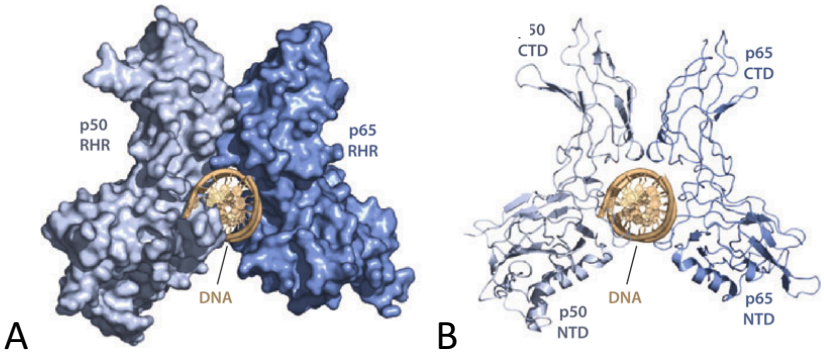

Figure 16: The butterfly p50/p65 heterocomplex bound to DNA with space-filling model of crystal structure (A) and as ribbon diagramm (B) [67].

1.12. The classic (canonical) NF-κB pathway

A simplified NF-κB pathway is depicted in Figure 17 [74]. NF-κB is bound to IκB, which is localised in the cytoplasm and prevents NF-κB from binding to DNA. Extracellular stimuli, in this example TNF-α can cause this interaction to break. TNF-α docks to TNFR receptor and activates the IκB kinase (IKK). Active IKK phosphorylates the IκBα of NF-κB-IκBα and causes ubiquitination of IκBα, this leads to the degredation of IκBα, and NF-κB becomes unbound. Unbound NF-κB can translocate into the nucleus and bind to its target sequences to activate gene transcription [67].

NF-κB up regulates the gene expression of IκBα. Newly synthesised IκBα then binds to NF-κB. This results in its inactivation by prohibiting NF-κB to translocate freely into the nucleus [65, 74, 75]. This effect is considered as a negative feedback loop.

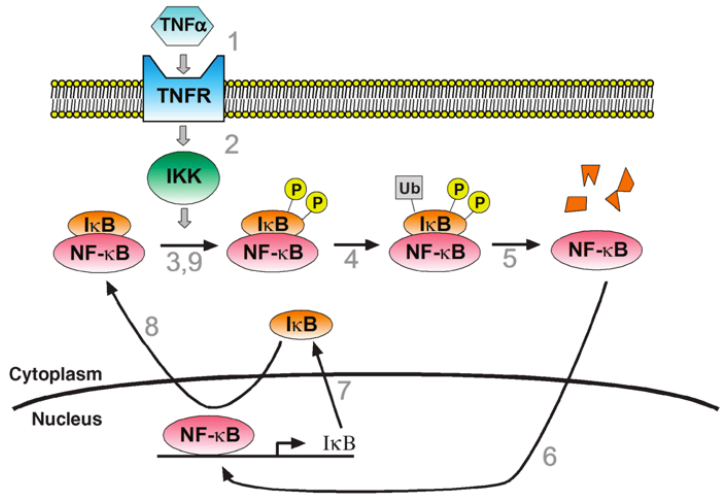

Figure 17: The NF-κB pathway model upon stimulation by TNFα. 1. TNFα binds to the TNF receptor. 2.TNFR activates IKK. 3. IKK dually phosphorylates NF-κB-IκB. 4. Phosphorylated IκB is targeted for ubiquitination. 4. IκB degrades mediated by proteasome. 5. Unbound NF-κB enters the nucleus. 6. NF-κB modulates gene transcription. 7. NF-κB upregulates the gene expression of IκB. 8. Newly synthesised IκB binds to NF-κB and shuttles it back to the cytoplasm. 9. New NF-κB-IκB complexes may unbound again if TNFα stimulation is still persistent, creating a loop [74].

1.13. The complexity NF-κB

A schematic diagram of the NF-κB pathways triggered by multiple sources is depicted in Figure 18. It shows that the signaling cascade of NF-κB can be triggered by different factors, including TNF receptors, TLR/IL-1, GF-Rs, LTβR, CD40, and BR3. From the diagram, the key role of IKK is evident, as all the stimuli cause IKK to activate.

As previously described, IKK phosphorylates and degrades IκBα. This causes the activation of NF-κB (classical or canonical NF-κB pathway). A second NF-κB pathway is described through receptors like LTβR, CD40, and BR3. Moreover, the kinase NIK is activated, which in turn activates IKKα. IKKα then phosphorylates NF-κB2 p100/RelB, which results in the nuclear translocation of the NF-κB p52/RelB complex (alternative or non-canonical NF-κB pathway).

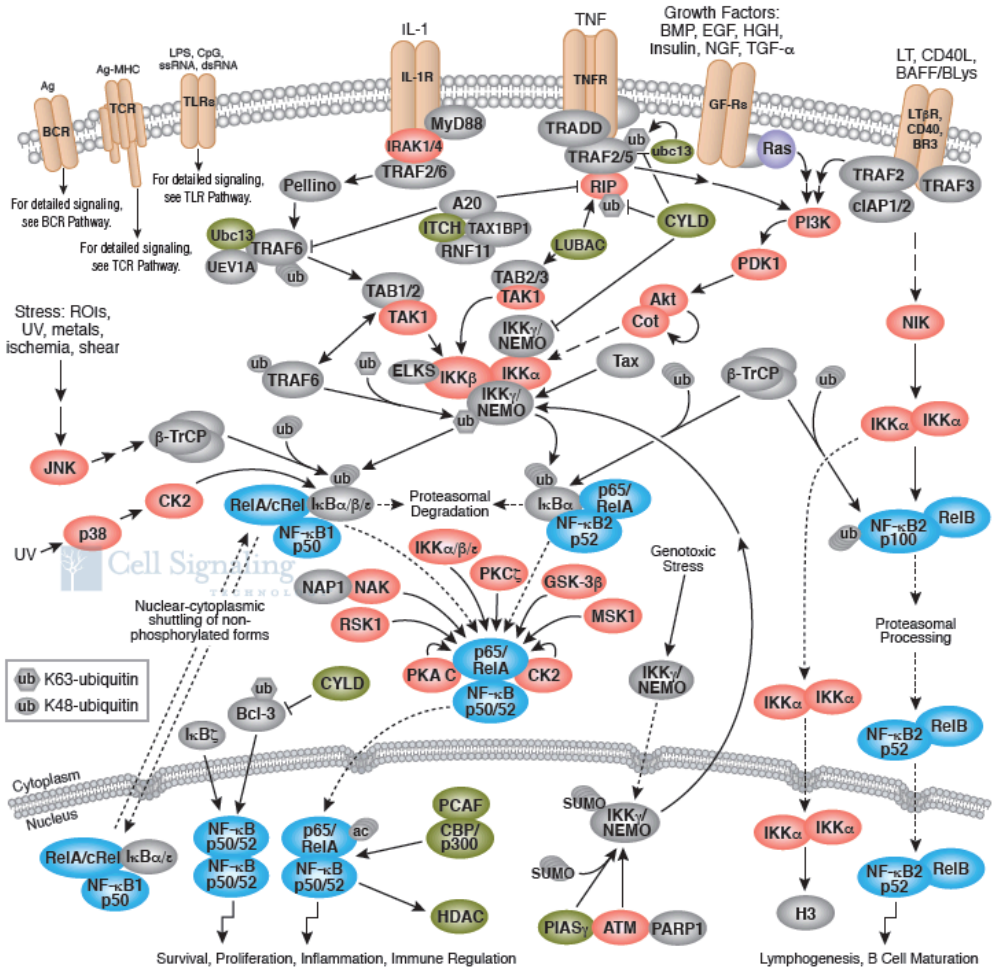

Figure 18: The full NF-κB complexity induced by various triggers [76].

1.14. The IκB protein family

The protein family of inhibitor κB (IκB) are an inhibitor and regulator of NF-κB. The IκB family members are the classic IκB proteins (IκBα, IκBβ, and IκBε), NF-κB precursor proteins (p100 and p105), and nuclear IκBs (IκBζ, Bcl-3, IκBNS). NF-κB can regulate the transcription of IκBα. This leads to the activation of IκB and inactivation of NF-κB. Activated NF-κB that translocate into the nucleus, transcribe IκBα. Transcribed IκBα expressed in the cytoplasm bind to and inactivate NF-κB [67].

1.15. The IKK complex

IKK consist of three subunits: IKKα, IKKβ and IKKγ. Activation of IKK is caused by phosphorylation of two serines in IKKα and IKKβ. Actived IKK leads to the rapid degradation of IκBα. Activated IKK also autophorsphorylates its own C-terminus, resulting in decreased kinase activity and thus it stops its own activity[77].

1.16. Observations and mathematical description of the temporal dynamics of nuclear NF-κB

Carlotti *et al.* [78, 79] provided the first evidence for the specific temporal dynamics of nuclear NF-κB. They transfected human gingival fibroblasts and monkey smooth muscle cells with a pEGF-RelA (RelA is a different name for NF-κB 1) construct. Using a confocal microscope, they observed the nuclear shuttling of pEGF-RelA induced by IL-1β. A large increase in nuclear pEGF-RelA concentration was observed at 20 to 60 minutes [78]. In a further study, they defined a mathematical model to describe the nuclear translocation of pEGF-RelA [79]. However, their model only covered the first 60 minutes and did not include a negative feedback loop.

Hoffmann *et al.* [75] proposed a complete model of the canonical IkBa-NF-κB pathway. This included the IkBa feedback-loop based on EMSA measurements. The measurement of human Jurkat T cells, human U937 monocytes and mouse fibroblast stimulated with 10ng/mL TNF-α (Figure 19.A) revealed that the nuclear NF-κB concentration has an oscillating temporal dynamic. Cells under TNF-α stimulation experience a very high nuclear NF-κB concentration at 30 minutes. This is followed by a drop in concentration at 60 minutes, and a medium nuclear NF-κB concentration at 90 minutes, which slowly fades out until 6 hours. Hoffmann *et al.*

presented a mathematical model for the NF-κB pathway as shown in Figure 19.B, C and D.

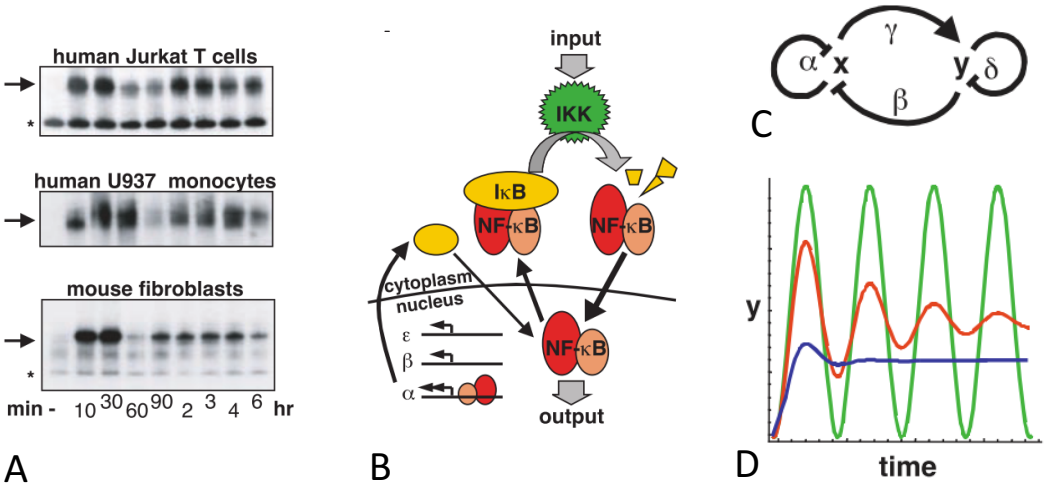

Figure 19: A: The negative feedback NF-κB pathway model by Hoffmann et al. [75]. A: EMSA of nuclear NF-κB in human T cells, human monocytes and mouse fibroblast stimulated with 10ng/mL TNF-α. B: IκBα-NF-κB signaling module. Stimulation activates IKK, which leads to phosphorylation and degradation of IκB proteins. NF-κB is freed and translocates to the nucleus, where it activates genes (IκBα, beta and theta). C: A system of two variables (*x* and *y*) with a negative feedback with feedback controller parameters (β and gamma – persitant oscillation) and selfregulator parameters (α and h – oscillating damping) hoffmann. D: Persistent oscillations (green line, high feed back efficiency and no damping, α=δ=0), damped oscillation (red line) and rising to plateau level (blue line, low feedback and high damping).

IKK is activated by stimulation that leads to phosphorylation and degradation of IκB proteins. Unbound NF-κB travels to the nucleus and transcribes from DNA new IκB proteins, which bind to NF-κB and inhibit its free movement. Thus, IκB proteins act as a negative feedback.

The authors mathematically described the model as a system of two variables (*x* and *y*) with a negative feedback. They included feedback controller parameters (β and γ – responsible for persitant oscillation) and selfregulator parameters (α and δ – responsible for dampening the oscillating). The relationship of the variables is defined as

$$\frac{dx}{dt} = S - \alpha \cdot x - \beta \cdot y \quad (3)$$

$$\frac{dy}{dt} = \gamma \cdot x - \delta \cdot y \quad (4)$$

with S being the stimulus. This model has been largely modified [74].

A notably extension of the Hoffman model has been made by Lipniacki *et al.* [80], whom added an IKK module that accounts for neutral, active and inactive cells. The Lipniacki model is sketched in Figure 20. In additional, they added the inhibitor factor A20. These additions have proven very useful, as they allow for the modelling of the activation of the NF-κB pathway based on stimulus variations.

Nelson *et al.* [81] have demonstrated nuclear NF-κB oscillation at single cell level. They showed that single cells in a population have phase differences in peaks and oscillation. In addition, they observed that the nuclear translocation of NF-κB is out of phase and decreased in frequency with and increased IkBa transcription rate. By varying the IkBa transcription rate of the Hoffmann model they could reproduce these findings with a mathematical model.

Pogson *et al.* proposed the first agent based model of the NF-κB pathway. They successfully demonstrated the NF-κB pathway model in a 3D environment. The model was subsequently extended with a negative feedback loop [82].

Lipniacki *et al.* [83] extended their model to a population level by incorporating stochastic switches for gene transcription (intrinsic noise), to create heterogeneity. Their models showed that early responses were synchronised while subsequent responses were out of phase.

Subsequently, Hayot *et al.* [84] investigated whether the NF-κB signaling model is prone to intrinsic (randomness in reaction taking place) or extrinsic fluctuations

(randomness in cytoplasmic or nuclear volume). They demonstrated that intrinsic noise has very little influence and only if DNA transcription is weak. However, extrinsic fluctuations lead to large cell-to-cell variations in amplitude and periodicity of nuclear NF-κB concentrations. As cell-to-cell differences are always present [85], extrinsic noise might be more suitable to capture heterogeneity of cell populations.

Choeng *et al.* [86] have studied the NF-κB pathway when stimulated with different TNF-α doses. They concluded that the duration and dosage of TNF-α has little effect on the initial NF-κB peak. They proposed that the IKK activation rate has a temporal profile that quickly decays after the onset of a TNF-α stimulus.

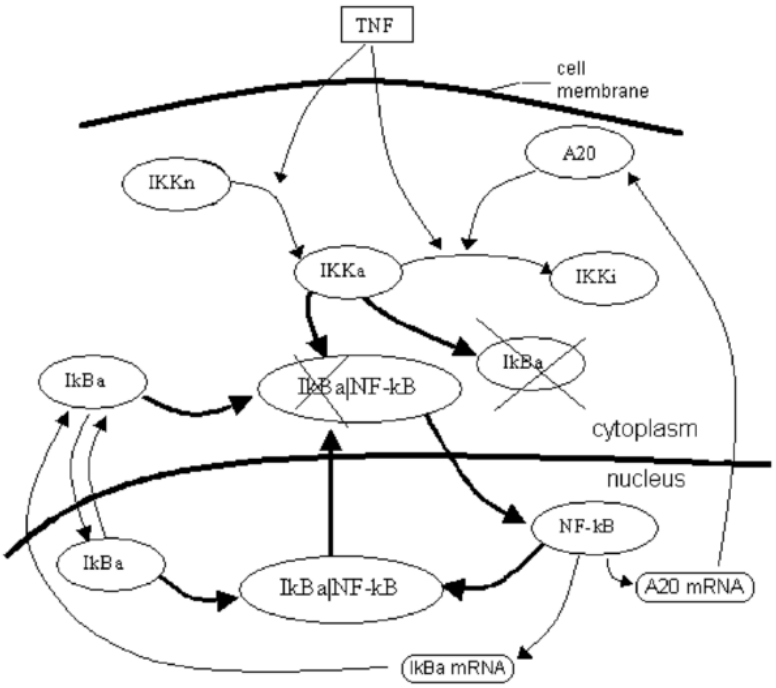

Figure 20: The mathematical model of the NF-κB pathway by Lipniacki at al. [80] including the extension of a IKK module (neutral IKK – IKKn, Active IKK – IKKa, and inactive IKK – IKKi) and A20. Crosses indicate ubiquitination of IκBα.

Further extensions of the NF-κB model have been made. These include the addition of a fourth IκBα inhibitor [87], new degradation rates for bound NF-κB and unbound IκB [88]. Moreover, Lipniacki *et al.* [89, 90] again extended their initial deterministic

model by incorporating stochastic switches for TNF-α receptors (including a threshold – minimum of receptors required to be active) and the transcription of IκBα and A20 (semi-stochastic model). They defined that there is a lower probability of a cell being activated using a lower TNF-α dose. However, the TNF-α dose had little influence on the nuclear NFκB peak. Shih *et al.* [91] determined that IκBα is mainly responsible for the temporal profile of nuclear NF-κB. By removing the initiating cytokine stimulus compound of the TNF gene, lethality of IκBα-/- mice was recovered with no evidence of inflammation or secondary lymphoid organ abnormalities.

Ashall *et al.* [92] stimulated SK-N-AS or MEF-cells with repeated pulses of TNF-α. Using live cell imaging, synchronisation of nuclear translocation of NF-κB (RelA-dsRedxp – knock in) was measured at different pulse intervals. Higher frequencies resulted in reduced translocation, which might be an effect of restlessness, whereas lower frequency pulses caused a high nuclear translocation at each pulse (Figure 21). The authors used a deterministic model to reproduce their findings. They defined that the activation of IKK and the inactivation of IKK by A20 is dependent of a stimulus switch (TNF-α).

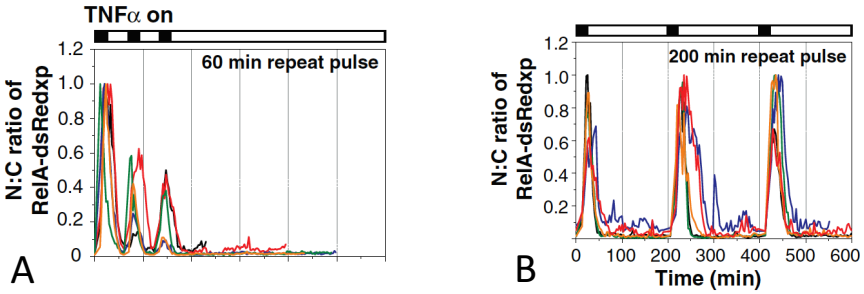

Figure 21: Temporal profile of nucleus to cytoplasm ratio of RelA-dsRedxp stimulated with three TNF-α pulses (5 min) with intervals of 60 (A) and 20 minutes (B) [92]

In a further study, Timothy *et al.* [93] analysed the NF-κB pathway triggered by LPS using live-cell imaging in 3T3 relA-/- cell line transfected with p65-dsRed and H2B-GFP. They observed noisy nuclear NF-κB translocation across the population. In particular, low stimuli created a large noise. With their single cell measurements, they defined a cell population model of the NF-κB pathway in which TRIF activation is a random event (intrinsic noise). Noisy patterns of single cell studies of the NF-κB pathway triggered by LPS has been shown in other recent work [94].

Using a microfluidic device, Tay *et al.* [95] investigated the IκBα-NF-κB pathway at a single-cell level in p65-knockout mouse fibroblast 3T3 cells. Figure 22.A and B shows live measurments of the nuclear NF-κB concentration of activated cells stimulated with either 10 or 1 ng/mL TNF-α. They showed that the NF-κB activity in a cell population is heterogeneous and the fraction of activated cells depends on TNFα concentration (Figure 22.C). They also applied and extended the model by Lipniacki *et al.* [80, 83, 90].

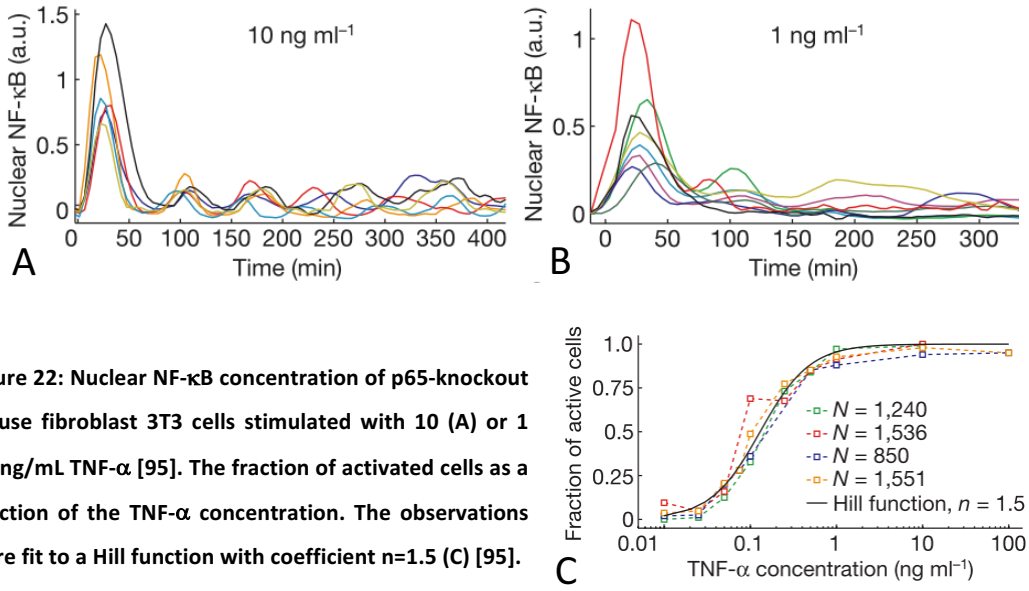

Figure 22: Nuclear NF-κB concentration of p65-knockout mouse fibroblast 3T3 cells stimulated with 10 (A) or 1 (B) ng/mL TNF-α [95]. The fraction of activated cells as a function of the TNF-α concentration. The observations were fit to a Hill function with coefficient n=1.5 (C) [95].

Turner *et al.* [96] modified the activation parameter of IKK to be dose dependent. In addition, the activation rate of IKK included a decay and random number to create stochastic fluctuations within the NF-κB system.

The NF-κB pathway was also extend with an agent based granuloma model [97] and the non-canonical pathway [98]. Moreover, Zambrano *et al.* [99] measured the GFP-RelA intensity in more than 2000 transfected mouse embryonic fibroblast stimulated with different TNF-α concentrations. Measurements of nuclear to cytoplasm ratio in GFP-p65 knock in fibroblast stimulated with 10 and 1 ng/mL TNF-α by Zambrano *et al.* [99] are shown in Figure 23. They demonstrated heterogeneity of nuclear translocation of GFP-RelA in a cell population. In addition, they confirmed that some cells did not show any oscillation as reported by Hoffmann *et al.* [75]. Furthermore, they measured that a small percentage of unstimulated cells experienced spontaneous nuclear translocation of GFP-RelA. Subsequently, Zambrano *et al.* [100] demonstrated that NF-κB is able to synchronise to periodic stimuli without memory.

The NF-κB model has gained much attention and many model improvements/additions have been established over the years. A concise overview is provided by Cheong *et al.* [74].

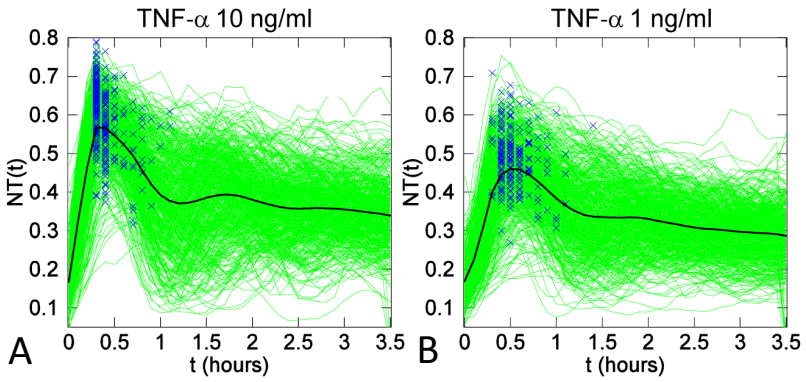

Figure 23: The nuclear to cytoplasm ratio for cells exposed to 10ng/mL (A) and 1ng/mL TNF-α (B). Blue crosses indicate the first peak observed. Black is the average of the total population [99].

The nuclear translocation of NF-κB has also been studied in vascular endothelial cells (HUVECs) with 20ng/mL TNF-α stimulation up to 60 minutes using IHC and ELISA at various time points [75, 101]. They measured a nuclear NF-κB peak at 30 minutes.

1.17. Activation of NF-κB in endothelial cells upon exposure to shear stress

Several studies have demonstrated that shear stress can activate NF-κB in endothelial cells [102-113]. Lan *et al.* [110] showed for the first time that in vascular endothelial cells DNA binding activities of NF-κB can be stimulated by shear stress. They exposed bovine aortic endothelial cells to shear stress of 12 dyne/cm^2. Under these conditions, DNA binding of NF-κB occured within 30 minutes and reached a maximum at 1 hour. Khachigian *et al.* [109] demonstrated that NF-κB p50-p65 heterodimers accumulated in the nucleus of cultured bovine aortic endothelial cells and bind to the PDGF-B shear stress response element. Mohan *et al.* [108] showed that low, high and pulsatile shear stress trigger the activation of NF-κB differently in human aortic endothelial cells (Figure 24). Whereas high shear stress (12 dyne/cm^2) showed an early transient increase in NF-κB DNA binding activity, low shear stress (2

dyne/cm^2) and pulsatile low shear stress (2 ± 2 dyne/cm^2) showed maximum activity of NF-κB DNA binding activity after exposure of 16 hours.

In-vitro studies by Bhullar *et al.* [103] showed that IKKs (IKKα and IKKβ) in bovine aortic endothelial cells are activated by shear stress (dyne/cm^2) in a rapid and transient manner (Figure 25). They also demonstrated that IKK activation causes IκBα to degrade (Figure 25.A), which frees and activates NF-κB (Figure 25.B). They also showed that integrins are involved in shear stress induced IKK activation. Hay *et al.* [106] studied the activation of NF-κB in human umbilical vascular endothelial cells on exposure to shear stress (15 dyne/cm^2). They confirmed a rapidly and transient activation of IKKs, a transient degradation of IκB and an increase in nuclear translocation of NF-κB (p50/p65 heterodimer) (Figure 26).

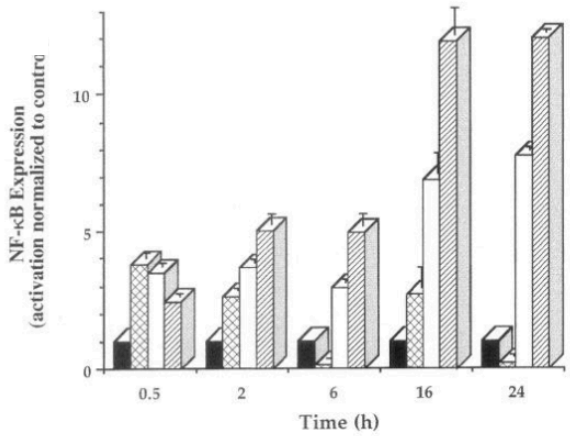

Figure 24: NF-κB DNA binding activity in HAEC exposed to high shear stress (crosshatched bars), low shear stress (open bars), pulsatile low shear stress (hatched bars) [108].

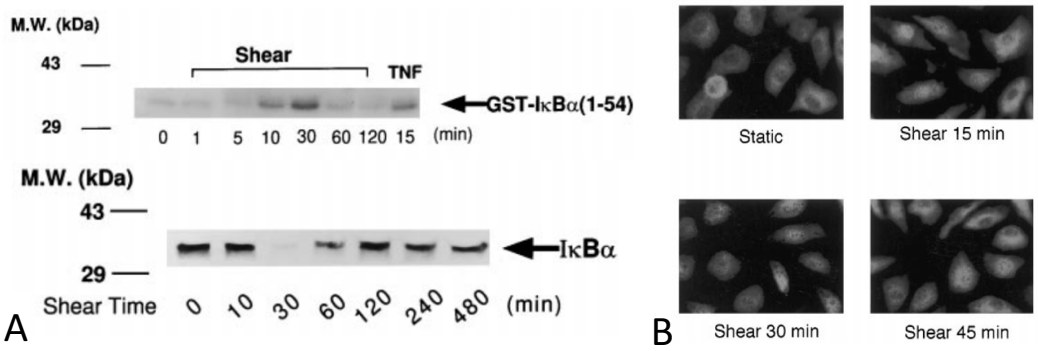

Figure 25: A: Immunoblots of shear stress (12 dyne/cm^2) activated IKK (top) and IκBα degradation (bottom) in BAECs for the indicated times of exposure [103]. B: Fluorescencemicroscope images of BAECs exposed to shear stress (12 dyne/cm^2) showing the NF-κB location in the cell at the indicated time. At 30 minutes NF-κB is mainly located in the nucleus [103].

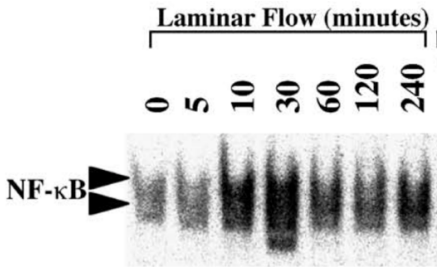

Figure 26: An increase in p50/p65 binding to an SSRE – increase in nuclear NF-κB activity in HUVECs exposed to shear stress (15 dyne/cm^2) for the indicated times [106].

Ganguli *et al.* [102] showed that transient degradation of IκB also occurs in ECs exposed to very low shear stress (1 dyne/cm^2). Further investigation by Mohan *et al.* [107] showed that IKK activity is significantly up regulated over a pro-longed timeframe (120 minutes) by shear stress (2 dyne/cm^2) in human aortic endothelial cells. Wang *et al.* [104] illuminated the shear induced NF-κB activation pathway. They suggested that shear stress and VEGF converge at the membrane receptor Flk-1 and recruits the adapter protein Cbl, which activates IKK. This also indicates that AKT acts upstream to IKK. In a follow up study, Wang *et al.* [105] revealed a potential pathway describing the link from shear stress to NF-κB activation, as shown in Figure 27.

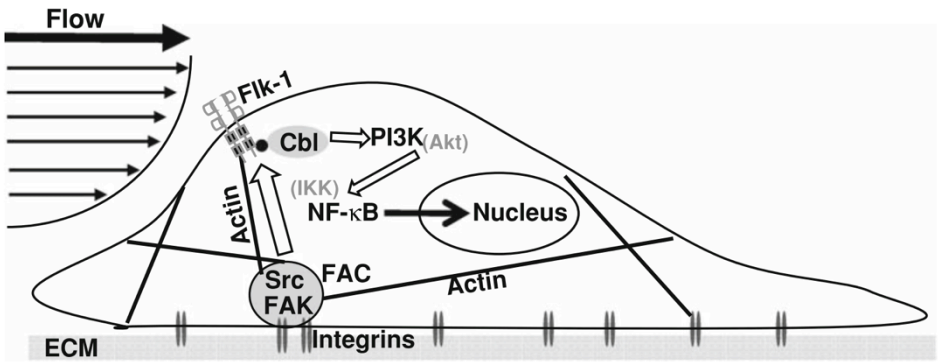

Figure 27: A potential pathway for shear stress induced NF-κB activation. Shear stress is sensed by integrins and transmitted via the actin network to turn on the Flk-1/Cbl complex. The phosphorylated Cbl recruits PI3K that causes phosphorylation of AKT, which subsequently activates the IKK complex that causes the activation of NF-κB [105].

The pathway is described as follows. Shear stress initiates signal transmission from integrins by integrin-associated tyrosine kinase and actin cytoskeleton. These then moderate the Flk-1/Cbl/PI3K/NF-κB pathway. The authors confirmed that Flk-1 and Cbl are involved in the shear stress induced activation of NF-κB. In addition, they demonstrated that PI3K – acts between Cbl and AKT – is essential for the shear induced NF-κB activation. Partridge *et al.* [113] demonstrated that p65 was accumulated exclusively in the cytoplasm after exposing HUVECs for 16 hours.

Recently, Feaver *et al.* [114] have applied manipulated frequency harmonics from human carotid shear stress waveforms to HUVECs. They demonstrated that the 0th and 1st harmonics are inflammatory regulators and uplift NF-κB activity. Furthermore, they suggested that PECAM-1 plays an evidential role in endothelial cell sensitivity to complex shear stress pattern, as PECAM-1 knockout mice showed reverse frequency-dependency.

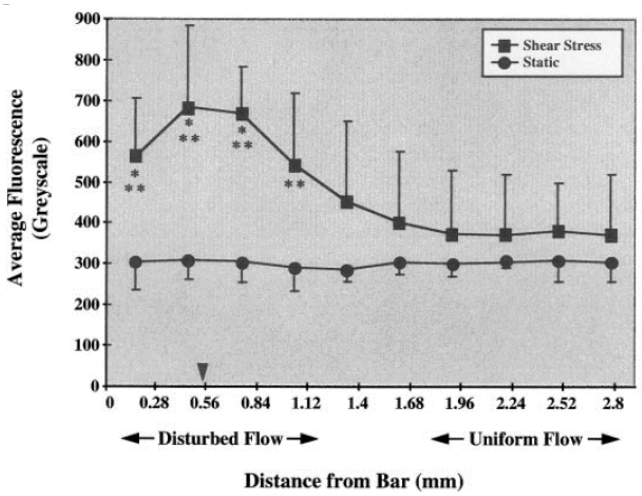

Figure 28: The average fluorescence of nuclear p65 in HUVECs exposed to a disturbed and uniform flow area for 30 minutes compared with static conditions [111].

Nigel *et al.* [111] created a disturbed flow in a cone-plate apparatus with a rectangular bar in front of the tissue culture coverslip. They observed, after 30 minutes of flow, an increased nuclear p65 concentration at the disturbed flow area in comparison with the uniform flow area (Figure 28). Won *et al.* [112] built a step channel flow chamber and studied the p65 concentration in porcine aortic endothelial cells at the disturbed and uniform flow area. They measured an increase of 1.5x p65 expression at the disturbed flow area. A further study exposed HAECs to shear stress gradients of 2 to 20 dyne/cm^2 with a media containing 1ng/mL TNF-α. The gradient channel had an increasing width. Using IHC, the authors measured an increased activation of NF-κB at higher shear stress magnitudes (9 to 16 dyne/cm^2) after 60 minutes of flow with additional 1ng/mL TNF-α. In addition, there have been investigations reported in the literature involving in vivo NF-κB studies. These have demonstrated upregulation of NF-κB in low shear regions, when compared with high shear regions [112, 115, 116]

1.18. Other important inflammatory molecules

Cell adhesion molecules (CAMs) such as VCAM-1, ICAM-1 and E-selectin are another important inflammatory molecule group. They play a crucial role in the attachment and transendothelial migration of leukocytes [117]. Migration of leukocytes into endothelial cells is a main inflammatory characteristic and is observed in atherosclerosis lesions [117] and aneurysms [60]. In-vitro studies have shown that the expression of CAMs, particularly VCAM-1 and ICAM-1, is directly linked to activation of NF-κB and shear stress [118-122].

Migrated leukocytes such as macrophages can secrete matrix metalloproteinases (MMP) in response to inflammatory stimuli. MMP is a zinc-dependent endopeptidase, produced by cells (mast cells or macrophages) and present in the vascular wall. The degradation of extracellular matric (ECM) components has been assigned to be the key function of MMPs, while MMP-9 has named to be a major component in vascular remodelling [123]. Studies have shown that MMP-9 production can be induced by shear stress and is NF-κB dependent [124-126]. MMP-9 proteins are normally inhibited by TIMP-1. Studies have shown that TIMP-1 is not affected by shear stress [124]. In this work, it is speculated that an overproduction of NF-κB occurs due to abnormal shear stress, and consequently results in an overproduction of MMP-9. Consequently, a large amount of MMP-9 cannot be fully inhibited by the TIMP-1 present. It is well known that MMP-9 leads to the degradation of ECM, in case of an aneurysm this is favourable for further growth [127]. Recently, TIMP-1 has been suggested as a possible drug to prevent the growth of aneurysms [128].

1.19. Live-cell imaging – Plasmids, transfection, microscopy and quantitative analysis

Fluorescent tools have enabled the study of stochasticity and heterogeneity in biology. Tagging of molecules of interest allows for investigation of the full dynamics, including temporal and spatial concentration or reactions. The most common methods employed include, fluorescent protein fusion, fluorescent non-natural amino acids, in situ chemical labelling, fluorescent and antibody labelling [129].

Fluorescent protein fusion is very popular and many companies offer plasmids of target gens tagged with a fluorescent protein. *Addg*ene (Cambridge, MA, USA) is a non-profit organisation, which offer a wide range of plasmids. Other companies that offer plasmids include *Promega (Madison, Wisconsin, USA)* and *Clontech (Mountain View, CA, USA)*.

A more direct approach would be the use of a CrisPr-Cas9 system, which allows for the insertion of a fluorescent protein tag into the protein of interest [130]. However, CrisPr-Cas9 systems are still in their infancy. Moreover, they still have still big challenges to overcome when applied to primary human cells.

Plasmids of fluorescent fusion proteins must be inserted into cells via a transfection process. The most common transfection processes are viral transfection (+high efficiency, +easy to use, - potential hazard to worker, -insertional mutagenesis and –immunogencity), cationic lipids (+easy to use, +many available products, -difficult to apply to specific cells), and electroporation (+no need for vector, -high experimental skills required, -high cell death) [131]. In this work, electroporation has been found to be the most suitable transfection method for primary human cells, despite the

high cell death. Once the plasmid is transfected into the cells, the successful expression of the fluorescent fusion protein has to be imaged with microscopy.

Traditional microscopy of fluorescents is facilitated with a wide-field or confocal microscope [132]. Drawbacks in wide-field microscopy are emitted photons from out-of-focus molecules, which cause non-uniform illumination. This decreases the precision of localisation. Confocal microscopy abolishes light from out-of-focus molecules due to the pinhole and hence the noise level is low. However, confocal microscopy has a very slow acquisition time and is unsuitable for high-throughput measurements [132].

Quantification of live-cell imaging recordings is still a technical challenge. Popular cell quantification software suites include TimeLapseAnalyzer, TLM-Tracker, Icy, TrackMate, CellProfiler and the Tracking Tool [133]. Schwarzfischer *et al.* [134] have documented a very efficient fluorescence image normalisation algorithm. The algorithm includes background removal of non-uniform illumination and a bleaching correction. Tracking particles in time lapses can be built on old concepts such as Particle Image Velocimetry (PIV) [135], which uses the approach of comparing distance and size per time frame.

In this thesis, live-imaging was performed with a confocal and widefield microscope. The confocal microscope was used for initial test, while high-throughput experiments were perfomerd with a widefield microscope.

1.20. Exposing cells to shear stress in-vitro

It is well known that hemodynamic forces activate signal transduction and gene expression [6]. Due to the difficulty of measuring these effects in-vivo, in-vitro

experiments with isolated endothelial cells have been performed with various devices to simulate in-vivo like flow conditions. The most popular devices are parallel plate flow chambers, cone-plate apparatus, orbital shakers or customised microfluidic channels [136]. The first three are shown in Figure 29. The parallel plate flow chamber is also a popular device. The chamber consists of rectangular channel, with a height of few hundred micrometers and a bottom surface area in the order of 5x50mm. Cells are grown on the bottom surface. The rectangular channel has an inlet and an outlet to allow perfusion. The pressure drop across the parallel plate flow chamber is very small. The flow is driven by a peristaltic pump or gravity. Moreover, cells experience a constant uniform shear stress [136-138]. Advantages of this system include, constant shear stress, controllable flow, easy to grow cells and ease of use for live imaging. Disadvantages include, 1 – 5 samples at a time, low throughput and that it is expensive.

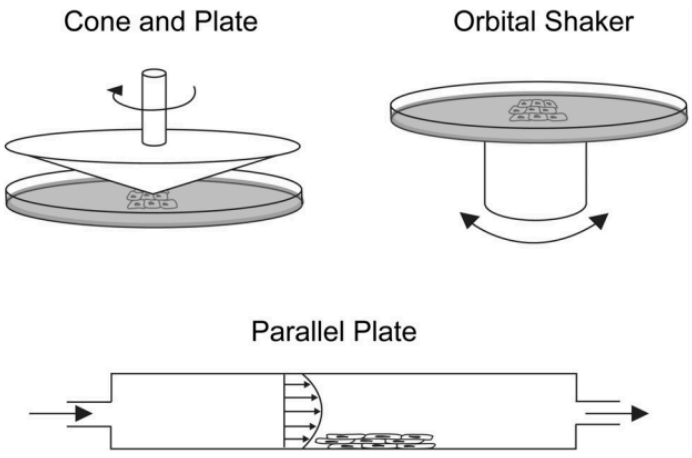

Figure 29: Standard methods to apply shear stress. The cone and plate creates a Couette flow. The orbital shaker has a flow profile created by rotational inertia created by a swirling plate. The parallel plate has a Poiseuille flow profile [136].

Parallel plate chambers can be modified by changing the shape and keeping the directional flow. Usami *et al.* [139] have designed a linear increasing shear stress

flow chamber, which is a parallel flow chamber with increasing width in the direction of flow. The increasing width creates an increasing shear stress. Dolan *et al.* [140] created a flow chamber with a converging shear stress gradient, followed by a straight section (constant uniform shear stress region), which generated a diverging shear stress gradient. Wang *et al.* [141] designed a flow chamber that enabled a change in the direction of the flow by rotating the sample glass slide.

Customised parallel plate chambers allow for the investigation of the flow profiles of interest such as gradients, stenosis or directional changes. Disadvantages include the expensive process of channel validation (CFD and for absolute certainty particle image velocimetry (PIV)), manufacturing a new device for each experiment (ca. 2-4 hours of work), and unforeseen complications (commercial devices are tested and should be more reliable).

A cone and plate device creates a shear stress by rotating the top cone. The flow has a Couette profile [142]. The cells are grown at the bottom surface and are exposed to the rotating shear stress. Moreover, alteration of shear can be generated by changing the rotation speed [114] or by inserting obstacles to disturbed the flow [111]. The cone and plate device is difficult to use in live imaging. However, advantages include high throughput and control over the applied shear stress.

The orbital shaker creates a complex flow profile within wells placed on top of the orbital shaker. It has been used to study the chronic effect of shear stress [143, 144]. Advantages of an orbital shaker are high throughput and inexpensive equipment. However, a big disadvantage is the complex flow due to inertia effects that is very difficult to characterise (or computationally expensive) [145]. For example the physics of a fluid on a see-saw rocking device [146].

The hollow fibre bioreactor is another device that can be used. In this device cells are seeded directly into hollow fibres. The hollow fibre is then perfused with the same setup as applied for parallel plate chambers. Hollow fibre bioreactors have been used for long exposure experiments (days) [147]. Hollow fibre bioreactors provide a very realistic reproduction of the cardiovascular environment. Disadvantiges are sterility and imaging of samples (difficult to image live).

Another option is to build customised microfluidic devices that precisely mimic the effect of shear stress on cells. Microfluidic devices are made of PMDS chips and are perfused with a syringe, gravity, or a peristaltic pump system [148, 149]. Advantages of microfluidic systems are precise shear control, live imaging and broad design options. Disadvantages include low throughput, custom design, each device must be fabricated individually for each experiment.

In this thesis, cells have been exposed to a parallel plate (Ibidi slides - see methods) and a custom made shear stress gradient device. The effect of uniform low or high shear stress on the nuclear translocation of NF-κB has been studied using parallel plate devices. Moreover, a custom made shear stress gradient device has been used to investigate if a monolayer of endothelial cells exposed locally to different shear stress magnitudes causes the same effect as under uniform shear stress at specific shear stress magnitudes, and if a gradient alters the NF-κB dynamics in a cell population.

2. Experimental Methods

Summary: *This chapter lays out the experimental methods used. First, the tissue culturing methods are described. These include cell culturing, cryopreservation, plasmid DNA purification, and transfection of cells. Next, the preparation of cells for experiments with TNF-α and flow are described. The setup for the flow experiments with its perfusion system, flow rate and pressure, channel setup and shear stress on cells have been described in detail. The design and manufacturing of the custom-made gradient channel is outlined. The procedure for immunohistochemistry and the antibodies used are presented. The imaging method for both immunohistochemistry and live-cell imaging are described. Furthermore, the algorithm to track and quantify the nuclear GFP-RelA intensities of single cells is outlined in detail*.

2.1. Cell Cultures

Human umbilical endothelial vein cells (HUVECs) with a purity of > 95% were purchased (PromoCell, Heidelberg, Germany). Cells were maintained in endothelial cell growth medium (PromoCell, Heidelberg, Germany) containing fetal calf serum 0.02 mL/mL, endothelial cell growth supplement 0.004 mL/mL, epidermal growth factor 0.1 ng/mL, basic fibroblast growth factor 1ng/mL, heparin 90 ug/mL and hydrocortisone 1 ug/mL. HUVECs were grown in T25 or T75 tissue culture flasks (Corning, MA, USA), together with 7 mL or 21 mL endothelial growth media. The flasks were incubated at 37 °C and humidified with 5 % CO2.

On reaching confluence within the culture flask, HUVEC cells were washed with PBS, incubated with 1 mL/3 mL of trypsin for the detaching of cells, and neutralised and collected with a supernatant. The supernatant was Dulbecco's modified eagle medium (DMEM), which contained 10% fetal bovine serum, and 2% L-glutamine. The cell suspension was centrifuged at 280 RCF at 37 °C for 5 minutes. Following centrifugation, the supernatant was removed and the cell pellet mixed with various growth media. These were adapted to the environment. For example in the culture

flasks, well plates or flow channels for further passaging and cultivation. Cells were tested for mycoplasma (negative).

HUVECs were used due to their availability, easy maintance and cost-efficiency. In addition, the live-cell imaging of p65 in primary human cells has only been poorly achieved. Therefore, this study delivers a better verification of the setup and for this HUVECs were a very suitable cell line. HUVECs are normally exposed to a shear stress between 4-10 dyne/cm^2[6]. As shown later in the experiments, HUVECs show a normal generic response to a inflammatory stimulus such as TNF-α.

The cell growth media contained hydrocortisone 1 ug/mL (anti-inflammatory), which may have had an effect on the translocation of NF-κB. A previous study has demonstrated that intravenous injections of hydrocortisone (100 mg) in humans led to an increase in IκBα levels and a decline in nuclear translocation of NF-κB [150]. However, the TNF-alpha and flow experiments carried out in this work were perfomed using DMEM solution without any hydrocortisone, hence the hydrocortisone effect from the growth medium can be regarded as negligible.

2.2. Cryopreservation and Storage of Cells:

HUVECs (500 000 cells per batch) were received (shipped from *PromoCell*) at passage 0. On seeding they became passage 1. A batch was split into two T25 and one T75 tissue culture flask filled with growth media. The growth media was renewed after one day. Storing at the initial passages was desirable. However, storage of a large volume of passage 3 and a reasonable amount of passage 2 was desirable. The large volume of passage 3 cells was used for trial and error experiments and the passage 2 cells were used for experiments and regrowth of cells.

Storage of passage 3: Following 3-4 days, the T25 flask (passage 1) reached confluence and each T25 (passage 1) was split into three T75 flasks (passage 2). Following a further 3-4 days, the six T75 flasks (passage 2) reached confluence. The cells were detached and mixed in 54 mL of DMEM containing 10 % FBS, 2 % L-glutamine and 10 % DMSO. The cell mixture was aliquoted into 54 cryotubes and immediately stored with Mr.Frosty at -80 °C. The following day, the 54 cryotubes were moved into liquid nitrogen and kept at -196 °C for up to 1-2 years. The 54 cryotubes were then seeded passage 3.

Storage of passage 2: Following 4-5 days, the T75 (passage 1) reached confluence. Cells were detached and mixed into 18 mL of DMEM containing 10 % FBS, 2 % L-glutamine and 10 % DMSO. The cell mixture was aliquoted into 18 cryotubes and stored as described for passage 3 cells.

2.3. Plasmid DNA purification

GFP-RelA and H2B-mCherry (*AddGene, MA, USA*) were received in E.coli and stored in agar stab (stable for 2 weeks). GFP-RelA was a gift from Warner Greene (Addgene plasmid # 23255) and H2B-mCherry was a gift from Robert Benezra (Addgene plasmid # 20972). The full sequence maps of GFP-RelA and H2B-mCherry are shown in Figure 30 and Figure 31, respectively. The cultures were streaked on a 10 mm culture dish (*Corning, MA, USA*) containing LB agar medium (*Merck, Darmstadt, Germany*) using a 10 µL inoculation loop (Sigma Aldrich, MO, USA). Moreover, the appropriate antibiotic for each culture was added (Kanamycin 50 µg/mL for GFP-RelA and Ampicillin 100 µg/mL for H2B-mCherry). The plate was left for 18 hours at 37 °C in a bacterial incubator (*Labnet, NJ, USA*). Following initial incubation, a single

pure colony was selected and inoculated into a 15 mL snap cap tube (BD Falcon, CA, USA) with 10 mL of LB agar medium (*Merck, Darmstadt, Germany*) plus the appropriate antibiotic and transferred to a rotating incubator (*Weisstechnick, Loughborough, UK*) at 37 °C for 18 hours. Subsequently, the 10 mL culture was transferred to a flask with 1 L LB agar medium, which contained the appropriate antibiotic for each plasmid and was left to grow for 18 hours in a rotating incubator at 37 °C. The following day the plasmids were isolated and purified from the 1 L culture using the PureLink HiPure Plasmid Megaprep Kit (*ThermoFisher Scientific, MA, USA*) according to the manufacturer protocols. Subsequently, the plasmids were stored at -20 °C for later usage.

The following day, the concentration of each batch was measured with a NanoDrop2000 (*NanoDrop, DE, USA*). DNA concentrations per batch have been listed in Table 1. The plasmids were sequenced using the services of GATC Biotech (*Constance, Germany*) and the absence of mutation was confirmed.

Table 1: DNA concentration per batch. All values reported in ng/mL

DNA concentration\Batch:	1	2	3	4
H2B-mCherry:	2089	1715.9	2445	1885.7
GFP-RelA:	1249	1050	985	1597

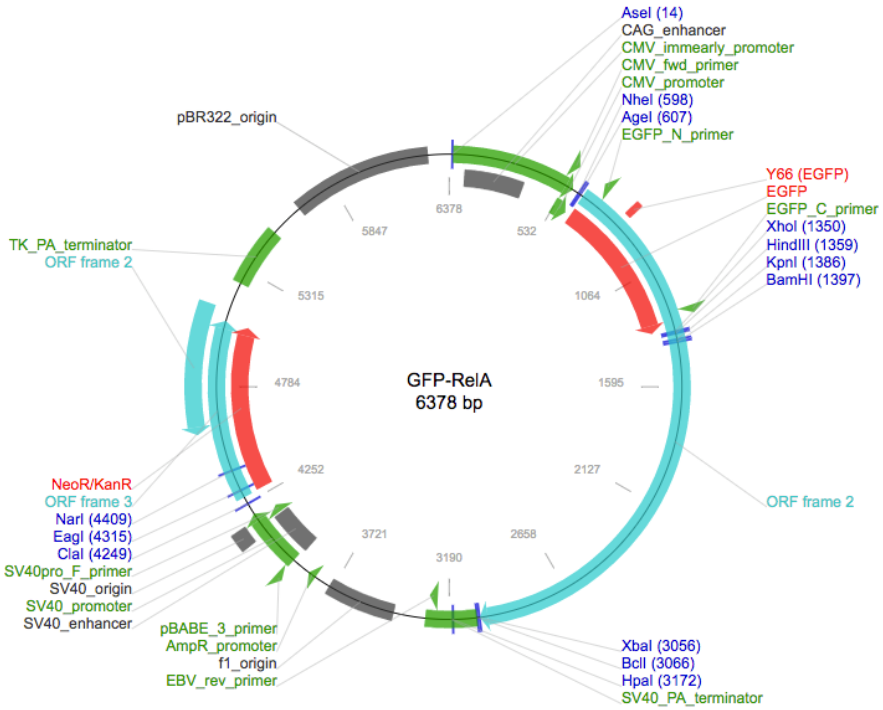

Figure 30: Full sequence map of GFP-RelA. RelA sequence was inserted in the ORF frame 2 [151].

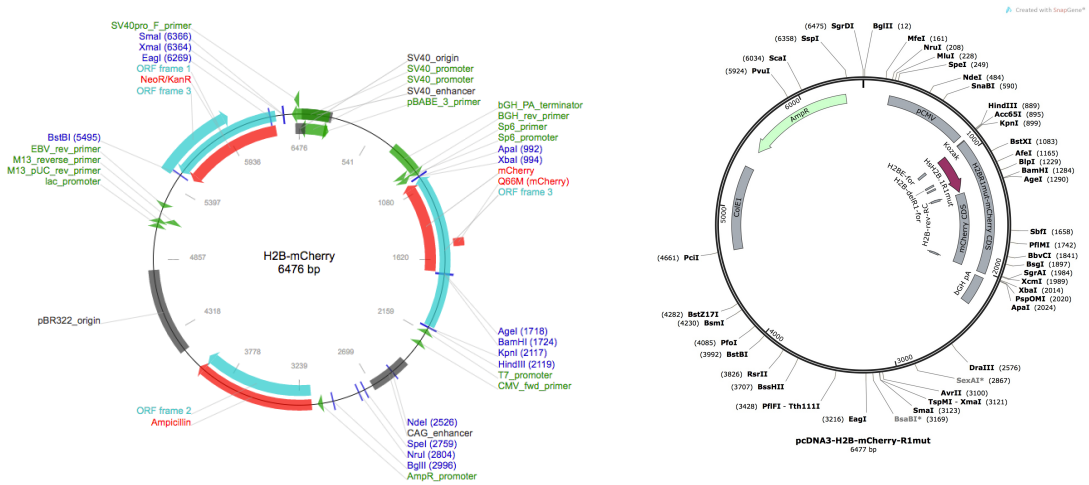

Figure 31: Full sequence map of H2B-mCherry [151].

Furthermore, electrophoresis was used to examine the bandlength of the plasmid. The plasmid was cut at the XBal and BamHI sequence into the GFP-RelA sequence and the remaining plasmid vector. Both snaps were run with electrophoresis.

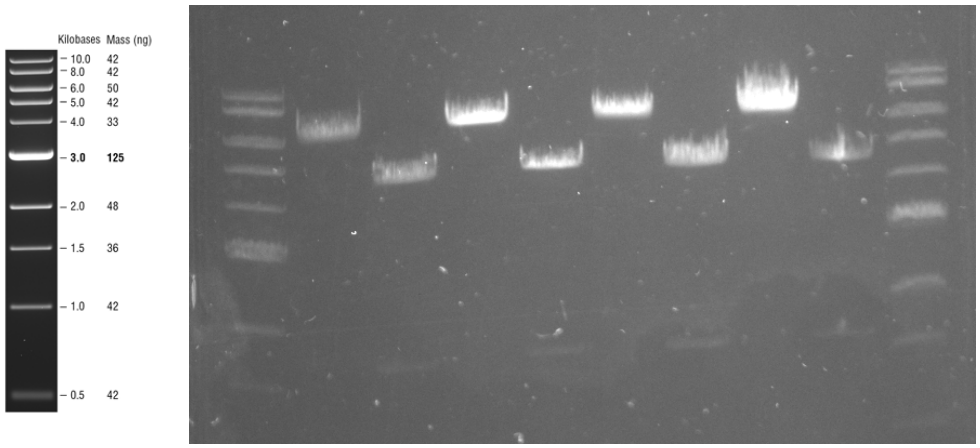

Figure 32: Gel to confirm base pair size of GFP-RelA. Ladder metrics on the left.

The results are presented in Figure 32. In the gel, the ladder is seen in the first row and the full plasmid vector in the second row. The third row is the plasmid vector without GFP-RelA, and the fourth row is again the full plasmid vector. The plasmid vector showed a base pair size of approximate 7000 base pair. Excluding GFP-RelA, the plasmid vector had a length of approximate 5000 base pair. This agrees with the sequence map of GFP-RelA in Figure 30.

2.4. Transfection of Primary Cells

Confluent HUVECs in a tissue culture flask were trypsinised and incubated for 2 minutes at 37 °C. Supernatant was added to neutralise the trypsin and the solution was centrifuged at 280 RCF for 5 minutes at 37 °C. The supernatant was removed and the cell pellet was used for transfection.

The NEON Transfection System (*Thermo Fisher Scientific, MA, USA*) uses electroporation for transfection of cells. The system was used according to the manufacturer protocols.

A mixture of 500 000 cells, 60 uL R Buffer, 20 uL H2B-mCherry and 20 uL GFP-RelA was prepared for each transfection. The most efficient and successful transfection

setting was found at 1000 V, and 2 times a pulse of 20 us. Following transfection, the cells were immediately collected and diluted in endothelial growth media. The mixture was then centrifuged, the remaining buffer and plasmid solutions were removed and fresh growth media was added. The final solution of transfected HUVECs was used in well plates or for flow experiments.

2.5. TNF-α experiments

24/48 plastic or 24 glass bottom well plates (*Greuber Bio-One, Stonehouse, UK*) were covered with 0.1 % sterile gelatine solution for 1-2 hours at 37 °C – long enough for the gelatine to react with the surface. A 2 % gelatine solution, suitable for tissue culture (*Sigma-Aldrich, MO, USA*), was diluted to 0.1% with PBS. Following incubation, the remaining gelatine solution was removed and the plates were air dried for 10 minutes.

TNF-α experiments were performed with immunohistochemistry of non-transfected cells and live-cell imaging of transfected plasmid cells. Immunohistochemistry provides snapshots of the molecular states of a population at single time points. Moreover, the advantage of live-cell imaging with transfeceted cells is that the molecular changes are tracked live. This allows for observations of the single cell dynamics in real time.

2.5.1. Untreated Cells

Cells were seeded at a variety of densities, according to the needs of each experiment. To achieve next day confluency, a density of 80 000 cells/cm^2 was used. For confluency in 2-3 days, a density of 30 000 cells/cm^2 was found to be adequate. Wells were filled with the recommended volume per well. Media was

renewed every 2-3 days, first by washing the plates with PBS for 1 minute and then adding fresh media.

2.5.2. Transfected Cells

The cell density for transfected cells was doubled as a result of a ca. 50% death rate caused by electroporation. Therefore, a density of 160 000 cells/cm^2 of transfected cells was used to seed the well plates. Cells were transfected and directly seeded into the wells with fresh media. Cells were washed with PBS and fresh media containing 2 % Penicillin-Streptomycin was added on the day following seeding.

2.6. Flow experiments

Flow experiments of uniform low and high shear stress were performed with immunohistochemistry of non-transfected cells and with live-cell imaging of plasmid transfected cells. However, the gradient channel experiments were performed with live-cell imaging only.

Flow experiments were performed over 6 hour periods only. The transient response was studied to verify the system, and to compare live-cell measurments to previously reported data for nuclear translocation in vascular endothelial cells reported with non-live imaging methods [102-113]. Chronic exposure was not studied due to experimental and time limitations. For future research, monitoring live nuclear GFP-RelA for more than a week is suggested.

2.6.1. 6-channel Ibidi

For uniform low and high shear stress experiments, premanufactured 6-channelled flow chambers (µ-Slide I 0.4 Luer-ibiTreat and µ-Slide VI 0.4-ibiTreat, *Ibidi, Planegg /*

Martinsried, Germany) were used. We neglect the effect of soluable mediators that travels downwards the channel, as we investigate the effect of shear stress only. The channels were coated with 0.1 % gelatine solution at 37 °C for 1-2 hours as previously described for the well plates in the TNF-α experiments. The remaining gelation solution was removed and the channels were air dried for 10 minutes.

2.6.2. Untreated Cells

The 6-channelled flow chamber consists of channels with dimensions 17 mm in length, 3.8 mm in width and 0.4 mm in height (Surface area = 0.646 cm^2). Each channel was seeded with the same density (80 000 cells/cm^2). Each channel was filled with 60 000 cells in 30 uL of endothelial growth media. Following 2 hours, each inlet pillar was filled with 60 uL of endothelial growth media.

For optimal growth conditions, the media was renewed everyday by washing the channel with PBS followed by the addition of new media. Media exchange in channels was performed as described in the manufacturer protocols. In brief, the right pillar was emptied while the channel remained filled. New media (190 uL) was added in the left pillar, allowing flushing through the channel. The remainder of the old media was assembled in the right pillar and could be easily removed. It is recommended to flush 2-3 times to assure that all old media is removed. Moreover, it is important not to expose the cell to air, as the surface tension in a microchannel is high and can lead to the tearing off of cells.

HUVECs were grown for 5 days in the ibidi flow chamber until full confluency was reached as shown in Figure 33.A. A quick stain experiment for VE-Cadherin was performed to confirm the establishment of cell-to-cell connections (Figure 33.B).

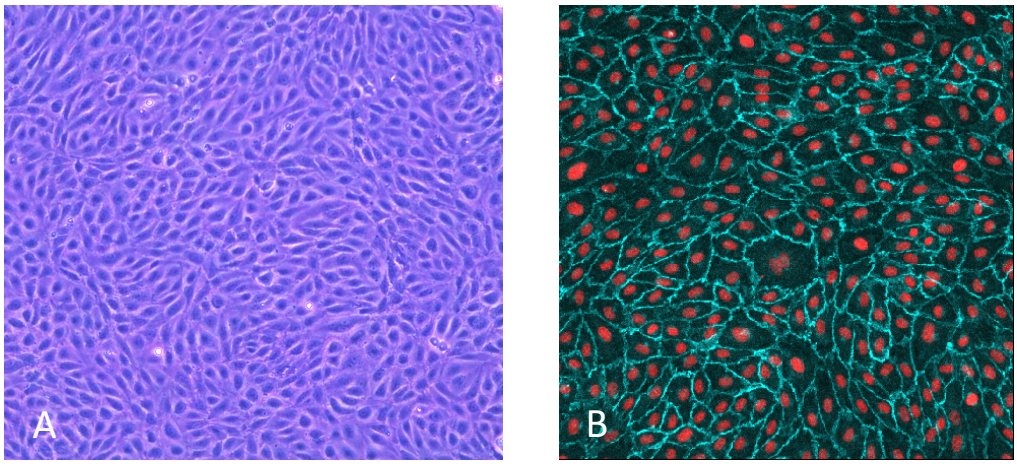

Figure 33: HUVECs grown to confluency after 5 days in an ibidi flow chamber (A). A stain was performed to confirm the establishment of cell-to-cell connections with VE-Cadherin (B)

2.6.3. Transfected Cells

Electroporation of HUVECs with GFP-RelA and H2B-mCherry caused a cell death rate of 50 %. Consequently, for transfected cells the cell density was doubled to 160 000 cells/cm^2.

The single flow chambers were seeded with 400 000 transfected cells in 120 uL. Each channel of the 6-channeled flow chambers was seeded with 104000 transfected cells in 30 uL of media.

The day following transfection, cells were washed with PBS and new endothelial growth media containing 2 % Pen-Strep was added. For optimal cell growth, the channels were washed every day and the media renewed with growth media containing 2 % Pen-Strep. As mentioned previously, exposing the cells to air was avoided to eliminate the possibility of tearing the cells..

2.7. Gradient channel

The gradient channel as described in section 2.12, was coated with 0.01 % poly-L-lysine solution (*Sigma Aldrich, Mo, USA*) for 2 hours at 37 °C. The remaining solution

was removed and the channel air-dried for 20 minutes. A second coating was added with a 0.1 % gelation solution by incubation for 1-2 hours at 37 °C. The remaining solution was removed and the channel was air-dried for 10-20 minutes.

2.7.1. Untreated Cells

Cells were seeded with a cell density of 80 000 cells/cm^2. As the surface area of the gradient channel was 2.68 cm^2, this led to a density of 215 000 cells. Cells were washed every 1-2 days with PBS followed by the addition of new media.

2.7.2. Transfected Cells

Cells were transfected and directly seeded into the gradient channel. Similarly, the cell density was doubled to 160 000 cells/cm^2. Therefore, the gradient channel was filled with 200 uL containing 500 000 cells. On the day following transfection, cells were washed with PBS and new media containing 2 % Pen Strep was added. As mentioned previously, it was important to not expose cells to air.

2.8. Perfusion System

A perfusion system was constructed to generate shear stress on cells grown in flow channels. The perfusion system consisted of a media reservoir, two dampers, a peristaltic pump Perista SJ-1220 (*Atto, Tokyo, Japan*), silicone tubing (*Colepalmer, London, UK),* a disposable blood pressure transducer (*AdInstruments, Oxford, UK*), an ultrasound flow meter (*Transonic, NY, USA*) and the corresponding flow chambers. A schematic diagram and image of the perfusion system is depicted in Figure 34.

The media reservoir and dampers were custom-made and externally fabricated (Cambridge Glass Blowing, Cambridge, UK). The media reservoir (Figure 35.A)

incorporated an outlet at the bottom, inlet at the top, a gas exchange (connected to a 0.2 µm filter) at the top and a cap for filling and washing of the reservoir. The Damper (Figure 35.B) was an 8 cm tall cylinder. The inlet and outlet were set at the same height of 4cm. However, the inlet had a guided inner tube towards the glass bottom. The cylinder was tightly closed with a cap to ensure a closed system with an internal pressure.

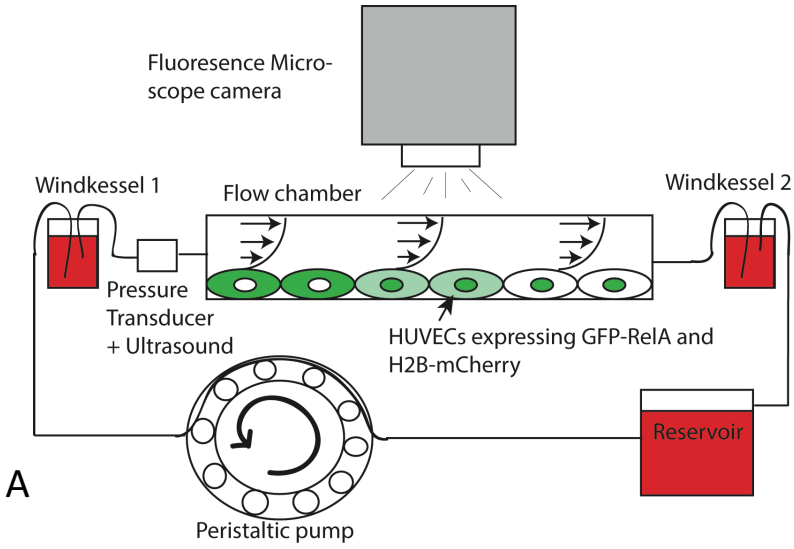

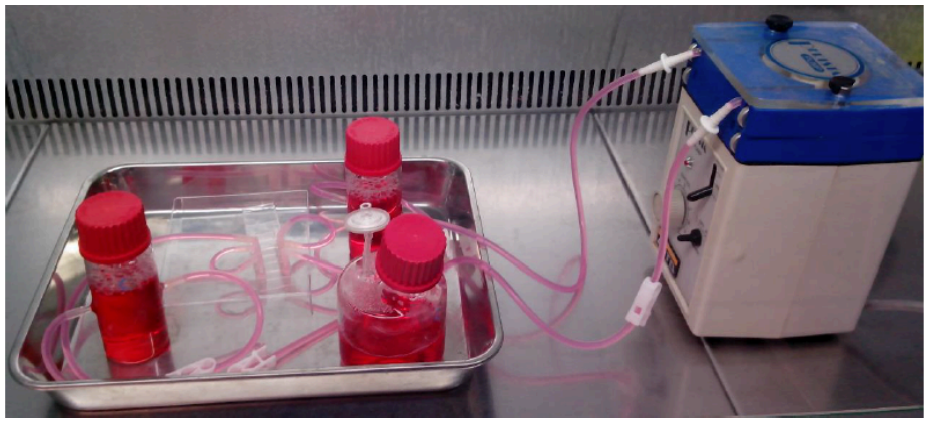

Figure 34: A: Schematic diagram of the perfusion system containing a peristaltic pump, two dampers, a pressure transducer, an ultrasound probe and a flow chamber. All parts were connected using silicon tubes and connectors. The flow chamber was placed directly under a microscope when performing live-cell imaging experiments. For immunohistochemistry, the experiment was performed in an incubator. B: Image of the perfusion system when connected in a sterile enviroment (Pressure sensor and ultrasound are not connected).

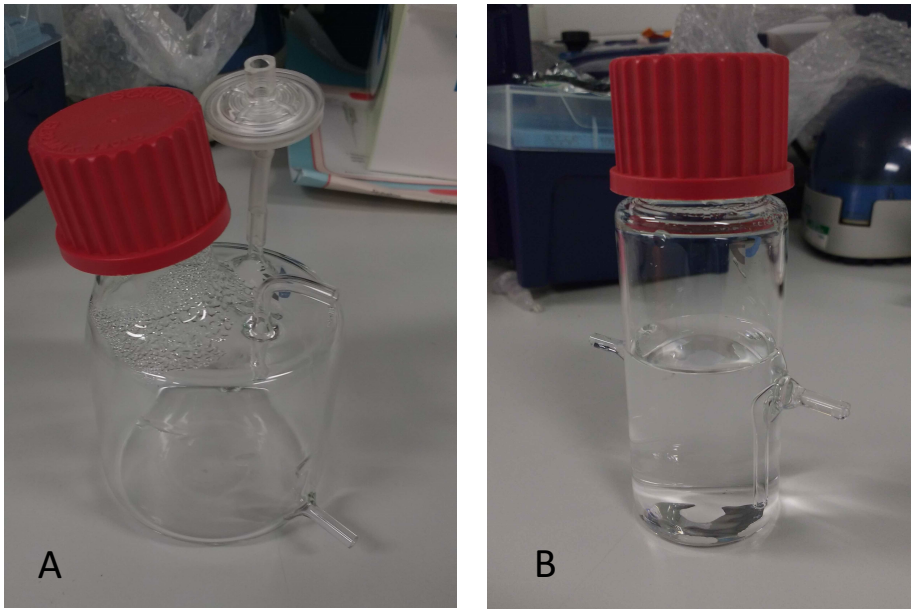

Figure 35: Custom made glass media reservoir with sterile gas exchange (A) and glass flow damper (B). The inlet of the flow damper has a guided glass tube to the bottom inside the jar.

2.9. Flow rate and pressure

The flow rate was measured with an ultrasound flow meter system (*Transonic, NY, USA*) using a 4PSB probe. The 4PSB probe has a resolution of 0.8 mL/min and an accuracy of ±4 mL/min. The ultrasound flow meter was used according to the manufacturers manual. Flow rates were measured under real conditions prior to flow experiments. During shear stress experiments the ultrasound meter was not connected to the perfusion system. In Figure 36.A, the measured flow rates for different pump speed settings are shown. In Figure 36.B, the linear relationship between pump speed and flow rates is shown. In Figure 37.A, flow rate measurements are shown for the perfusion system with and without 2 flow dampers at a pump speed of 10x.

The pressure was measured using a disposable blood pressure transducer (*AdInstruments, Oxford, UK*) and the signal was amplified with a custom-made amplifier (Amplifier circuit is depicted in the Appendix Figure 200). The signal was fed via an Arduino UNO R3 (*Arduino, Italy*) into a computer and live monitored in MATLAB (*MathWorks, MA, USA*). The pressure measurements for a flow rate of 15 mL/min of the perfusion system with and without 2 flow dampers are shown in Figure 37.B. The pressure was measured under real conditions prior to experiments. During experiments the pressure transducer was not connected to the perfusion system.

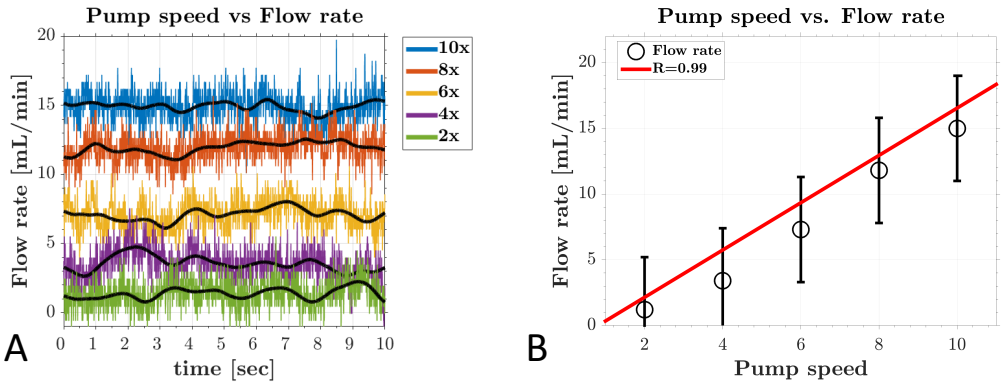

Figure 36: A: Flow rate measurements at different pump speeds. B: Average flow rates as a funciton of pump speed with a indicated regression line.

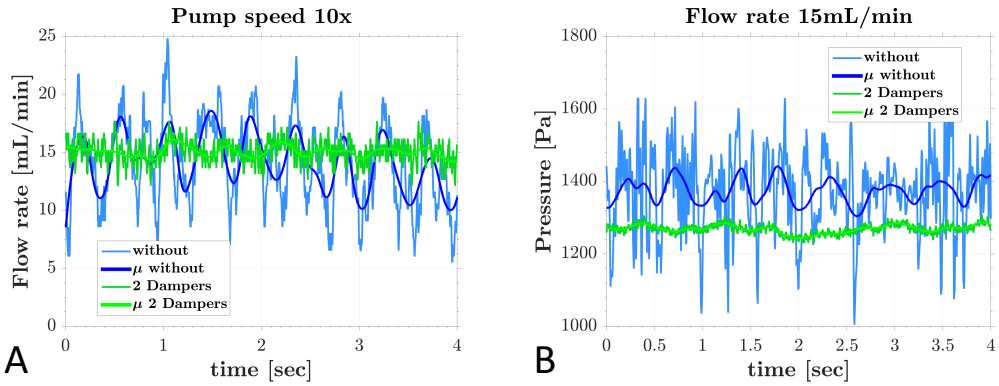

Figure 37: Flow rate (A) and pressure (B) measurements of the perfusion system without and with 2 dampers at a pump speed of 10x.

2.10. Multichannel experiments

Diagrams of the 6-channelled Ibidi slide setup used for flow experiments with immunohistochemistry (Figure 38.A) and live-cell imaging (Figure 38.B) are shown in Figure 37. In experiments with immunohistochemistry, 3 channels were connected in series and 3 channels were kept in static conditions as a control. In the live-cell experiments, 5 channels were connected in series as depicted in the diagram. The shear stress gradient channel was a single channel and was connected with its inlet and outlet as depicted in Figure 34.A.

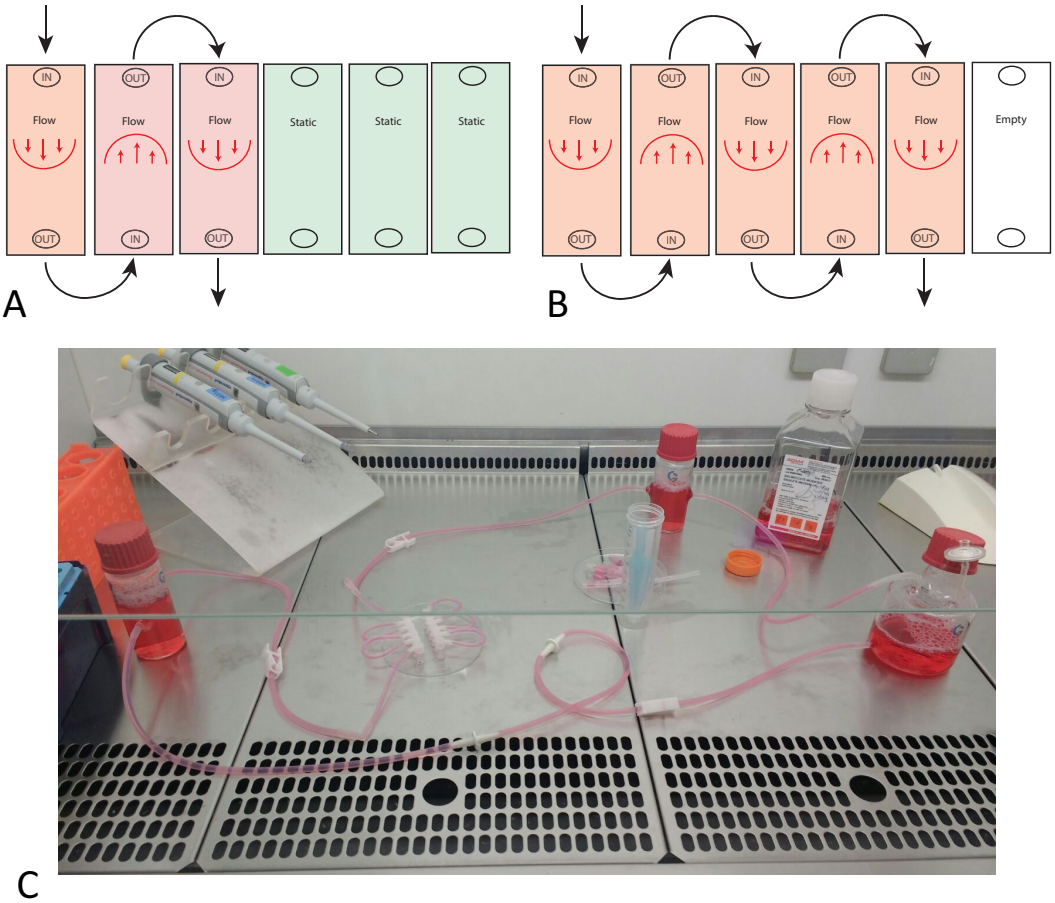

Figure 38: The 6 channelled Ibidi slide setup for flow experiments with immunohistochemistry (A) and live-cell imaging (B). The 6 channelled Ibidi connected in sterile conditions with the live-cell imaging setup (C).

2.11. Shear stress created on HUVECs

6-channelled Ibidi slide: The shear stress at the bottom wall in the 6-channelled Ibidi slide was calculated using the equation provided by the manufacturer:

$$\tau = \mu \cdot 176.1 \cdot Q \qquad (5)$$

where μ is the dynamical viscosity in dyne*s/cm^2 and Q the flow rate in mL/min. The dynamical viscosity was 0.0078 dyne*s/cm^2. The shear stresses generated in a 6-channelled Ibidi slide, based on the measured flow rates, are plotted as a function of the pump speed in Figure 39.

For low shear stress experiments, HUVECs were exposed to a shear stress of 2 dyne/cm^2. This corresponds to a pump speed of ca. 2.5x. For high shear stress experiments, HUVECS were exposed to a shear stress of 20 dyne/cm^2. This corresponded to a pump speed of 10x.

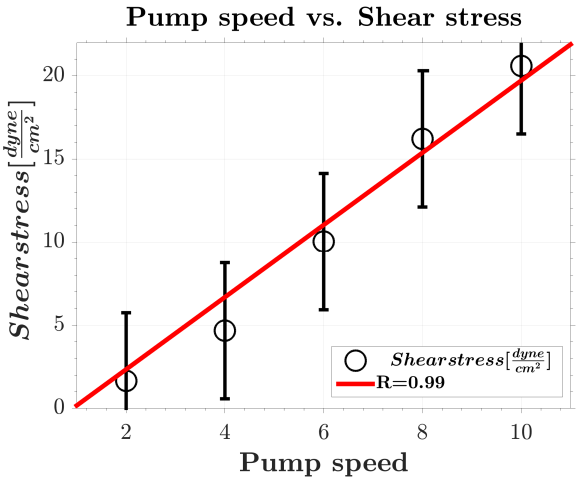

Figure 39: Shear stress created in the 6-channelled Ibidi slides as a function of the pump speed.

Gradient channel: The gradient channel was manufactured as described in Chapter 2.12 and validated with computational fluid dynamics using the method described in

Chapter 5. The gradient channel created a linearly increasing shear stress along the channel's bottom wall as shown in Figure 40.

Cells experienced an increase in shear stress from 2 to 16 dyne/cm^2 over a length of 3.7 cm with a flow rate of 15 mL/min at a pump speed of 10x.

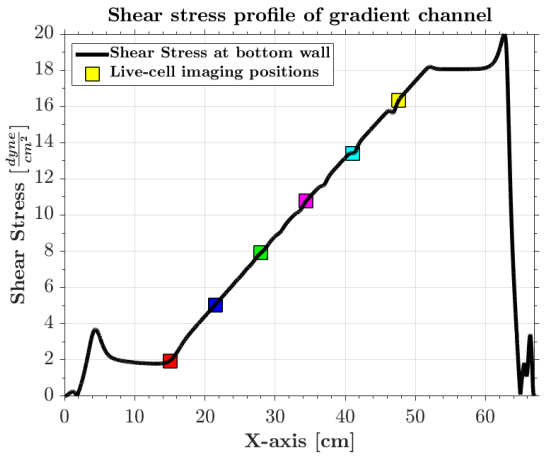

Figure 40: Gradient channel shear stress profile along the bottom wall.

2.12. Gradient channel design

2.12.1. Shear stress gradient calculations

The gradient channel was constructed to have a shear stress gradient from 2 to 16 dyne/cm^2. The height for both end-points was calculated using

$$h_\tau = \sqrt{\frac{6\mu Q}{w\tau}} \qquad (6)$$

With Q = 2.5e-7 m^3/s (15 mL/min), μ = 0.78e-3 Pa.s (DMEM at 37 ºC) and w=4cm. For a shear stress of 2 dyne/cm^2, the corresponding height was h_1 = 400 μm. Moreover, for 16 dyne/cm^2 the height was h_2 = 1400μm.

To calculate a linear increasing shear stress, the following formula given by Usami *et al.* [139] was used

$$\tau = \frac{6\mu Q}{h^2 w}\left(1 - \frac{z}{L}\right) \qquad (7)$$

The channel height as a function of the *z* derivate from Equation (6) and (7) is given as:

$$\frac{6\mu Q}{wh(z)^2} = \frac{6\mu Q}{h_1^2 w}\left(1 - \frac{z}{L}\right) \quad (8)$$

$$h(z) = \sqrt{\frac{h_1^2 L}{L - z}} \quad (9)$$

In addition, the entrance length was calculated to ensure an established flow before and after the gradient section. This was calculated with the formula for the entrance length in laminar flows:

$$L = 0.05 \cdot Re \cdot d_h \quad (10)$$

$$Re = \frac{\rho \cdot U \cdot h(z)}{\mu} \quad (11)$$

$$d_h = \frac{2h(z)w}{h(z) + w} \quad (12)$$

The entrance lengths with expected velocities at h_1 and h_2 would be 5.6 mm and 0.91 mm, respectively. To increase the safety margin, the entrance and exit section were both set to 10 mm. In addition, the gradient channel was perfused from the large cross-section to the smaller one. There is greater probability of attaining a stable flow for a converging channel. The final 3D gradient channel with the calculated dimension is shown in Figure 41. The flow within the 3D structure was validated with computation fluid dynamics (CFD) as discussed in Chapter 5.

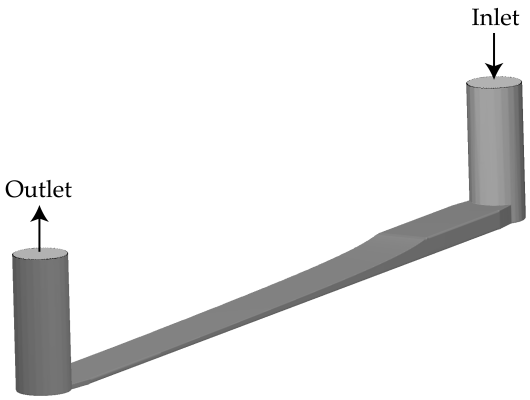

Figure 41: 3D gradient channel domain for flow validation with computational fluid dynamics.

2.12.2. Mould and channel fabrication

A mould of the final geometry was designed in SolidWorks (*Dassault Systèmes, Vélizy-Villacoublay, France*). The final designs are shown in Figure 42. The gradient channel was milled without the inlet pillars. The inlet pillars were added separately by first drilling two holes and then hammering in two pillars with the appropriate diameters. The gradient channel mould was manufactured using a DATRON C5 - 5 AXIS machine (*Datron, Milford, US*), which is available at the Hamlyn Center at Imperial College London. The machine has an accuracy of 2 µm. Stainless steel was used as a material.

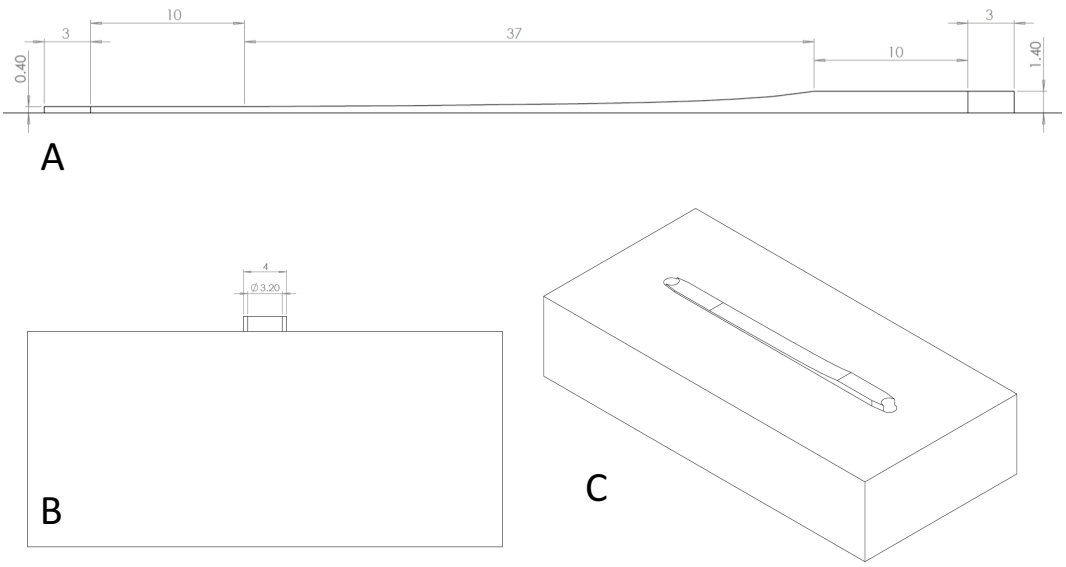

Figure 42: A: The gradient channel side view with two entrance lengths of 10mm, a gradient section length of 37mm and two buffer spaces of 3mm for the pillar hole. Pillar hole is drilled with circle centre at the end of both sides (0 and 63mm). B: The width of the channel was 4mm and the pillar hole was drilled with a 3.2mm diameter. C: The 3D view of the gradient channel mill out of a block.

The final manufactured mould is shown in Figure 43. Other manufacturing methods, such as rapid prototyping or 3D printers were not suitable due their lack of accuracy. The accuracy had to be below dimensional features of the channel, and the gradient channel had an exponential increment of height from 400 µm to 1400 µm. Moreover, the mould material must resist 60-90 °C during the curing process of PDMS. Some 3D print materials may melt at these temperatures. Once the mould was manufactured, an additional case made of PVC was fitted around the model to create a basin/mould cast for the liquid PDMS (Figure 44). The actual channel was then manufactured by pouring liquid PDMS into the mould cast (Figure 44). We used Sylgard® 184 Silicone Elastomer Kit (*Dow Corning, Auburn, US)* with a mixture of 10:1. The PDMS was then cured at 60 °C for 1.5 hours, after which it was carefully removed from the mould.

We used Menzel Gläser (*Thermo Scientific, Waltham, US)* for the bottom of the channel, as a growth surface for the cells. To bind the PDMS gradient channel to glass, we treated the surface with Plasma Prep (*Gala Instrument, Manchester, UK*) for 30 seconds at 0.4 mbar. After treating the surfaces, the PDMS and glass were immediately put together.

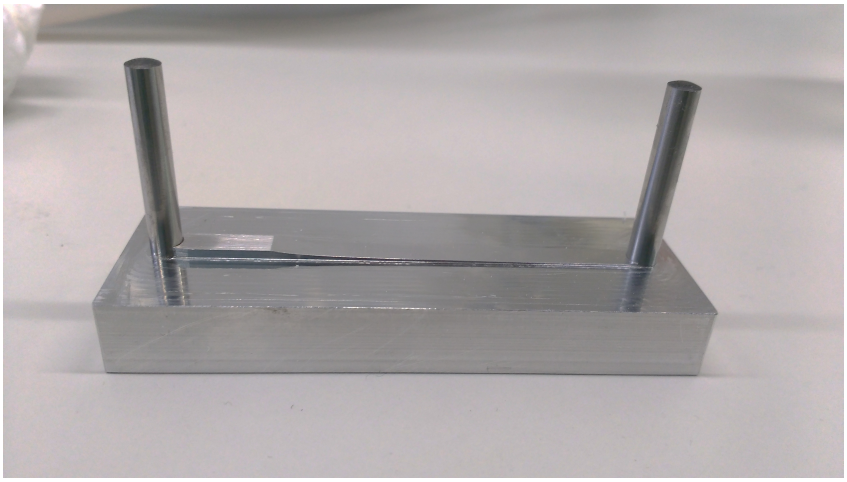

Figure 43: The gradient channel mould geometry manufactured with a micro milling machine.

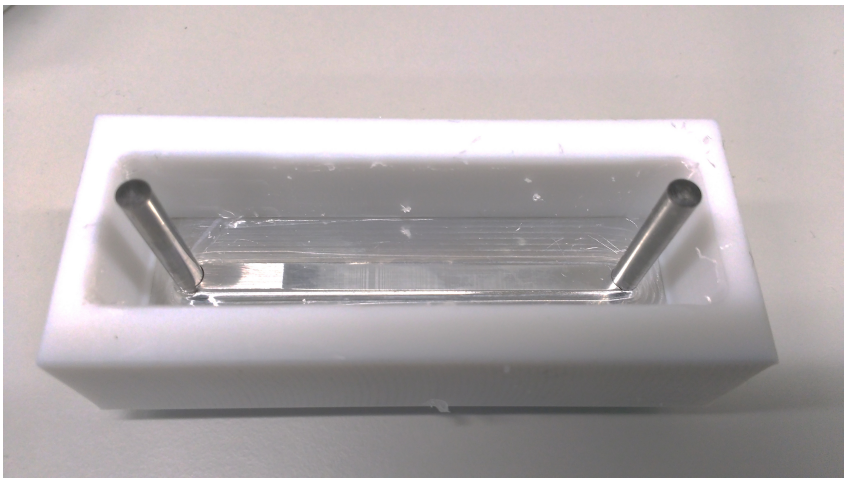

Figure 44: The mould with PVC case.

To improve the strength of adhesion between glass and PDMS, the channel was placed directly after binding for 2 hrs at 60 °C. The final gradient channel is shown in Figure 45. Prior to using the gradient channel for tissue culture applications, the

gradient channel was cleaned by flushing with ethanol and distilled water and then autoclaved for sterility.

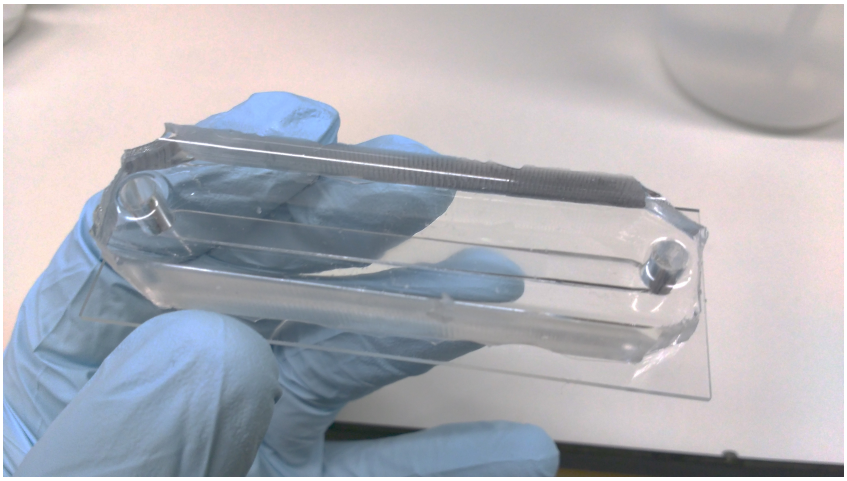

Figure 45: The final gradient channel after the PDMS and glass are bonded together.

2.13. Immunohistochemistry

Following the experiments, cells were immediately washed with PBS. PBS was removed and the cells were fixed with 4% PFA (diluted in water) for 5 minutes. PFA was then removed. This was followed by three washes with PBS, each for 5 minutes. Cells were then fixed with 0.1 % Triton-X in PBS for 5 minutes. Triton-X was then removed with a quick wash of PBS. This was followed by a second wash of 10 minutes. Subsequently, unspecific binding was blocked with 0.5 % Bovine Serum Albumin (BSA) in PBS for one hour. After the blocking agent was removed, the primary antibody was added and stored overnight at 4 °C. All primary antibodies are listed in Table 2.

For multi-staining experiments, all primary antibodies (F-6, H-4 and Ser180/Ser181) were mixed together.

The soluble primary antibody was removed the next day and cells were washed twice with PBS for two minutes. Subsequently, the secondary antibody was added for two hours. Secondary antibodies are listed in Table 3

After two hours, the unbound secondary antibody was removed with a quick wash. This was followed by two washes with PBS for 5 minutes. To colour up the nucleus, the following antibodies were used (Table 4).

Table 2: Primary Antibodies

Antibody	Species	Dilution	Company
NF-κB p65 (F-6) Alexa Fluor 488, sc-8008 AF488	Mouse monoclonal raised against human	1:300	Santa Cruz Biotechnology Inc., CA, USA
IκBα (H-4) Alexa Fluor 647, sc-1643 AF647	Mouse monoclonal against human	1:300	Santa Cruz Biotechnology Inc., CA, USA
p-IKKα/β (Ser 180/ Ser 181), sc-23470-R	Rabbit polyclonal against human	1:500	Santa Cruz Biotechnology Inc., CA, USA
VE-Cadhering (C-19), sc-6458	Goat polyclonal against human	1:300	Santa Cruz Biotechnology Inc., CA, USA

Table 3: Secondary Antibodies

Antibody	Species	Dilution	Company
Alexa Fluor 568: A10042	Donkey anti-Rabbit IgG	1:300	Thermo Fisher Scientific, MA, USA
Alexa Fluor 568: A11057	Donkey anti-Goat	1:300	Thermo Fisher Scientific, MA, USA

Table 4: DNA stains

DNA cell stain	Dilution	Company
HOECHST 33342, 10ng/mL	1:5000	Thermo Fisher Scientific, MA, USA
DRAQ5 (5mM)	1:1000	Biostatus, Leicestershire, UK

2.14. Image acquisition

Cells were imaged using an inverted Leica DMI 6000 CS confocal microscope, located in the Department of Bioengineering, and a Zeiss Axio Observer wide-field microscope at the Facility for Imaging by Light Microscopy at Imperial College London.

2.14.1. Imaging immunohistochemistry

Immunohistochemistry images were acquired with a wide-field microscope using a 20x magnification lens. Sequential scanning with 4 LEDs at wavelengths of 395nm (Violet for HOECHST), 470nm (Cyan for AF488), 550nm (Green/Yellow for AF568), and 640nm (Red for AF647) was used to image all secondary antibodies and nuclear stains. The excitation and emission spectra of all 4 fluorescence antibodies (HOECHST, AF488, AF 568 and AF 647) are shown in Figure 46 [152]. Excitation overlapping was found to be minimal and negligible.

In Figure 47, wide-field images of HUVECs stained for HOECHST (Figure 47.A), p65-Alexa Fluor 488 (Figure 47.B), p-IKKα/β-Alexa Fluor 568 (Figure 47.C), and IκBα-Alexa Fluor 647 (Figure 47.C) are shown. Per sample, 12 images evenly distributed along the sample well or flow channel were acquired.

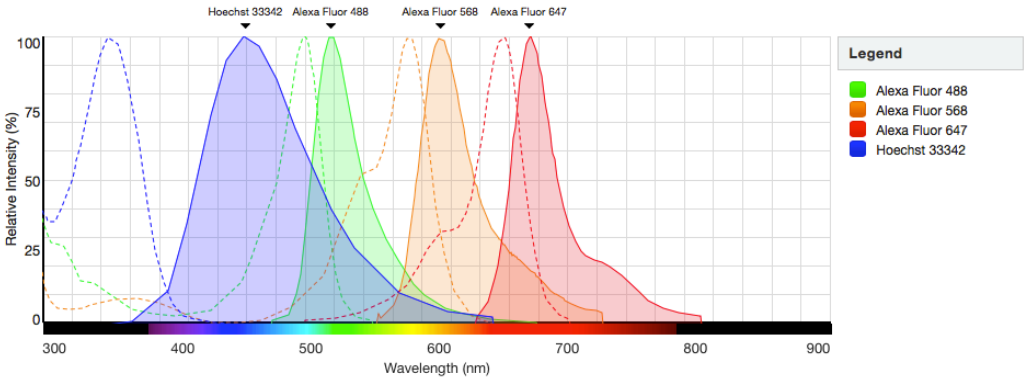

Figure 46: Wavelengths of HOECHST, Alexa Fluor 488, Alexa Fluor 569 and Alexa Fluor 647 [152]. The excitation and emission spectrum are overlapping by a minimum.

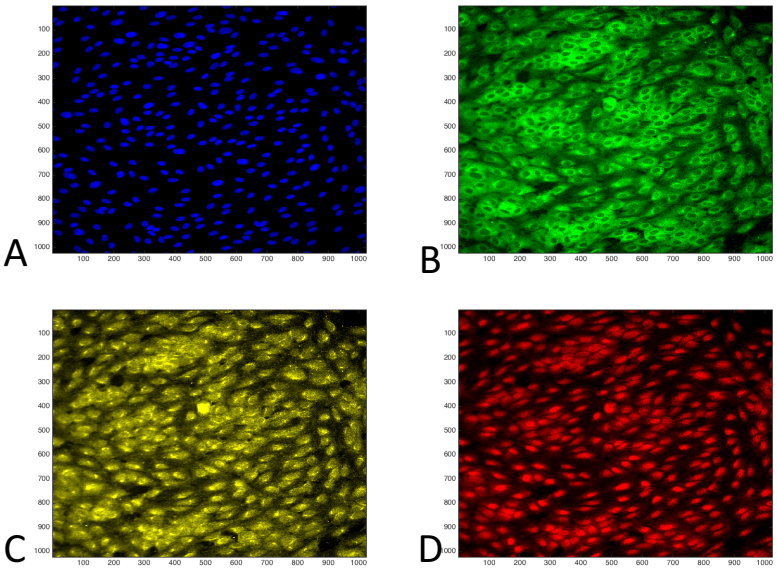

Figure 47: Wide-field images of stained HUVECs for HOECHST (A), p65-AF488 (B), p-IKKα/β-AF568 (C) and IκBα-AF647 (D)

2.15. Live-cell imaging

Live-cell imaging was performed with a confocal microscope and a wide-field microscope as described above. For the TNF-α experiments the confocal was used with a 20x magnification lens. Low and high shear experiments were performed with the wide-field microscope using a 20x magnification lens. The gradient channel experiments were performed with the wide-field microscope using a 40x magnification lens. The inherent properties of confocal microscope – rejection of

out-of-focus information – limits blurring. However, the acquisition time for the confocal is extremely long. Therefore, this limited the recording of only a few cells in "real time". In comparison, the wide-field acquisition speed fast. This allowed for high through put recording in live-cell imaging experiments.

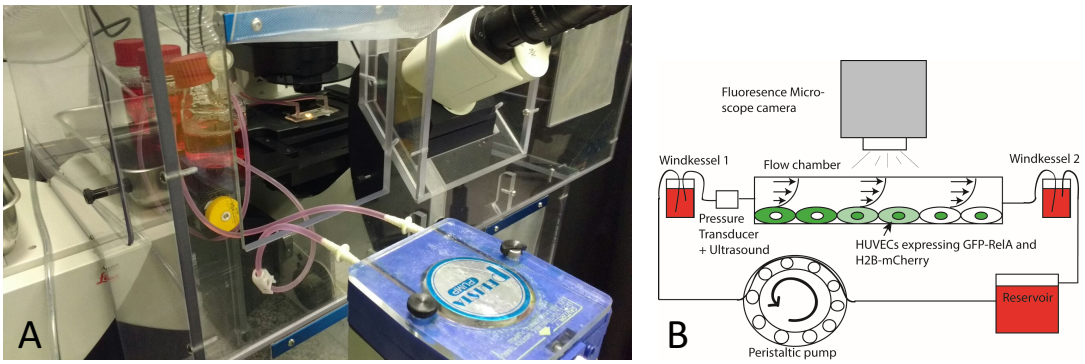

Figure 48: The perfusion system with a single Ibidi flow channel installed at the confocal microscope (A). Schematic of the live-cell imaging setup (B).

Figure 48 shows a test run with the perfusion system installed at the confocal microscope at the Department of Bioengineering at Imperial College London. The microscopes were covered with a heating box to maintain a working temperature of 37 °C. Humidity (CO2) was directly controlled via a silicon tube through a sterile filter (0.2 μm) into the gas exchange of the media reservoir.

2.15.1. Wide-field live-cell imaging

The flow experiments were performed at the FILM facility using a Zeiss Axio Observer wide-field microscope (*Zeiss, Oberkochen, Germany*). After placing the sample in the holder at the microscope, the tubing, media reservoir and dampers were placed inside the heating box (37 ºC). Moreover, an external C02 supply was connected directly to the gas exchange outlet of the media reservoir. The pump was placed outside the heating box due to a lack of space within the heating box. Once the perfusion system and the sample were placed, the recording system was

configured. LED lamps for GFP and mCherry were run in series to image the intensity of GFP-RelA and H2B-mCherry. In addition, a phase contrast image was taken for orientation, but was not used for processing. In total 3 images were taken per position: GFP LED, mCherry LED and phase contrast. The software was set to autofocus on the mCherry signal to avoid blurring during cell movements.

Six channelled Ibidi slide: In all 5 channels (5 out of 6 channels were used to grow cells), 7 positions were marked as shown in Figure 49. Spots were marked in the developed flow area and with a high confluence of transfected cells. The time for a full slide scan (6 channels x 7 positions x 3 images = 105 images) was 11 min 25 sec. The experiment duration was set to 360 minutes, which resulted in 32 time steps. The initial time of the last position was used as the reference point for normalisation. For the low and high shear stress experiment this time was t*=11min.

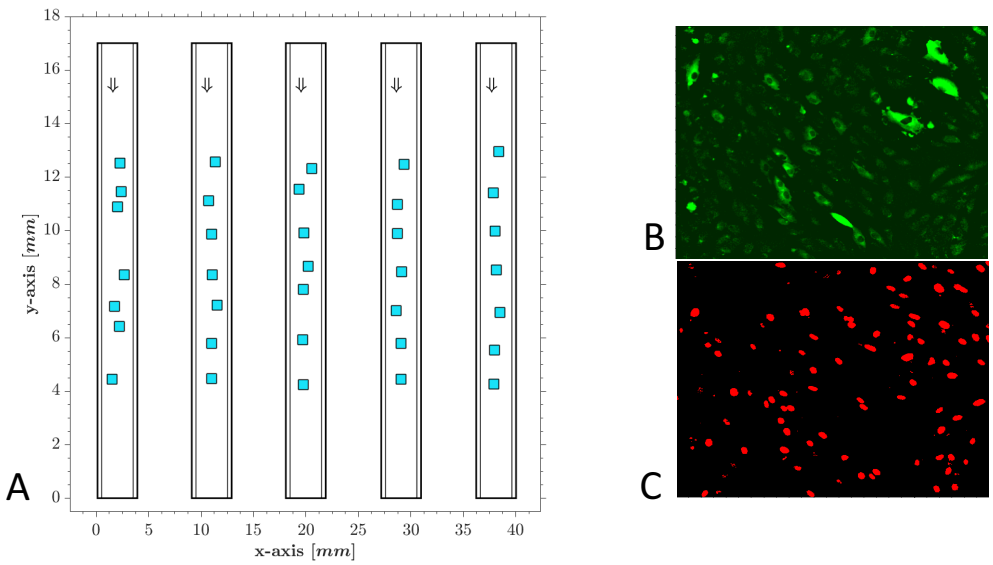

Figure 49: Recording positions during live-cell imaging experiment with a 6-channelled Ibidi slide. Positions are placed in the developed flow area.

It is arguable that cells after the initial position are exposed to soluble mediators that are transported via convective transport. We neglect this hyposis as we investigate if pure shear stress is affecting the inflammatory response of a monolayer. As it will be

shown later, there might be small effexts of solubale mediates that has to be investigated in the future. However, for this setup we perform the experiments with regard of the effect of shear stress only.

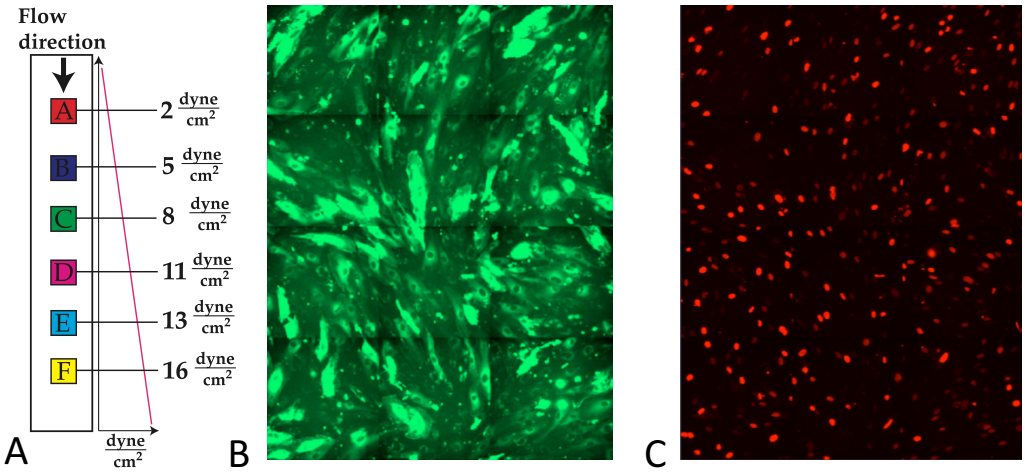

Figure 50: Positions at different shear stress magnitudes along the gradient channel (A). 3x4 tiles scan of GFP-RelA signal (B) and H2B-mCherry signal (C).

Gradient channel: Six positions corresponding to shear stress magnitudes of 2, 5, 8, 11, 13 and 16 dyne/cm^2 in the gradient channel were marked and recorded as shown in Figure 50.A. The positions were recorded on a tile scan of 3x4 images as shown in Figure 50.B and C. The tile scan was necessary due to the 40x magnification lens. A full scan of the gradient channel was completed in 17 min 14 sec (3x4 tile positions x 6 shear stress positions x 3 images = 216 images). This resulted in 22 time steps for a 360 minutes long experiment. The initial starting time of the tiles was average to 1, 4, 5, 7, 10, 12 and 15 minutes for tile 1 to 6. The initial time of the last tile was used as the earliest time point for normalisation t* =15min.

Well plates: Twenty-four glass well plates were used with three wells of untreated and three other wells with HUVECs stimulated with TNF-α. Four positions were recorded per well. The time interval was 15 minutes with 25 time points in 360 minutes.

2.15.2. Confocal live-cell imaging

TNF-α experiments were performed using the confocal microscope. An example image of HUVECs expressing GFP-RelA is shown in Figure 51. This demonstrates the high quality achieved with the confocal image. Cells were prepared in the tissue culture lab, transported to the confocal and placed in the preheated incubation box of the confocal. Positions with high confluency of transfected cells were chosen for imaging. For GFP-RelA, the argon laser with excitation at 488nm was used. For H2B-mCherry, the HeNe laser with excitation at wavelength 594nm was used. The power of both lasers was set to 15%. Higher powers resulted in cell death.

TNF-α was added and the experiment was started after a careful calibration of marker positions. As the Leica software was not advanced, each time step was carefully monitored and quality control was performed for the first 10 time steps. The experiments were then run overnight without a time limit. This resulted in 12 hours long recordings with time interval of 13 mins 50 sec and 47 time steps. The speed of scanning could be improved by using reversed scanning. The 10 ng/mL TNF-α experiments were recorded using reversed scanning, this resulted in time steps of 7 minutes.

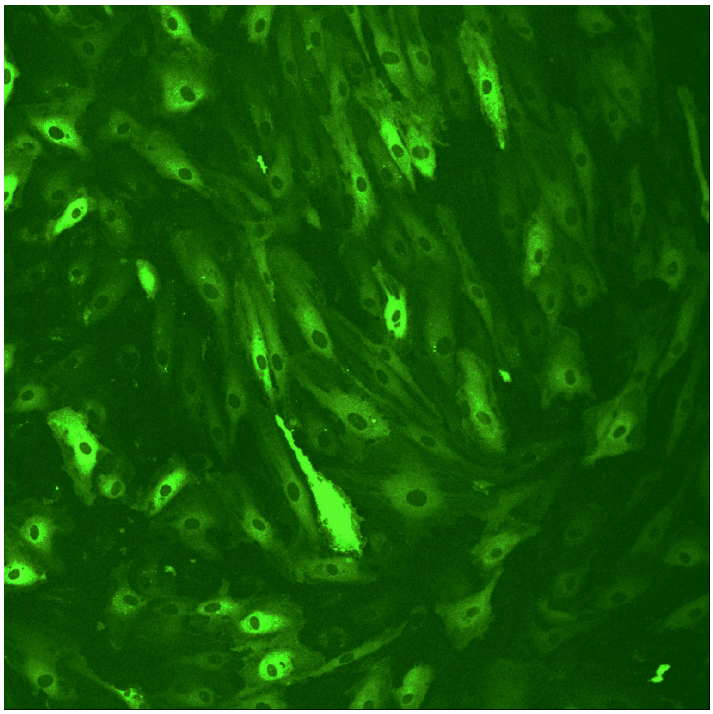

Figure 51: HUVECs expressing GFP-RelA imaged with a confocal microscope at a high resolution.

2.16. Image quantification of immunohistochemistry

Wide-field images were imported into MATLAB (*MathWorks, MA, USA*) using Bio-Formats [153]. These were then analysed by calculating the cytoplasmic and nuclear intensity. To achieve this, the nuclear image was made binary (Figure 52.A) to obtain nuclei coordinates. Subsequently, the nuclear and cytoplasmic intensity of the three other stains (Figure 52.B-D) were calculated based on the obtained coordinates. The nuclear and cytoplasmic extraction of p65 are shown in Figure 52.B and Figure 52.C.

The background was manually corrected for by applying a threshold that was defined by empty spots (areas were no cells were grown). The sum of the nuclei and cytoplasmic intensity was normalised by the sum of the pixels. Once the nuclei and cytoplasm were calculated the mean and standard deviation of the ratio between experimental and static conditions were calculated using the following formulas:

$$E\left(\frac{R}{S}\right) \approx \frac{ER}{ES} - \frac{Cov(R,S)}{E^2S} + \frac{Var(S)ER}{E^3S} \quad (13)$$

$$Var\left(\frac{R}{S}\right) = \frac{{\mu^2}_R}{{\mu^2}_S}\left[\frac{{\sigma^2}_R}{{\mu^2}_R} - \frac{Cov(R,S)}{\mu_R\mu_S} + \frac{{\sigma^2}_S}{{\mu^2}_S}\right] \quad (14)$$

Where *ER* is the expected value of *R*, *ES* is the expected value of *S*, $E\left(\frac{R}{S}\right)$ is the expected value of the ratio *R* to *S*. μ is the mean of *E* or *S*, σ is the standard deviation of *E* or *S*. *Var* is the variance, and finally the standard deviation is the root of the variance. In this work, *R* was the mean of experiment sample and *S* the mean of the static conditions sample. The purpose of equations 13 and 14 are to closely approximate the expectation and variance value of a ratio. The ratios of mean and standard deviation were calculated for the cytoplasm and nuclear concentration for p65, IκBα and p-IKKα/β.

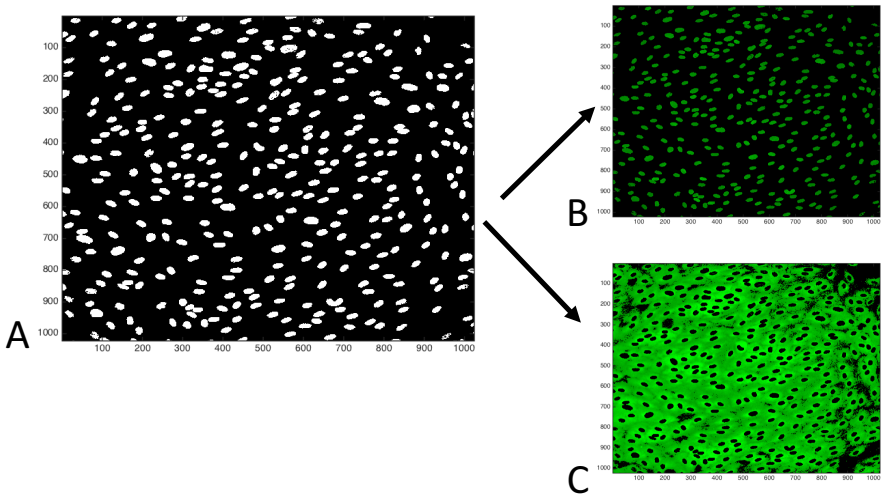

Figure 52: The binary nuclei image (A) and the nuclei (B) and cytoplasm (C) extraction of the p65 image.

2.17. Single cell tracking and quantification

Live-cell image series were loaded into MATLAB (*MathWorks, MA, USA*) using Bio-Formats [153]. The tracking algorithm is depicted schematically in diagram of Figure 53.

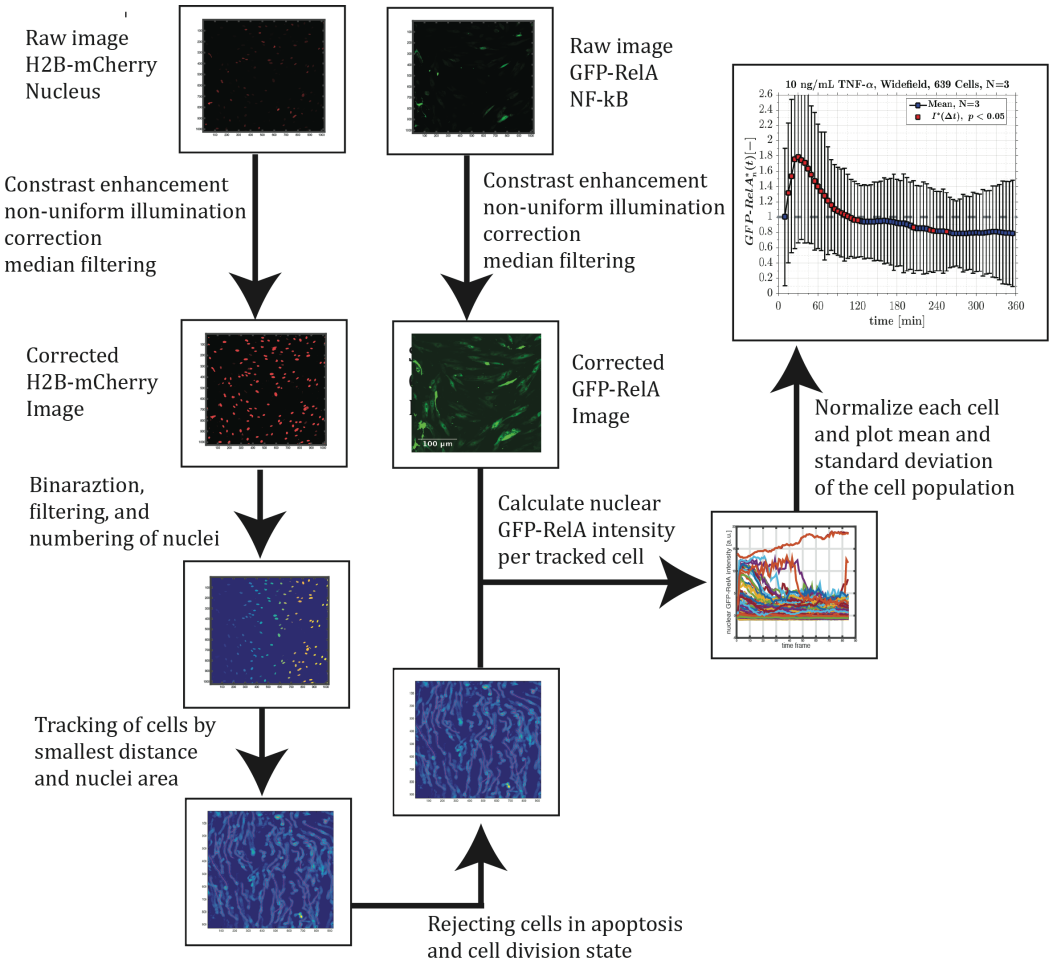

Figure 53: Schematic diagram of single cell tracking algorithm and nuclear GFP-RelA intensity calculation. First, the raw image of H2B-mCherry and GFP-RelA were processed by enhancing the contrast, correcting non-uniform illumination and removing noise with a median filter. Then the H2B-mCherry image was made binary and the nuclei were numbered. The numbered nuclei were tracked throughout all time frames. The coordinates from the tracked nuclei were used to calculate the nuclear GFP-RelA intensity in the corrected GFP-RelA image. Cells nuclear GFP-RelA intensity were plotted, and later normalised by either time average or earliest common time point. The population mean of the normalised nuclear GFP-RelA intensity including standard deviation was plotted as the final result.

First, the raw images of H2B-mCherry and GFP-RelA were corrected for the background [134] as shown in Figure 54. The correction involved the following steps: The contrast of the raw image was enhanced (Figure 54.B), then the non-uniform background (Figure 54.C) and the regression (Figure 54.D) were calculated. Subsequently, the final image (Figure 54.E) was calculated using Equation (15).

$$\frac{\text{Enhanced Image} - \text{Background}}{\text{Regression}} = \text{Final Image} \qquad (15)$$

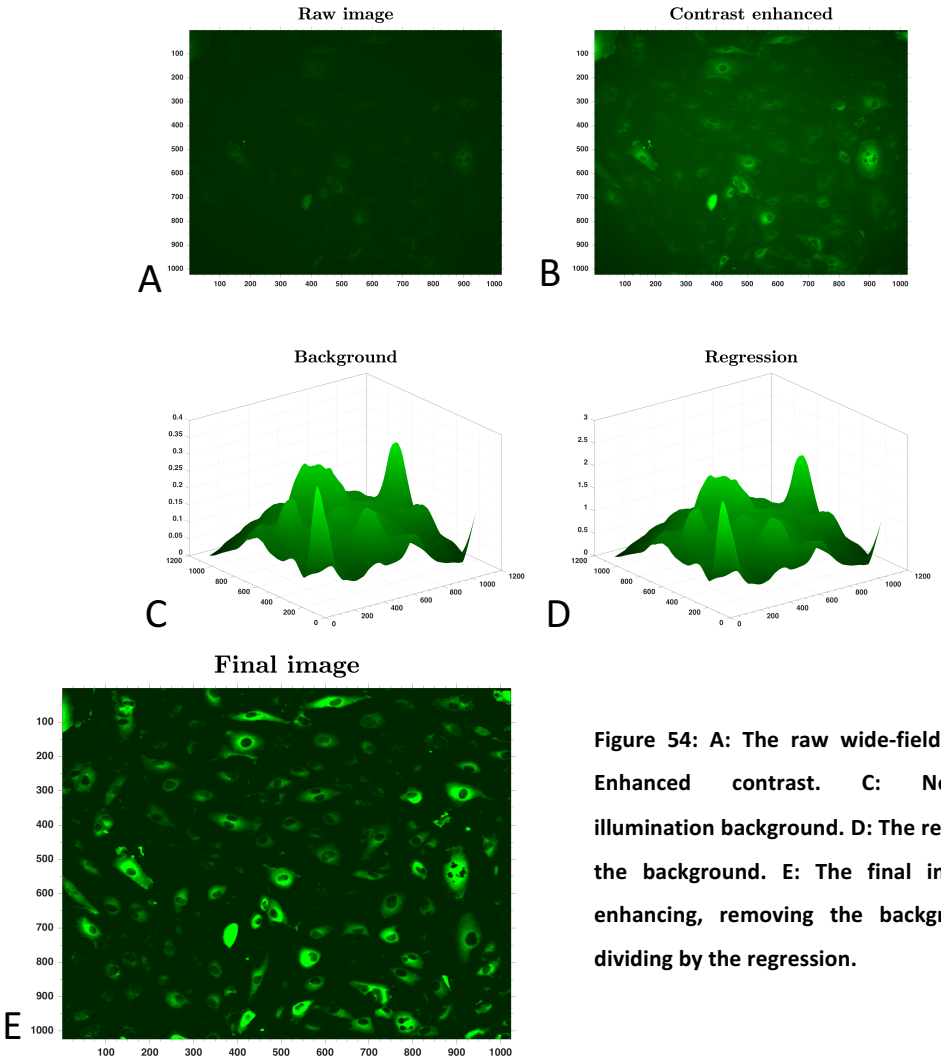

Figure 54: A: The raw wide-field image. B: Enhanced contrast. C: Non-uniform illumination background. D: The regression of the background. E: The final image after enhancing, removing the background and dividing by the regression.

The background was calculated by dividing the image into 32 equal squares. Each square was averaged and blurred with its surrounding to create a smooth background. The regression was calculated by dividing the background image using the mean of the background image. Regression aimed to overcome photo bleaching in time. The H2B-mCherry image was made binary as shown in Figure 55. Each white dot represents a nucleus.

Software was developed to compare the position of each nucleus between each time step. The smallest difference in position and the similarity of area determined

which cell, in the next time frame, was the cell from the previous time frame. The tracking of cells under two experimental conditions is shown in Figure 56. The time series of nulcei were superimposed and a thin pink line indicates the pathways of the nuclei. Not all cells could be tracked.

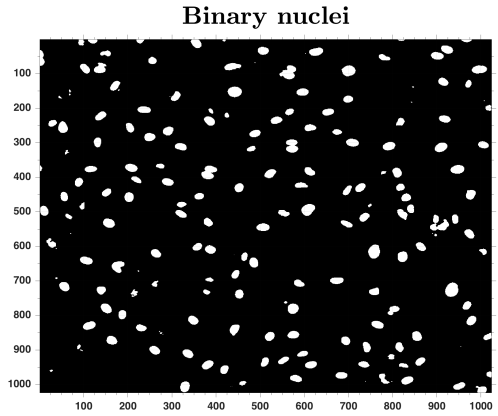

Figure 55: The H2B-mCherry image made binary, representing the cells' nucleus.

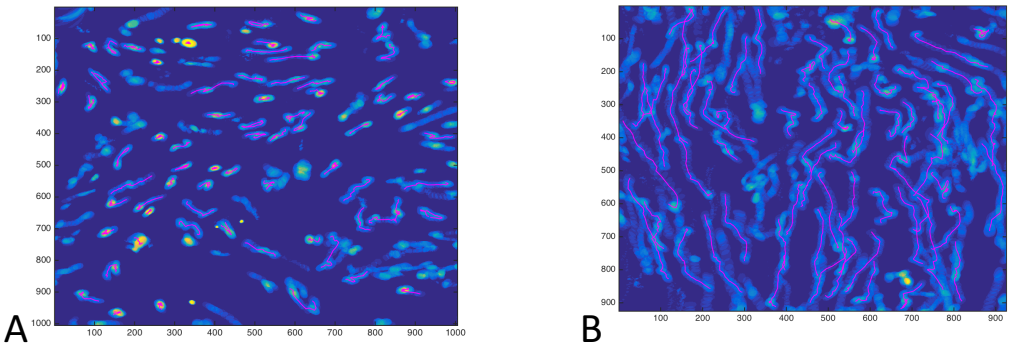

Figure 56: The pathways (pink line) of tracked nuclei when stimulated with TNF-α (A) and exposed to high shear stress (B)

Cells that went into apoptosis and cells that divided were rejected. Cells that suddenly appeared from outside the frame after the first time step were also ignored. Approximate 30% of the cells were rejected.

The tracking of cells revealed cell mobility of HUVECs under different flow conditions. The cell mobility observations are presented in the results section for each experimental condition. A measure for the persistence of cell mobility is given

by the directionality ratio. The directionality ratio is defined as the ratio of the start to end point distance (d) and the actual length of the travelled path (D). This is depicted in Figure 57 [197] and described in Equation (16). A high ratio indicates low persistence, while a low ratio indicates strong persistence.

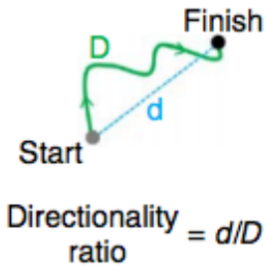

Figure 57: Directionality ratio [197]

$$directionality\ ratio = \frac{d}{D} \quad (16)$$

Once cells were tracked in their pathway, the GFP-RelA intensity at the coordinates of the nucleus per time step was calculated for each cell as the mean pixel intensity:

$$I_n(t)[a.u] = \frac{\sum_i^P G_{i,n}(t)}{P_n(t)} \quad (17)$$

Where $G_{i,n}(t)$ is the nuclear GFP-RelA intensity per i-th pixel for the n-th nuclei at time point *t*. $P_n(t)$ is the number of pixel per nuclei at time point *t*. $I_n(t)$ is the mean pixel nuclear GFP-RelA intensity per cell at time point *t*. This quantity is always referred to as the nuclear GFP-RelA intensity in this work.

In addition, a very weak smoothing was applied to remove major noise (Savitzy-Golay, degree = 0.1). However, the filter was very weak (almost not noticeable) to avoid filtering any possible oscillation of the signal. The strengthening of the filter was chosen so that the TNF-α measurement with the wide-field still peaked at 30 minutes. Stronger filters resulted in offsetting or cutting out the major peak when

stimulated with TNF-α. This was due to the large recording time interval. Due to the large time interval (dT = 10-15 min) a nuclear GFP-RelA peak of 30 minutes was captured with approximated 3 points. A strong filter cuts out any peak occurring within these 3 measurement points. Therefore, any common moving averaging filter is not suitable for this work as it cuts off/shifts signals from the major peaks. Savitzy-Golay is a polynomial filter which is suitable for filtering noise of signals with large frequency spans [154].

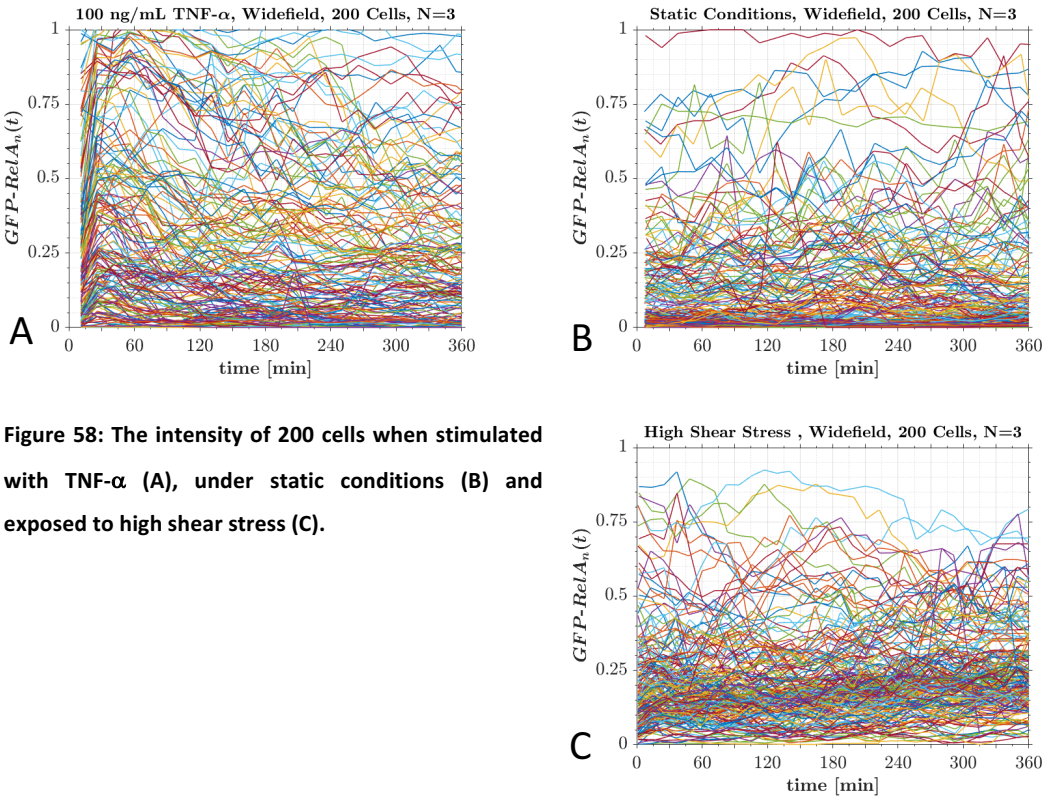

Figure 58: The intensity of 200 cells when stimulated with TNF-α (A), under static conditions (B) and exposed to high shear stress (C).

In Figure 58, the nuclear GFP-RelA intensity of 200 cells for three different experiments (TNF-α, static conditions and high shear stress) is shown. The distinctive features between the experiments can be seen.

However, the single cell measurements include a large amount of noise and a huge cell-to-cell variability. Therefore, proper normalisation of the data was necessary to

draw meaningful conclusions. Different approaches to normalise the single cell measurements are presented in the following sections.

2.17.1. Normalisation methods

2.17.1.1. Normalisation by time average

All cells are normalised using their time average (mean):

$$I_n^M = \frac{I_n(t)}{\langle I_n(T_{start} < t < T_{end}) \rangle} \quad (18)$$

T_{start} is the start time for all recording positions. Due to camera speed, the last position of the gradient channel was recorded for the first time at t=15 minutes. Therefore, we define $T_{start} = 15\ min$. T_{end} is the end all positions. In this work $T_{end} = 360\ min$. Normalisation using the time average is demonstrated in Figure 59.

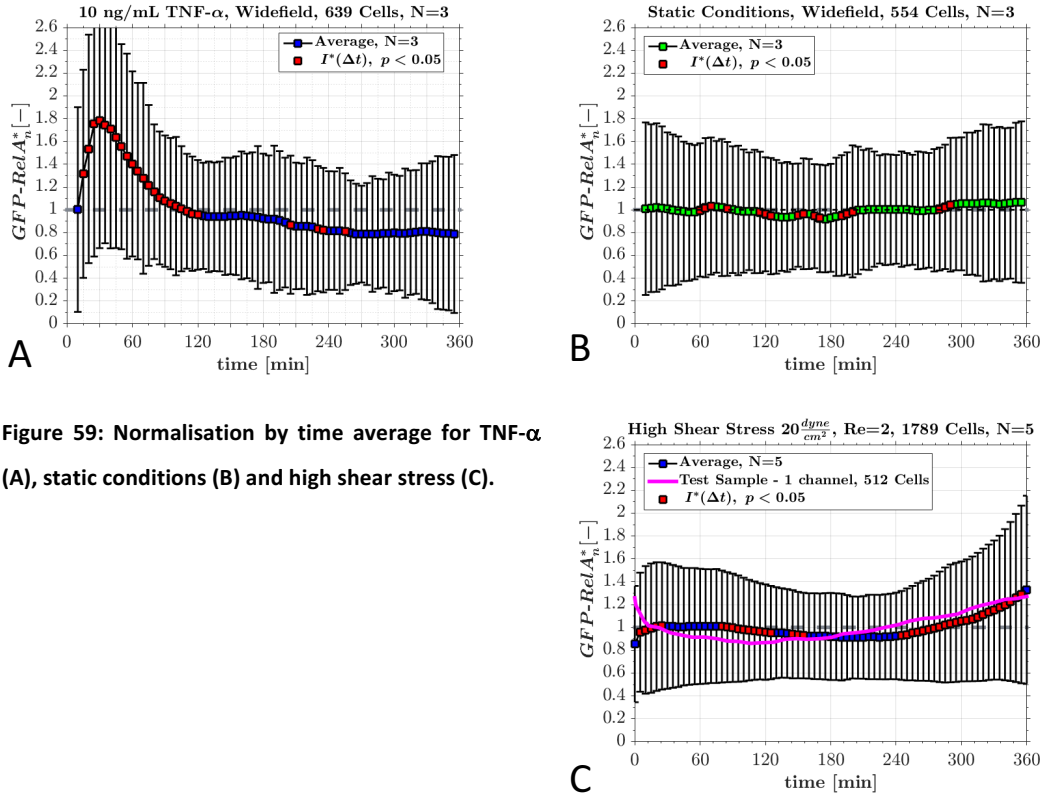

Figure 59: Normalisation by time average for TNF-α (A), static conditions (B) and high shear stress (C).

2.17.1.2. Normalisation by earliest common time point

A further normalisation method is to normalise the intensity using the earliest common time point:

$$I_n^T = \frac{I_n(t)}{I_n(t^* = T_{start})} \quad (19)$$

Due to the camera speed the first and the last picture were a time interval apart (11.25 minutes for the straight channel and 15 minutes for the gradient channel). The average acquisition speed was 0.32 seconds between two positions. Therefore, each cell was normalised using the intensity at the earliest common time point. This is schematically shown in Figure 60.

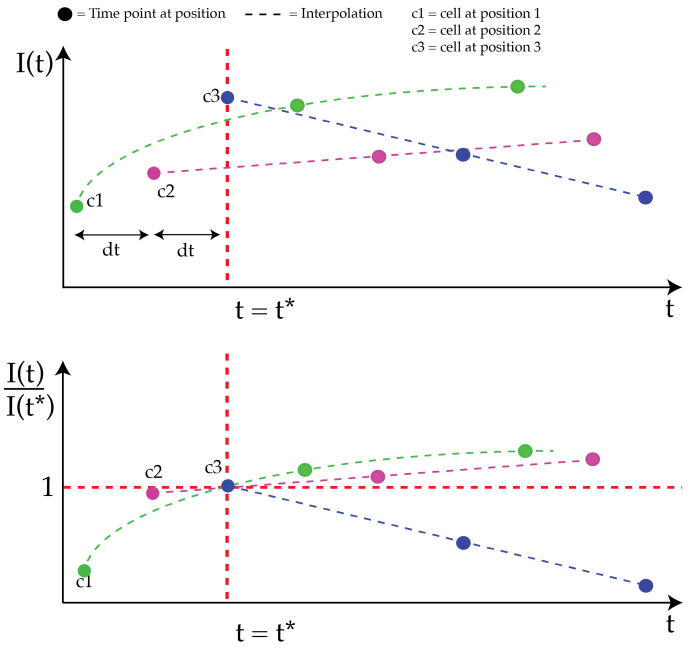

Figure 60: Positions are a time interval *dt* apart due to microscope speed. C1, C2 and C3 represent cells recorded from different initial time points. The signal of each cell is made dimensionless by t*, a time point which was obtained for all cells.

C1, C2 and C3 are cells that were recorded at different starting positions. The intensity between time points was interpolated for each cell, and intensities were obtained at t*. The intensity at t* for each cell was then normalised. Accordingly, all

cells show a change in respect to t*. Using the example shown in Figure 58, cell 1 increases in value, cell 2 remained practically steady, while cell 3 decreases in respect to t*. Moreover, following normalisation a second weak filter was added to the signal (Savitzy-Golay, degree = 0.1) and back interpolated to obtain the missing time points. A second filter was used to flatten the signal further (without losing major peaks), and improve the clustering process (explained in the following sections).

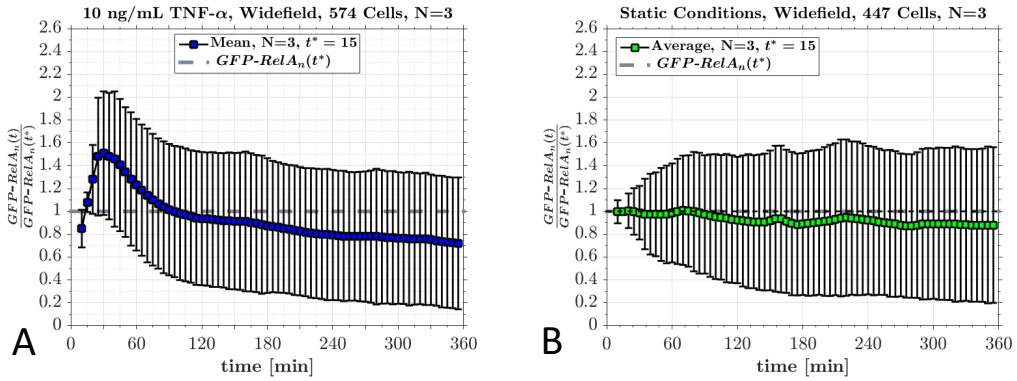

Figure 61: Normalisation by earliest common time point *t*=15 min* for TNF-α (A), static conditions (B) and high shear stress

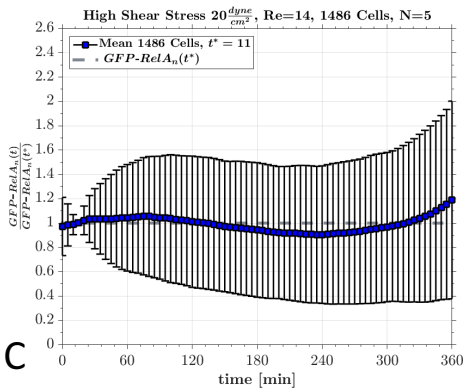

Furthermore, all cells that experienced a change greater than 4 were removed. This was done with the aim of eliminating cells that were in the process of apoptosis or cell division, and cells that expressed much larger amounts of plasmids.

Cells with larger plasmid expression might react more strongly, which would add greater variability to the chaotic system. By accounting for cells that only change by 4-fold the intensity, the aim was to only analyse cells of similar expression levels.

Normalisation by the earliest common time point *t*=15 min* (TNF-α and static conditions) and *t*=11 min* (high shear stress) is illustrated in Figure 61.

2.17.1.3. Normalisation by maximum value

It is also possible to normalise by the maximum intensity of each cell:

$$I_n^{MAX} = \frac{I_n(t)}{\max(I_n(t))} \qquad (20)$$

However, this amplifies noise very drastically. This might lead to interpret non-reactive cells as reactive cells as the noise is scaled up and might appear as strong as a nuclear translocation of GFP-RelA. Normalisation by maximum intensity is exemplified in Figure 62.

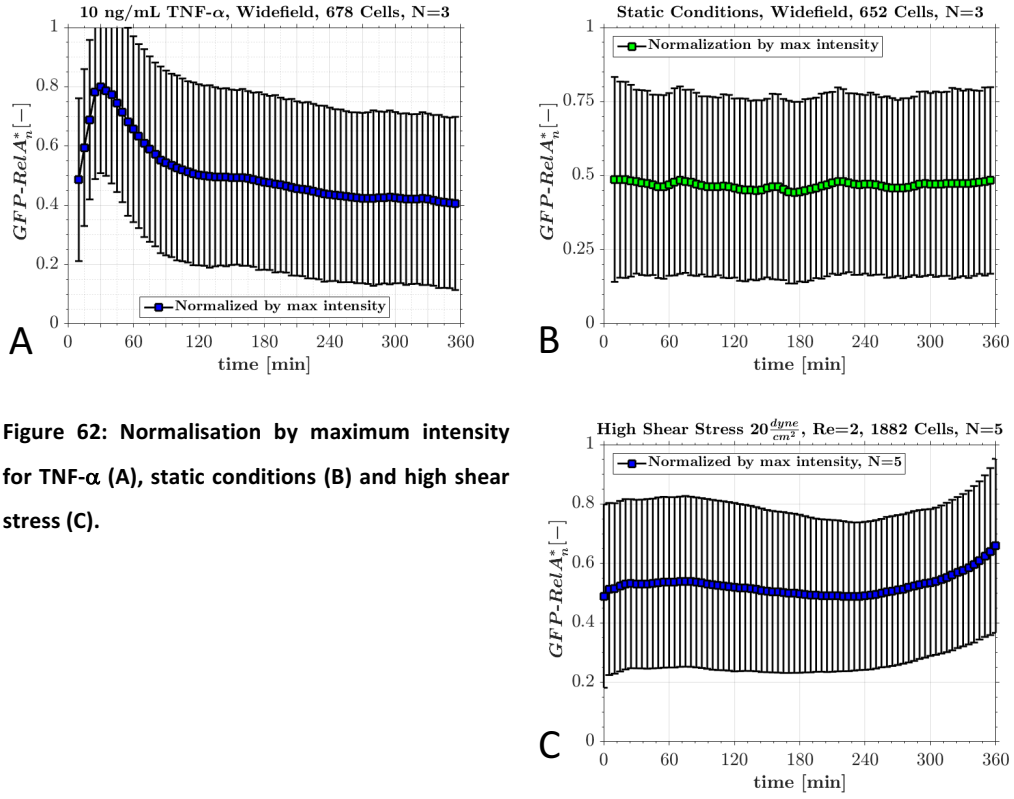

Figure 62: Normalisation by maximum intensity for TNF-α (A), static conditions (B) and high shear stress (C).

2.17.1.4. Standardisation

The signal can also be standardised:

$$I_n^{STD} = \frac{I_n(t) - \mu_n}{\sigma_n} \quad (21)$$

μ_n is the cells' intensity mean and σ_n the intensity standard deviation. However, standardisation also amplifies the noise and makes it difficult to distinguish between reactive cell and non-reactive cell. Standardisation would work well if all cells react in a same manner. Standarisation is exemplified in Figure 63. For example, standardisation of the TNFα single cell measurements resulted in a clear mean and smaller standard deviation (Figure 63.A).

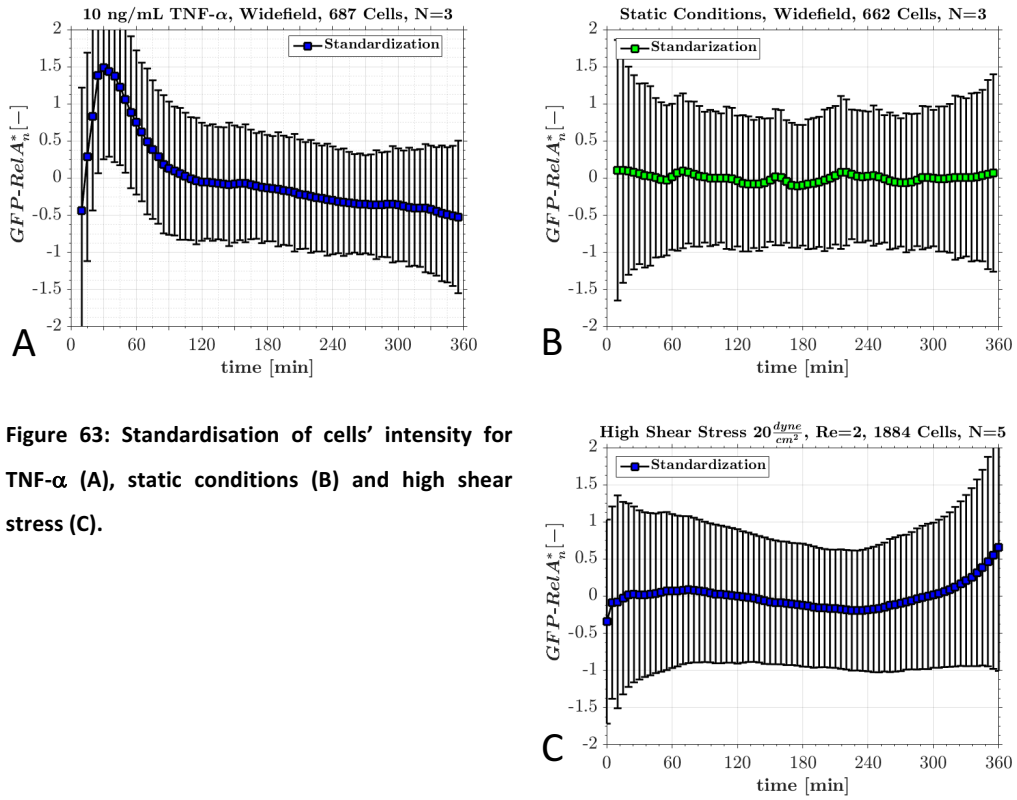

Figure 63: Standardisation of cells' intensity for TNF-α (A), static conditions (B) and high shear stress (C).

2.18. Normalisation used in the results section

In this work, normalisation was carried out using the time average and the earliest common time point. These normalisation methods were employed as they can

distinguish between inactive, weak and strong activated cells. Whereas, normalisation by maximum value or standardisation produced noise signals as big as a translocation signal.

Initially, single cell measurements were analysed using normalisations to the earliest common time point. Evaluation of this analysis revealed single cells to have a large heterogeneity. Therefore, it was decided that other normalisation methods might be more suitable. Hence, normalisation by time average was used for the general analysis. Results will be presented with normalisation using time average, which will always be referred to as

$$GFP{-}RelA_n^*(t)[-] \qquad (22)$$

Initial data analysis with normalisation using the earliest common time is also shown. This will be referred to as

$$\frac{GFP - RelA(t)}{GFP - RelA(t^*)}[-] \qquad (23)$$

2.19. Statistical methods

The mean is given for the whole cell population as

$$\mu = \frac{1}{n}\sum_{i=1}^{n} x_i \qquad (24)$$

With n being the number of cells and x_i the intensity per cell. The errorbars of the measurements were calculated with the standard deviation defined as

$$\sigma = \sqrt{\frac{1}{n}\sum_{i=1}^{n}(x_i - \mu)^2} \qquad (25)$$

Throughout this thesis, *N* indicates the number of repeats.

Standard two-sample t-test and Anova [156] were applied to point out statistical significance.

2.20. Different approaches to find clusters of single cells

In this dissertation, one of the main aims was to cluster single cell measurements of the nuclear GFP-RelA intensity into groups with in order to identify different cell characteristics such as in- and active cells, and temporal sorting of intensity peaks. This task was very challenging and as will be shown later in the results section, clustering did not lead to a unique solution. The single cell analysis was an iterative process during the write up of this thesis. As mentioned previously, the normalisation method was amended during this work to normalisation by time average. However, to draw a comparison between normalisation methods, the clustering attempts for both normalisation methods: Normalisation by time average as the main analysis and normalisation by earliest common time point as secondary analysis, will be presented.

Four clustering methods were applied in this work: Kmeans [155], pulse search, thresholding and hierarchical clustering [156]. The four methods could only give a close approximation and no unique solution of how the single cell behaviour could be grouped. Therefore, interpretation of these results was carried out with caution. The methods are described below and the results are shown for each experiment. These approaches provide an initial framework for further research with the aim to

identify groups of temporal nuclear NF-κB dynamics when exposed to different stimuli.

2.20.1. Kmeans clustering – performed with normalisation by time average and earliest common time point

Signals were clustered into groups using *kmeans* [157]. The *kmean* algorithm associates data points in an iterative method into groups. It applies the following steps:

1. Random initialisation of centroids (number of centroids is defined as k-groups)
2. Calculates squared Euclidean distances to centroid

$$d(x, c) = (x - c)\text{^}2 \qquad (26)$$

3. Assigns the point to the centroid with minimum distance.
4. Calculates the average of the observation per centroid and uses it as a new centroid location
5. Repeats steps 2 to 4 until the cluster group converges.

Kmeans is very effective. However, the number of cluster that was sought must be provided. Hence, a method to find the right number of cluster was needed. To determine the right number of cluster the gap statistic approach was used [158]. The gap statistic out performs other methods such as Calinski-Harabasz or Silhouette evaluation [156]. The gap value is the difference between the sum of error of the cluster means with the expectation of the data in an appropriate null reference distribution. The maximum gap value should indicate the number of clusters within the data. Unfortunately, for large families trees (many sub groups) this approaches mostly fails as no maximum peak can be found. This work includes a very noisy

signal, which incorporates many sub groups. The gap statistic was carried out (Figure 64) for the normalisation method by the earliest common time point and by time average. The gap value did not show a maximum number for all experiments (Standardising of the data also proved unsuccessful). It appeared as if the gap value converge at clusters > 15. Using visually inspection of the data with k>15, the peaks appeared to be distributed in very small groups.

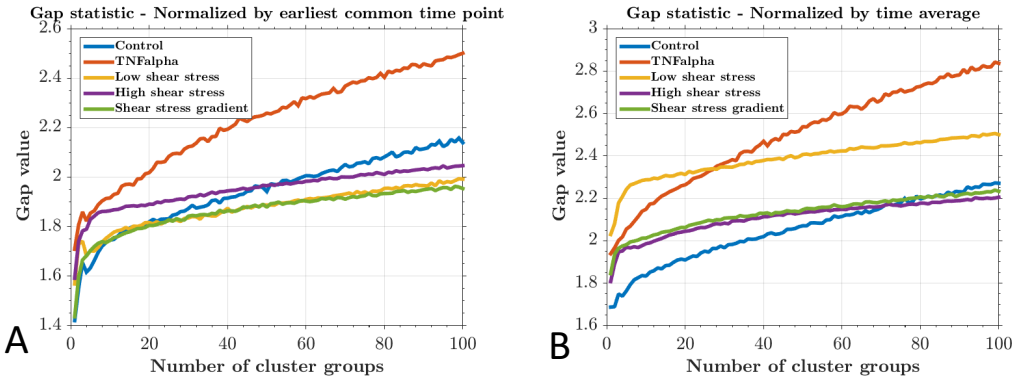

Figure 64: Gap statistic of all measurements applied to normalisation by earliest common time point (A) and time average (B). For both cases, no maximum cluster number was identified within 100 groups.

No clear pattern could be identified. Consequently, clustering with a large number did not produce any useful information. Examining the data using lower cluster groups resulted in more meaningful results. Therefore, identification of the number of cluster groups was undertaken by visual inspection.

The appropriate number of cluster was defined using the following criteria: Three peak groups were identified: early peaks at 0-120 mins, mid peaks 120 – 240 mins and late peaks at 240 – 360 mins. When the difference in subgroup amplitudes between observed groups at *k* and *k+1* cluster is small, then it was concluded that *k* clusters were found. Using this approach and normalisation by time average, the following was found: 3 groups for 10ng/mL TNF-α, 5 groups for static conditions, 6

groups for low shear stress, 5 groups for high shear stress and 5 groups for the shear stress gradient. For normalisation by earliest common time point: 3 groups for 10ng/mL TNF-α, 6 groups for static conditions, 7 groups for low shear stress, 5 groups for high shear stress and 6 groups for the shear stress gradient were found.

In Figure 65A a random set of sinusoidal waves

$$X_n(t) = \sin\left(\frac{1}{180 \cdot r} \cdot 2 \cdot \pi \cdot (t - r)\right) \quad (27)$$

are plotted, where *r* is a random number and *t* the time. In Figure 65B the random sinusoidal waves are clustered with Kmeans into 7 groups. It shows 6 distiguished groups of similar responses, and one single large group of extrem variablitiy that resembles a noisy group.

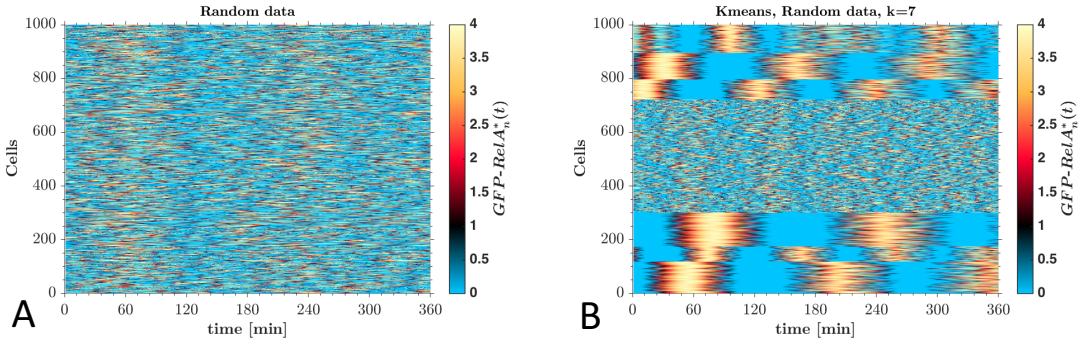

Figure 65: Random sinusoidal waves (A) clustered with Kmeans into 7 groups (B).

2.20.2. Pulse search – performed with normalisation by time average and earliest common time point

It was observed with Kmeans that cells peak at different time points. Therefore, to capture this dynamic a pulse search algorithm was used. A pulse search algorithm was programmed as follows: The correlation of the data to a straight line and multiple pulses was calculated. The straight line represents inactive cells, while the

pulses should mimic a strong nuclear translocation peak. If there are ***n*** pulses then each *i-th* pulse is described as:

$$O_i(t) = \begin{cases} 2.4, & (i-1)\cdot\frac{T_{max}}{n} < t < i\cdot\frac{T_{max}}{n} \\ 1, & t > i\cdot\frac{T_{max}}{n} \\ 1, & (i-1)\cdot\frac{T_{max}}{n} \end{cases} \quad (28)$$

$$L(t) = 1 \quad (29)$$

Where O_i is the i-th pulse and $L(t)$ is the inactive straight line. T_{max} is the length of the pulse. In Figure 66, examples of 1, 3 and 8 pulses are given with their corresponding sorted clustering results.

The k-nearest neighbour method was used to associate each temporal nuclear GFP-RelA profile to each pulse or straight line. Association for 1, 3, and 8 pulses are illustrated with the nuclear GFP-RelA intensity in cells exposed to low shear stress in Figure 66.

After associating each cell to a pulse, the correlation coefficient and the percentage of inactive cells can be calculated. The correlation and the percentage of cells associated with a straight line for a number of clusters (1-50) are shown in Figure 67.

It was observed that the correlation was best at 3 pulses for all experiments (normalised by earliest common time point). However, the percentage of inactive cells converged to a final value when the numbers of pulses were increased. The right number pulses were chosen such that the change of inactive cells is less than 1e-3. This change is indicated with an **X** in each plot (Figure 67)**.** Based on the convergence of inactive cells, for all experiments (normalisation by earliest common

time point and time average) it was decided that approximately 20 pulses is the optimal number. Including the inactive cell group, this makes a total of 21 groups. Therefore, the population measurments for 20 pulses with a time interval of 18 minutes will be screened. Pulse search was applied to both normalisation methods used.

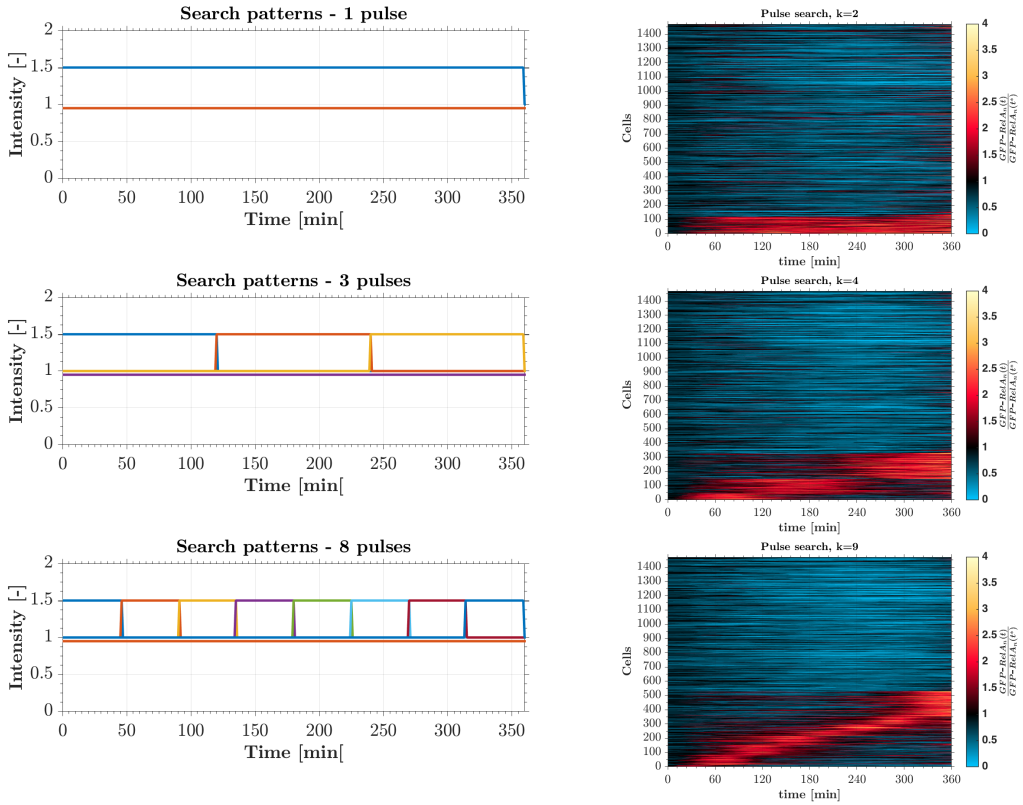

Figure 66: Example of pulse profiles with 1, 3 and 8 pulses. On the left are the corresponding cluster results of the shear stress gradient presented when normalised by earliest common time point.

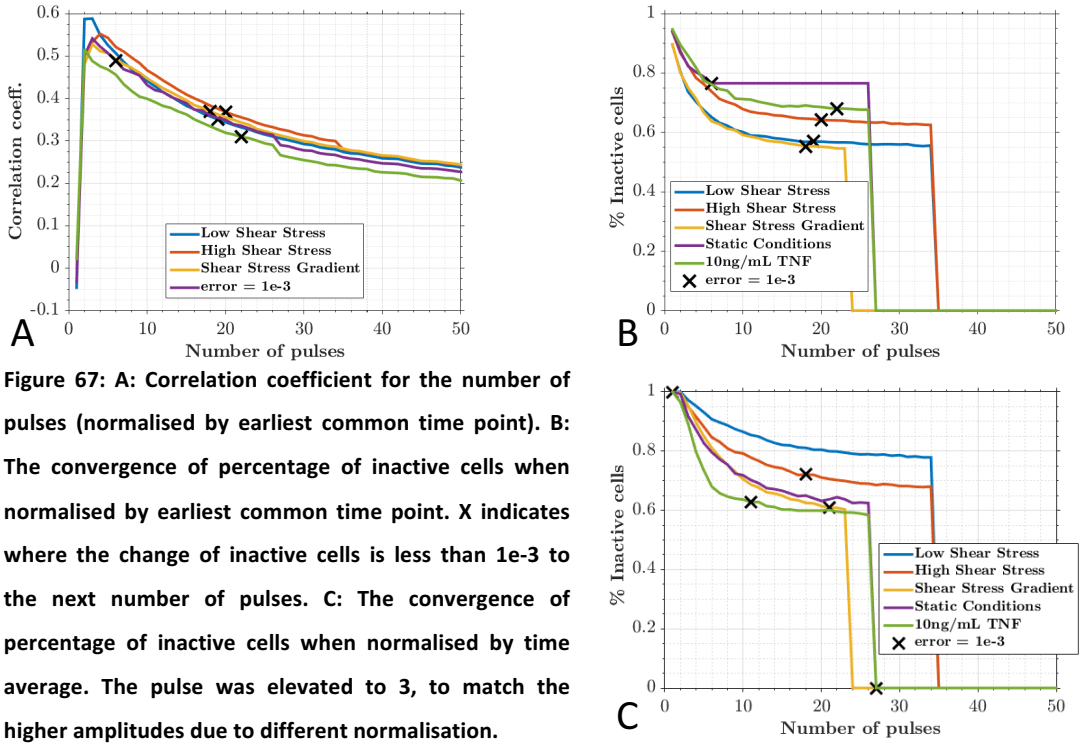

Figure 67: A: Correlation coefficient for the number of pulses (normalised by earliest common time point). B: The convergence of percentage of inactive cells when normalised by earliest common time point. X indicates where the change of inactive cells is less than 1e-3 to the next number of pulses. C: The convergence of percentage of inactive cells when normalised by time average. The pulse was elevated to 3, to match the higher amplitudes due to different normalisation.

2.20.3. Hierarchical clustering – only performed with normalisation by time average

Hierarchical cluster maps were created for all experiments using *Matlab* and the built in function "clustergram.m" [156]. The maps are presented as a heat map including dendograms. Such presentations are standard visualisation methods for microarrays [159] and demonstrated families of similar reaction profiles. Hierarchical clustering was only performed with normalisation by time average.

2.20.4. Thresholding - only performed with normalisation by earliest common time point

Thresholding of the nuclear GFP-RelA intensity and categorisation of cells into different intensity groups was carried out. Three intensity groups were defined: High, medium and low.

$$High = 1.7 < Intensity \quad (30)$$

$$Medium = 1.3 < Intensity < 1.7 \quad (31)$$

$$Low = Intensity < 1.3 \quad (32)$$

The threshold numbers were based on observation of the nuclear GFP-RelA intensity when stimulated with 10ng/mL TNF-α (wide-field). The mean of 500 cells stimulated with TNF-α had a maximal difference in intensity of 0.7 (max. mean peak = 1.5, min. mean peak = 0.8).

All cells were screened if they experienced a nuclear GFP-RelA intensity for more than 15 minutes above the high threshold (1.7). If yes, they were assigned to the high group. If no, then they were screened to see if the signal remained above the medium threshold (1.3) for 15 minutes. If so they were assigned to the medium group. If not, the cells were assigned to the low group. In Figure 68, the threshold ranges are indicated and overlaid on the nuclear GFP-RelA intensity of 100 cells experiencing a low shear stress. Thresholding was only performed with normalisation by earliest common time point.

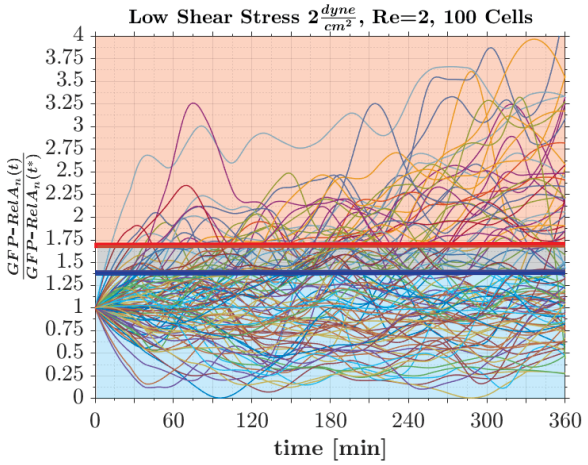

Figure 68: Thresholding of nuclear GFP-RelA intensity. Above red line is high intensity, above blue line is medium intensity, below blue line is considered as low.

3. Nuclear Translocation of NF-κB in HUVECs in response to TNF-α stimulation

Summary: *This chapter presents nuclear translocation of NF-κB (p65 and GFP-RelA) in response to different TNF-α concentrations. The results presented are based on the experimental methods described in Chapter 2. First, non-transfected HUVECs were stimulated with 1 and 10 ng/mL TNF-α, fixed at different time points and stained for p65, p-IKKα/β and IκBα. With IHC, a clear peak of nuclear p65 was observed at 30 minutes when stimulated with 10 ng/mL TNF-α. A lower TNF-α dose, 1ng/mL showed a much smaller peak at 30 minutes. Although IκBa showed unspecific binding, ubiquitination of IκBα in response to 1 and 10 ng/mL TNFα was observed. A peak of p-IKKα/β was observed at 15 minutes for both 1 and 10 ng/mL TNF-α concentrations. HUVECs were successfully transfected with a GFP-RelA and H2B-mCherry plasmid. The transfection efficiency was high at approximatlye 80%. HUVECs expressing GFP-RelA and H2B-mCherry stimulated with TNF-α of different concentrations (1, 10 and 100 ng/mL) showed dynamic translocation. Stimulated with 10 and 100 ng/mL TNF-α, the nuclear GFP-RelA intensity peaked around 30-45 minute, while for 1 ng/mL TNF-α a small peak was observed between 30 and 60 minutes. A lower TNF-α dose resulted in a low nuclear intensity peak. The maximum peaks of cells stimulated with 10 ng/mL TNF-α most likely occurred between 30 and 60 minutes. Under static conditions, the maximum peaks were more evenly distributed in time with a higher tendency at 60 and 300 minutes. Single cells were clustered by applying Kmeans. Cell responses to 10ng/mL TNF-α were clustered into three groups, and static conditions were clustered into five groups. Under static conditions, a fraction of cells experienced spontaneous nuclear translocation of GFP-RelA (approximate 50% of the population – four activation groups). Therefore, it is believed that under static conditions, HUVECs are not at rest but are chaotic. Furthermore, the movement of individual cells could be tracked. Cells, under static conditions and stimulated with TNF-α, moved randomly and at almost equal paces.*

3.1. Immunohistochemistry

HUVECs of passage 3 grew to full confluence and formed a monolayer. Subsequently, the monolayers were stimulated with 1 ng/mL and 10 ng/mL TNF-α for 15, 30, 60, 120, 240 and 360 minutes. The cells were then immediately fixed and stained for

p65, IκBα and phosphorylated IKK. The intensity of the cytoplasm and nucleus are shown as a ratio to the control.

$$I^*[-] = \frac{I_{Experiment}}{I_{Control}} \quad (33)$$

NOTE FOR THIS CHAPTER: Static conditions always refer to untreated cells.

3.2. Nuclear Translocation of p65:

Figure 69 shows monolayers of HUVECs stimulated with 10 ng/mL TNF-α that were fixed and stained for p65 at different time points. In Figure 69.A, HUVECs were fixed in static conditions. A high cytoplasmic p65 concentration was clearly visible, while the nuclear concentration was low. 30 minutes stimulation with 10 ng/mL TNF-α resulted in a strong nuclear translocation of p65 as seen in Figure 69.B.

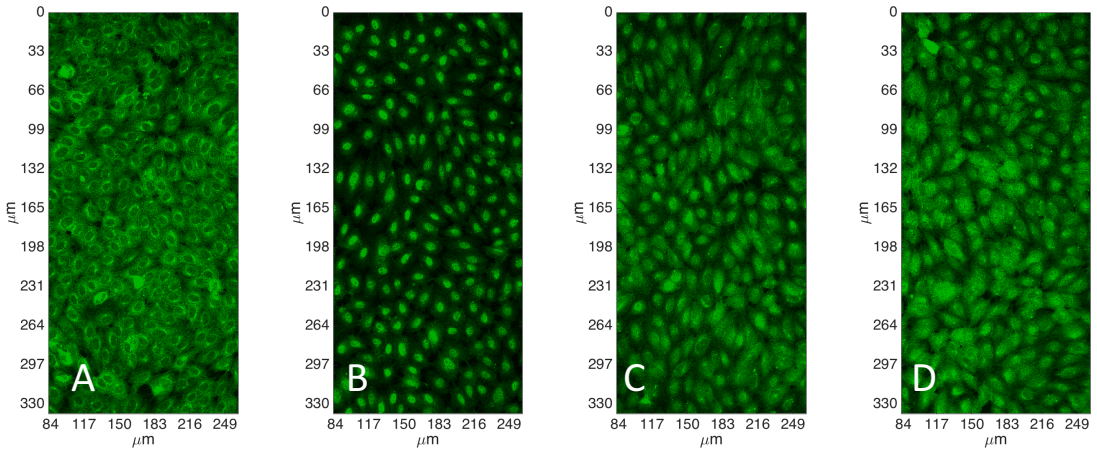

Figure 69: HUVECs fixed and stained for p65 at static conditions (A) and after stimulation with 10 ng/mL TNF-α for 30 minutes (B), 240 minutes (C) and 360 minutes (D).

The nuclei appeared very bright. Moreover, the cytoplasm was almost black (very weak signal), indicating a low cytoplasmic p65 concentration. In Figure 69.C and D,

TNF-α stimulation for 240 and 360 minutes resulted in a more uniform distribution of p65 across the cells in both the nucleus and cytoplasm.

Figure 70 shows the averaged and normalised nuclear and cytoplasmic intensity of p65-AF488 in HUVECs stimulated with 10 ng/mL TNF-α.

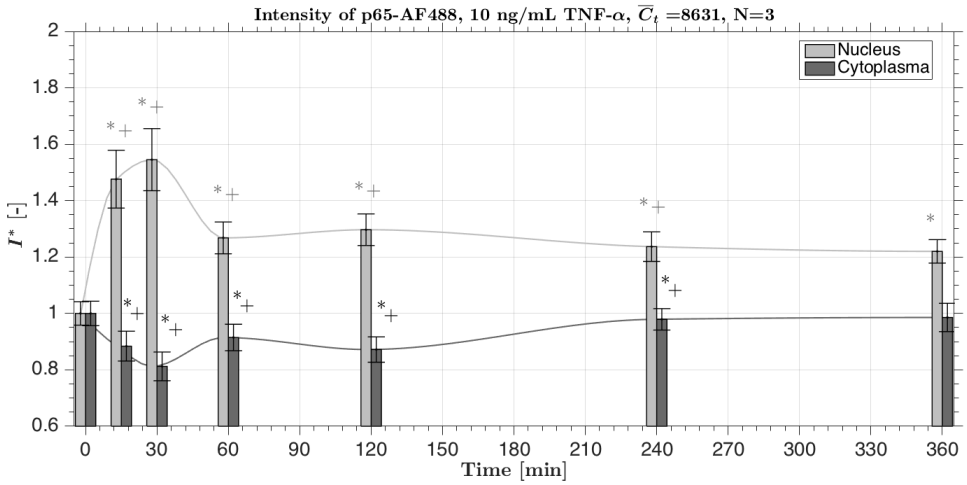

Figure 70: Mean nuclear and cytoplasmic intensity of p65-AF488 in HUVECs stimulated with 10 ng/mL TNF-α at different time points with standard deviations. Average number of detected cells was 8635 per time point. N=3 repeats with each repeat having n=12 images taken. Statistical significance (p<0.05) is indicated versus static control (*) and versus the previous time step (+). The data points are fitted to a curve to represent a trend.

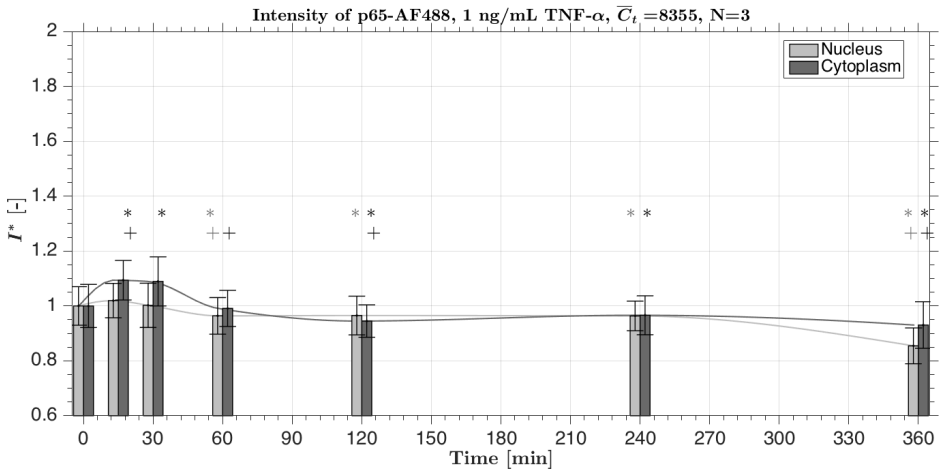

Figure 71: Mean nuclear and cytoplasmic intensity of p65-AF488 in HUVECs stimulated with 1 ng/mL TNF-α at different time points with standard deviations. The average number of detected cells was 8355 per time point. N=3 repeats with each repeat having n=12 images taken. Statistical significance (p<0.05) is indicated versus static control (*) and versus the previous time step (+). The data points are fitted to a curve to represent a trend.

When stimulated with 10 ng/mL TNF-α, the nuclear intensity increased significantly from initial conditions to 15 minutes and peaked at 30 minutes. Moreover, the nuclear intensity decreased at 60 minutes. This was followed by a slight increase (statistically significant) at 120 minutes. After 240 minutes the nuclear intensity remained at a level comparable to half of the peak value at 30 minutes.

The cytoplasmic intensity behaved almost opposite to the nuclear intensity. It decreased and reached a minimum at 30 minutes. This was followed by an increase at 60 minutes and a subsequent decrease at 120 minutes. After 240 minutes, the cytoplasmic intensity returned to its initial state.

The averaged and normalised nuclear and cytoplasmic intensity of p65-AF488 in HUVECs stimulated with 1 ng/mL TNF-α at different times points are shown in Figure 71. At the lower TNF-α concentration, the nuclear intensity of p65-AF488 decreased slightly at 60 minutes, and remained slightly lower than initial conditions until 240 minutes. At 360 minutes the nuclear intensity decreased again. This indicated a downward trend in nuclear intensity from time zero.

The cytoplasmic intensity when stimulated with 1 ng/mL TNF-α followed the same trend as the nuclear. However, a small but statistically significant peak was seen at 30 minutes. In addition, the intensity decreased to below 1 after 360 minutes. This was slightly higher than the nuclear intensity.

3.2.1. Ubiquitination and production of IκBα

HUVECs stimulated with 10 ng/mL TNF-α and stained for IκBα at different time points are shown in Figure 72. It is believed that the antibody caused unspecific binding that resulted in a bright signal in the nucleus. This was probably due to the

IκBα antibody specification. The IκBα antibody was raised against the full length (1-317 amino acids) of the human IκBα. Therefore, it is highly likely that unspecific binding occurred due to the full amino acid length of the antibody. However, as demonstrated later, the IκBα concentrations showed a trend to TNF-α stimulation as defined previously [75]. It was hard to observe by eye a difference in fluorescence intensity, but at 30 minutes, the cytoplasmic intensity appeared to be lower compared to the other time points.

In Figure 73, averaged and normalised intensities of IκBα-AF647 in HUVECs, when stimulated with 10 ng/mL TNF-α, are shown at various time points. The cytoplasmic intensity decreased gradually from 0 to 30 minutes. At 60 minutes the cytoplasmic IκBα-AF647 intensity wasn't significantly different to that observed at 30 minutes.

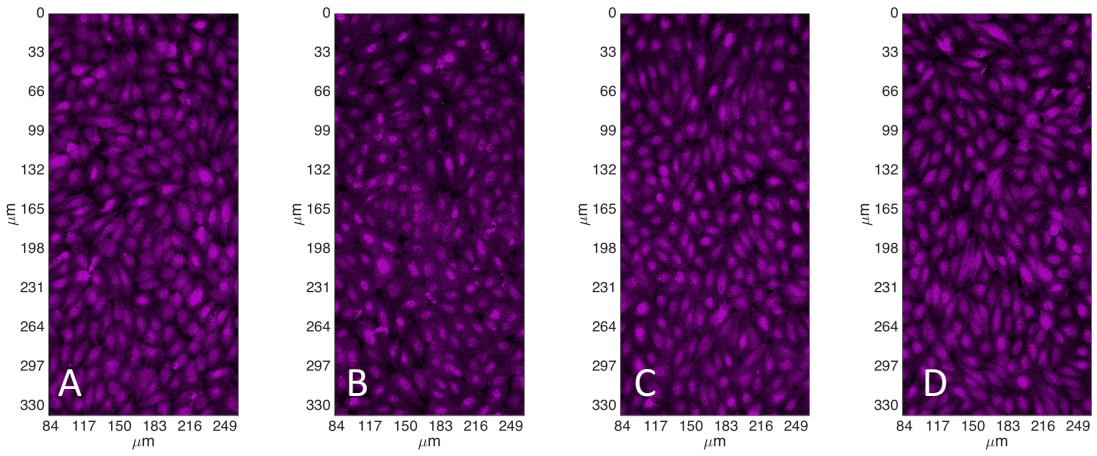

Figure 72: HUVECs fixed and stained for IκBα at static conditions (A) and after stimulation with 10 ng/mL TNF-α for 30 minutes (B), 240 minutes (C) and 360 minutes (D).

The cytoplasmic IκBα-AF647 intensity reached a minimum at 120 minutes. This was followed by a gradual increase back to its initial value at 360 minutes. The nuclear intensity followed the same trend as the cytoplasmic intensity.

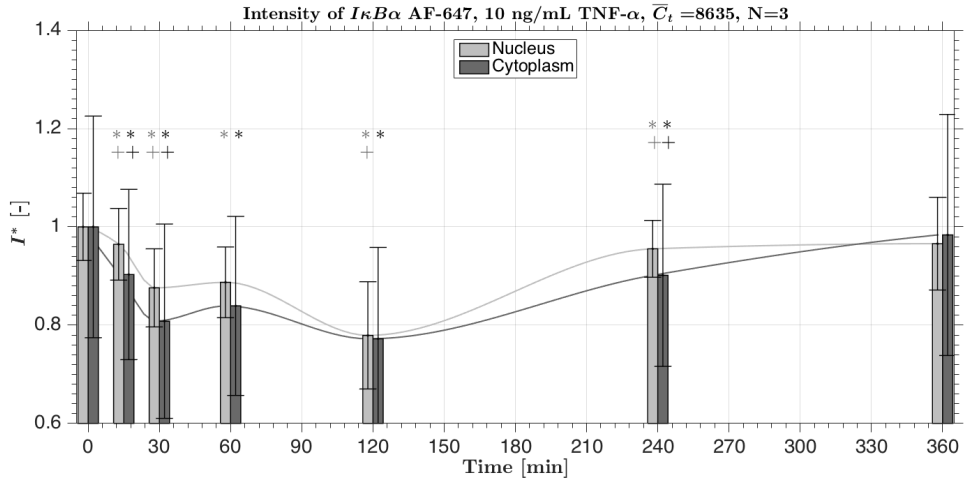

Figure 73: Mean nuclear and cytoplasmic intensity of IκBα-AF647 in HUVECs stimulated with 10 ng/mL TNF-α at different time points with standard deviations. Average number of detected cells per time point was 8635. N=3 repeats with each repeat having n=12 images taken. Statistical significance (p<0.05) is indicated versus static control (*) and versus the previous time step (+). The data points are fitted to a curve to represent a trend.

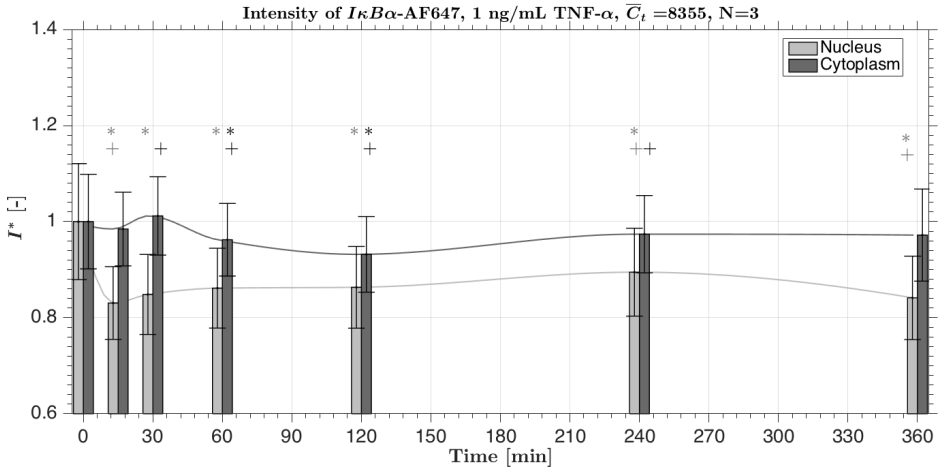

Figure 74: Mean nuclear and cytoplasmic intensity of IκBα-AF647 in HUVECs stimulated with 1 ng/mL TNF-α at different time points with standard deviations. Average number of detected cells was 8355 per time point. N=3 repeats with each repeat having n=12 images taken. Statistical significance (p<0.05) is indicated versus static control (*) and versus the previous time step (+). The data points are fitted to a curve to represent a trend.

The change in IκBα-AF647 intensity with a stimulation of 1ng/mL TNF-α is shown in Figure 74. The cytoplasmic concentration decreases slightly after 60 and 120 minutes, but reaches a basal level again at 240 minutes. The nuclear intensity

dropped to a lower value after 10 minutes and remained low for the remaining time points.

3.2.2. Activation of the IKK complex

In Figure 75, HUVECs were fixed and stained for phosphorylated IKKα/β after stimulation with 10 ng/mL TNF-α at 30, 240 and 360 minutes and under static conditions. Qualitatively, the phosphorylated IKKα/beta signal was slightly brighter at 15 minutes.

In Figure 76, stimulation with 10 ng/mL TNF-α caused the cytoplasmic intensity of phosphorylated IKKα/β to peak at 15 minutes. Subsequntly, the peak was followed by a decline until 60 minutes. From 60 to 360 minutes the intensity slowly rose again and returned to basal level at 360 minutes.

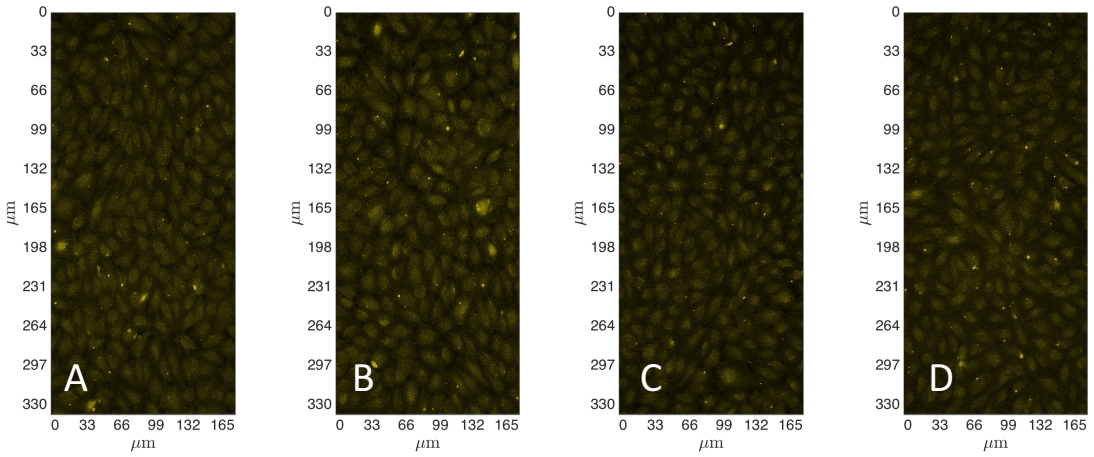

Figure 75: HUVECs fixed and stained for phosphorylated IKK after exposure to 10 ng/mL of TNF-α for different time durations. Control (A), 30 minute (B), 240 minutes (C) and 360 minutes (D).

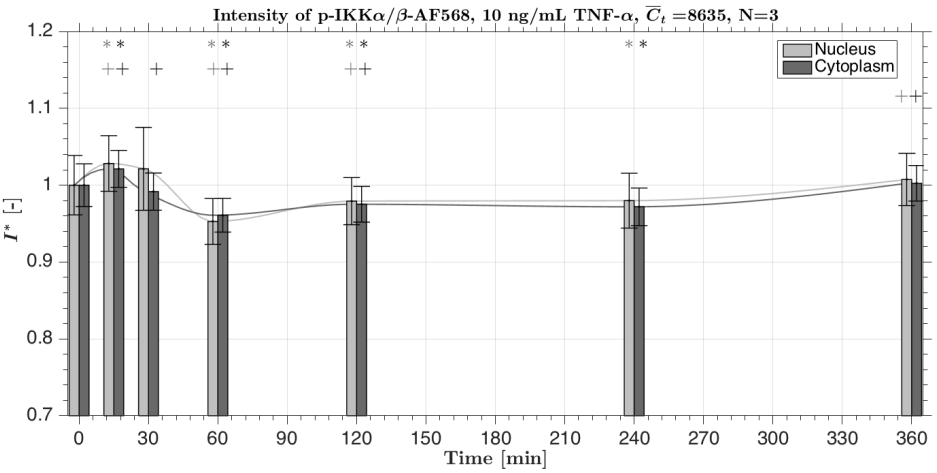

Figure 76: Mean nuclear and cytoplasmic intensity of p-IKKα/β-AF568 in HUVECs stimulated with 10 ng/mL TNF-α at different time points with standard deviations. Average number of detected cells per time point was 8635. N=3 repeats with each repeat having n=12 images taken. Statistical significance (p<0.05) is indicated versus static control (*) and versus the previous time step (+). The data points are fitted to a curve to represent a trend.

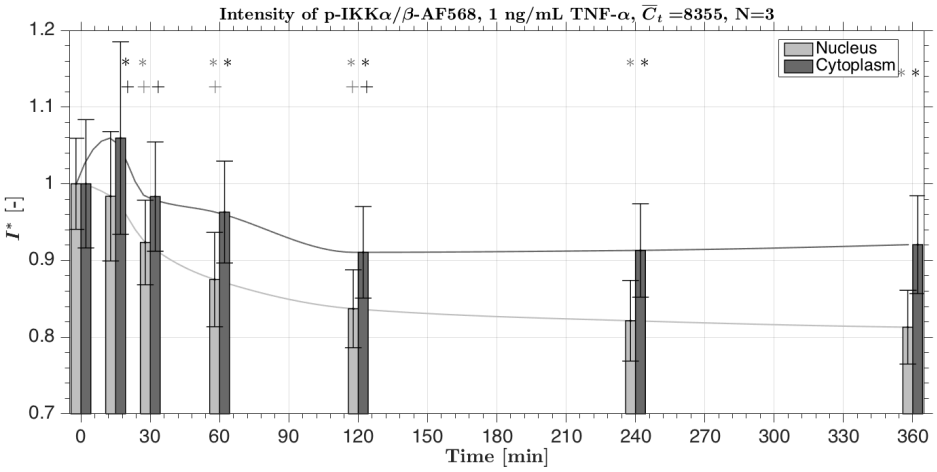

Figure 77: Mean nuclear and cytoplasmic intensity of p-IKKα/β-AF568 in HUVECs stimulated with 1 ng/mL TNF-α at different time points with standard deviations. Average number of detected cells was 8355 per time point. N=3 repeats with each repeat having n=12 images taken. Statistical significance (p<0.05) is indicated versus static control (*) and versus the previous time step (+). The data points are fitted to a curve to represent a trend.

In Figure 77, stimulation with only 1ng/mL TNF-α caused a similar reaction in cytoplasmic intensity to a concentration of 10 ng/mL. A peak of phosphorylated IKKα/β was observed at 15 minutes.

The cytoplasmic intensity declined to a minimum at 120 minutes. Instead of reaching basal level again, the cytoplasmic intensity remained low until 360 minutes. It was noted that the standard deviation was much larger in this system compared to stimulation with the higher 10 ng/mL TNF-α concentration.

3.3. Live-cell Imaging: HUVECs expressing GFP-RelA and H2B-mCherry

The HUVECs of passage 3 were transfected with GFP-RelA and H2B-mCherry and cultured for four days. In Figure 78, confocal images of the HUVECs expressing GFP-RelA and H2B-mCherry under static conditions are shown. The transfection efficiency was high at approximately 60-80 %. Despite confluency of cell population, the transfection efficiency of approximate 60-80 % makes the GFP-RelA cells look not fully confluent (as some cells were not transfected).

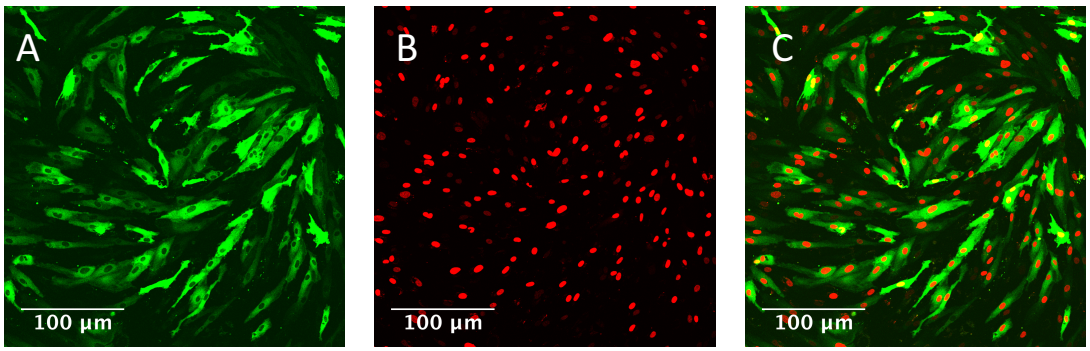

Figure 78: Confocal image of HUVECs expressing GFPRelA (A) and H2B-mCherry (B) under static conditions. Both channels are merged (C) and thus the nuclear concentration of GFPRelA can be calculated.

Expression intensity of both plasmids varied between cells as seen in Figure 78. Several cells showed an overexpression of GFP-RelA, which resulted in very bright green spots. However, most cells showed a low to normal, and clear expression of GFP-RelA. The H2B-mCherry expression also varied from low to high, from cell to cell. An overexpression of H2B-mCherry plasmid was not observed. Most cells were successfully transfected with both plasmid, only a small percentage (< 5%) had only

one plasmid. Both images (Figure 78.A and B) were merged to obtain Figure 78.C. The GFP-RelA intensity was then calculated in the H2B-mCherry signal, which represented the nuclear GFP-RelA concentration. The nuclear GFP-RelA concentration is allegorical for nuclear p65 concentration.

3.4. TNF-α stimulation caused nuclear translocation of GFP-RelA

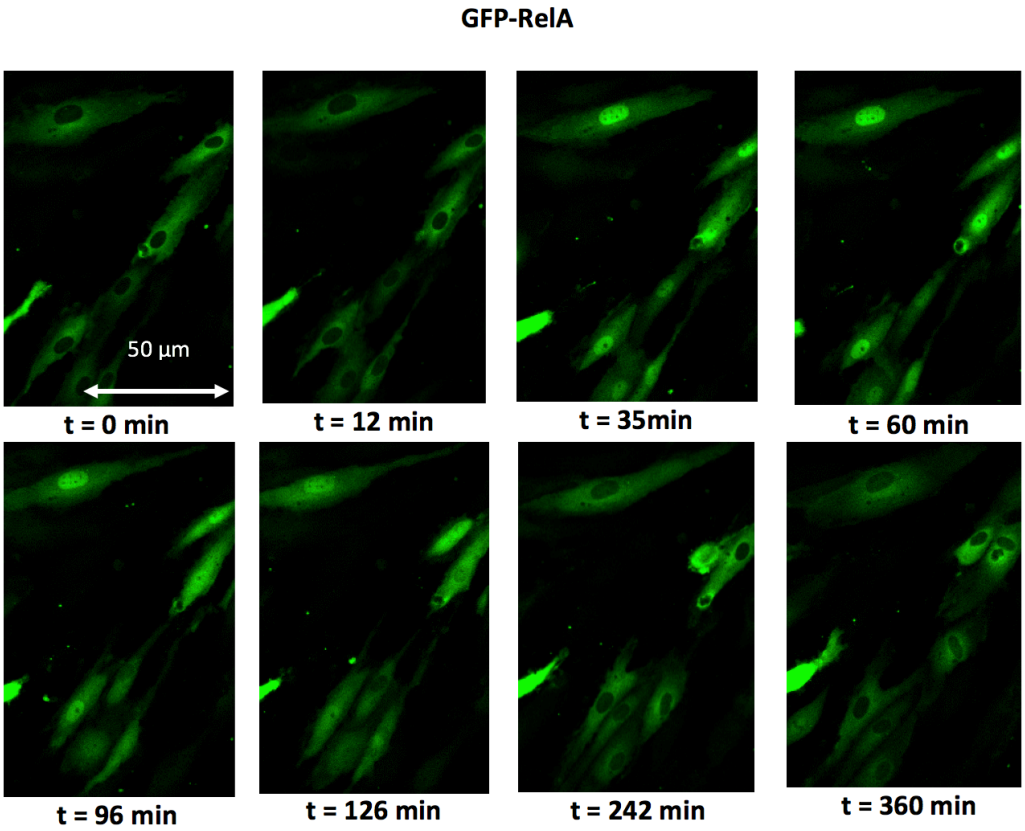

Figure 79: HUVECs expressing GFP-RelA after exposure to 10 ng/mL TNF-α at different time points. High nuclear GFP-RelA intensity in the nucleus is observed at 38, 60, 96 and 126 minutes. At 242 and 360 minutes, nuclear GFP-RelA concentration is low and almost as at 0 minutes. This⁄ movie like time frame demonstrates live the translocation of GFP-RelA. Variations between cells can be observed. Imaged with confocal.

Transfected HUVECs were stimulated with TNF-α of different concentrations (1, 10 and 100 ng/mL). The spatial molecular movement of the GFP-RelA in single cells

when stimulated with 10 ng/mL TNF-α is shown after 0 - 360 minutes in Figure 79 for the GFP-RelA channel only and in Figure 80 for GFP-RelA and H2B-mCherry.

Initially, GFP-RelA was solely in the cytoplasm and the nucleus appeared empty (black). After 35 minutes, a high nuclear GFP-RelA concentration was clearly visible. This remained until 60 minutes and the nuclear intensity started to fade at 96 and 126 minutes. After 240 minutes, the spatial distribution of GFP-RelA within the cell regained roughly its initial state. The nuclear GFP-RelA concentration was low and most of the GFP-RelA was concentrated again in the cytoplasm. This remained the case after 360 minutes. In addition, one can observe in Figure 79, variability in cell size, expression intensity and temporal nuclear intensity between cells.

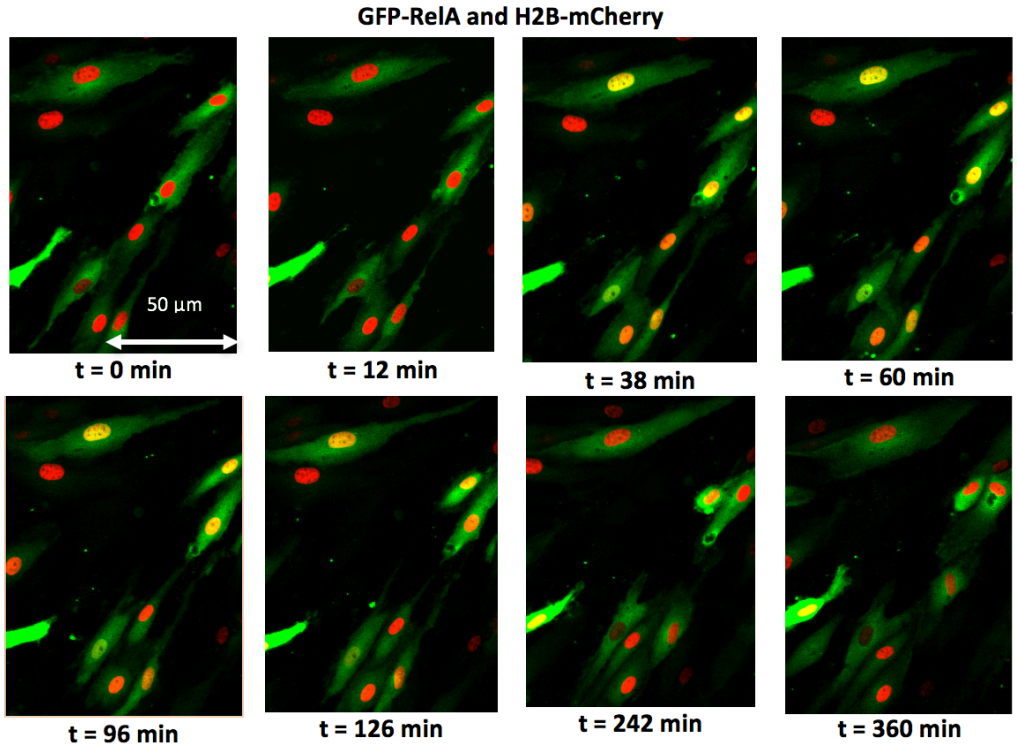

Figure 80: HUVECs expressing GFP-RelA and H2B-mCherry after exposure to 10 ng/mL TNF-α at different time points. High nuclear GFP-RelA intensity in the nucleus is observed at 38, 60, 96 and 126 minutes. At 242 and 360 minutes, nuclear GFP-RelA concentration is low and almost as at 0 minutes. This movie like time frame demonstrates live the translocation of GFP-RelA in and out of the nucleus. Variations between cells can be observed. Imaged with confocal.

During all experiments, a frame was recorded at each time point that included approximately 200 transfected cells. In Figure 81, three example frames are displayed, showing the GFP-RelA of transfected HUVECs after stimulation with 100 ng/mL TNF-α at 0, 35 and 240 minutes. Under close inspection a high nuclear GFP-RelA concentration could be observed at 35 minutes. While at the other time points, the GFP-RelA was mainly located in the cytoplasm. Again, a high variability between cells was visible.

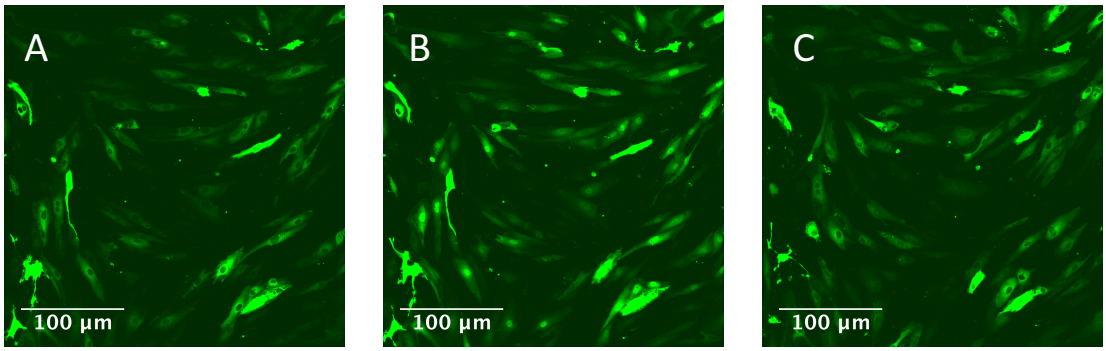

Figure 81: A cell population of HUVECs transfected with GFP-RelA after exposure to 100 ng/mL TNF-α at 12, 35 and 360 minutes (A, B and C, respectively). Imaged with confocal.

3.5. Single cell nuclear translocation of GFP-RelA

Cells stimulated with different TNF-α concentration were imaged using a confocal and wide-field microscope. With the confocal, transfected HUVECs stimulated with 1, 10 and 100 ng/mL TNF-α were imaged for a long duration of 620 minutes. With the wide-field, transfected HUVECs stimulated with 10 ng/mL TNF-α and under static conditions were imaged for 360 minutes. The temporal intensity of nuclear GFP-RelA was calculated using a custom-made single-cell tracking software for each single cell as explained in the methods in section 2.17.

The normalised nuclear GFP-RelA intensity for 100 cells stimulated with 10 ng/mL TNF-α when recorded with a confocal (Figure 82.A) and 10 ng/mL TNF-α when

recorded with a wide-field (Figure 82.B) are shown in Figure 82. Due to technical difficulties with the confocal (software not suitable for live imaging and long-scan time), the timinig of the measurments were not very accurate and thus the peak is slightly off at approximately 30 to 45 minutes. The more suitable wide-field microscope setup allowed better precision in recording time and thus resulted in a clear peak at 30 minutes as reported in the literature [75, 101]. In addition, the confocal scan time was very slow. This resulted in scan times of approximate 8-12 minutes for 3 positions. To capture the GFP-RelA dynamics a maximum time interval of 15 minutes had to be considered. With the wide-field microscope, the scan speed was around 0.35 seconds per positions, which allowed imaging of several positions and thus a much larger quantity of cells.

For the TNF-α experiments, approximately 100 cells per experiment were tracked with the confocal, while 500 – 700 cells were captured with the wide-field microscope. In the flow experiments between 1000 and 2000 cells were captured. The main experiments in this thesis were peformed with the wide-field microscope.

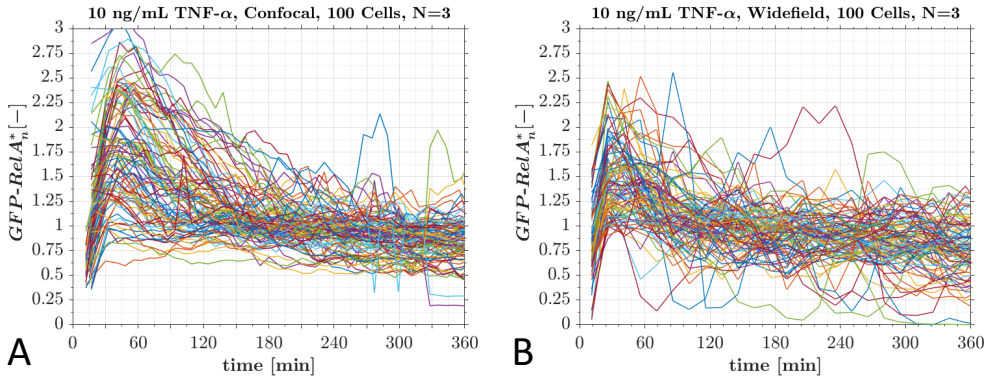

Figure 82: Nuclear GFP-RelA intensity normalised by time average in HUVECs stimulated with 100 ng/mL TNF-α imaged with a confocal microscope (A) and 10 ng/mL TNF-α imaged with a wide-field microscope (B).

100 ng/mL TNF-α - Confocal: In Figure 83.A and Figure 83.B, the nuclear GFP-RelA intensity and the intensity normalised by time average are shown for the population

stimulated with 100 ng/mL TNF-α. The dimensional intensity in Figure 83.A showed large variations between the three samples. Hence, the normalised intensity offers a much better comparison. In Figure 83.B, a clear peak of nuclear GFP-RelA occurred at 30 – 50 minutes. After 30 - 50 minutes, the high nuclear intensity plummeted to almost half of the peak value at 120 minutes. The nuclear intensity then gradually decreased until 620 minutes. A very high TNF-α concentration of 100 ng/mL caused a very synchronised reaction of all cells, as reflected in the small standard deviation shown in Figure 83.B.

10 ng/mL TNF-α - Confocal: The intensities of the 3 samples (Figure 83.C) were also very different, but normalisation as shown in Figure 83.D revealed a better insight into the single cell dynamics. A strong peak was observed at around 30-45 minutes, followed by gradual but slower decay of nuclear intensity. After 240 minutes the nuclear intensity was approaching its basal level. Stimulating with 10 ng/mL TNF-α caused a less synchronised signal (larger standard deviation) than for 100 ng/mL TNF-α.

The live-cell measurements of nuclear GFP-RelA can be directly compared with immunohistochemistry of non-transfected HUVECs exposed to 10 ng/mL TNF-α as shown in Figure 83.E. Both measurements are in agreement, as immunohistochemistry showed a peak of nuclear p65 at 30 minutes and live-cell imaging a nuclear GFP-RelA intensity peak at around 30 to 45 minutes. There is a slight difference at 60 minutes, as the reported protein GFP-RelA appeared to shuttle slower from the nucleus back to the cytoplasm than the endogenous p65. However, this difference could also be due to measurement noise, which may have extracted strongly occurring oscillations.

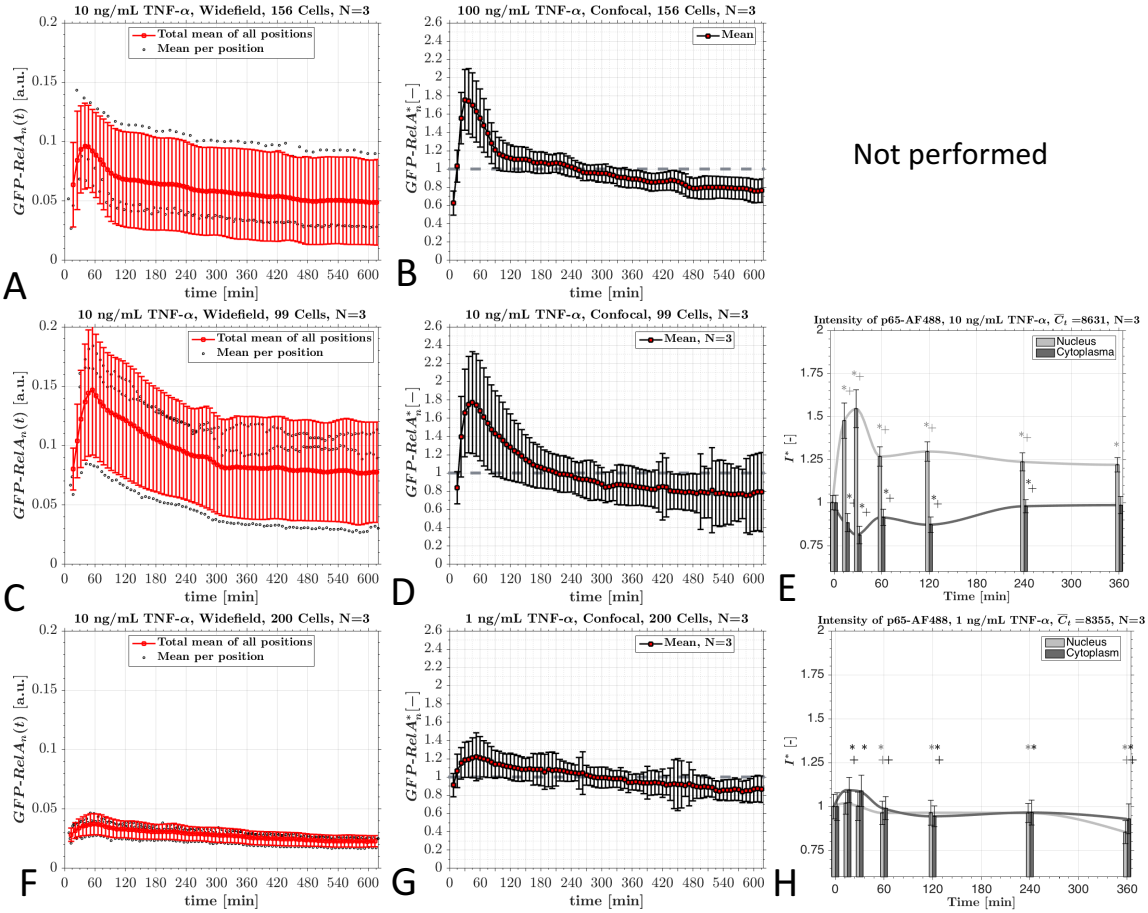

Figure 83: Mean and standard deviation of nuclear GFP-RelA intensity of transfected HUVECs stimulated with 100 ng/mL TNF-α imaged live using a confocal microscope (A= Intensity [a.u.], B = Intensity normalised by time average [-]), 10 ng/mL (C= Intensity [a.u.], D = Intensity normalised by time average [-]), and 1 ng/mL (F= Intensity [a.u.], G = Intensity normalised by time average [-]). Total number of cells tracked is indicated and number of repeats was N=3. Live-cell imaging experiment with 10 and 1 ng/mL TNF-α can be directly compared to immunohistochemistry of non-transfected HUVECs stimulated with the same TNF-α concentration stained for p65 at different time points (E and H).

1 ng/mL TNF-α - Confocal: A very small TNF-α concentration, 1ng/mL TNF-α, caused only a small increase in nuclear intensity as depicted in Figure 83.F and G. The nuclear GFP-RelA intensity peaked at 30 to 60 minutes and then gradually decreased until 620 minutes. Surprisingly, the standard deviation of the normalised intensity (Figure 83.G) was small, suggesting better synchronisation at 1 ng/mL than at 10 ng/mL TNF-α. The live-cell imaging measurements of nuclear GFP-RelA can be directly compared with immunohistochemistry of HUVECs exposed to 1 ng/mL TNF-α in Figure 83.H.

Moreover, at a lower TNF-α concentration both measurements showed agreement. Nuclear p65 peaked at 30 minutes and then significantly dropped in all following time points. Live-cell measurements showed a small peak of nuclear GFP-RelA intensity at around 30 to 60 minutes.

In general, measurements with the confocal microscope resulted in peaks of nuclear GFP-RelA intensity between 30-60 minutes. The peaks were a bit delayed in comparison to observations in the literature [75]. The scan time per position (1-3 minutes) might have caused this effect. Moreover, this may have been caused by the delay created from inserting TNF-α solution in the tissue culture lab, running to the microscope room, placing the sample and finding positions and starting the image recording. The confocal software was found to not be very suitable for live imaging as it had no autofocus and scans could not be interrupted.

10 ng/mL TNF-α - Wide-field: GFP-RelA expressing HUVECs stimulated with 10 ng/mL TNF-α imaged with wide-field microscope are shown for different time points (15, 30, 180 and 360 minutes) in Figure 84. The strong nuclear translocation can be observed at 30 minutes. In Figure 85, the 10 ng/mL TNF-α stimulation was repeated using a wide-field microscope. The intensity of nuclear GFP-RelA of each cell is shown in Figure 85.A. The big spread of points indicates huge variability in intensities between cells. This variability was due to different expression levels of plasmid, light differences between wells and recording time differences between positions. In Figure 85.B, each of the 12 recording positions was averaged (ca. 50 cells per position). In Figure 85.C, the intensity signal was normalised by the time average. A strong peak at 30 minutes that drops again until 120 minutes was observed. From 120 to 360 minutes the nuclear GFP-RelA intensity decreases slowly in time and it

appears to oscillate with local peaks at 150 and 330 minutes. The red squares indicate if a time point is significantly different to the previous one. The single cell measurements can then be compared with IHC of non-transfected cells fixed and stained for p65 at different time points. We observed agreement of a strong nuclear p65 peak at 30 minutes. IHC showed that nuclear p65 at 60 minutes is lower than at 120 minutes. However, it appeared as if the GFP-RelA was slower in leaving the nucleus and this may have caused the higher nuclear GFP-RelA intensity at 60 minutes compared to at 120 minutes.

Static conditions (untreated cells) - Wide-field: GFP-RelA expressing HUVECs under static conditions are shown at different time points (10, 30, 180 and 360 minutes) in Figure 84. Almost no GFP-RelA nuclear translocation can be observed visually. In Figure 85**.**E, the intensities of each of the cells, including their mean and standard deviation were plotted. Again, a big spread is observed for all measurements. This indicates a large variability in the measurements. In Figure 85.F, the average of each of the 12 positions are shown. The normalised intensity by time average is depicted in Figure 85.G. The mean was observed to hover around 1. This indicates that there is no/little change of the total population with time. Red points indicate when a time point was significantly different than the previous point. Significant changes were found to occur seven times during the control measurement. This might indicate that the control is not at absolute rest, and under goes spontaneous nuclear translocation of GFP-RelA. A spontenous occurring nuclear translocation is highlighted in Figure 86. The cell indicated with a red arrow experienced an increased nuclear GFP-RelA concentration at 120 minutes.

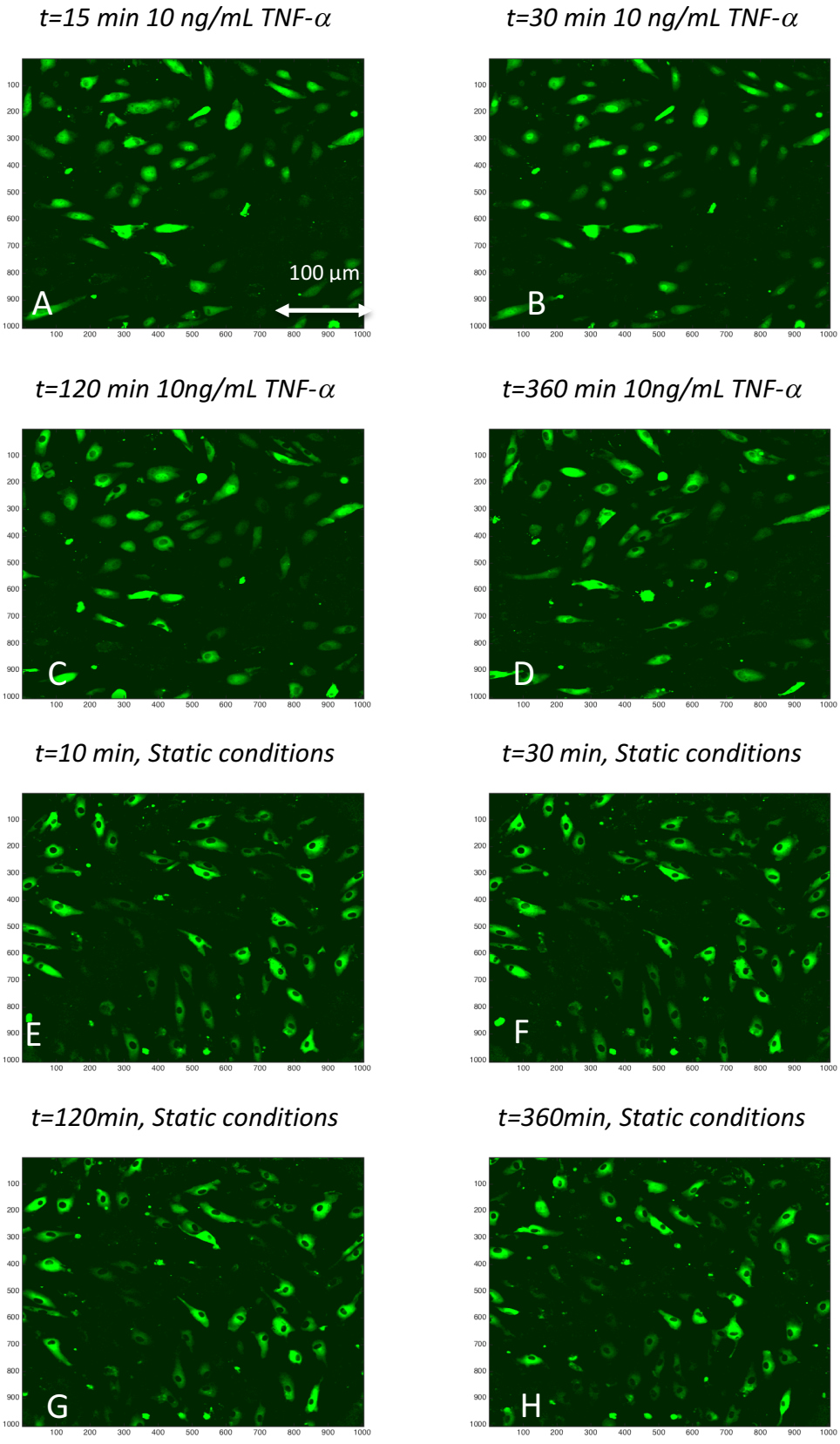

Figure 84: Post-processed widefield images of GFP-RelA express HUVECs stimulated with 10 ng/mL TNF-α (A, B, C, D) and under static conditions (untreated) (E, F, G, H) at time points 0, 30, 120 and 360 minutes.

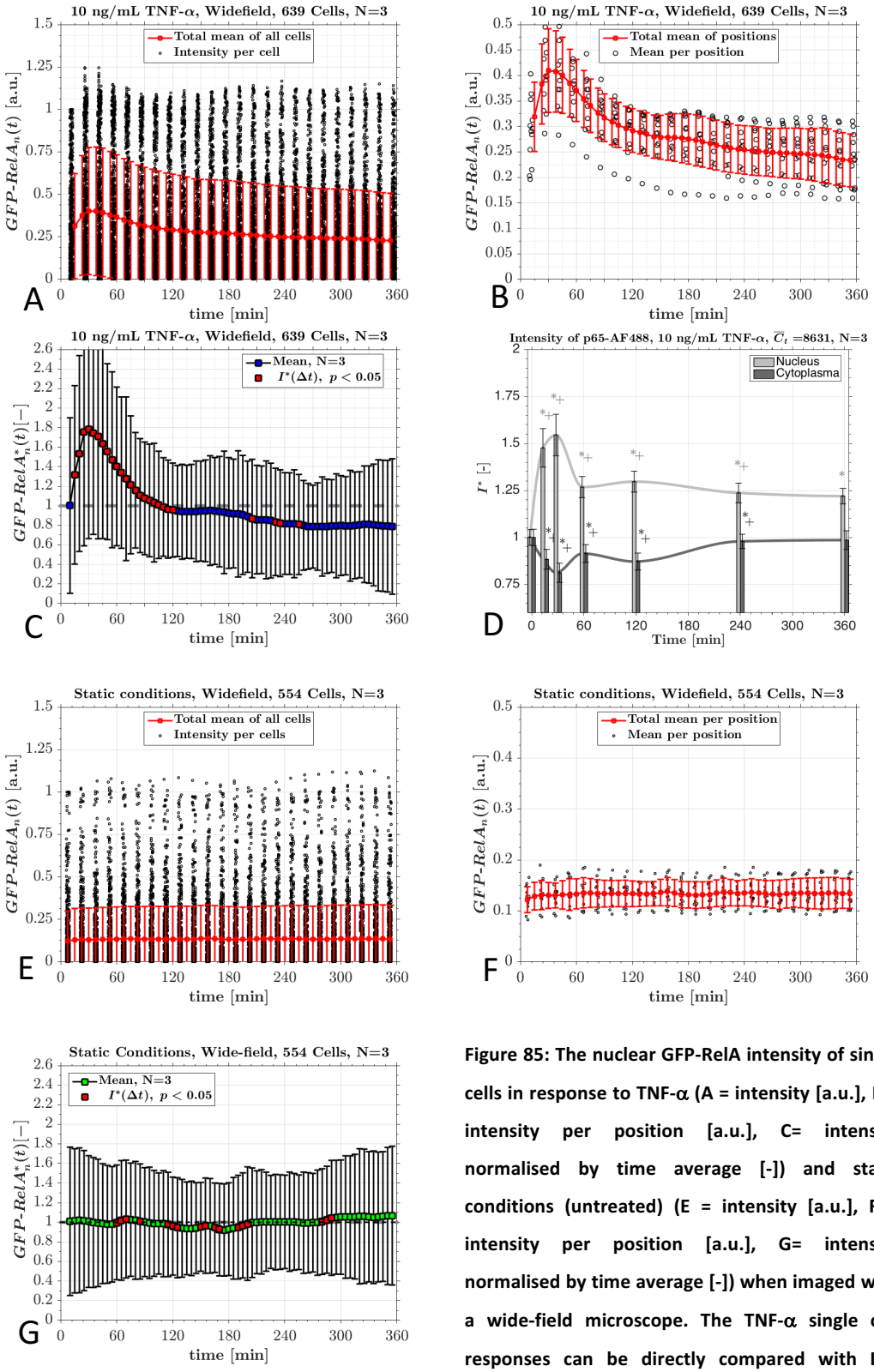

Figure 85: The nuclear GFP-RelA intensity of single cells in response to TNF-α (A = intensity [a.u.], B = intensity per position [a.u.], C= intensity normalised by time average [-]) and static conditions (untreated) (E = intensity [a.u.], F = intensity per position [a.u.], G= intensity normalised by time average [-]) when imaged with a wide-field microscope. The TNF-α single cell responses can be directly compared with IHC measurements (D).

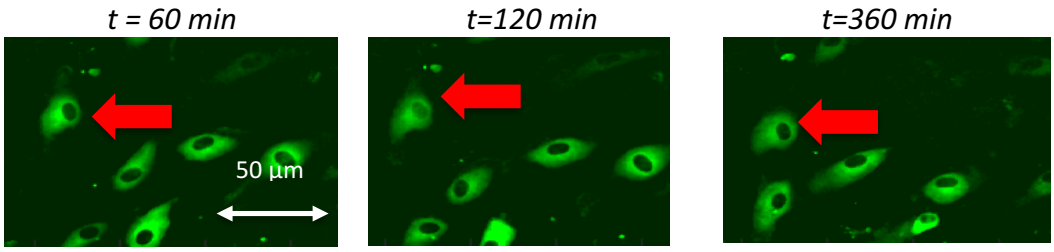

Figure 86: Example of a spontaneous occurring nuclear translocation of GFP-RelA in a HUVEC under static conditions (untreated). The red arrows indicate the HUVEC of interest.

3.6. Maximum peak analysis with normalisation by time average

10 ng/mL TNF-α - wide-field: In Figure 87.A, each of the cells nuclear GFP-RelA intensities are shown in a projected view, where the projection is made according to the intensity axis. A high intensity (red) can be seen early in the experiment between 0 and 60 minutes.

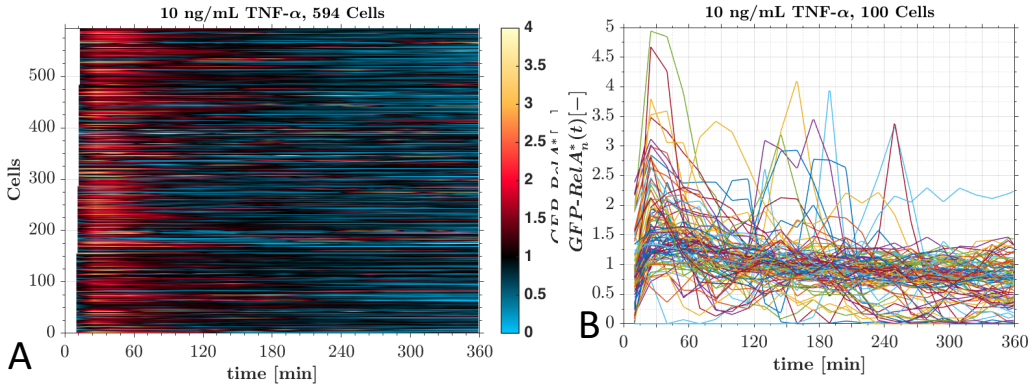

Figure 87: Nuclear GFP-RelA intensity normalised by time average when stimulated with 10 ng/mL TNF-α in all cells shown as intensity projection map (A), super imposed temporal profile of 100 cells (B) and the maximum peak distribution in time (C).

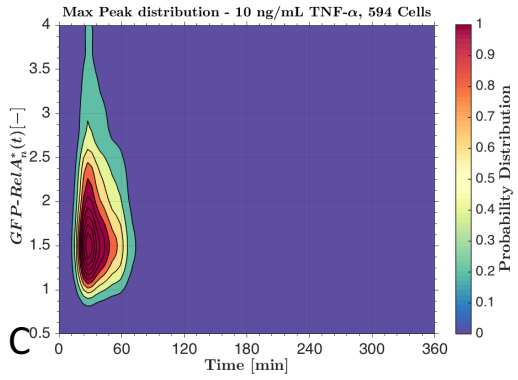

At later times, the map shows a dark blue signal, indicating low nuclear GFP-RelA intensities. In Figure 87.B, the temporal nuclear GFP-RelA profile is shown for 100

cells A tendency for cells to peak at 30 minutes can be seen. In Figure 87.C, the maximum peak distribution over time is depicted. The maximum peak for each of the cells appeared to be dominantly distributed close to 30 minutes at about amplitude of 1.5.

Static conditions (untreated cells) - wide-field: In Figure 88.A, an intensity projected map of all the cells is shown. Many cells appear to experience an increase in nuclear GFP-RelA intensity (red), which is randomly distributed in time and amongst the cells. No clear pattern can be identified, as was observed with TNF-α. The temporal nuclear GFP-RelA intensity for 100 cells is shown in Figure 88.B. It can be seen that a few cells experience peaks distributed randomly throughout the experiment. It is questionable if these peaks are amplified noise or a real nuclear translocation of GFP-RelA.

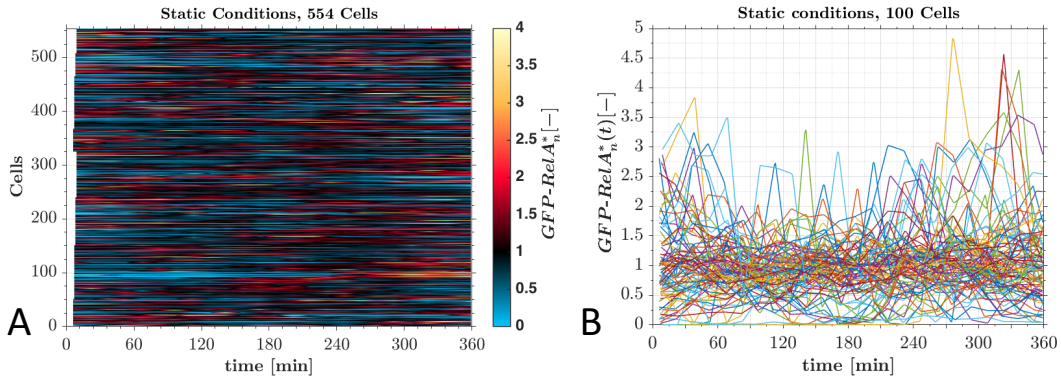

Figure 88: Nuclear GFP-RelA intensity normalised by time average under static conditions (untreated) in all cells shown as an intensity projection map (A), super imposed temporal profile of 100 cells (B) and the maximum peak distribution in time (C).

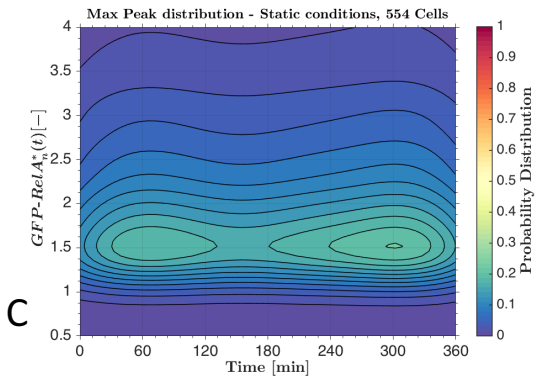

The maximum peak distribution with respect to time is shown in Figure 88.C. Under static conditions, the maximum peaks for each cell appeared to be distributed along the experiment time with a slight higher tendency at 60 and 300 minutes. This may indicate either a large heterogeinity or a random noise distribution.

3.7. Clustering of single cell measurements

In the first attempt of analysing the single cell measurements, each cell was normalised by its earliest common time point. This gave an initial insight on how chaotic the system is. As shown, many cells drastically moved from their original point: some go up, remain at one or decrease. The normalisation method was later changed to normalisation by the time average, which was found to be more suitable for general analysis (as demonstrated in all previous results). As demonstrated in paragraph 2.20.1, evaluating the single cell measurements with gap statistics did not lead to a unique cluster number in the experiments. Therefore, a simple approach was followed to identify the number of groups by visual inspection. The clustering attempts for both normalisation methods are presented. First, the clustering attempts using time average normalisation are shown from which the main conclusions (primary analysis) are drawn. Second, clustering attempts using normalisation by earliest common time point are shown, as this was the initial data analysis (secondary analysis).

3.7.1. Clustering attempts with intensity normalised using time average – Main analysis

10 ng/mL TNF-α - wide-field: In Figure 89, the single cell measurements are clustered into 3 groups using Kmeans. All the groups showed a peak at 30 minutes. A

medium sized group (14%) experienced a very high nuclear GFP-RelA intensity peak at 30 minutes.

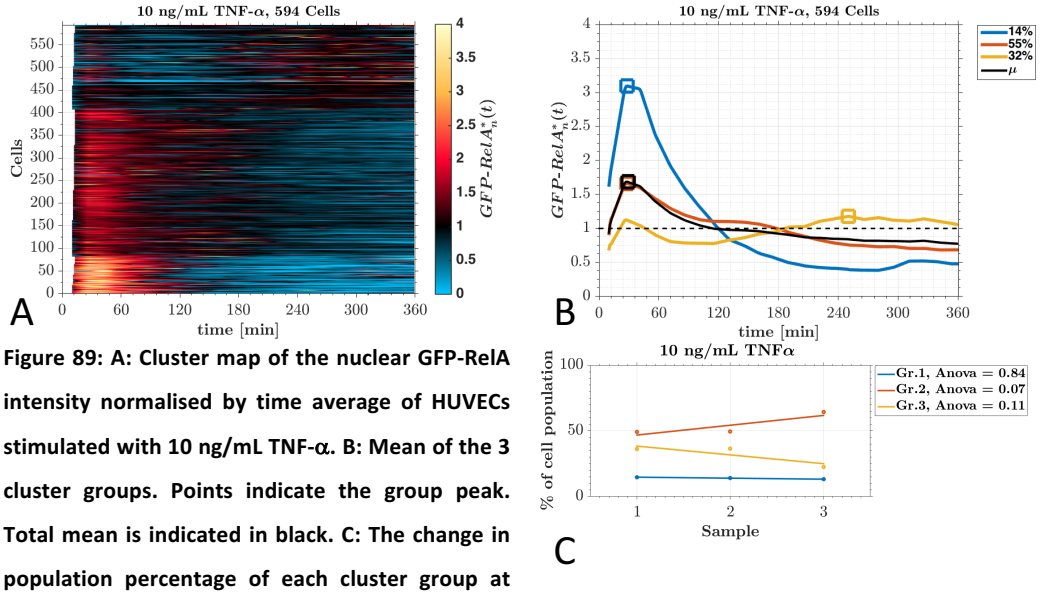

Figure 89: A: Cluster map of the nuclear GFP-RelA intensity normalised by time average of HUVECs stimulated with 10 ng/mL TNF-α. B: Mean of the 3 cluster groups. Points indicate the group peak. Total mean is indicated in black. C: The change in population percentage of each cluster group at different shear stress positions fitted to a linear regression. P-value is calculated with a one way Anova.

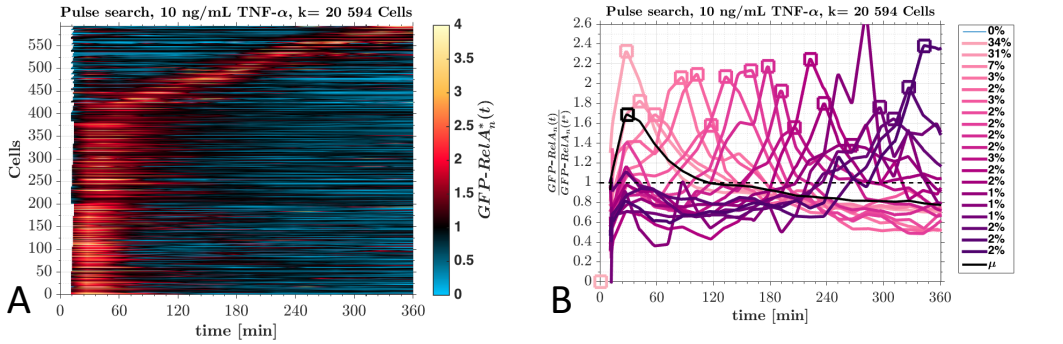

Figure 90: Pulse search (k=21) applied to nuclear GFP-RelA intensity normalised by time average of HUVECs stimulated with 10 ng/mL TNF-α. A: Projected map of the signals sorted with pulse search B: The mean of the pulse search groups.

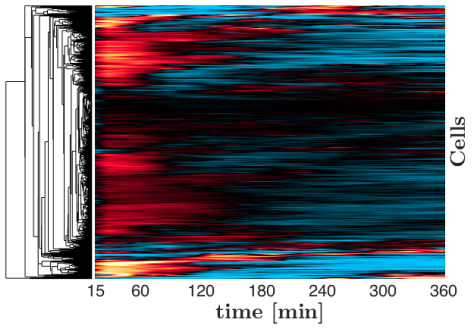

Figure 91: Hierarchical clustering of the nuclear GFP-RelA intensity normalised by time average of HUVECs stimulated with 10 ng/mL TNF-α.

The largest group (55%) had a high peak at 30 minutes. The last group (32%) peaked at 30 minutes, but experienced a second increase in intensity from 180 minutes onwards. The change in percentages per sample showed variations between the samples (Figure 89.C). This could be due to unsuitable clustering methods or technical noise. For example, different recording times between wells.

In Figure 90, the single cell measurements were clustered using pulse search with 20 uniformly distributed pulses and 1 inactive group (k=21). It was observed that most of the cells (65%) are assigned to an early pulse with peaks at 5 and 30 minutes. A few cells (35%) appeared to peak once at these times during the experiment.

In Figure 91, the single cell measurements of nuclear GFP-RelA were clustered using hierarchical clustering. Hierarchical clustering demonstrated the large variability between cells when stimulated with TNF-α. Similar grouping trends were also identified for Kmeans and pulse search.

Static conditions (untreaded cells) - wide-field: In Figure 92, the single cell measurements of nuclear GFP-RelA intensity of HUVECs under static conditions were clustered into five groups using Kmeans. One small group (6%) peaked early at 0 to 30 minutes. Three groups of similar sizes (11%, 21% and 14%) peaked at 90, 220 and 345 minutes. It appears that the peaking groups (52% of the population) represent cells that experienced spontaneous nuclear translocation of GFP-RelA. The groups also appeared to peak at distinct intervals. Most of the cells (48%) remained unchanged and thus close to their initial value of 1. The number of cells assosciated with groups did not change significantly amongst the samples (Figure 92.C). This indicated that the observed peaks were independent of the well position. The spontaneous nuclear translocation can be regarded as natural reactions, cell division

and apoptosis. The tracking algorithm was programmed to reject dividing or dying cells. However, some cells in these states may have been tracked within the last 30 minutes due to their unfinished state. Therefore, these cells might have increased the recorded nuclear GFP-RelA intensity within the last 30 minutes due to the cells bundling movements.

Because of the wide-field microscope properties, the bundling of the cells created a signal that appeared to be in the nucleus. However, this was just cytoplasmic intensity covering the nucleus. It is notable, that the experiment was not performed under ideal conditions; the microscope was in a different building across the campus and the samples had to be transported during all weather conditions for 10-15 minutes. This may have disturbed their state.

In Figure 93, the single cell measurements of nuclear GFP-RelA in HUVECs under static conditions were clustered using pulse search. This showed that approximately 40% of the population experienced a high nuclear translocation of GFP-RelA. The cells appeared to experience random spontaneous nuclear translocation of GFP-RelA, which when clustered appeared to be uniformly distributed in time. It was observered, that there was a tendency of higher occurrences of tall peaks at early (0 -120 min) and later times (270 - 360min). This tendency was previously observed for the maximum peak distribution of the entire population (Figure 88.C).

In Figure 94, the single cell measurements of nuclear GFP-RelA were clustered using hierarchical clustering. Hierarchical clustering demonstrated the large variability between cells when under static conditions.

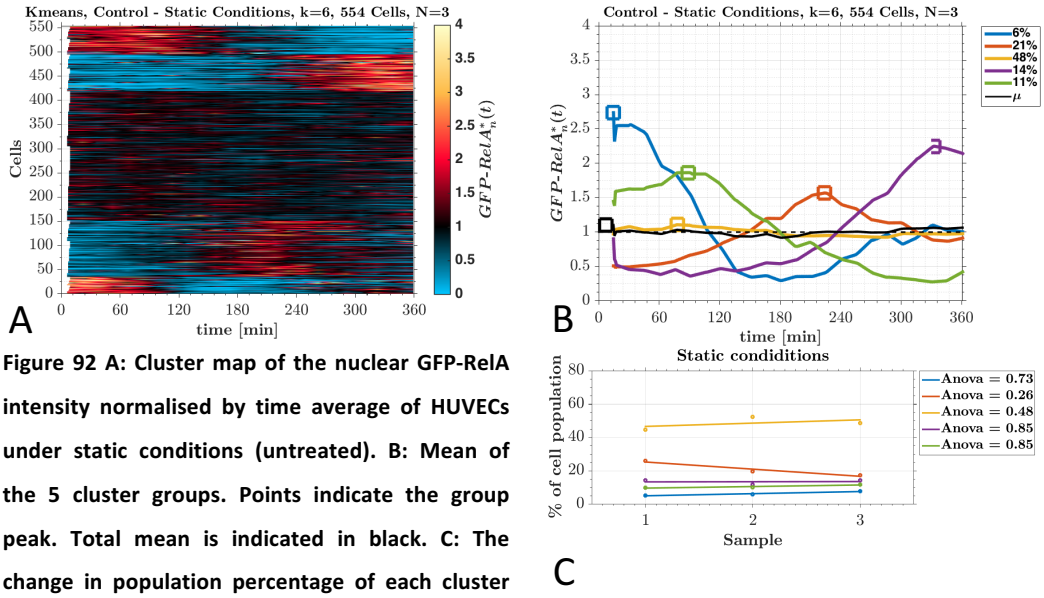

Figure 92 A: Cluster map of the nuclear GFP-RelA intensity normalised by time average of HUVECs under static conditions (untreated). B: Mean of the 5 cluster groups. Points indicate the group peak. Total mean is indicated in black. C: The change in population percentage of each cluster group at different shear stress positions fitted to a linear regression. P-value is calculated with a one way Anova.

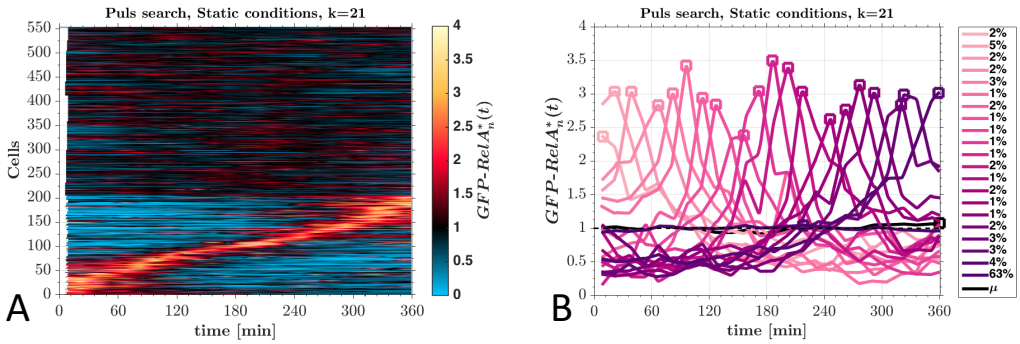

Figure 93: Pulse search (k=21) applied to nuclear GFP-RelA intensity normalised by time average of HUVECs stimulated with 10 ng/mL TNF-α. A: Projected map of the signals sorted with pulse search B: The mean of the pulse search groups.

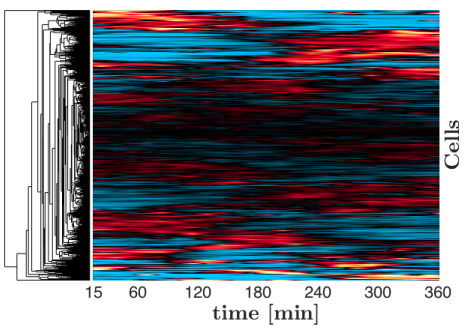

Figure 94: Hierarchical clustering of the nuclear GFP-RelA intensity normalised by time average of HUVECs under static conditions (untreated)

3.7.2. Clustering attempts with intensity normalised by earliest common time point – Secondary analysis

10 ng/mL TNF-α - Wide-field: The single cell analysis for HUVECs stimulated with 10 ng/mL TNF-α is shown in Figure 95., The intensity was normalised using the earliest common time point. Figure 95.A shows the nuclear GFP-RelA intensity for all cells and Figure 95.B plots an example of 100 cells. It was observed that most cells experience a nuclear GFP-RelA peak at 30 minutes.

All cells intensities normalised to t=15min*

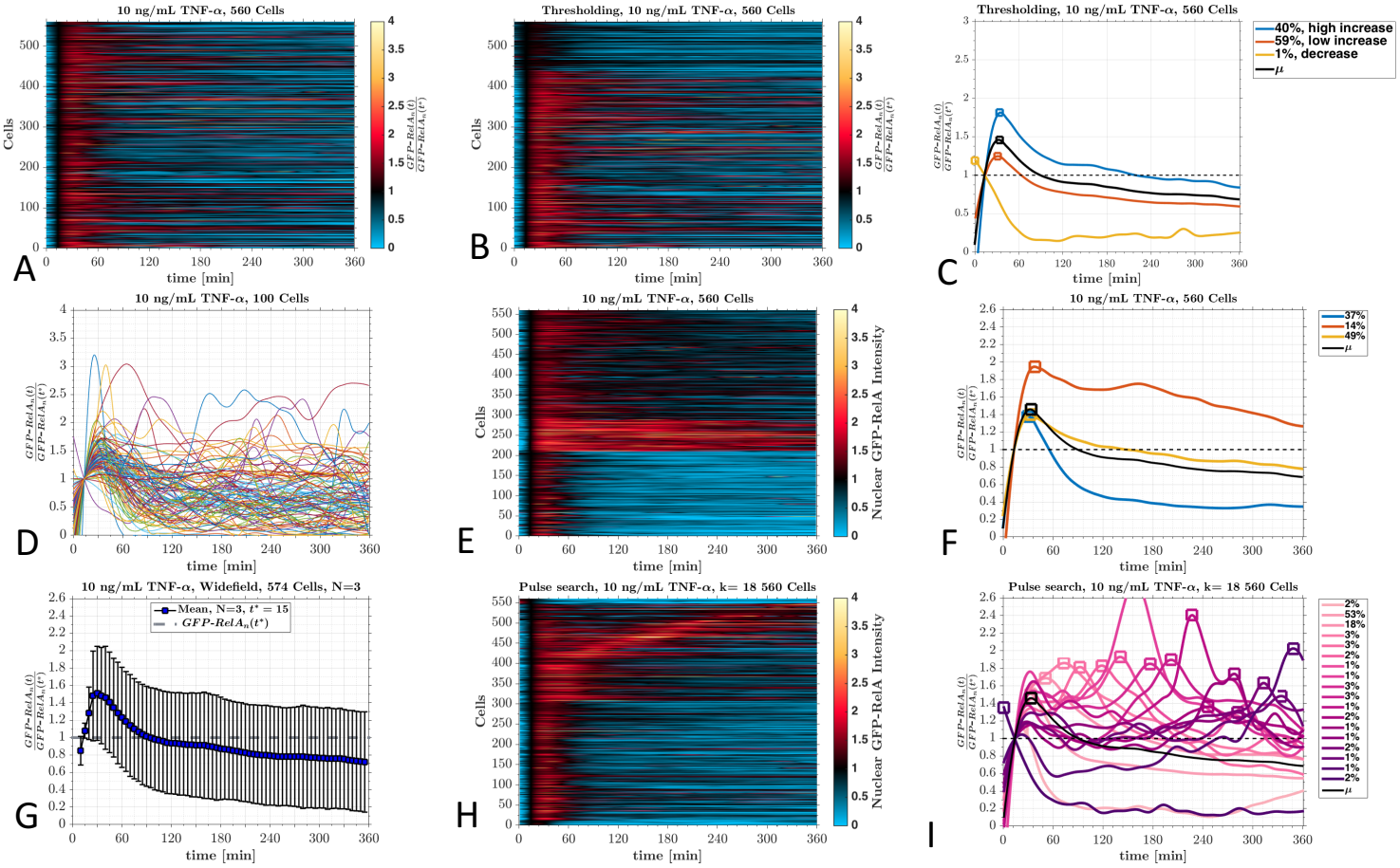

Figure 95: Single cell analysis of nuclear GFP-RelA intensity normalised by earliest common time point (t*=15min) of HUVECs stimulated with 10 ng/mL TNF-α. A: The nuclear GFP-RelA intensity map of all cells recorded. B: Cells were clustered using thresholding. C: The mean of the thresholding groups. D: Superimposed nuclear GFP-RelA intensity of 100 cells. E: Cells clustered using Kmeans. F: The mean of the kmeans clustering groups. G: Mean and standard deviation population nuclear GFP-RelA intensity when normlised by earliest common time point. H: Cells clustered using pulse search. I: The mean of each pulse group. The squares in the mean plots indicate the peak, and in the legend the percentage of the cell population per line is given.

On clustering the cells with thresholding (Figure 95.C and D), it was observed that ca. 80 % experienced a high nuclear GFP-RelA intensity peak at 30 minutes and ca. 20 % a low peak at 30 minutes. However, thresholding failed for the TNF-α experiment, as all of the cells had an elevated state at the time of the normalisation. Therefore, the starting value of the thresholding was adjusted to an estimate of 0.4 (This meant that most cells were incorporated in the high and low groups). This meant that cells above 1.2 had a high activation. However, no cells could be associated with inactive cells as they would have had a value lower than 0.8. This is impossible with normalisation. Threshold was found to be only suitable for the control and shear experiments. Clustering with *Kmeans* resulted in three groups of different intensities, each of these had a strong peak at 30 minutes. In addition, clustering with pulse search meant that peaks occurred early (0 to 60 minutes) for ca. 70 % of the cell population. Later peaks were also observed, but only for a small number of cells.

Static conditions (untreated cells) - wide-field: The single cell analysis for HUVECs expressing GFP-RelA under static conditions is shown in Figure 96. In addition, Figure 96.A shows the nuclear GFP-RelA intensity forall cells under static conditions.

It was observed that under static conditions a few cells experienced spontaneous nuclear translocation. Figure 96.B shows an example of the nuclear GFP-RelA intensity, normalised using the earliest commont time point, of 100 cells under static conditions. It can be seen that some cells have a clear peak randomly distributed along the 360 minutes, and that the population is very chaotic.

Threshold clustering revealed that ca. 30 % of cells experienced a random spontaneous high nuclear translocation of GFP-RelA. Using *Kmeans*, two groups were observed peaking at 180 minutes, and one group peaked at ca. 330 minutes.

All cell intensities normalised to t=15min*

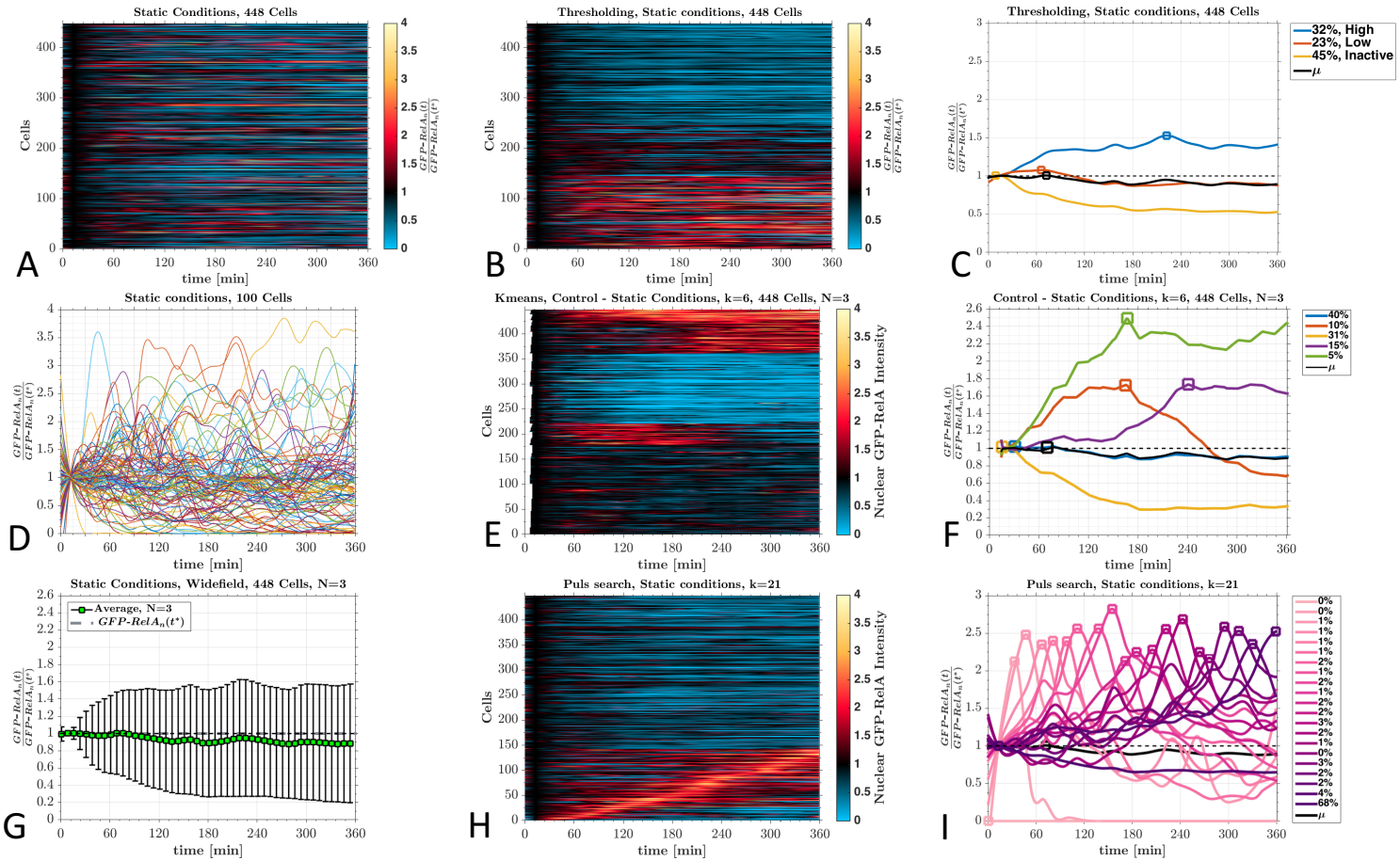

Figure 96: Single cell analysis of nuclear GFP-RelA intensity normalised by earliest common time point (t*=15min) of HUVECs under static conditions (untreated). A: The nuclear GFP-RelA intensity of all cells recorded. B: Example of the nuclear GFP-RelA intensity of 100 cells. C: Cells were clustered using thresholding. D: The mean of the thresholding groups. E: Cells clustered using Kmeans. F: The mean of the kmeans clustering groups. G: Cells clustered using pulse search. H: The mean of each pulse group. The squares in the mean plots indicate the peak, and in the legend the percentage of the cell population per line is given.

The two active groups account for ca. 30 % of the population, confirming the finding with thresholding. With the pulse search, 30% of the cells were observed to experience spontaneous nuclear translocation distributed over 360 minutes.

3.8. Movements of cells vs. nuclear GFP-RelA intensity

The movement of cells indicates the cell motility during the experimental conditions. In Figure 97 (wide-field only) depicts the movement of cells under TNF-α stimulation (Figure 97.A) and static conditions (Figure 97.C) including the average cell velocity. The orientation and direction of cell movements under both conditions appear to be random.

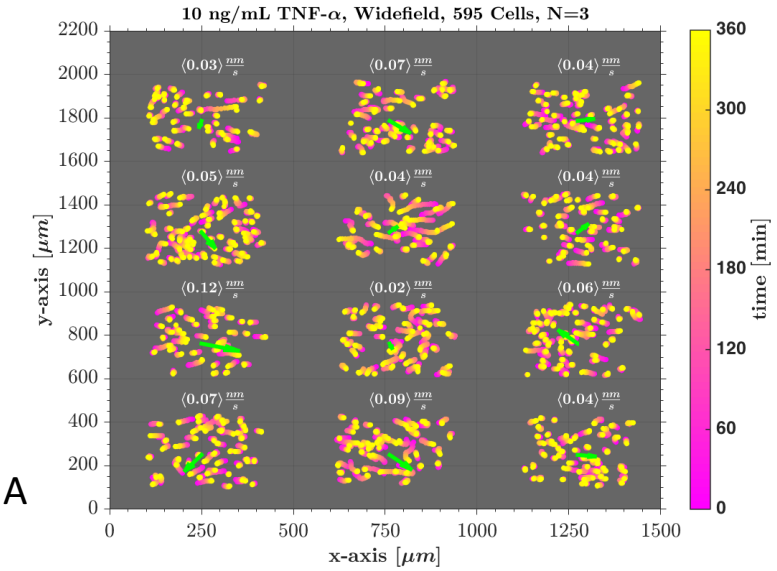
10 ng/mL TNF-α, Widefield, 595 Cells, N=3
⟨0.03⟩ nm/s
⟨0.07⟩ nm/s
⟨0.04⟩ nm/s
⟨0.05⟩ nm/s
⟨0.04⟩ nm/s
⟨0.04⟩ nm/s
⟨0.12⟩ nm/s
⟨0.02⟩ nm/s
⟨0.06⟩ nm/s
⟨0.07⟩ nm/s
⟨0.09⟩ nm/s
⟨0.04⟩ nm/s
y-axis [μm]
x-axis [μm]
time [min]
0
250
500
750
1000
1250
1500
0
200
400
600
800
1000
1200
1400
1600
1800
2000
2200
0
60
120
180
240
300
360

A

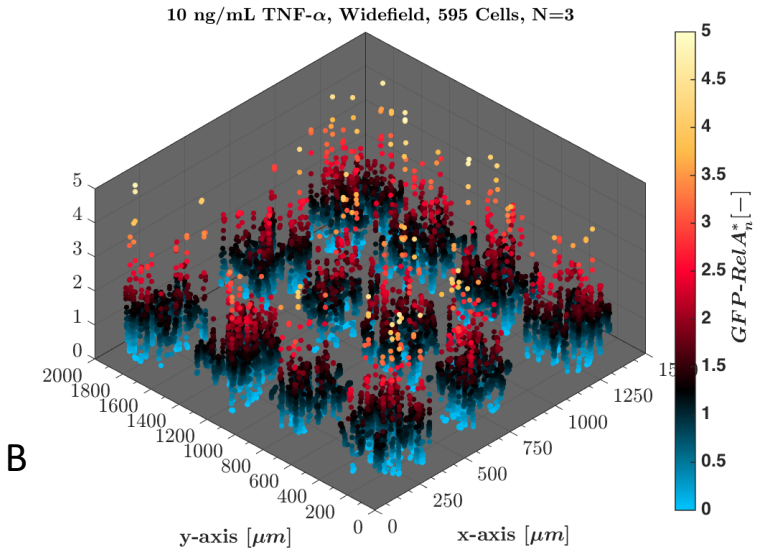
10 ng/mL TNF-α, Widefield, 595 Cells, N=3
y-axis [μm]
x-axis [μm]
GFP-RelA*n [—]
0
1
2
3
4
5
0
200
400
600
800
1000
1200
1400
1600
1800
2000
0
250
500
750
1000
1250
0
0.5
1
1.5
2
2.5
3
3.5
4
4.5
5

B

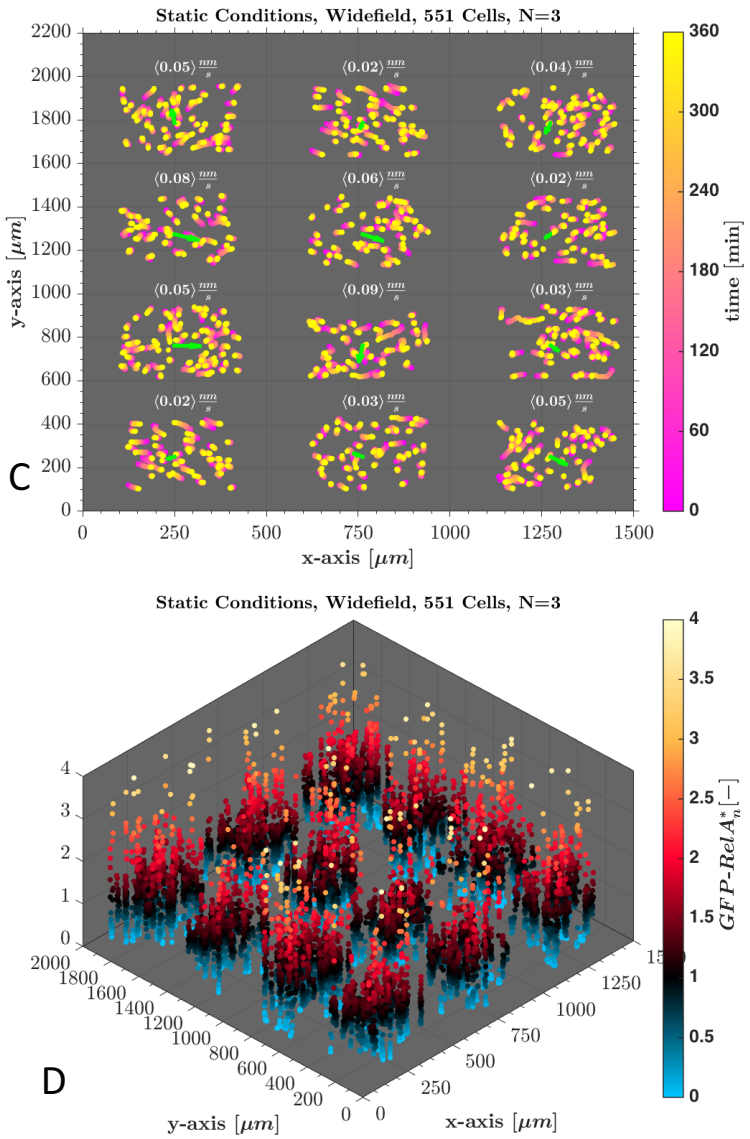

Figure 97: A and C: The cell movement of HUVECs expressing GFP-RelA and H2B-mCherry when stimulated with 10 ng/mL TNF-α (A) or under static conditions (untreated cells) (C) were recorded at 12 different well positions. Purple corresponds to time zero and yellow to 360 minutes. A green arrow, scaled to its velocity, shows the total direction of all cells at each position. The average velocity per cell is indicated on top of each position. B and D: The nuclear GFP-RelA intensity normalised by time average at its location over time for TNF-α stimulation and static conditions

The average velocity under TNF-α stimulation was 0.057 nm/s, while under static conditions the average velocity was 0.047 nm/s. The directionality ratio under TNF-α stimulation was 3.67 and for untreaded cells (static conditions) 3.53. This indicates

that the persistence of migration was not affected by TNF-α stimulation (statistically insignificant).

Figure 97.B and Figure 97.D show the nuclear GFP-RelA intensity at its location over time for TNF-α stimulation and static conditions. Due to normalisation, cells exposed to TNF-α show a more distributed nuclear GFP-RelA intensity at low intensities (0-1). Under static conditions it appears as if the nuclear GFP-RelA intensity is uniformly spread across all the cells.

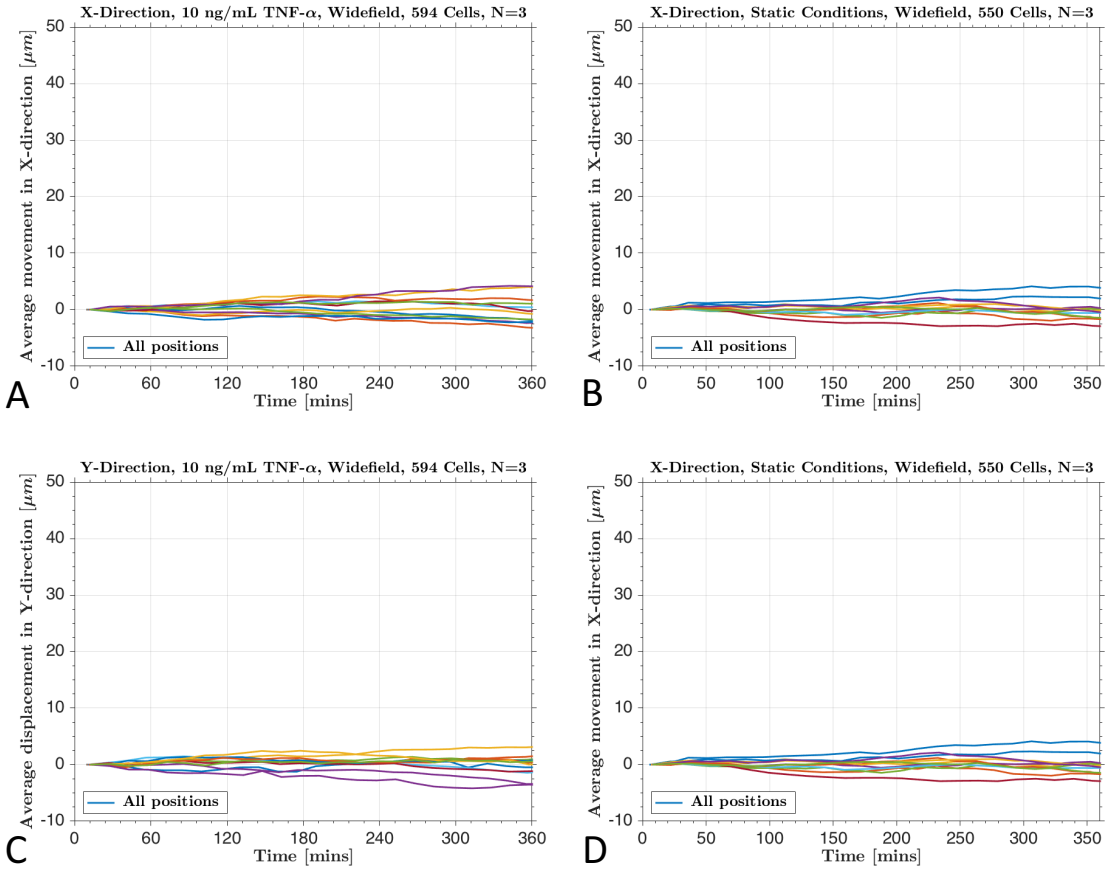

Figure 98: The average movement of cells per recorded position in the X- and Y-direction when stimulated with 10 ng/mL TNF-α (A and C) and under static conditions (untreated cells) (B and D).

The average movements of cells in the X- and Y-directions under TNF-α (Figure 98.A and B) and static conditions (Figure 98.C and D) are shown in Figure 98. Cells in both cases moved randomly in the positive and negative X- and Y-directions within a small

displacement range. The average range of motion was between ca. -2 and +6 um. The scale of the graph is large for later comparison with flow experiments.

In Figure 99, the probability distribution of the displacement of the cells versus time averaged normalised nuclear GFP-RelA intensity is shown for both TNF-α stimulation (Figure 99.A) and static conditions (Figure 99.B). The only difference observed is that the TNF-α distribution has a longer "leg" towards zero intensity.

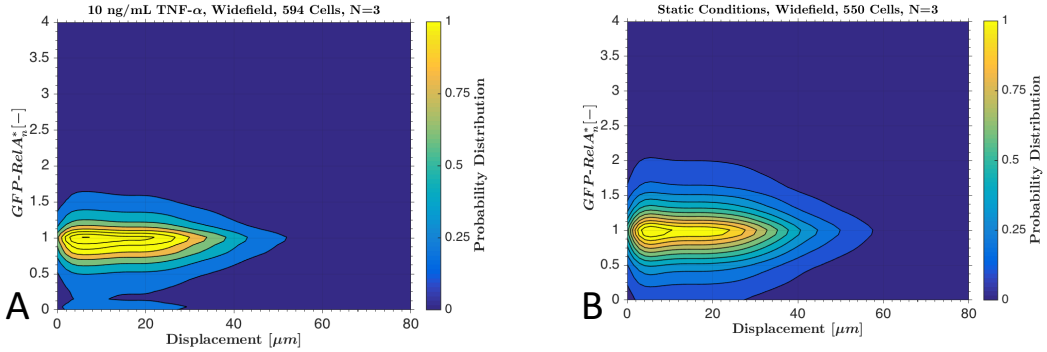

Figure 99: The probability distribution of the cells displacement versus nuclear GFP-RelA intensity normalised by time average for stimulation with 10 ng/mL TNF-α (A) and under static conditions (untreated cells) (B).

4. The Impact of Flow on the Nuclear Translocation of NF-κB

Summary: *This chapter presents the effect of low shear stress, high shear stress and a shear stress gradient on the nuclear translocation of GFP-RelA and p65 in HUVECS. The effect of low shear is shown followed by the effect of high shear stress and the effect of a shear stress gradient. Each section begins with a summary of the main findings observed for the specific flow conditions.*

4.1. The Effect of Low Shear Stress on the Nuclear Translocation of NF-κB in HUVECs

Summary: *This section presents the effect of a low shear stress of 2* dyne/cm^2 *on the nuclear translocation of p65 and GFP-RelA in HUVECs. The results presented are based on the experimental methods described in Chapter 2. In the first part, the effect of low shear stress was investigated with immunohistochemistry. HUVECs were exposed to low shear stress, fixed and stained at different time points for the molecules p65, p-IKK and IκBα. Immunohistochemistry indicated that nuclear and cytoplasmic p65 concentrations were weakly affected by low shear stress. However, the cytoplasmic p65 concentration appeared to be lower in cells exposed to low shear stress. The nuclear and cytoplasmic IκBα also showed little change in response to low shear stress. An increased phosphorylation of IKK under low shear stress was measured at 120 minutes.*

In the second part, the effect of low shear stress was studied with live-cell imaging. More than 1000 cells in 5 channels at 7 positions per channel were tracked. The mean of tracked single cells showed an early increase (bump) in nuclear GFP-RelA intensity at 30 to 60 minutes. The increase then dropped to a slightly lower intensity at 120 minutes. From 120 minutes onwards, the nuclear GFP-RelA intensity increased constantly until 360 minutes. However, in general the effect of low shear stress on the nuclear translocation of GFP-RelA was weak. A significant number of passing bubbles were detected and these might play a role in the increase in nuclear GFP-RelA intensity from 180 minutes onwards. All 5 channels had similar temporal nuclear GFP-RelA profiles. The maximum peaks of each cells mostly occurred between 30 and 60 minutes or at 240 to 360 minutes. Single cells were clustered into 6 groups using Kmeans. The clustered groups either peaked early (30-60min) or late (240-360min), while the latter group was larger in percentage. Small positional dependency of cluster groups was identified. Cells under low shear stress experienced

an average displacement of up to 10 µm in flow direction and the average displacement velocity of all cells was 0.083 nm/s.

4.1.1. Immunohistochemistry

Cells were exposed to a low shear stress of 2 dyne/cm^2 and immediately fixed after 30, 60, 120, 240 and 360 minutes. The fixed cells were stained for p65 (Figure 100), IκBα (Figure 101), and phosphorylated IKKα/β (Figure 102).

The intensity of the cytoplasm and nucleus are shown as a ratio to the control.

$$I^*[-] = \frac{I_{Experiment}}{I_{Control}} \qquad (34)$$

The nuclear and cytoplasmic intensity of p65 at set time points for cells exposed to low shear stress are shown in Figure 100. The nuclear intensity (Figure 100.A) increased significantly at 60 minutes and then returned to the basal level at 120 minutes. At 240 minutes the nuclear p65 intensity decreased slightly. At 360 minutes, nuclear p65 intensity was observed at the basal level again.

The cytoplasmic p65 intensity (Figure 100.B) decreased after 60 minutes and remained significantly lower than the control up to 360 minutes.

In Figure 101, cells exposed to low shear stress were stained for IκBα and evaluated for nuclear (Figure 101.A) and cytoplasmic (Figure 101.B) intensity.

The nuclear IκBα intensity at low shear exceeded the control at all time points from 30 to 360 minutes. The cytoplasmic intensity only statistically significantly exceeded the control at 120 and 240 minutes. No significant change was observed at the other time points.

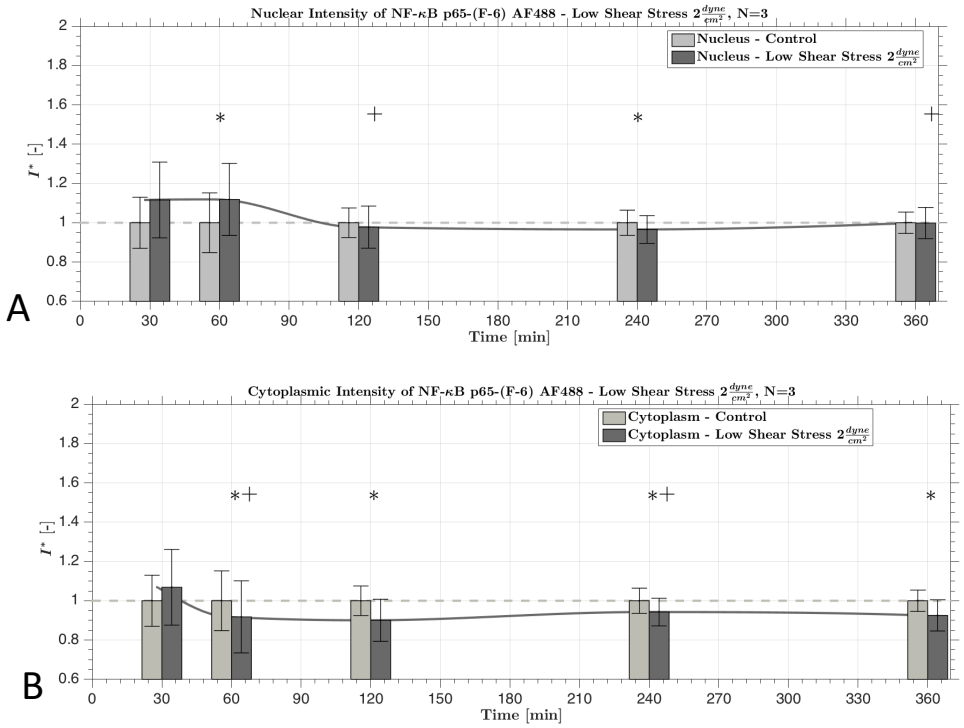

Figure 100: Cells exposed to low shear stress of 2 dyne/cm^2 fixed after certain time points and stained for p65. The p65 intensity was evaluated for the nucleus (A) and cytoplasm (B). Statistical significance (p<0.05) is indicated versus static control (*) and versus the previous time step (+).

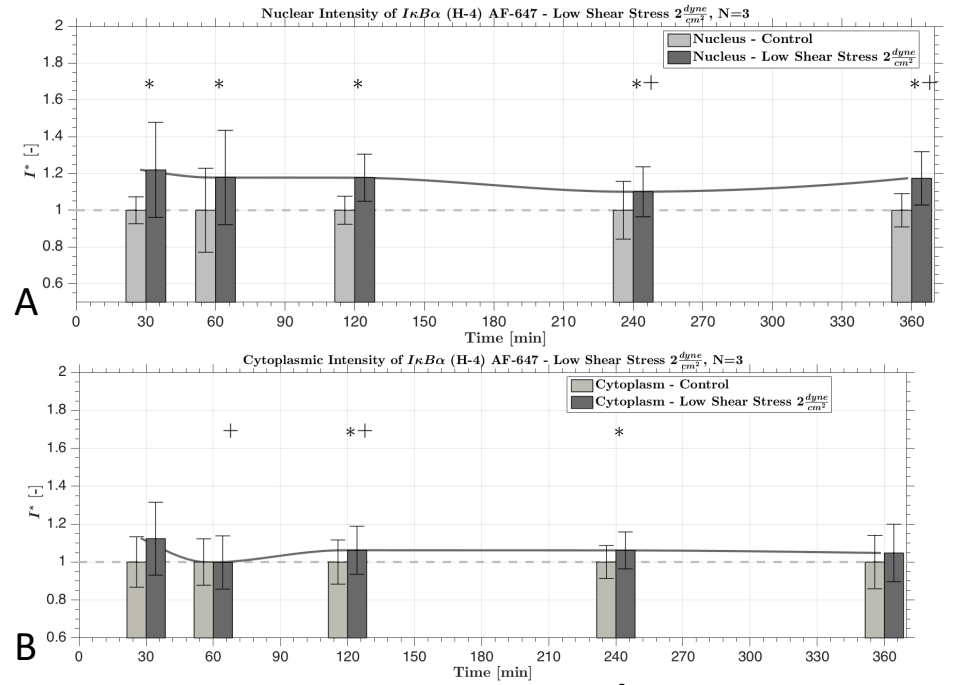

Figure 101: Cells exposed to low shear stress of 2 dyne/cm^2 fixed after certain time points and stained for IκBα. The IκBα intensity was evaluated for the nucleus (A) and cytoplasm (B). Statistical significance (p<0.05) is indicated versus static control (*) and versus the previous time step (+).

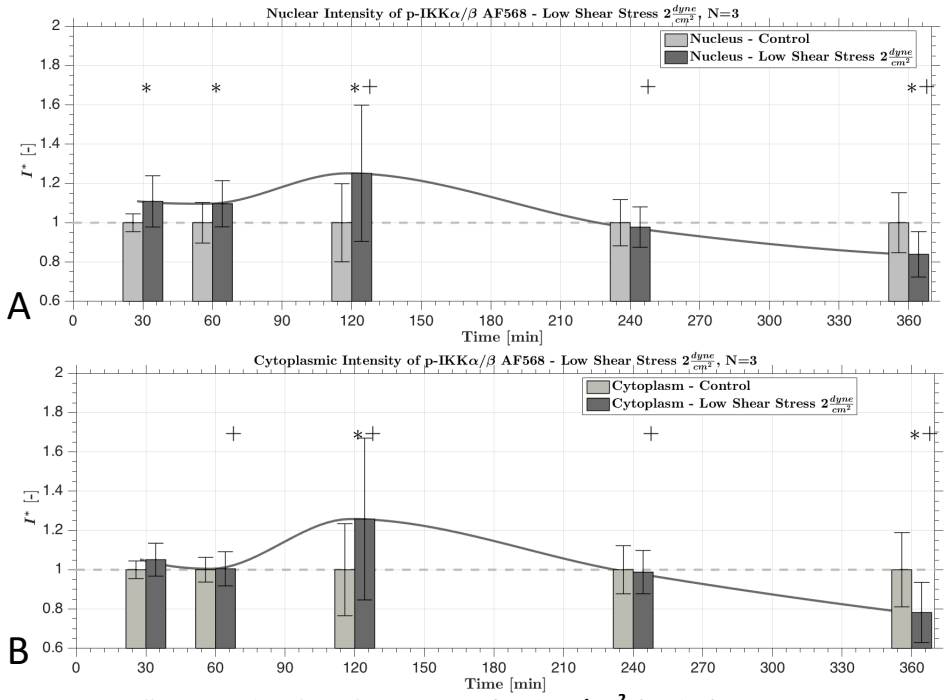

Figure 102: Cells exposed to low shear stress of 2 dyne/cm^2 fixed after certain time points and stained for phosphorylated IKKα/β. The p- IKKα/β intensity was evaluated for the nucleus (A) and cytoplasm (B). Statistical significance ($p<0.05$) is indicated versus static control (*) and versus the previous time step (+).

In Figure 102, cells were exposed to low shear stress and stained for phosphorylated IKKα/β. The nuclear intensity of phosphorylated IKKα/β (Figure 102.A) was found to be slightly elevated at 30 and 60 minutes. It peaked at 120 minutes and then gradually decreased, reaching the basal level at 240 minutes and a lower intensity, than the control, at 360 minutes. The cytoplasmic intensity (Figure 102.B) increased and peaked at 120 minutes. This peak was followed by a gradual decline until 360 minutes. At 360 minutes the cytoplasmic intensity was lower in comparison to the control.

4.1.2. Live-Cell Imaging

HUVECs of passage 3 were transfected with GFP-RelA and H2B-mCherry and exposed to a low shear stress of 2 dyne/cm^2. In Figure 103, HUVECs expressing GFP-RelA and

H2B-mCherry grown in an Ibidi flow chamber and exposed to low shear stress are shown at time point 180 minutes.

The image quality with Ibidi flow chambers was low compared to that obtained using glass well plates. Image processing was required as described in methods (Chapter 2). Nevertheless, GFP-RelA and H2B-mCherry expressions were well detectable and trackable.

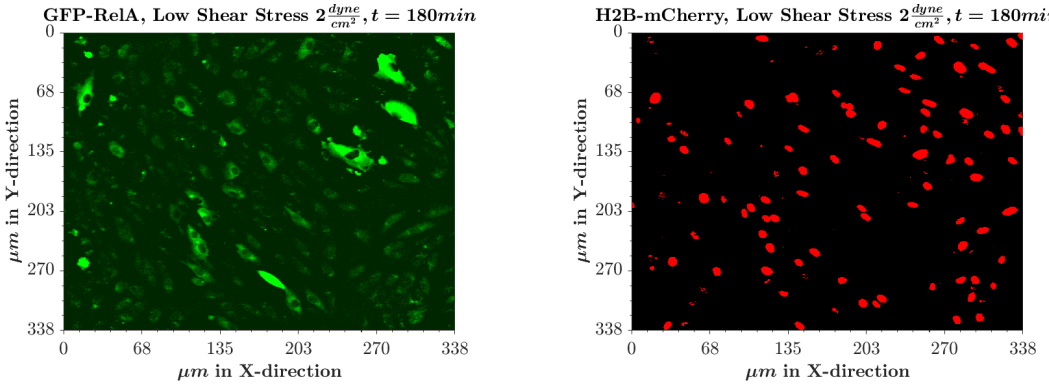

Figure 103: Processed images of HUVECs transfected with GFP-RelA (left column) and H2B-mCherry (right column) grown in a Ibidi flow chamber exposed to low shear stress of 2 dyne/cm^2 at time point 180 minutes.

4.1.3. Nuclear Translocation of GFP-RelA in response to low shear stress

Figure 104 highlights a HUVEC that experienced nuclear translocation of GFP-RelA at 280 minutes. A time series (0, 30, 90, 120, 240 and 360 minuites) of HUVECs expressing GFP-RelA exposed to low shear stress is shown in Figure 105. As for TNF-α, a large nuclear translocation of GFP-RelA was not observed visually. Moreover, the effect of flow appeared to be much weaker. The intensity of all the cells (1312) is presented in Figure 106.A. The intensities of the different cells appear variable. This is due to the large variety created by the expression level, light and autofocus. In Figure 106.B, the means for each recording position is plotted. Each position contains ca. 50 cells, where the intensity has been averaged. This display allows for

the mimicking of the IHC measurements. In Figure 106.C, all of the cells in each channel are averaged and the channel means are represented. The intensity difference between channels can be observed. This probably arises because of light differences in the microscopy room (was not absolutely dark). In Figure 106.E, all cells were normalised using their time average. During recording, bubbles were observed to pass through the image. Each observed bubble is indicated in the plot with a pink line. Red dots of the mean indicate a significant change compared to the previous time point. Under these conditions, the intensity was found to initially increase, drop at 120 minutes and then linearly increase until 360 minutes. We believe that the large amount of bubbles passing through the channel created a constant increase in nuclear GFP-RelA intensity after 240 minutes. Due to direct CO2 supply, bubbles accumulated in the silicon tubes and due to the low flow rate, they were released randomly one at a time. However, the general effect of low shear stress on the nuclear translocation of GFP-RelA appeared to be very weak within the 6 hours.

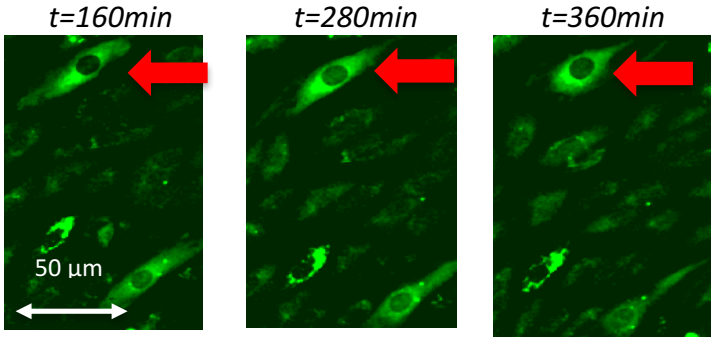

Figure 104: HUVEC (highlighted with red arrow) experiencing a weak nuclear translocation of GFP-RelA at 280 minutes of low shear stress of 2 dyne/cm^2.

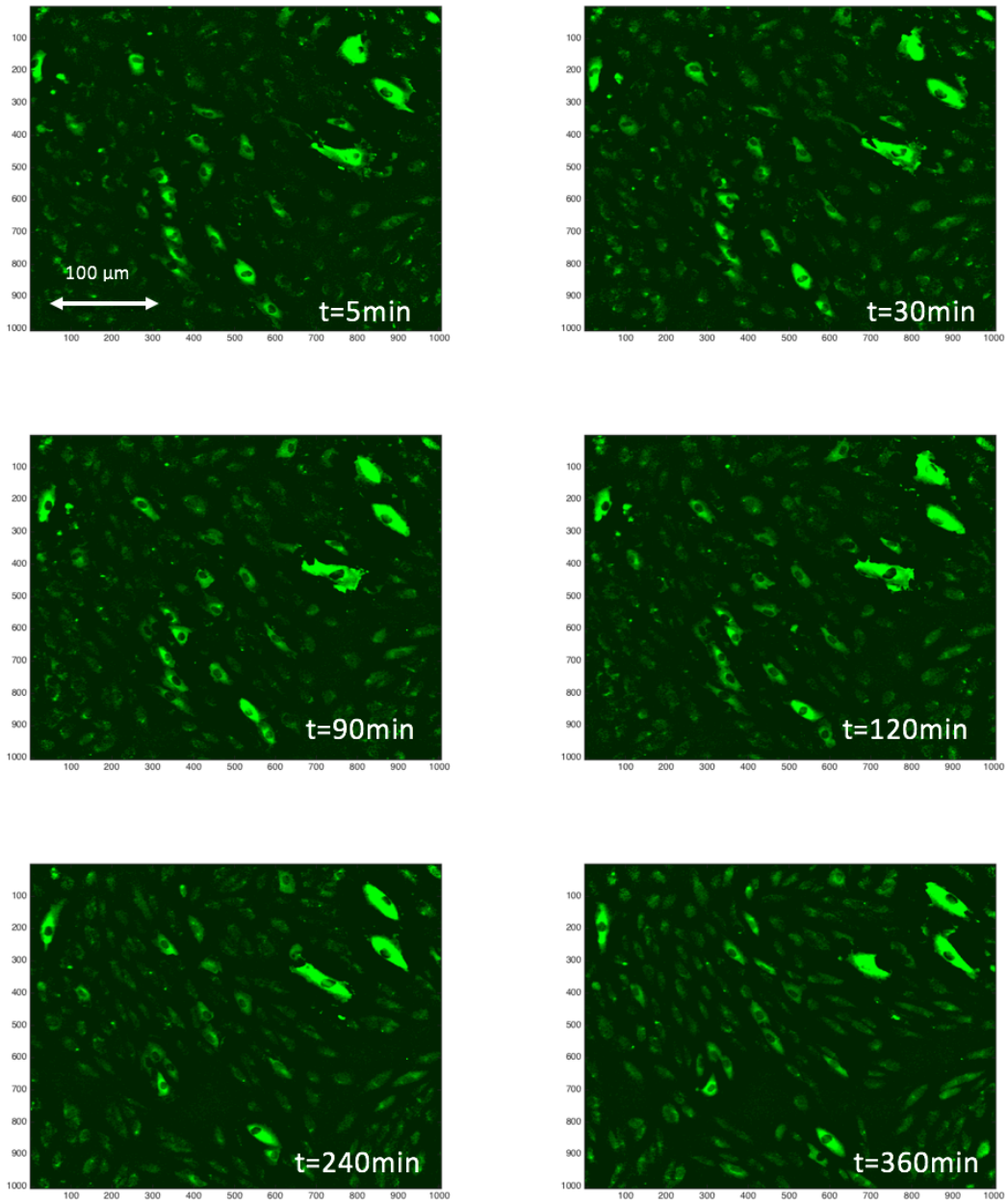

Figure 105: Post-processed images of HUVECs expressing GFP-RelA exposed to low shear stress (2 dyne/cm^2) imaged at different time points (5, 30, 90, 120, 240 and 360 minutes)

IHC of low shear stress at various points is shown in Figure 106.D, With IHC, an increase was only observed at 60 minutes. However, with live-cell imaging a slight increase in nuclear GFP-RelA intensity was observed between 0 and 60 minutes.

We can compare the normalised intensity to the intensity for the normalised static conditions (Figure 106.F). Under static conditions the mean hovers around one,

while an early bump and an increasing intensity from 180 minutes onwards is observed under low shear stress conditions.

The mean and standard deviation of all 7 positions of all repeats (5 channels) are displayed in Figure 107. The positions are arranged from inlet to outlet (top to bottom). The total channel mean is depicted in blue below the 7 positions. The exact location of each recorded position is indicated in Figure 107.F. In addition, at each position, the red lines indicate the occurrence of a passing bubble.

Nearly all positions in the channel showed a small increase in nuclear GFP-RelA intensity from 180 minutes onwards. No visual trend between location and temporal nuclear GFP-RelA intensity was observed. However, it appeared that the bubbles had a strong effect on the nuclear translocation of GFP-RelA. For example, the nuclear intensity increased significantly after a bubble in the first position of channel 3, and the first and second positions in channel 4. In channel 5, nearly all bubbles were followed by a change in nuclear GFP-RelA intensity.

Convective transport of effluent may have resulted in differences between nuclear translocation of GFP-RelA between the first and last channel.

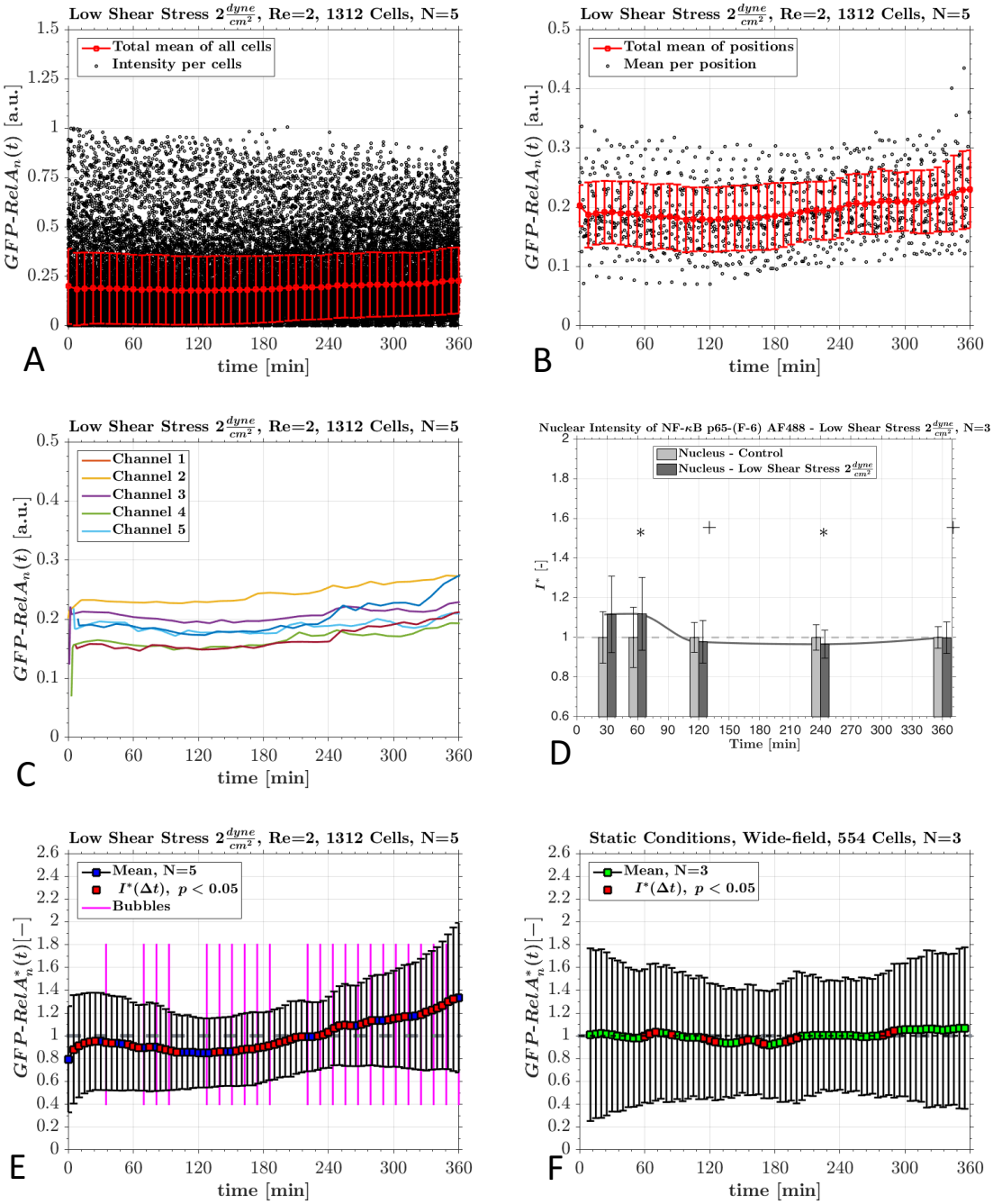

Figure 106: The nuclear GFP-RelA intensity of 1312 HUVECs exposed to a low shear stress of 2 dyne/cm^2. (A = Intensity [a.u.], B = Intensity per position [a.u], C = mean of each channel, E= Intensity normalised by time average [-]). IHC at different time point of non-transfected HUVECs exposed to low shear stress (D). For comparison, the normalised nuclear GFP-RelA intensity under static conditions (F)

In Figure 108, the mean nuclear GFP-RelA intensities for all the channels were interpolated and are displayed as a contour map. Each value "2" on the y-axis (shear stress) corresponds to a channel. The contour map shows that all of the channels experienced a small nuclear GFP-RelA intensity bump at ca. 30 minutes. The intensity

then gradually increased from 180 minutes onwards. Moreover, all of the channels showed the highest nuclear GFP-RelA intensity towards the end of the experiment between 330 and 360 minutes.

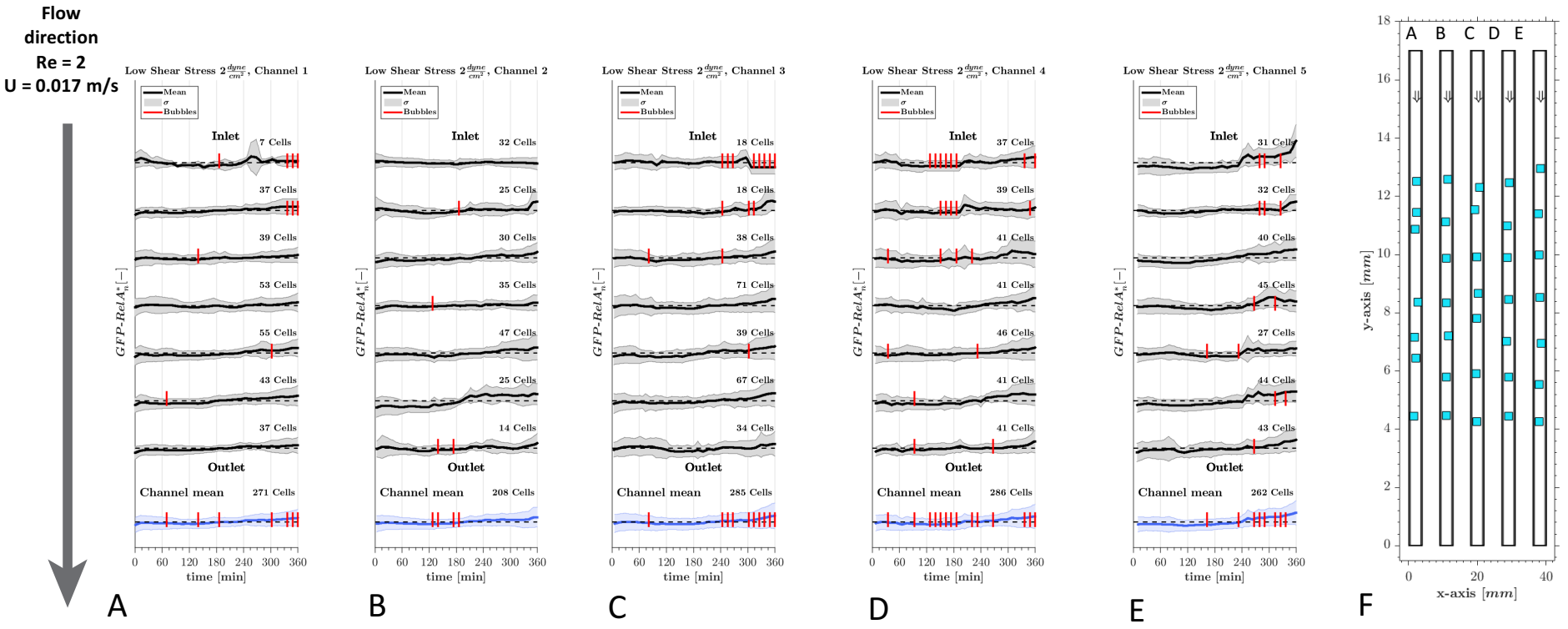

Figure 107: A-E: The nuclear GFP-RelA intensity normalised by time average in HUVECs exposed to shear stress of 2 dyne/cm^2 in 5 different channels at 7 positions across the channel (black), and each total average (blue). Bubbles are indicated with a red line at the occurring time point. The value 1 is represented with a dotted line. F: The exact location of each position within the channel. The inlet is at the top. Top positions in A-E correspond to top position in F.

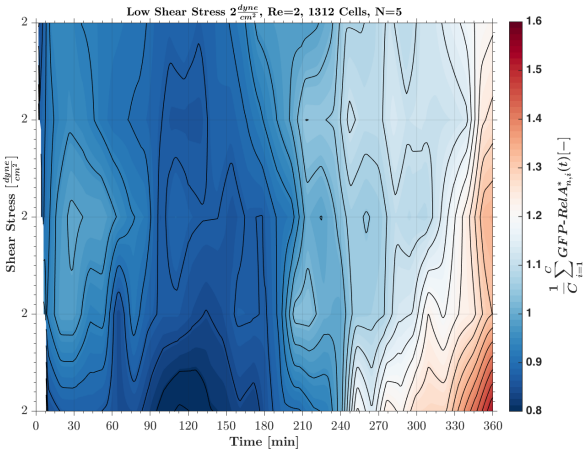

Figure 108: The mean nuclear GFP-RelA intensity normalised by time average interpolated between all 5 channels for HUVECs exposed to 2 dyne/cm^2. Each channel corresponds to an indicated value of shear stress.

4.1.4. Max peak analysis with normalisation by time average

In Figure 109.A, a projected view of all the cells normalised using time average is shown. The projection was made according to the intensity axis. It is seen that most cells experience a strong nuclear GFP-RelA intensity (red), which increases from 180 minutes onwards. The temporal nuclear GFP-RelA intensity profiles for 200 cells are shown in Figure 109.B. The resultant signal appears less noisy than under static conditions. In Figure 109.C, the maximum peak distribution is shown. The peaks are distributed early (0 to 60minutes) and from 180 minutes onwards. The highest density of the maximum peaks occurred at 345 minutes.

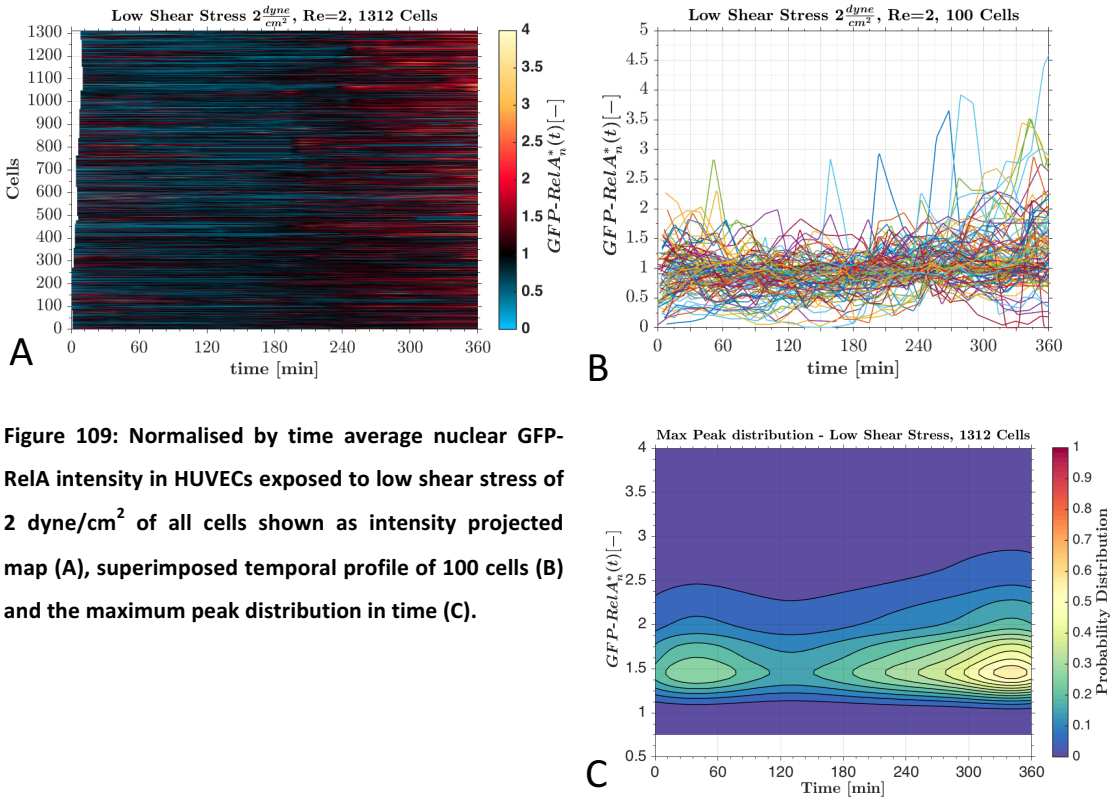

Figure 109: Normalised by time average nuclear GFP-RelA intensity in HUVECs exposed to low shear stress of 2 dyne/cm^2 of all cells shown as intensity projected map (A), superimposed temporal profile of 100 cells (B) and the maximum peak distribution in time (C).

This is only slightly different compared to the max peak distribution under static conditions (almost uniform max peak distribution). Consequently, we believe that the low shear stress condition has affected the GFP-RelA dynamics.

4.1.5. Clustering of single cell measurements

In the first attempt of analysing the single cell measurements normalisation for each cell was carried out using the earliest common time point. This gave a first insight into how chaotic the system is. Many cells were found to drastically change in relation to their original point: some went up, remained at one or decreased. The normalisation method was later amended, and time average was used. This method was found more suitable for the general analysis, as demonstrated in the previous results. As demonstrated in paragraph 2.19, evaluating the single cell measurements with gap statistics did not result in a unique cluster number for all experiments. Consequently, identification of the number of groups was carried out by visual

inspection. Herein, the clustering attempts for both normalisation methods will be presented. First, the clustering attempts using time average normalisation are shown. The main conclusion and main analysis have been determined from this data. Second, clustering attempts using normalisation by earliest common time point are shown as this provided results used in the initial data analysis (secondary analysis).

4.1.5.1. Cluster attempts with normalisation by time average – Main analysis

In Figure 110, the single cell measurements were clustered into 6 groups using Kmeans. It was observed that a large group (30 %, peak at 60 minutes) experienced a moderate early translocation of GFP-RelA. An additional large group (31 %, peak at 360 minutes) revealed a late large nuclear translocation of GFP-RelA. A smaller group (14 %) was found to have an elevated high initial GFP-RelA intensity and a late intensity peak (360 minutes). Moreover, two small groups (4 % and 7 %) peaked early at 60 minutes and late at 360 minutes. The last group (15 %) also showed a peak at 360 minutes.

In general, the cluster groups either peaked at 60 minutes or at 360 minutes. The total percentage of late peaking groups (63 %) was larger than for early peaking groups (37 %). This agrees with the maximum peak distribution shown in Figure 109.C. The change in percentages per positions (Figure 110.C), revealed that only the small group with a high late peak (purple line) had a significant change in percentages across the positions.

This mostly likely occurred because of the bubbles, which affect the nuclear translocation of GFP-RelA. Consequently, this made the translocation dependent on the positions of the bubbles, which appeared randomly in each of the 5 channels.

In Figure 111, the single cell measurements were clustered using pulse search with 20 uniformly distributed peaks and 1 inactive group. The majority of the high peaks occurred late between 240 and 360 minutes, and early between 0 and 120 minutes. This agrees with the max peak distribution observed in Figure 109.C.

In Figure 112, the single cell measurements of nuclear GFP-RelA under low shear stress were clustered using hierarchical clustering. Hierarchical clustering demonstratess the large variability between cells when exposed to a low shear stress.

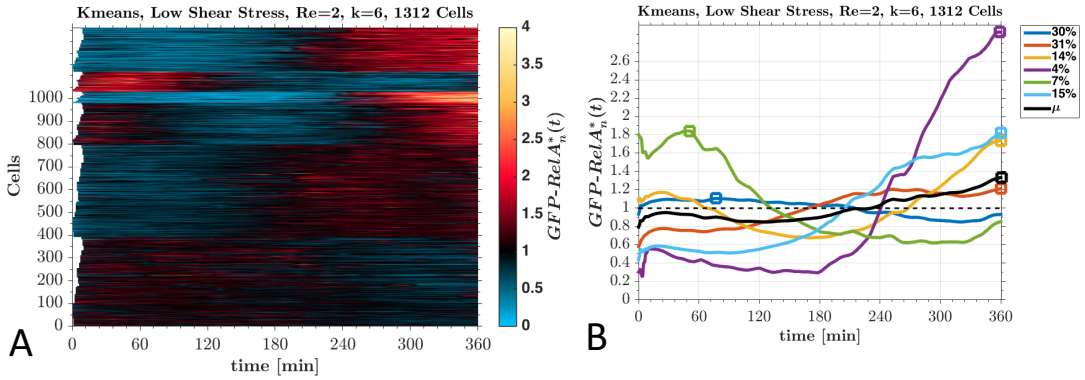

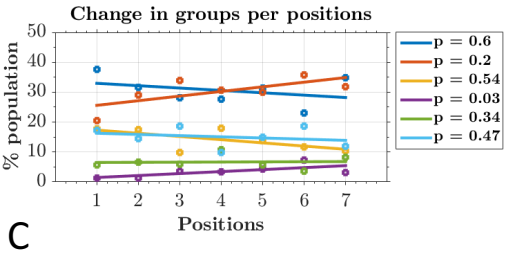

Figure 110: A: Cluster map of the nuclear GFP-RelA intensity normalised by time average of HUVECs exposed to a low shear stress of 2 dyne/cm^2. B: Mean of the 5 cluster groups. Points indicate the group peak. Total mean is indicated in black. C: The change in population percentage of each cluster group at different shear stress positions fitted to a linear regression. P-value is calculated with a one way Anova.

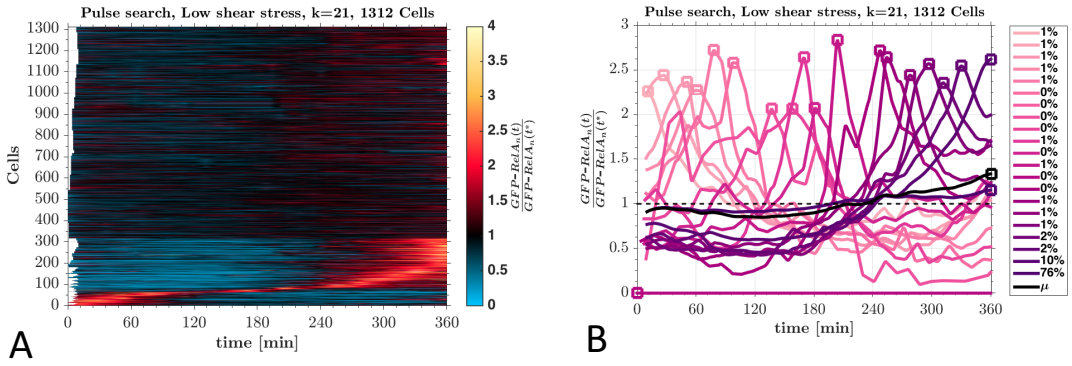

Figure 111: Pulse search (k=21) applied to nuclear GFP-RelA intensity normalised by time average of HUVECs exposed to a high shear stress. A: Projected map of the signals sorted with pulse search B: The mean of the pulse search groups.

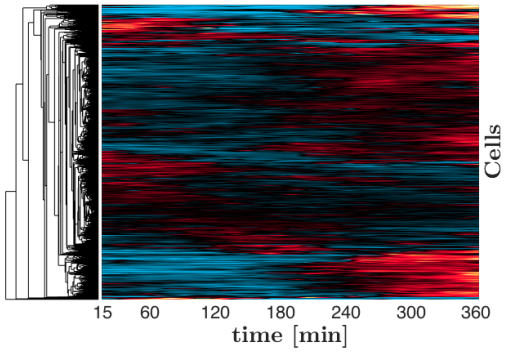

Figure 112: Hierarchical clustering of nuclear GFP-RelA intensity normalised by time average of HUVECs exposed to a low shear stress of 2 dyne/cm^2.

4.1.5.2. Clustering attempts with normalisation by earliest common time point – Secondary analysis

The single cell analysis of the nuclear GFP-RelA intensity of HUVECs exposed to a low shear stress of 2 dyne/cm^2 is shown in Figure 113. The nuclear GFP-RelA intensity profile for all of the cells profile is plotted in Figure 113.A. A strong trend of a increased nuclear GFP-RelA signal can be observed from 180 minutes onwards.

All cell intensities normalised to t=11min*

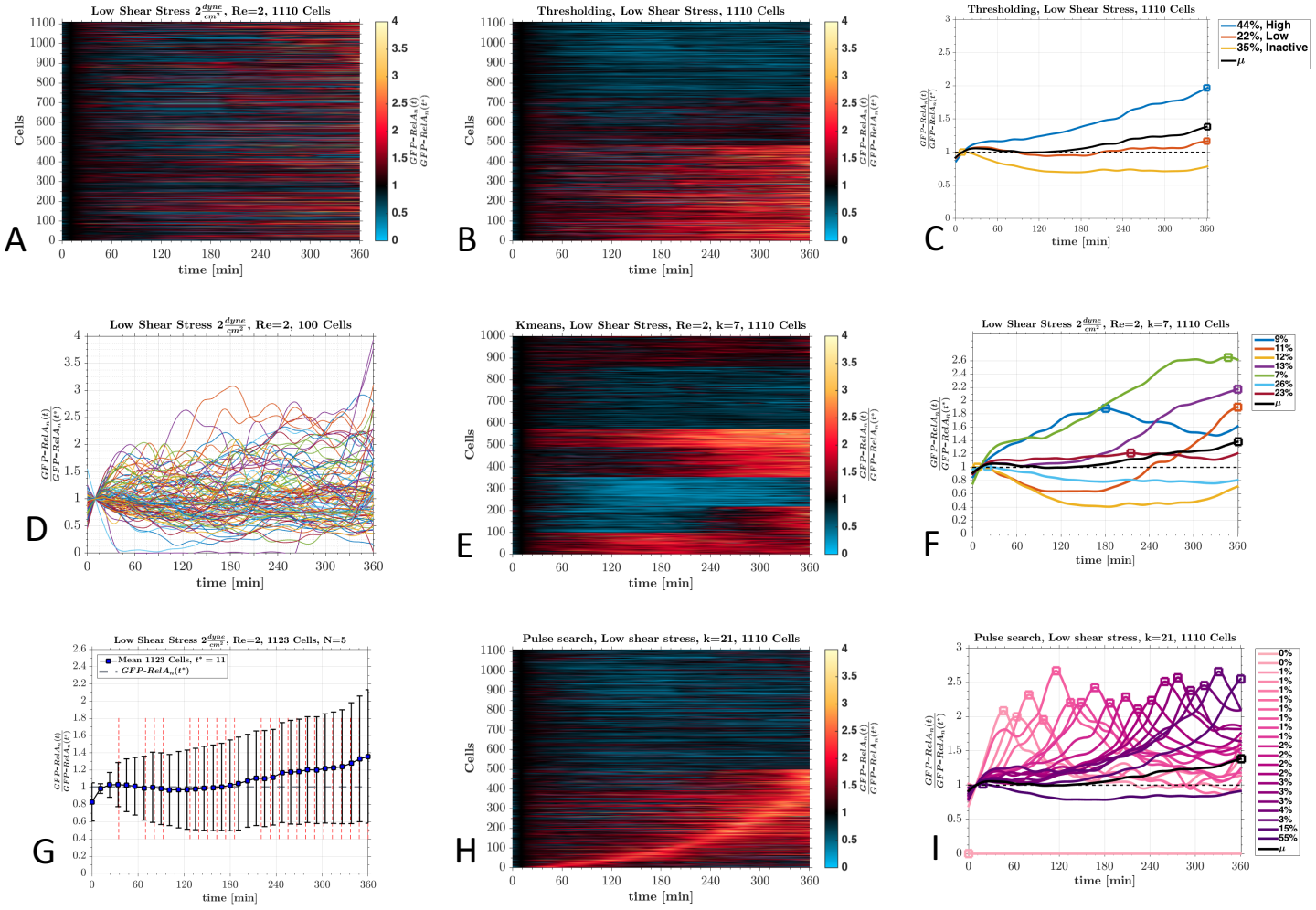

Figure 113: Single cell analysis of nuclear GFP-RelA intensity normlised using the earliest common time point of HUVECs exposed to a low shear stress of 2 dyne/cm^2. A: The nuclear GFP-RelA intensity of all cells recorded. D: Example of the nuclear GFP-RelA intensity of 100 cells. G: The mean and standard deviation of the normalised intensity by the earliest time point. B: Cells were clustered using thresholding. C: The mean of the thresholding groups. E: Cells clustered using Kmeans. F: The mean of the kmeans clustering groups. G: The mean and standard deviation of the nuclear GFP-RleA intensity normalised by earliest common time point for the full population. H: Cells clustered using pulse search. I: The mean of each pulse group. The squares in the mean plots indicate the peak, and in the legend the percentage of the cell population per line is given.

An example of the nuclear GFP-RelA intensity profile of 100 cells is depicted in Figure 113.D. The state of most cells appears to remain close to one, however some begin to increase after 180 minutes. In Figure 113.B and C, using thresholding, ca. 45 % of cells were found to experience a high nuclear GFP-RelA intensity. This is ca. 15 % more compared to under static conditions. Using Kmeans (Figure 113.E and F), seven groups were found to be most suitable. Most notable is the group that peaks at 180 minutes, and the four groups that peak at 360 minutes. Kmeans results indicated that ca. 45 % of the cells experienced a high nuclear GFP-RelA intensity (or at least 45 % showed an increased mean in nuclear GFP-RelA intensity). This is very close to the value obtained with the threshold method. With the pulse search (Figure 113.H and I), ca. 45 % of cells were found to experience a peak of nuclear GFP-RelA intensity. The peaks were distributed with a high tendency towards 360 minutes. Only the last peak at 360 minutes was associated with 14 % of the cell population. Moreover, The pulse search demonstrated constant activation of a small fragment of cells in the population.

4.1.6. Cells movement vs. nuclear GFP-RelA intensity

The movement of cells were tracked over time with a H2B-mCherry expression signal (The nuclei of each cell was tracked over time which is interpreted as the movement/motility of cells during the given experimental conditions). In Figure 114, the cell movements of each cell recorded at 7 different positions in each of the 5 channels are depicted. Purple corresponds to time zero and yellow to 360 minutes. The big arrow on the left indicates the direction of flow. The flow had a Reynolds

number of 2 and an approximate velocity of 0.017 m/s. Cells experienced a shear stress of 2 dyne/cm^2.

The cells moved slightly but predominantly in the flow direction (negative y-direction), with very low velocity. This implies that the monolayer moved as a whole. The total mean cell velocity was 0.083 nm/s. The cells also moved perpendicular to the direction of flow but with a smaller magnitude. This movement occurred in both the positive or negative X-direction.

The average movements of cells per position in the X- and Y-directions are shown in Figure 115. Cells moved in the direction of flow with a mean total displacement of 0 to 8 µm. In addition, cells moved perpendicular in both the positive and negative X-directions (towards the side walls of the channel) with a mean total displacement of -3 to 7 µm.

The directionality ratio under low shear stress was 2.783, which indicates an increase in persistence of mobility, as the directionality ratio is statisticial significantly lower than under static conditions. Hence, the cell mobility is affected by the superimposed shear stress.

In Figure 116, the nuclear GFP-RelA intensity of each cell is displayed at its time based location, under the influence of a low shear stress (2 dyne/cm^2). The nuclear GFP-RelA intensity appears to be strongly distributed from low to high. A low number of positions experience higher nuclear GFP-RelA intensities than others (e.g. third position from right in channel 2 and the first from left in channel 5). Cells in channel 1 to 3 appeared to experience a weaker nuclear translocation than those in channels 4 and 5.

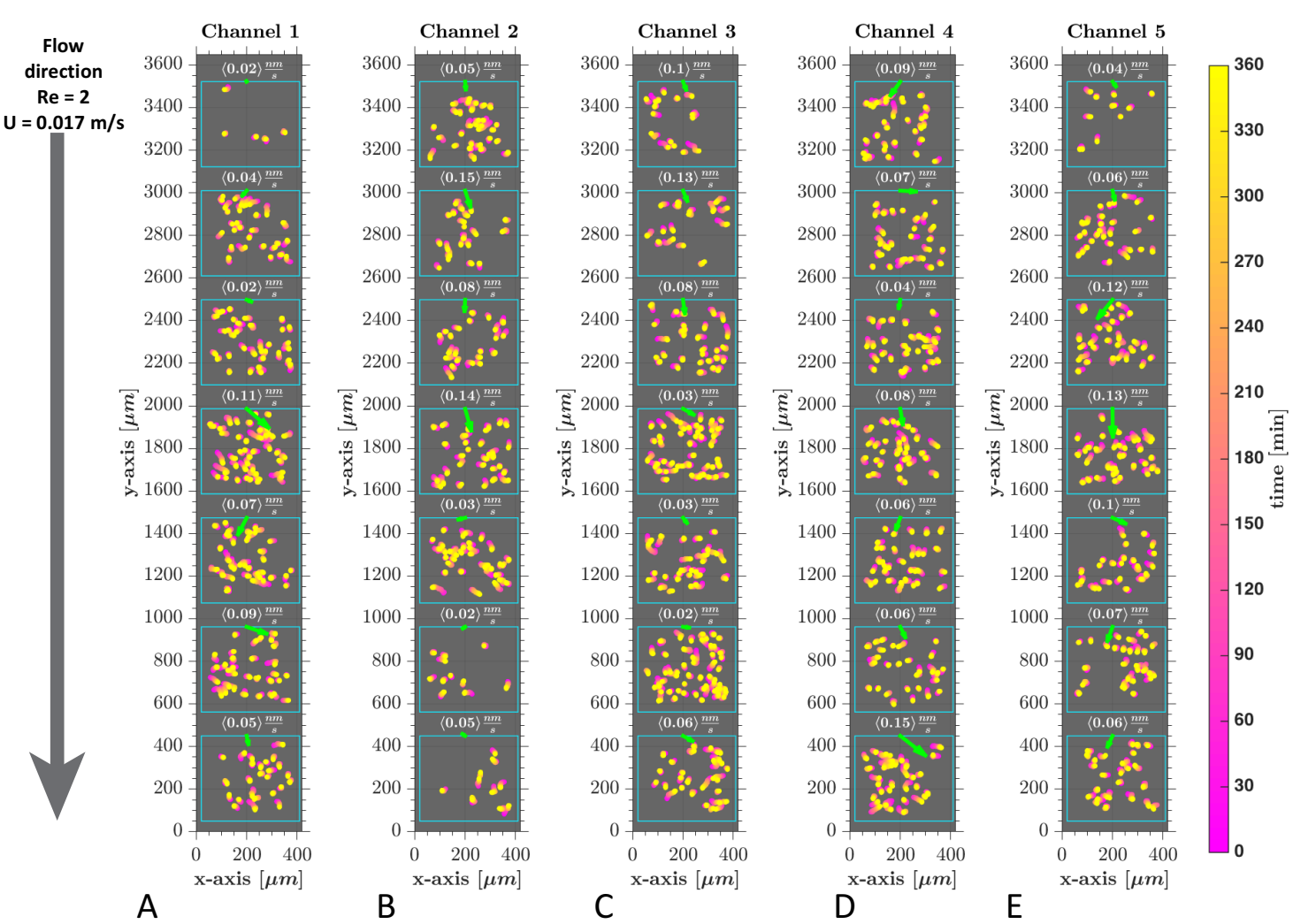

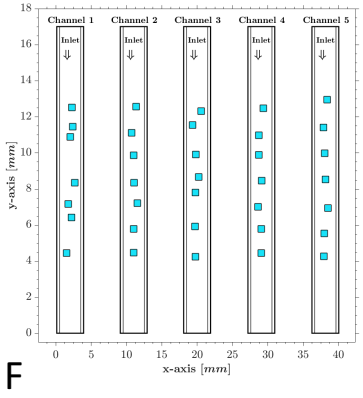

Figure 114: Movement of cells under a low shear stress of 2 dyne/cm^2. A-E: In each channel, 7 positions were imaged for 360 minutes. At each position, each tracked nucleus is displayed. Purple corresponds to time zero and yellow to 360 minutes. A green arrow, scaled to its velocity, shows the total direction of all cells at each position. The average velocity per cell is indicated on top of each position. F: The exact locations of the positions: The inlet is indicated at the top. Top position corresponds to top position in A-F.

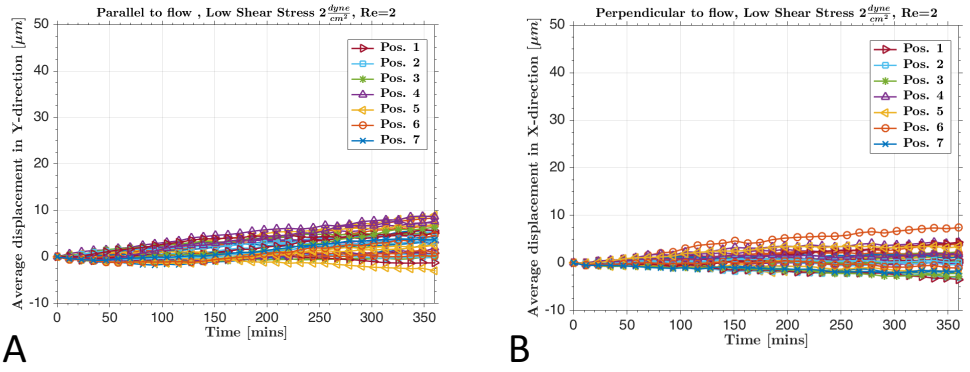

Figure 115: The mean movement of cells per position in the Y- and X-directions (A and B, respectively) for cells exposed to 2 dyne/cm^2.

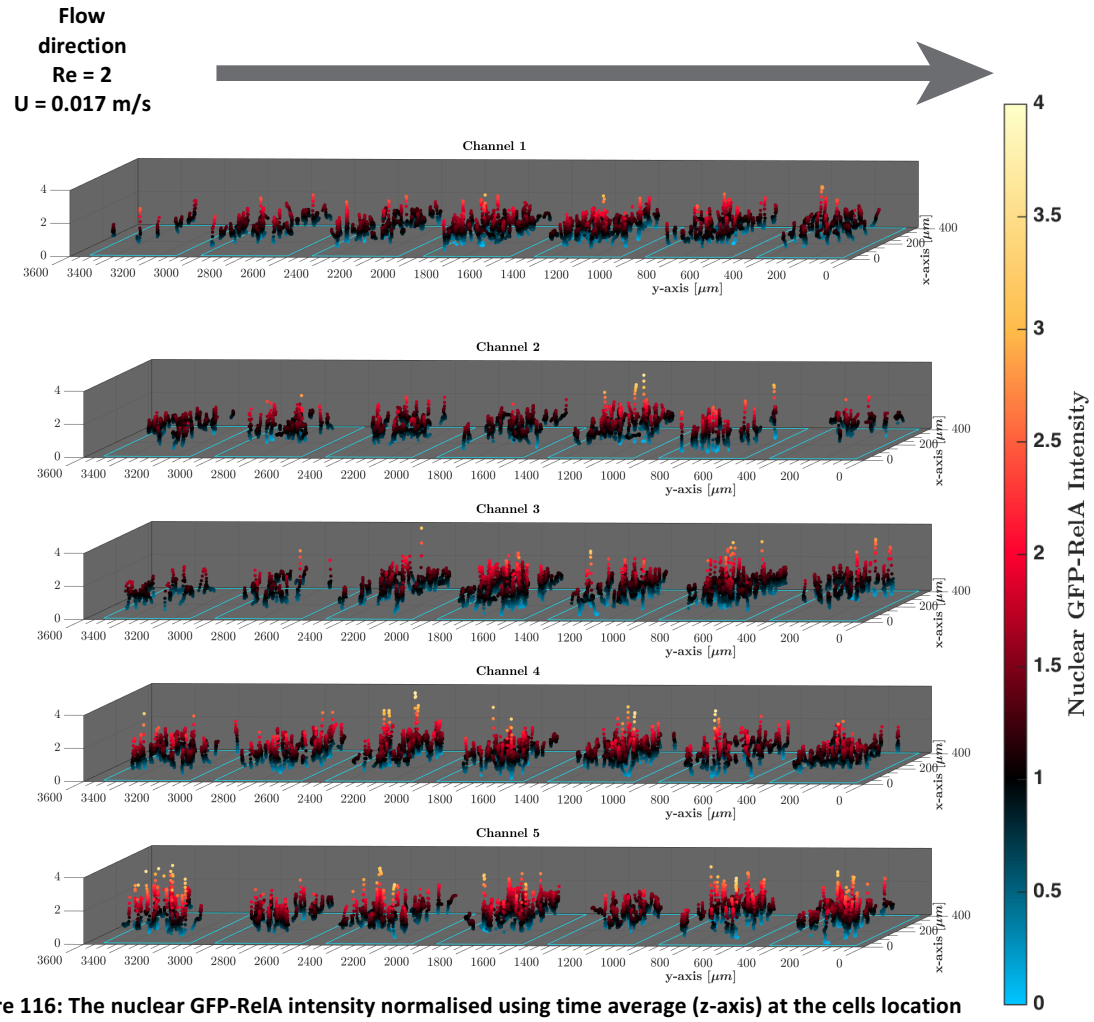

Figure 116: The nuclear GFP-RelA intensity normalised using time average (z-axis) at the cells location over time for all 5 repeats. The flow direction is from left to right.

The probability distribution for the displacement of cells versus nuclear GFP-RelA intensity, for cells exposed to 2 dyne/cm^2, is shown in Figure 117. The highest

probability is spread from 0 to 40 µm. The distribution between displacement and GFP-RelA under low shear stress appears to be similar to that under static conditions.

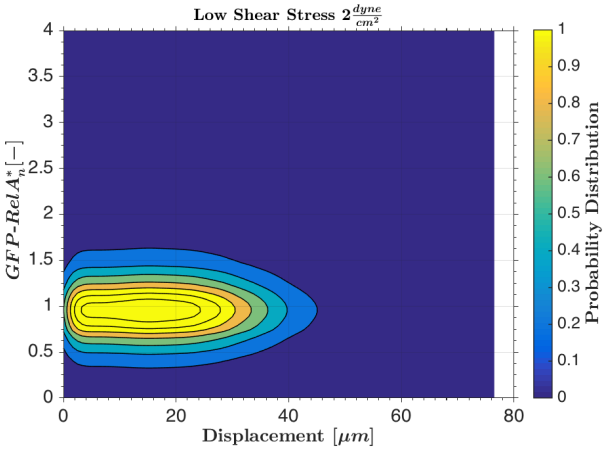

Figure 117: The probability distribution for the displacement of cells versus nuclear GFP-RelA intensity normalised using time average for cells exposed to a low shear stress of 2 dyne/cm^2.

4.2. The Effect of High Shear Stress on Nuclear Translocation of NF-κB in HUVECs

Summary: *This section presents measurements of the nuclear translocation of NF-κB in HUVECs grown in Ibidi channels that were exposed to a high shear stress of 20* dyne/cm^2*. The results presented are based on the experimental methods described in Chapter 2. First, HUVECs of passage 3 were exposed to high shear stress, fixed at certain time points and stained for p65, IκBα and p-IKKα/β. High shear stress caused nuclear p65 to oscillate, with small amplitude, around its control value. Cytoplasmic IκBα only degraded at 120 minutes and phosphorylated IKKα/β decreased after 60 to 240 minutes.*

Second, HUVECs expressing GFP-RelA and H2B-mCherry of passage 3 were exposed to a high shear stress. The mean of all single cell measurements resulted in a weak oscillating signal around the initial value. From 240 minutes onwards, the nuclear GFP-RelA intensity increased strongly until 360 minutes. The late increase is believed to be due to cells within unfinished apoptosis and cell division states. As with low shear stress, the effect of high shear stress on the nuclear translocation of GFP-RelA was weak and much less in comparison with TNF-α stimulation. All mean nuclear GFP-RelA intensities in all 5 channels experienced similar temporal profiles. The maximum peaks for all cells most likely occurred at 60 minutes and at 360 minutes. Single cells were clustered into 5 groups by applying Kmeans. The five groups either peaked at approximately 60 minutes or at 360 minutes. The groups were independent of their position within the channel.

Cells under high shear stress experience an average maximal displacement of 5 0μm in the flow direction with a total mean cell velocity of 0.2 6nm/s.

4.2.1. Immunohistochemistry

HUVECs were exposed to a high shear stress of 20 dyne/cm^2, immediately fixed after 30, 60, 120, 240 and 360 minutes and stained for p65 (Figure 118), IκBα (Figure 119) and phosphorylated IKKα/β (Figure 120).

The intensity of the cytoplasm and nucleus are shown as a ratio to the control.

$$I^*[-] = \frac{I_{Experiment}}{I_{Control}} \qquad (35)$$

In Figure 118, the intensity of nuclear p65 (Figure 118.A) and cytoplasmic p65 (Figure 118.B) is shown for HUVECs exposed to a high shear stress of 20 dyne/cm^2. The nuclear p65 intensity (Figure 118.A) was slightly reduced compared to the control after 30 minutes and achieved a basal level at 60 minutes. Moreover, the nuclear p65 decreased at 120 minutes, and then rose back to basal level at 240 minutes. Subsequently, it decreased at 360 minutes. The nuclear p65 intensity appeared to oscillate just below the control intensity with very low amplitude. Moreover, the cytoplasmic p65 intensity (Figure 118.B) showed the same trend as the nuclear intensity.

In Figure 119, HUVECs exposed to 20 dyne/cm^2 were stained for IκBα. The nuclear IκBα intensity (Figure 119.A) only statistically exceeded the control at 30 minutes. At each of the following time points the nuclear IκBα remained at the basal level (value=1). The cytoplasmic IκBα intensity (Figure 119.B) was low compared to the control at 120 minutes. Moreover, the intensity remained unchanged at each of the other time points

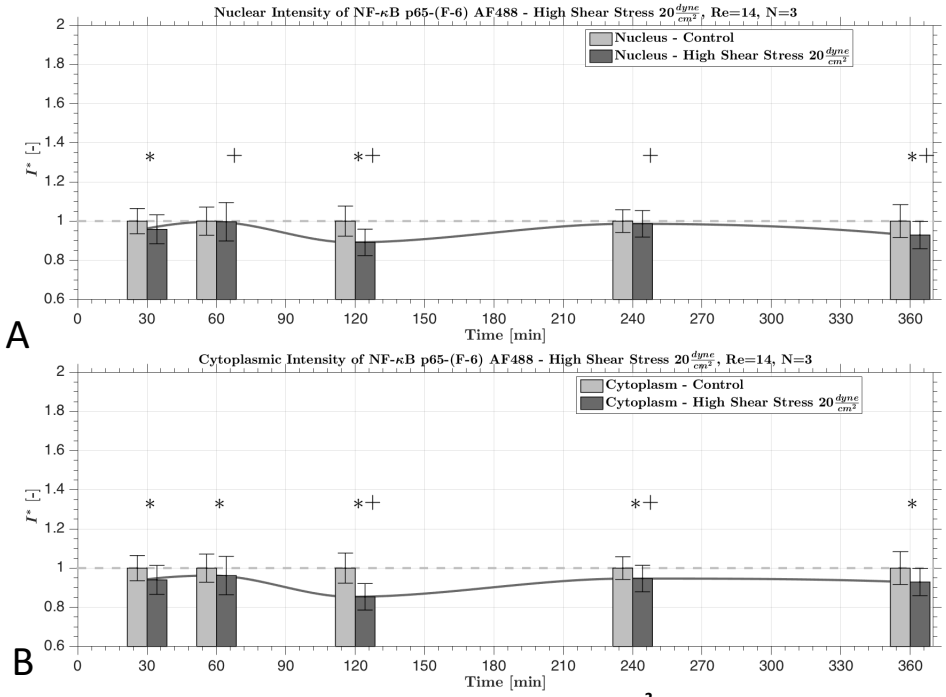

Figure 118: HUVECs exposed to a high shear stress of 20 dyne/cm^2 fixed after certain time points and stained for p65. The p65 intensity was evaluated for the nucleus (A) and cytoplasm (B). Statistical significance (p<0.05) is indicated versus static control (*) and versus the previous time step (+).

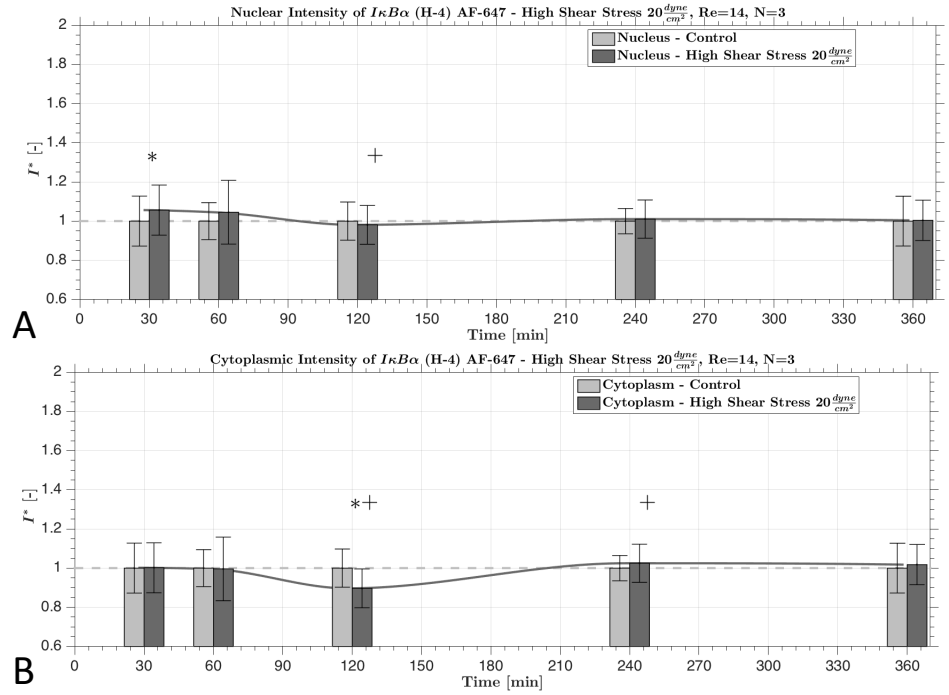

Figure 119: HUVECs exposed to a high shear stress of 20 dyne/cm^2 fixed after certain time points and stained for IκBα. The IκBα intensity was evaluated for the nucleus (A) and cytoplasm (B). Statistical significance (p<0.05) is indicated versus static control (*) and versus the previous time step (+).

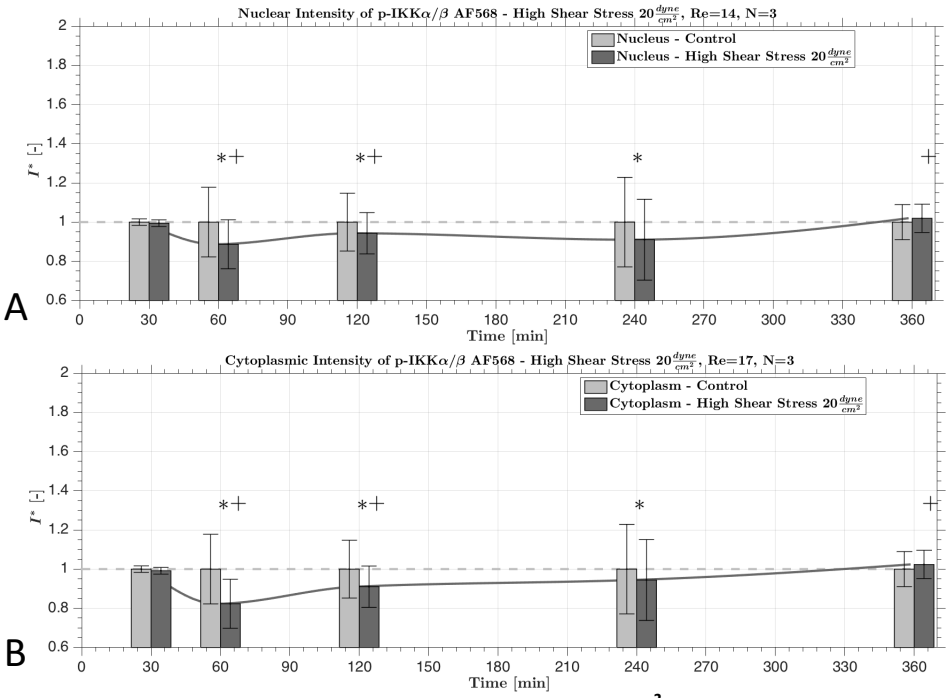

Figure 120: HUVECs exposed to a high shear stress of 20 dyne/cm^2 fixed after certain time points and stained for phosphorylated IKKα/β. The p-IKKα/β intensity was evaluated for the nucleus (A) and cytoplasm (B). Statistical significance (p<0.05) is indicated versus static control (*) and versus the previous time step (+).

In Figure 120, HUVECs exposed to high shear stress were stained for phosphorylated IKKα/β. The nuclear p-IKKα/β (Figure 120.A) intensity was reduced compared to the control at 60, 120 and 240 minutes. Moreover, the same trend was observed in the cytoplasmic p-IKKα/β intensity (Figure 120.B).

4.2.2. Nuclear Translocation of GFP-RelA

An example of a clearly visible shear stress induced nuclear translocation of GFP-RelA in a HUVEC is shown in Figure 121. The HUVEC experienced nuclear translocation of GFP-RelA with peak at 70 minutes after onset of a high shear stress (20 dyne/cm^2).

In general, HUVECs expressing GFP-RelA and H2B-mCherry were exposed to a high shear stress of 20 dyne/cm^2. A time series (0, 90, 120, 240 and 360 minuites) of HUVECs expressing GFP-RelA exposed to a high shear stress recorded with a wide-

field microscope is shown in Figure 122, No strong nuclear translocation of GFP-RelA was visually observed, similar to the results under low shear stress. However, change in shapes, positions and slight changes in nuclear GFP-RelA due to shear stress conditions could be observed.

The nuclear GFP-RelA intensity of all of the cells (1789) exposed to a high shear stress of 20 dyne/cm^2 are shown in Figure 123.A. The spread of the signal is large. This is due to the large variety of technical effects and cell heterogeneity. However, the mean shows a steady but slight oscillating trend. The intensity mean per position is given in Figure 123.B. This narrows down the variety, however differences between positions are large. In Figure 123.C, the mean for all five channels including an extra test channel are shown. (The test channel was run prior to the main experiment and could be included in the dataset as the experiment was successful). It is seen that the mean intensity between channels differs. This is believed to arise from to technical variation (light variations per channel) and cell heterogeneity. In Figure 123.E, all cells were normalised using their time average. This resulted in a mean close to 1 that appeared to peak slightly at 60 minutes. This is followed by a subsequent drop at 180 minutes and then a strong increase from 240 minutes onwards. The large standard deviation is due to the large heterogeneity within the population. As under low shear stress, high shear stress only caused a weak effect on the nuclear translocation of GFP-RelA.

The measurements described above can be compared to IHC in Figure 123.D. With IHC, a drop in nuclear p65 at 120 minutes was observed. This increased at 240 minutes and then dropped at 360 minutes. It is argued that the drop at 120 minutes is comparable with the drop observed in live-cell imaging at 180 minutes. However,

at 360 minutes, the live-cell imaging measurements differ. Furthermore, the normalised intensity of low shear stress is compared to the normalised mean under static conditions in Figure 123.F. This comparison indicates that high shear stress influenced the nuclear GFP-RelA intensity.

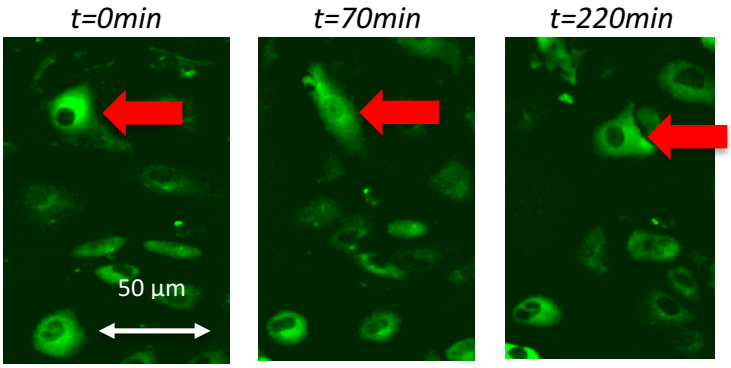

Figure 121: HUVEC (red arrow) exposed to high shear stress of 20 dyne/cm^2 experiencing nuclear translocation of GFP-RelA at 70 minutes of flow.

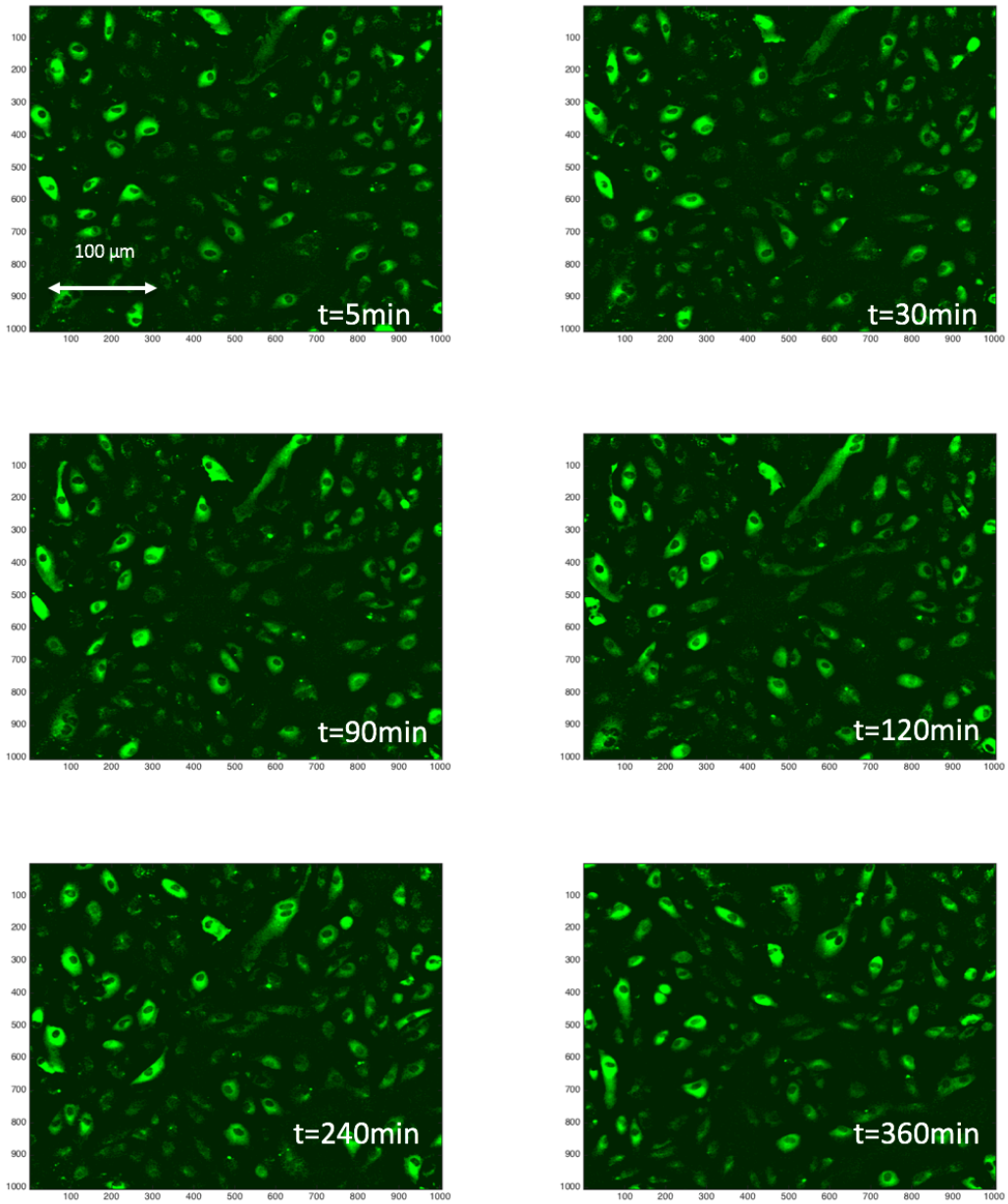

Figure 122: Post-processed images of HUVECs expressing GFP-RelA exposed to high shear stress (20 dyne/cm^2) imaged at different time points (5, 30, 90, 120, 240 and 360 minutes).

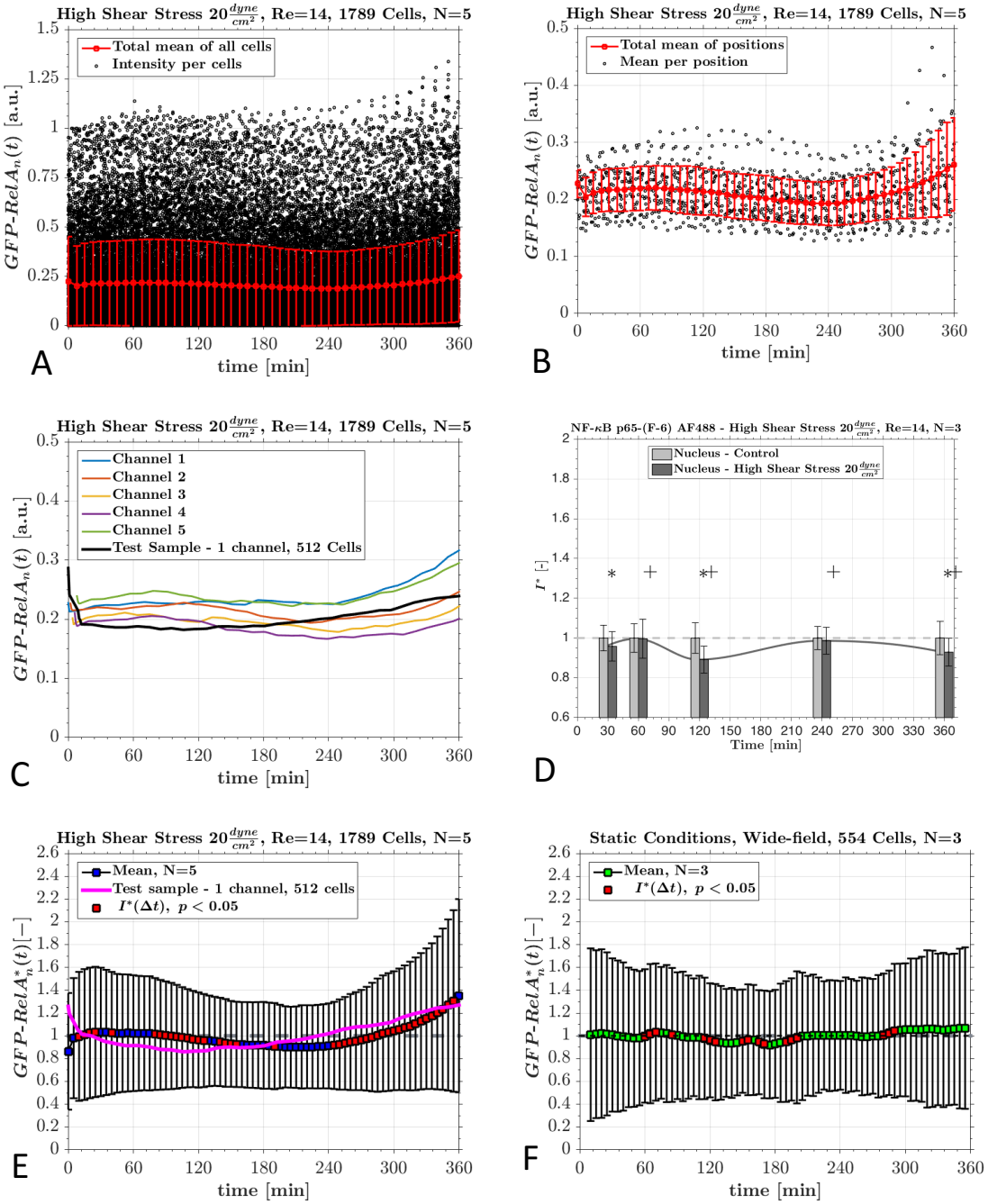

Figure 123: The nuclear GFP-RelA intensity of single cells exposed to a high shear stress of 20 dyne/cm^2. (A = Intensity [a.u.], B = Intensity per position [a.u.], C = Mean of each channel, E= Normalised intensity by time average [-]). IHC at different time point of non-transfected HUVECs exposed to high shear stress (D). For comparison, the nuclear GFP-RelA intensity normalised by time average under static conditions (F)

The phase contrast images taken at different time points are shown in Figure 124. These can be used to explain the strong increase (approximate 30 %) of nuclear GFP-RelA after 240 minutes. Cells appeared fine at t=0 minutes and 180 minutes. However, at t=360 minutes it is observed that a few cells died and others started an

apoptosis or proliferation process. Therefore, it is believed that the large increase in nuclear GFP-RelA after 240 minutes is mainly due to dying or splitting cells.

The tracking software was programmed to reject cells that disappear in time. However, if cells start to split or die at t=300 minutes, and this process takes until 360 minutes, then the tracking software included these cells. Hence, the strong increase after 240 minutes could be due to the inclusion of cells in apoptosis or in a proliferation state.

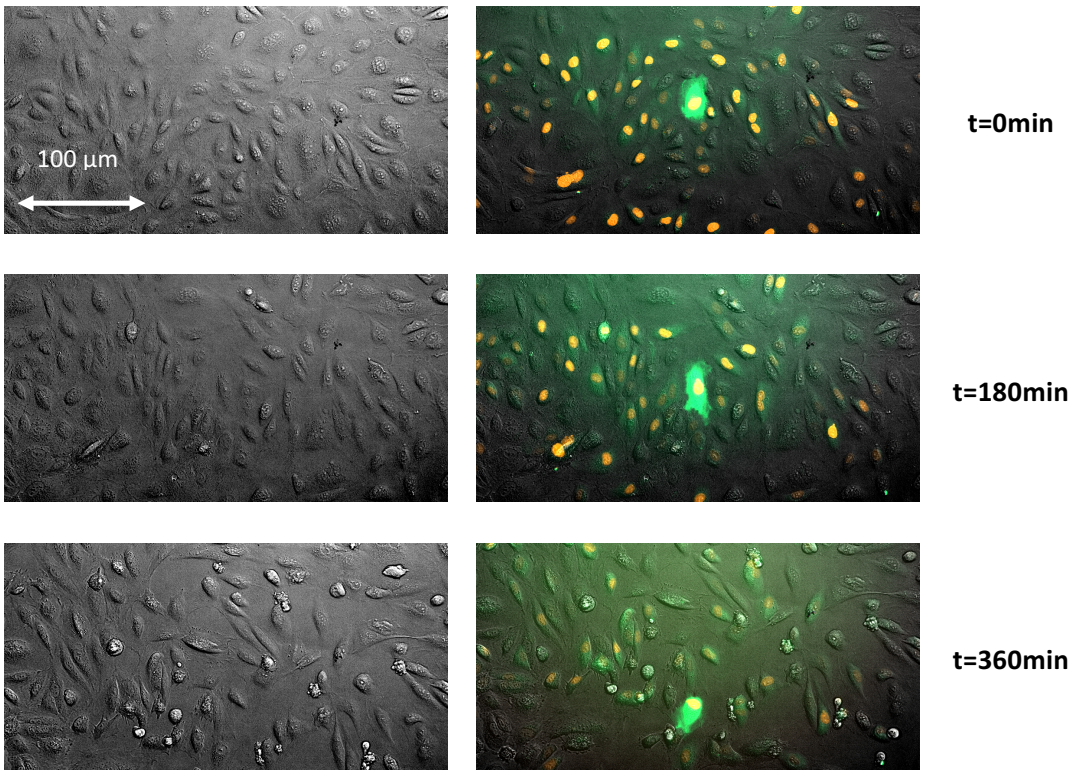

Figure 124: Many cells underwent apoptosis or proliferation after 180 minutes, which might be the reason for a strong increase in nuclear GFP-RelA intensity from 240 minutes onwards. Displayed images are contrast enhanced only.

The mean and standard deviation of all seven positions of all repeats (five channels) are depicted in Figure 125. The positions are arranged from inlet to outlet (top to bottom). The total channel average is depicted in blue below the 7 positions. The exact location of each recorded position is indicated in Figure 125.F. Two types of

temporal nuclear GFP-RelA intensity characteristics were observed: An early nuclear intensity peak at 0 to 120 minutes (for example: 4^{th} row in channel 2, 2^{nd} and 4^{th} rows in channel 4) and an increasing nuclear intensity from 240 until 360 minutes in nearly all channels. A visual pattern between position and nuclear GFP-RelA intensity within the channels was not observed.

It is noted that convective transport of effluent may have caused differences between nuclear translocation of GFP-RelA between the first and last channel.

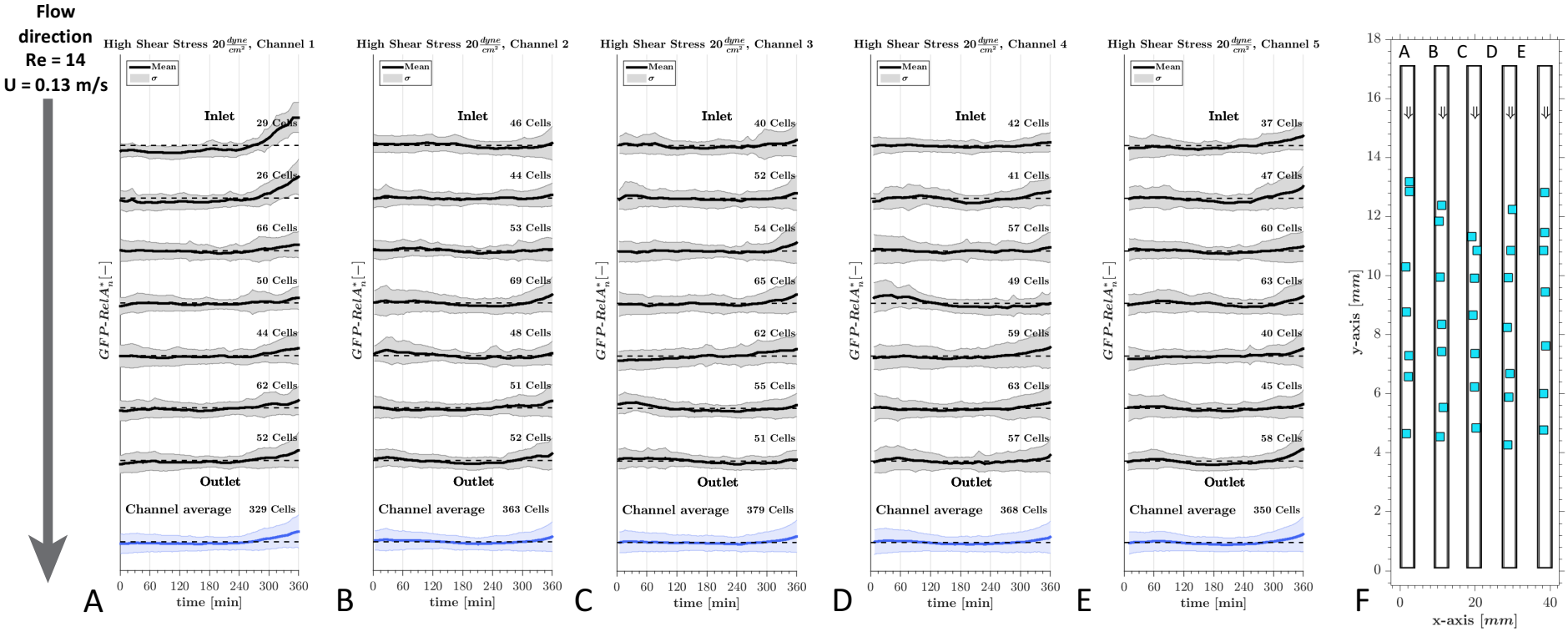

Figure 125: A-E: The GFP-RelA intensity normalised by time average in HUVECs exposed to high shear stress of 20 dyne/cm^2 in 5 different channels at 7 positions across the channel (black). The total channel mean is always shown at the bottom (blue). The value 1 is represented with a dotted line. F: The exact location of each position within the channel. The inlet is at the top. Top positions in A-E correspond to top position in F.

The mean nuclear GFP-RelA intensities for all of the channels were interpolated. These are displayed as a contour map in Figure 126. Each Y-axis (shear stress) value "20" corresponds to a channel. The figure indicates that each of the channels exhibited small increases in nuclear GFP-RelA intensity at 30 to 120 minutes. This was followed by a decline, with the minimum reqched between 150 to 240 minutes. After 240 minutes the nuclear GFP-RelA intensity increased. At 360 minutes, an increased nuclear GFP-RelA intensity is observed in all of the channels.

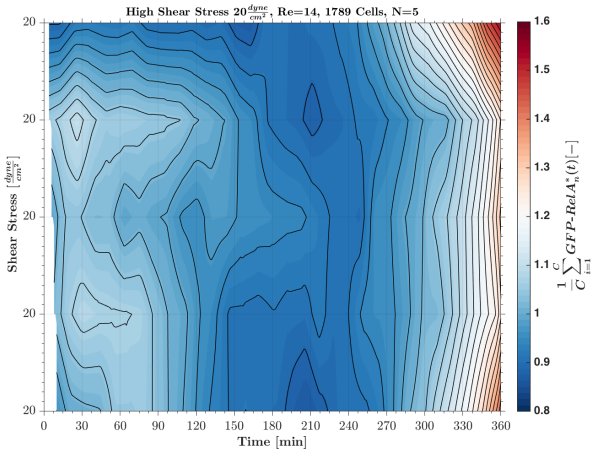

Figure 126: Interpolation of the mean nuclear GFP-RelA intensity normalised by time average for all 5 channels. In each channel HUVECs expressing GFP-RelA and H2B-mCherry were exposed to 20 dyne/cm^2. Each indicated value of shear stress corresponds to a channel.

4.2.3. Max peak analysis with normalisation by time average

Figure 127.A shows a projected view for each of the normalised cells. Normalisation has been carried out using time average and the projections were made according to intensity. Intermediate intensities (red) were found to occur early (0 – 120 minutes) and after 240 minutes.

The temporal nuclear GFP-RelA intensity profile of 100 cells are shown in Figure 127.B. These display a large heterogeneity. However, very few high peaks are observed. In Figure 127.C, the distribution of the maximum peaks of HUVECs

exposed to a high shear stress is depicted. This shows two regions with a high density of peaks: An early (0 -120 minutes) and a late region (240 to 360 minutes). This demonstrates that a high shear stress causes cells to most likely experience a high nuclear GFP-RelA intensity at the onset of flow (0 to 120 minutes) and after 360 minutes. Moreover, the maximum peak distribution is different compared to the distribution under static conditions. This demonstrates that a high shear stress affects GFP-RelA dynamics.

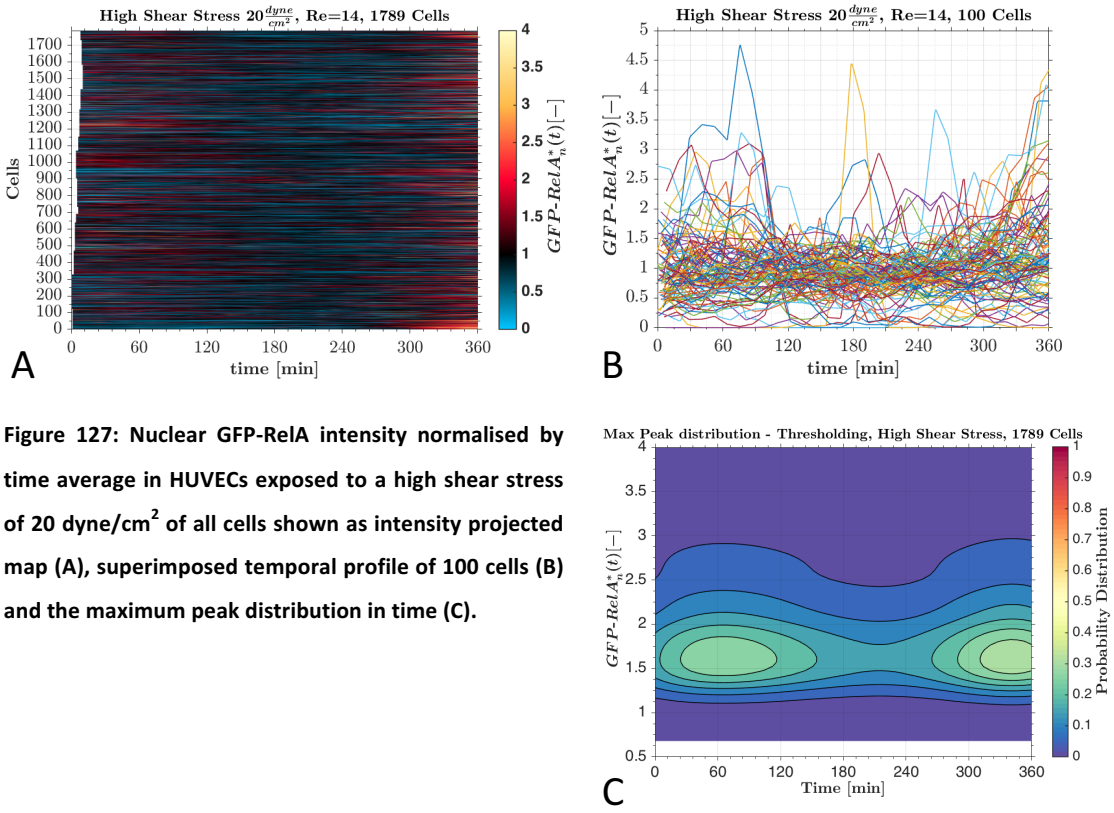

Figure 127: Nuclear GFP-RelA intensity normalised by time average in HUVECs exposed to a high shear stress of 20 dyne/cm^2 of all cells shown as intensity projected map (A), superimposed temporal profile of 100 cells (B) and the maximum peak distribution in time (C).

4.2.4. Clustering of single cell measurements

Normalisation and clustering of the single cell measurements was carried out in the same manner as for low shear stress (section 4.1.5). Identification of the number of groups was undertaken by visual inspection. Moreover, clustering was attempted using normalisation by time average (main analysis) and earliest common point

(secondary analysis). Results for both methods are presented in the following sections.

4.2.4.1. Clustering attempts with normalisation by time average – Main analysis

In Figure 128, the single cell measurements of nuclear GFP-RelA intensity were clustered into 5 groups with Kmeans. One large group (40 %) was observed to weakly peak at approximately 90 minutes. A smaller group (9 %) peaked more strongly at 30 minutes. Two groups (10 % and 25 %) experienced a high peak at 360 minutes. The last group (17 %) experienced a high initial nuclear GFP-RelA intensity. Subsequently, this dropped and then rose again from 300 until 360 minutes. Groups either peaked early at approximately 60 minutes or late at 360 minutes. The early and late peaking groups appeared to be in balance (ca. 50 % each). The percentage of groups did not change significantly amongst positions (Figure 128.C). Therefore, it is concluded that cells responded under a uniform high shear stress independent of their position within the channel.

In Figure 129, the single cell measurements were clustered using pulse search with 20 uniformly distributed peaks and 1 inactive group. It was observed that high peaks occurred throughout the experiment. These showed a high tendency to peak at early (0-120 mins) and late times (270 to 360 mins). This agrees with the maximum peak distribution observed in Figure 127.C.

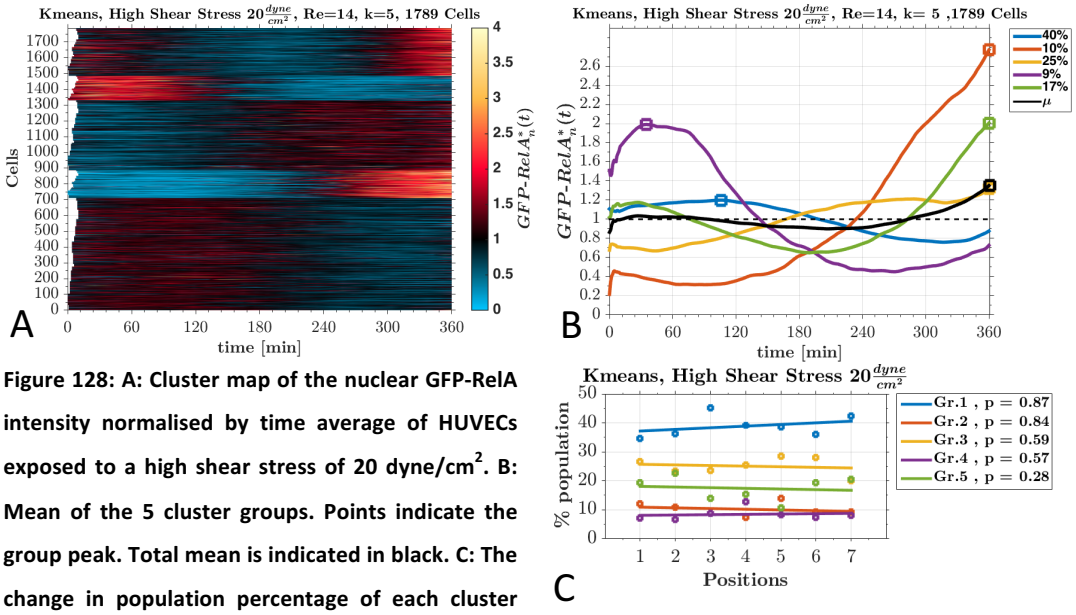

Figure 128: A: Cluster map of the nuclear GFP-RelA intensity normalised by time average of HUVECs exposed to a high shear stress of 20 dyne/cm^2. B: Mean of the 5 cluster groups. Points indicate the group peak. Total mean is indicated in black. C: The change in population percentage of each cluster group at different shear stress positions fitted to a linear regression. P-value is calculated with a one way Anova.

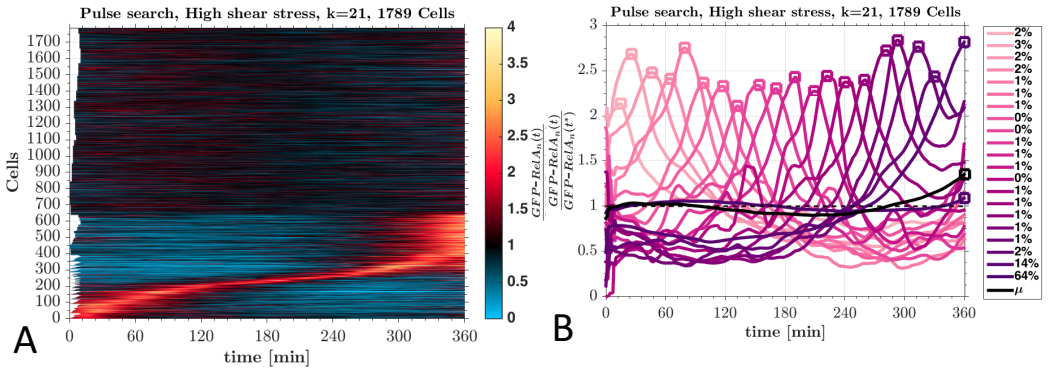

Figure 129: Pulse search (k=21) applied to nuclear GFP-RelA intensity normalised by time average of HUVECs exposed to a high shear stress. A: Projected map of the signals sorted with pulse search B: The mean of the pulse search groups.

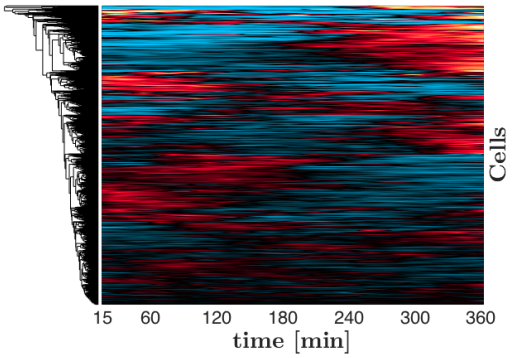

Figure 130: Hierarchical clustering of nuclear GFP-RelA intensity normalised by time average of HUVECs exposed to a high shear stress of 20 dyne/cm^2.

In Figure 130, the single cell measurements of nuclear GFP-RelA under high shear stress were clustered using hierarchical clustering. Hierarchical clustering demonstrated a large variability between cells when exposed to a high shear stress. However, similar patterns to Kmean clustering were found.

4.2.4.2. Clustering attempts with normalisation by earliest common time point – Secondary analysis

The single cell analysis after normalising by the earliest time point nuclear GFP-RelA intensity (t*=11min) is depicted in Figure 131. All of the cells are shown in a random order in Figure 131.A. A slightly higher signal was found between 30 and 120 minutes. In Figure 131.D, the nuclear GFP-RelA intensities for 100 single cells are plotted. The intensities appeared very chaotic and noisy. Moreover, most cells were found to remain close to 1, while very few experienced high intensity peaks.

In Figure 131.B and C, the single cells were clustered using thresholding. It was identified that ca. 30-40 % experience a high nuclear GFP-RelA intensity. This percentage is slightly higher than under static conditions. In Figure 131.E and F, the single cells were clustered using Kmeans. Seven suitable groups were found. These included a group (ca. 35 %) that showed a very low intensity. Moreover, a large group (31 %) showed a clear but mild peak at 90 minutes and a smaller group (11 %) also showed a peak at 90 minutes. This suggested that a high shear stress causes an early nuclear translocation of GFP-RelA in ca. 40 % of the cell population.

Two other groups showed a strong increase in nuclear GFP-RelA at 360 minutes. In Figure 131.H and I, the pulse search revealed that ca. 40 % experienced a strong nuclear translocation of GFP-RelA. The percentage of the peaks between 60 and 120 minutes are slightly higher than those at 120 to 240 minutes.

Overall, it appears that 40 % of the cell population experienced a high nuclear GFP-RelA intensity when stimulated with a high shear stress. Furthermore, Kmeans revealed a further 30 % experiences a mild nuclear translocation of GFP-RelA peak at 90 minutes.

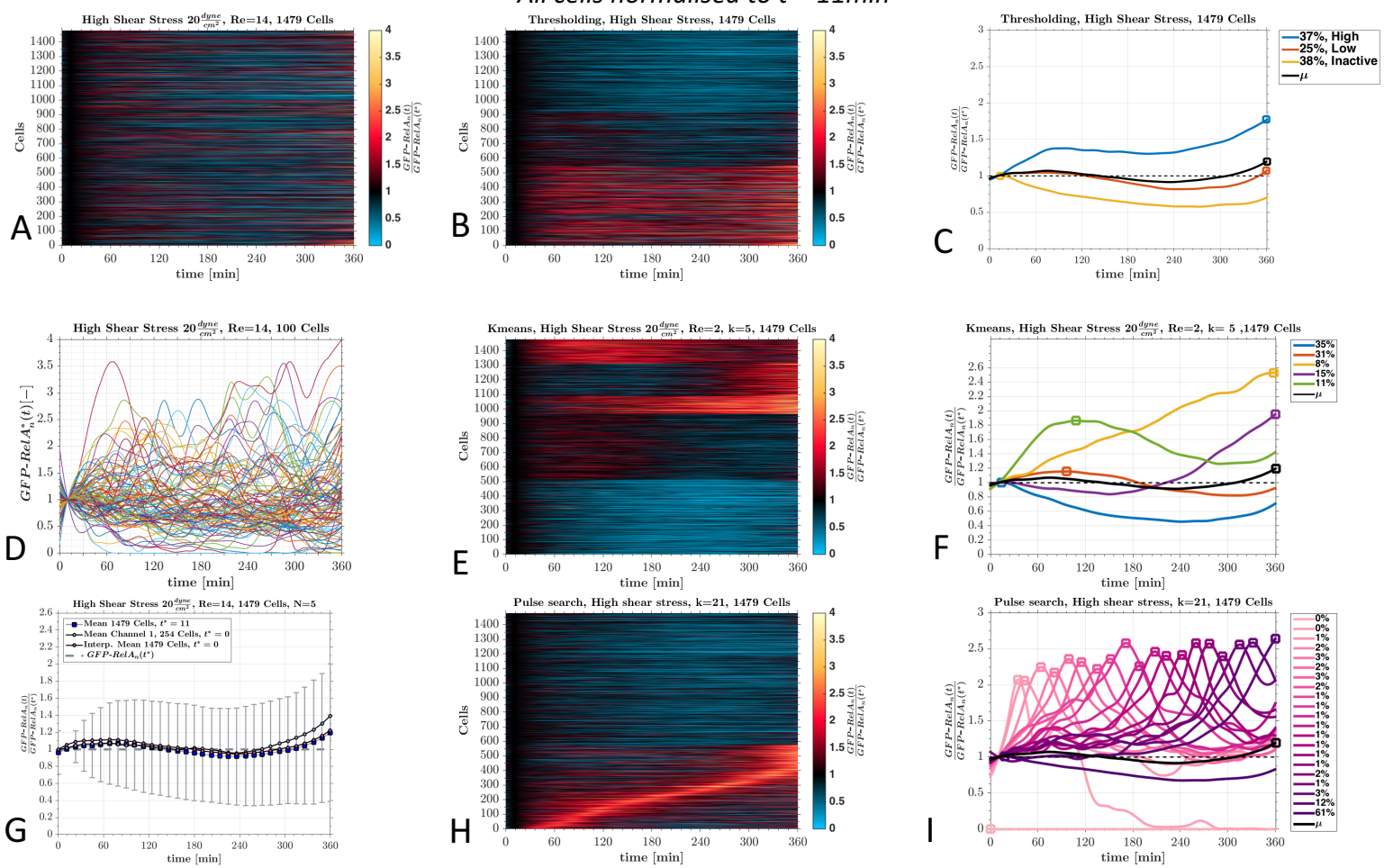

Figure 131: Single cell analysis of nuclear GFP-RelA intensity normalised using the earliest common time point (t*=11min) of HUVECs exposed to a high shear stress of 20 dyne/cm^2. A: The nuclear GFP-RelA intensity of all cells recorded. D: Example of the nuclear GFP-RelA intensity of 100 cells. G: The mean and standard deviation of the normalised intensity by the earliest time point. B: Cells were clustered using thresholding. C: The mean of the thresholding groups. E: Cells clustered using Kmeans. F: The mean of the kmeans clustering groups. G: The mean and standard deviation of the nuclear GFP-RleA intensity normalised by earliest common time point of the population. H: Cells clustered using pulse search. I: The mean of each pulse group. The squares in the mean plots indicate the peak, and in the legend the percentage of the cell population per line is given.

4.2.5. Cells movement vs. nuclear GFP-RelA intensity

The movement of cells was tracked over time with the H2B-mCherry expression (The nuclei of each cell was tracked over time which is interpreted as the movement/motility of cells during the given experimental conditions). In Figure 132, the cell movements of each cell recorded at seven different positions for each of the five channels is depicted. Purple corresponds to time zero and yellow to 360 minutes. A green arrow indicates the total mean velocity vector of all the cells at each position and the average velocity is noted above every position. The big arrow on the left indicates the direction of flow. The flow had a Reynolds number of 14 and an approximate velocity of 0.13 m/s. Cells experienced a shear stress of 20 dyne/cm^2. Cells moved strongly in the direction of flow with small perpendicular movements. The total mean cell velocity was 0.26 nm/s. The movement of all cells implies that the monolayer as a whole appears to be pushed towards the flow direction.

The average movements of all cells per positions in the X- and Y- directions are depicted in Figure 133, Cells moved very strongly in the direction of flow, reaching a total average displacement of 10 to 50 µm, after 360 minutes. In comparison, movements perpendicular to the flow were small with a total average displacement of ca. -10 to 10 µm.

The directionality ratio under high shear stress was 1.85, which is lower than under low shear stress (statistically significant), and indicateds that high shear stress

greatly influenced the mobility and increased persistence. Hence, cells mobility was strongly affected by high shear stress incomparison with static conditions.

In Figure 134, the nuclear GFP-RelA intensity of each cell is displayed at its location over time under a high shear stress of 20 dyne/cm^2. Nearly all the positions showed a large distribution of nuclear GFP-RelA intensity, without any visual pattern. In channel 4, only the first position from the left appeared to have a low nuclear GFP-RelA intensity

In Figure 135, the probability distribution of the cells displacement normalised by time average versus nuclear GFP-RelA intensity is shown for cells exposed to 20 dyne/cm^2. The probability distribution is spread widely in the X-direction from 0 to 75 µm. This was due the large movement induced by a high shear stress.

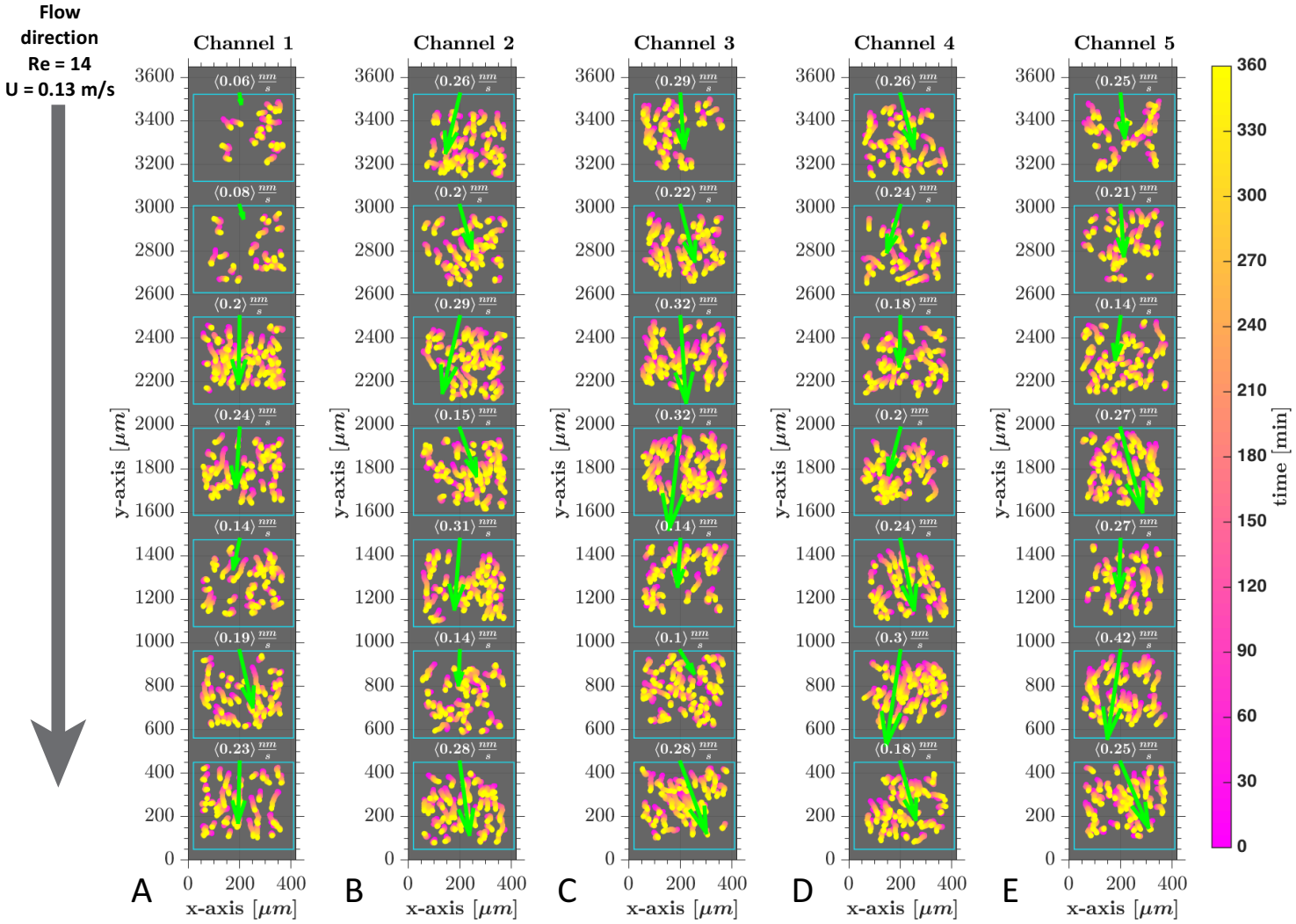

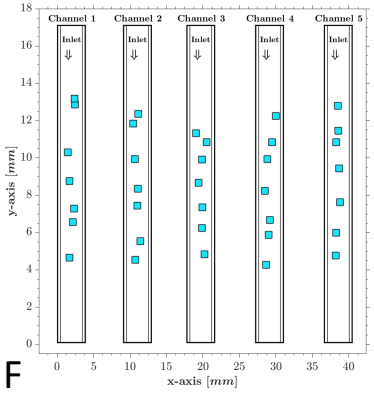

Figure 132: Movement of cells under high shear stress of 20 dyne/cm^2. A-E: In each channel, 7 positions were imaged for 360 minutes. At each position, each tracked nucleus is displayed. F: The exact locations of the positions within the channel are indicated in the channel map. The inlet is indicated at the top. Top positions in A-E corresponds to top position in F.

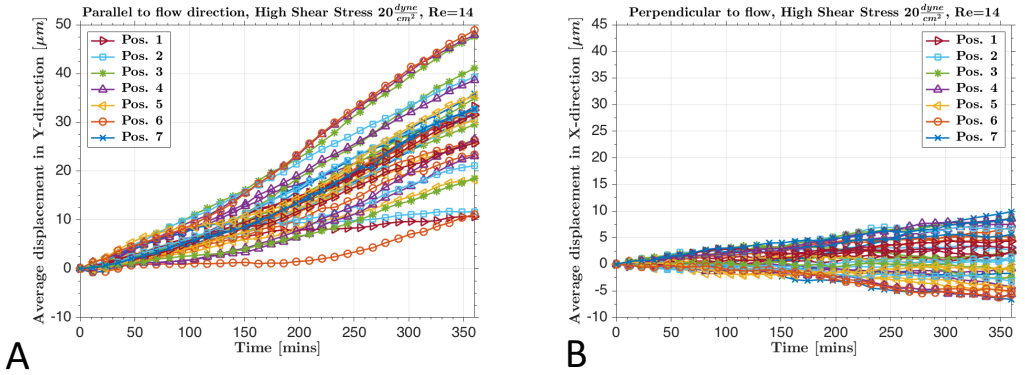

Figure 133: The mean movement of cells per position in the X- and Y-directions (A and B, respectively) for cells exposed to 20 dyne/cm^2.

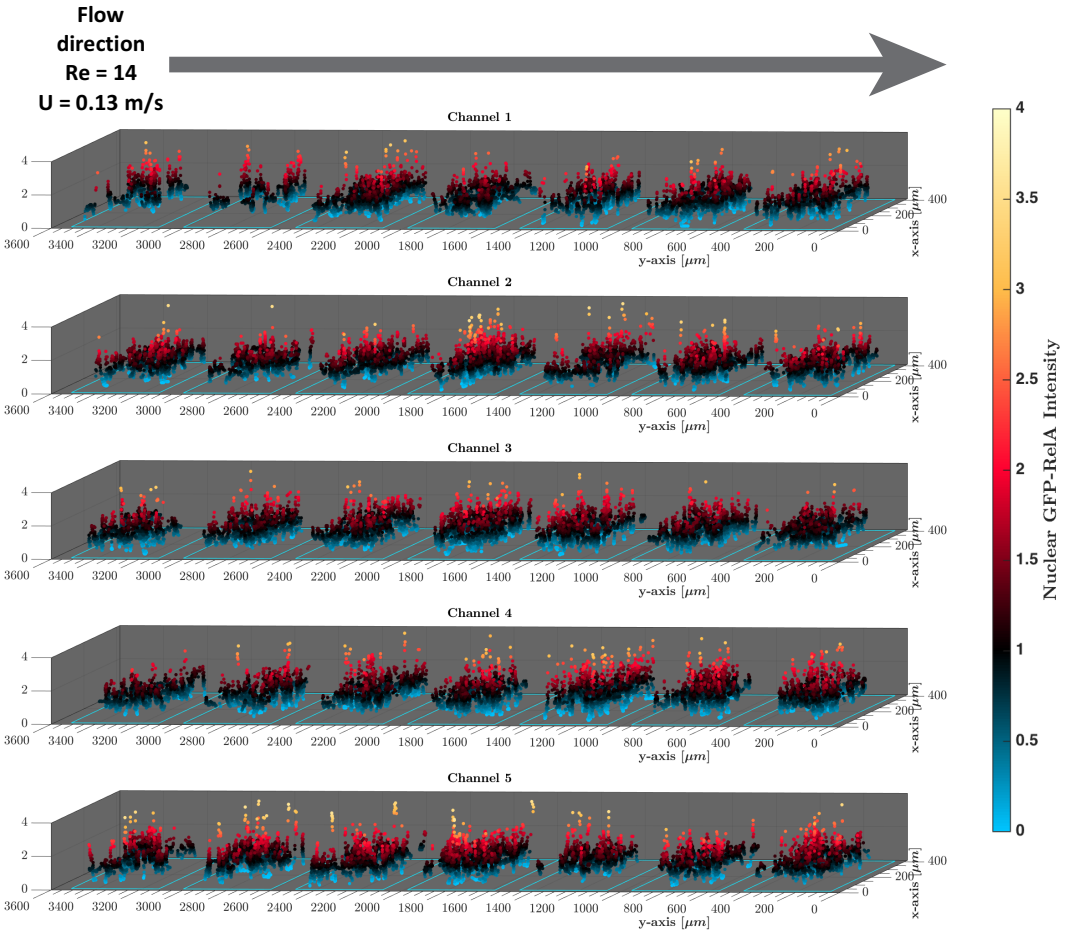

Figure 134: The nuclear GFP-RelA intensity normalised by time average (z-axis) at the cells location over time for all 5 repeats. The flow direction is from left to right.

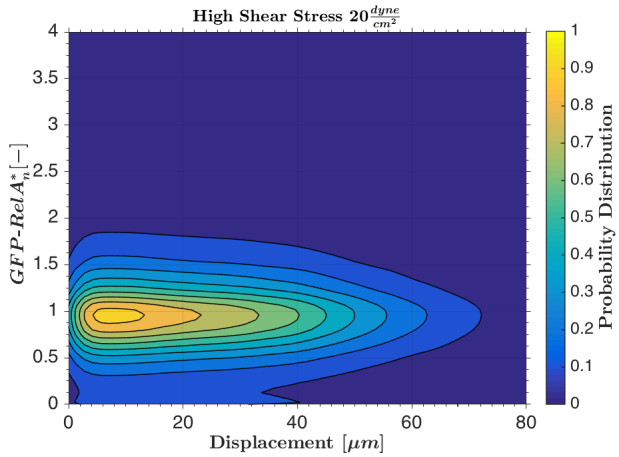

Figure 135: The probability distribution of cells displacement versus nuclear GFP-RelA intensity normalised by time average for cells exposed to a high shear stress of 20 dyne/cm^2.

4.3. The Effect of a Shear Stress Gradient on the Nuclear Translocation of GFP-RelA in HUVECs

Summary: *This section presents the nuclear translocation of NF-κB in HUVECs exposed to a shear stress gradient. The results presented are based on the experimental methods described in Chapter 2. HUVECs of passage 3, transfected with GFP-RelA and H2B-mCherry were grown in a custom made gradient channel and perfused for 360 minutes. The gradient channel generated a linear shear stress gradient from 2 to 16* dyne/cm^2 *at the bottom wall. The nuclear GFP-RelA intensity was recorded at 6 positions with shear stress magnitudes of 2, 5, 8, 11, 13, and 16* dyne/cm^2*. The total mean of all cells nuclear GFP-RelA intensity only showed an increase from 180 until 360 minutes. The nuclear GFP-RelA mean of cells per shear stress position revealed small variations between the temporal profiles at different shear stress magnitudes. Low shear stress (2, 5 and 8* dyne/cm^2*) appeared to increase the nuclear GFP-RelA intensity from 180 to 360 minutes. At high shear stress magnitudes (13 and 16* dyne/cm^2*) an additional small bump at approximately 60 minutes was observed. The effect of a shear stress gradient on the nuclear translocation of GFP-RelA was weak as seen before under low and high shear stress.*

The maximum peaks of all cells occurred at 60 and 330 minutes. The single cells were clustered into 6 groups by applying Kmeans: Initial activation, early activation, mid activation, late activation and inactive cells. A shear dependency of such groups was found. High shear stress caused earlier nuclear translocation, while low shear stress caused late nuclear translocation.

Cells in the gradient channel moved at high shear stress magnitudes (11–16 dyne/cm^2*) against the flow direction with an average displacement speed of up to 1.1 nm/s. Cells at lower shear stress magnitudes (2-8* dyne/cm^2*) moved slowly in the flow direction or perpendicular to the flow with an average displacement speed of up to 0.6 nm/s. Moreover, cells at 16* dyne/cm^2 *experienced an average displacement of approximately -20 μm against the direction of the flow.*

4.3.1. Nuclear Translocation of GFP-RelA in a shear stress gradient

A shear stress gradient was applied over a monolay of HUVECs to investigate two hypotheses:

- If the same responses under low and high shear stress in straight channels occur at low and high shear stress within the gradient.
- If the gradient over cells causes an increased nuclear translocation of GFP-RelA, as gradients are mostly observed in disturbed flows.

HUVECs expressing GFP-RelA and H2B-mCherry were grown in a custom-made shear stress gradient channel. The gradient channel was described in detail in Chapter 2 and its flow characteristics in Chapter 0. The gradient channel was perfused with a flow rate of 15 mL/min. This created a gradually increasing shear stress from 2 to 16 dyne/cm^2 along the channel. HUVECs were recorded live with a wide-field microscope, with a time interval of 15 minutes. HUVECs were tracked at six positions, where cells experienced a shear stress of 2, 5, 8, 11, 13 and 16 dyne/cm^2. At each of these positions cells were tracked and their nuclear GFP-RelA intensity evaluated. In Figure 136, images at shear stress 2, 8 and 16 dyne/cm^2 are shown at 0 and 360 minutes.

Strong alignment at higher shear stress mangitudes (8 and 16 dyne/cm^2) was observed. However, visually significant nuclear translocation of GFP-RelA, as with TNF-α, was not observed in the gradient channel. Time series of all shear stress magnitudes within the gradient are depicted in the appendix (Figures 186-191).

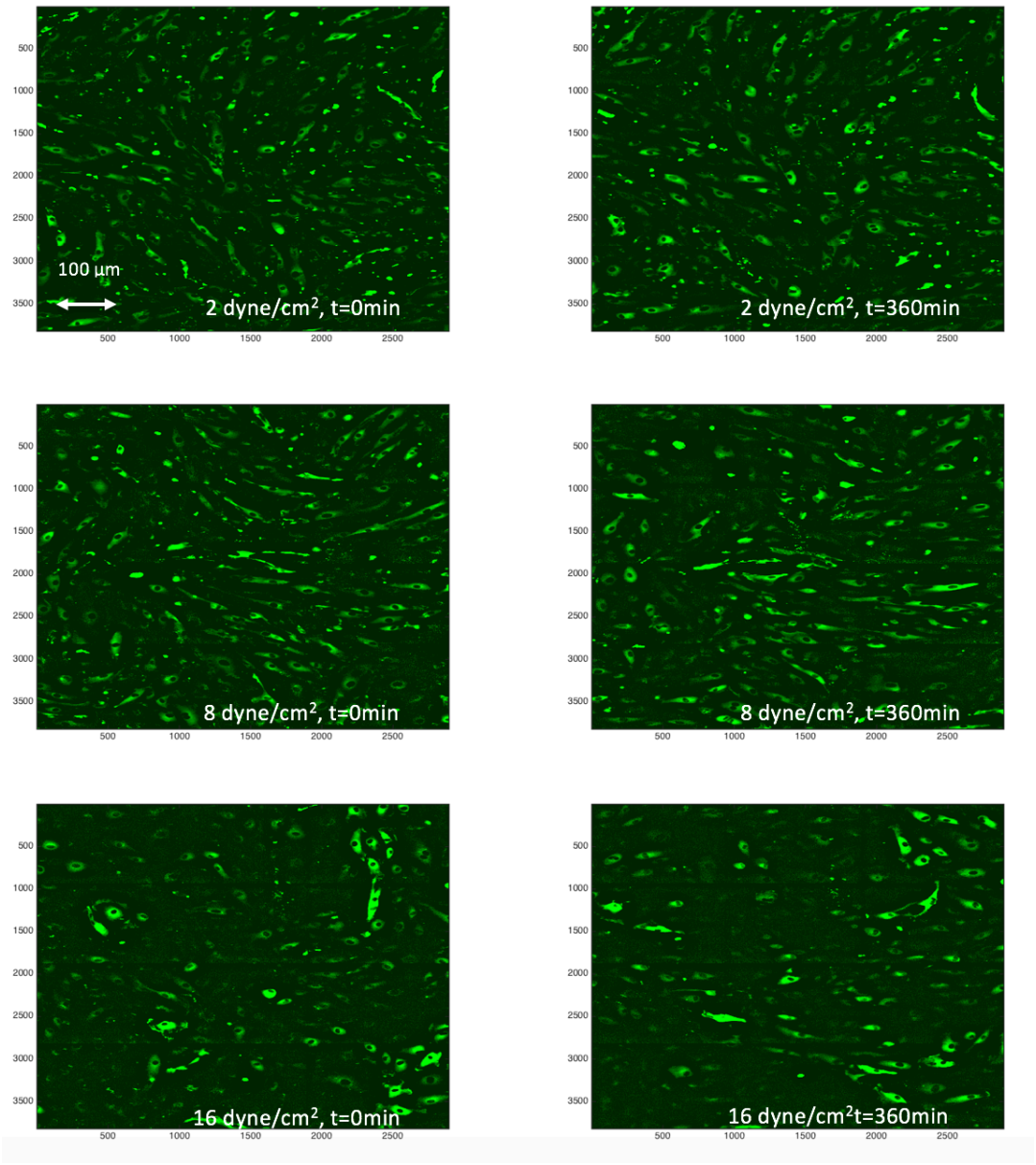

Figure 136: HUVECs expressing GFP-RelA were exposed to a shear stress gradient of 2 to 16 dyne/cm^2. Recordings of shear stress position 2, 8 and 16 dyne/cm^2 at 0 and 360 minutes are displayed.

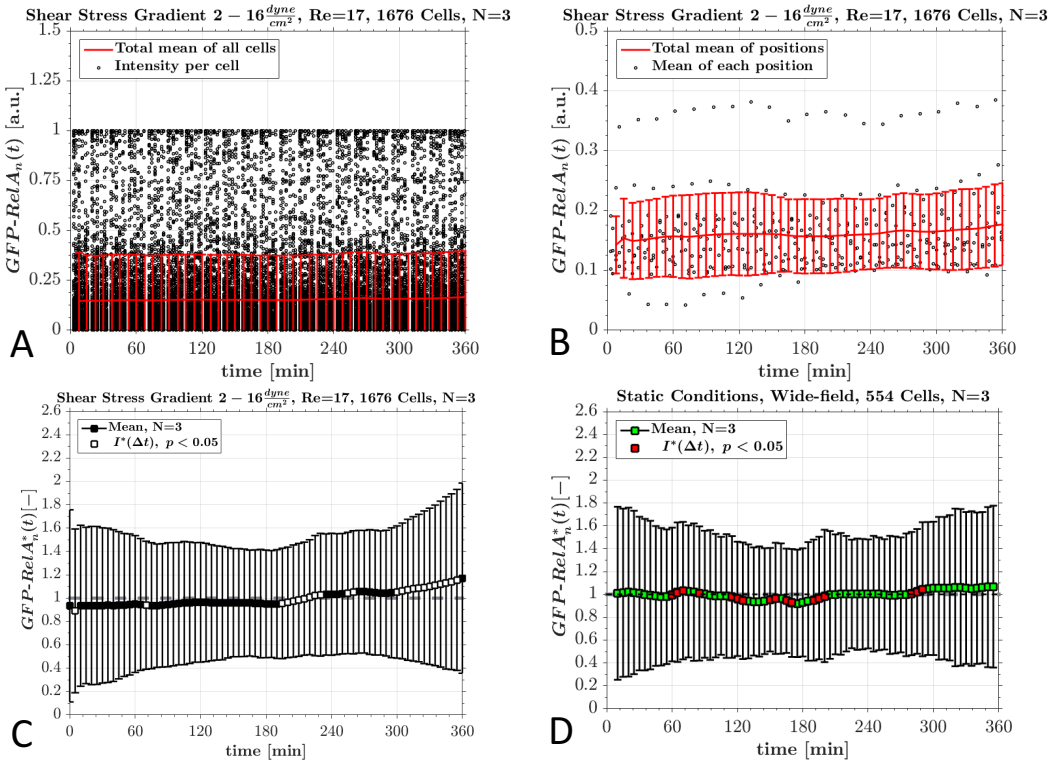

Figure 137: A: The nuclear GFP-RelA intensity of single cells exposed to a shear stress gradient of 2- 16 dyne/cm^2. (A = intensity [a.u.], B = intensity per position [a.u.], E= intensity normalised by time average [-]). For comparison, the normalised nuclear GFP-RelA intensity under static conditions (D)

Figure 137.A shows the intensity of each tracked cell within the gradient channel. The intensities observed to be largely variable due to a high cellular heterogeneity. Figure 137.B shows the mean intensity of each position (from 3 repeats). In Figure 137.C, the mean and standard deviation of the normalised nuclear GFP-RelA intensity are shown. It was observed that cells in a gradient channel were almost unaffected within the first 180 minutes. Following 180 minutes, their nuclear GFP-RelA intensity increased slightly and after 300 minutes the intensity increased strongly. Similar to the high shear stress, the strong increase towards the end of the experiment is believed to arise from the inclusion of cells that are in apoptosis or in a cell division state in the tracking algorithm.

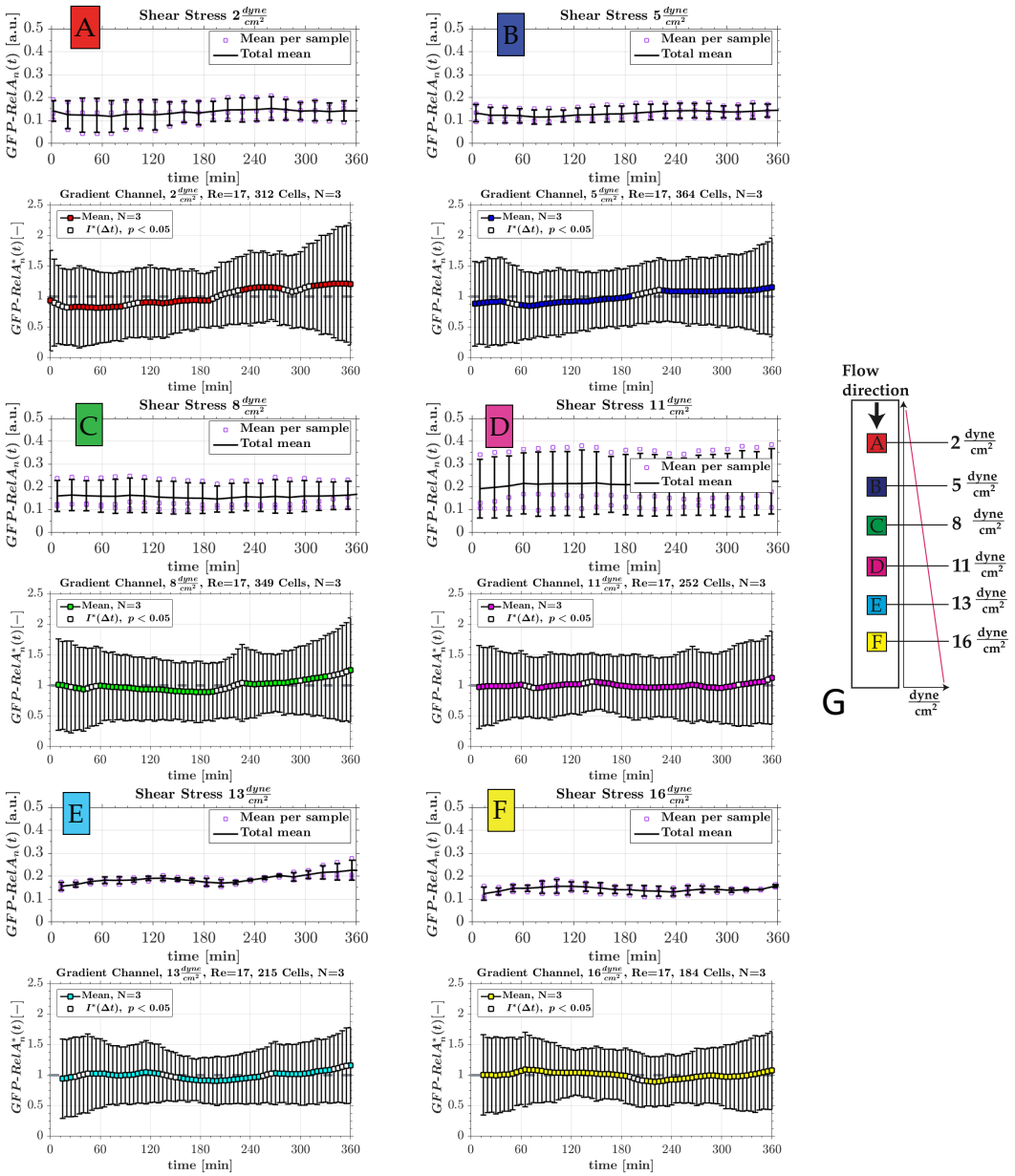

Figure 138: HUVECs expressing GFP-RelA and H2B-mCherry were exposed to a shear stress gradient. A-F: The mean of the nuclear GFP-RelA intensity (dimensional and normalised to time average) at shear stress magnitudes of 2, 6, 10, 14, 18 and 22 dyne/cm^2. G: Schematic diagram of the gradient channel. Locations of the positions are indicated with a letter and colour. An arbitrary plot shows the increasing shear stress along the channel.

In Figure 138, the total mean nuclear GFP-RelA intensity of all tracked cells at six different shear stress positions are depicted. Each position within the gradient channel corresponds to a shear stress magnitude. These positions are labelled with a letter and colour. A coloured square with letter indicates which means belongs to which position.

At 2 dyne/cm^2, the normalised mean was observed to increase after 180 minutes and was high until 360 minutes. Upstream at 5 dyne/cm^2, the normalised intensity increased slightly throughout the whole experiment.

At 8 dyne/cm^2, the normalised nuclear GFP-RelA intensity remained close to 1 and then increased slightly from 240 minutes onwards. At 11 dyne/cm^2, the intensity hardly changed with time. At a high shear stress of 13 dyne/cm^2, the normalised nuclear GFP-RelA intensity slightly peaked between 60 and 120 minutes. This was followed by a small drop, which increased again until 360 minutes. At 16 dyne/cm^2 the same trend as at 13 dyne/cm^2 was observed. The nuclear GFP-RelA intensity peaked at 60 to 120 minutes, fell again and rose slightly at 360 minutes. In general, the effect of different shear stress magnitudes within the gradient only showed weak effects on the nuclear translocation of GFP-RelA. This effect is much weaker than under TNF-α stimulation.

In Figure 139, the mean and standard deviation of all 6 shear stress magnitude positions (2, 5, 8, 11, 13 and 15 dyne/cm^2) of all repeats (three channels) are depicted. The positions are arranged from inlet to outlet, or low to high shear stress (top to bottom). The total channel average is depicted in blue below the six positions. Similar trends to those described above with Figure 138 were observed. The nuclear GFP-RelA mean at low shear stress positions (2 and 5 dyne/cm^2) appeared to be flat for the first 180 minutes and then increased slightly. Moreover, channel 2 experienced drops and larger standard deviations, which was probably due to more noise in this sample. At higher shear stress positions (13 and 16 dyne/cm^2), it appeared as if the nuclear GFP-RelA intensity showed slight increases early in the experiment (0 -180 minutes). This is slightly different from the low shear

stress positions. However, it is difficulut to identify an obvious pattern with the current representation.

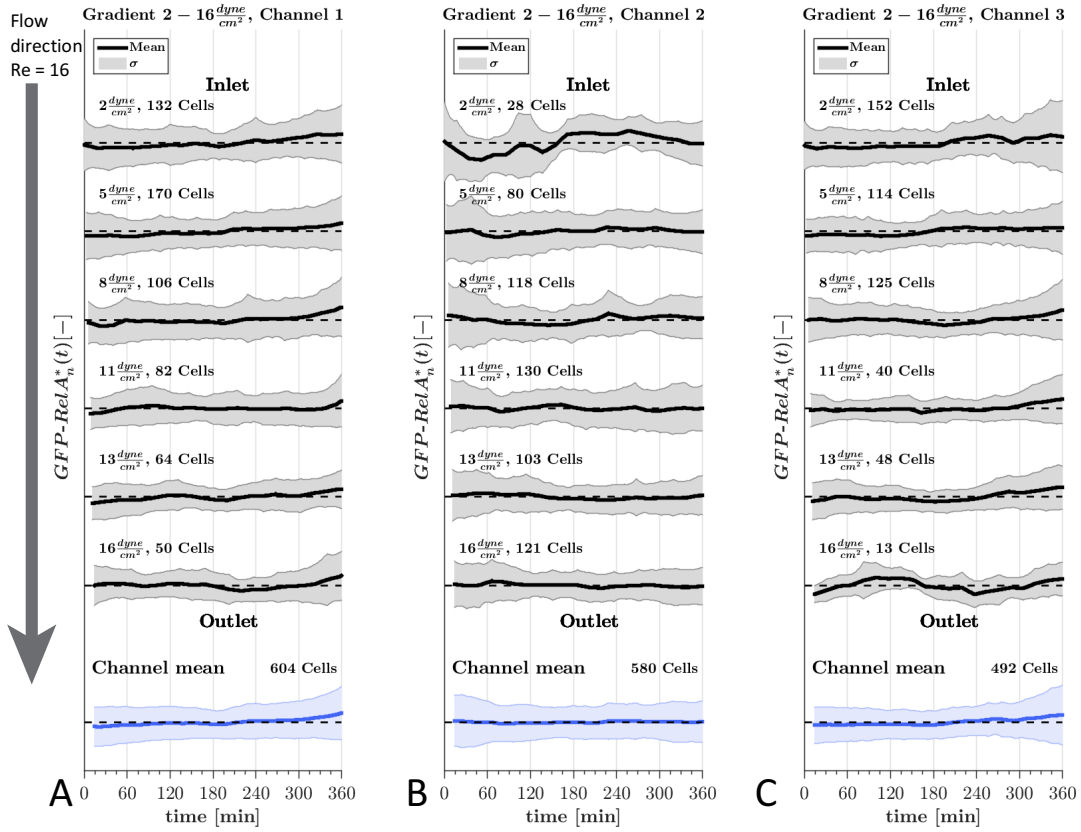

Figure 139: A-C: The GFP-RelA intensity normalised by time average in HUVECs exposed to a shear stress gradient of 2-16 dyne/cm^2 in 3 different channels at 6 shear magnitudes positions (2, 5, 8, 11, 13 1and 16 dyne/cm^2) across the channel (black). The total channel mean is shown at the bottom (blue). The value 1 is represented with a dotted line. Inlet, outlet and arrow indicate flow direction.

In Figure 140, the mean normalised nuclear GFP-RelA intensity per position were interpolated between shear stress magnitudes to represent a map of the temporal nuclear GFP-RelA intensity at different shear stress magnitudes.

Four regions could be approximately defined as indicated in Figure 140:

- An early low intensity region between 0 and 180 minutes for a shear stress range of approximate 2 to 10 dyne/cm^2.
- An early medium-high intensity region from 0 to 180 minutes for the shear stress range 10 to 16 dyne/cm^2.

- A late high intensity region between 180 to 360 minutes for 2 to 10 dyne/cm^2.
- A late medium intensity region from 180 to 360 minutes for 10 to 16 dyne/cm^2

These four different groups might indicate that there is a difference between low and high shear stress in nuclear translocation of GFP-RelA.

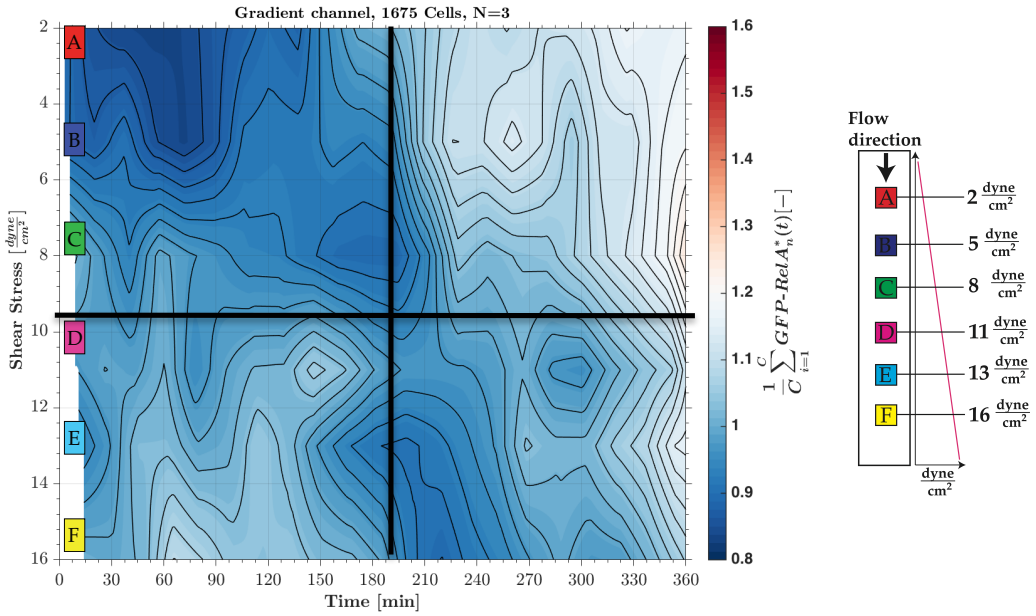

Figure 140: The mean of the nuclear GFP-RelA intensities normalised by time average for each measured shear stress (2, 5, 8, 11, 13 and 16 dyne/cm^2) were linear interpolated and plotted as a contour map. Each measured shear stress is indicated with a letter and colour that corresponds to the annotation in the schematic diagram on the right. The mean nuclear GFP-RelA intensity is the Z-axis and the colour bar indicates its values. The map is split into four possible sections with different temporal intensities.

HUVECs experiencing nuclear translocation of GFP-RelA when exposed to different shear stress magnitdues within the shear stress gradient are shown in Figure 141 and Figure 142. Figure 141.A and B shows a HUVEC experiencing a slightly increased nuclear GFP-RelA intensity from 200 to 360 minutes when exposed to a low shear stress (2 dyne/cm^2) within the shear stress gradient. In Figure 141.C, D and E, a HUVEC experiencing an increased nuclear GFP-RelA intensity at 60 minutes. This

subsequently dropped at 90 minutes, when exposed to a high shear stress (16 dyne/cm^2). In Figure 142, a HUVEC that experiences an increased nuclear translocation of GFP-RelA at 280 minutes is shown. These time series demonstrate the nuclear translocations of GFP-RelA recorded within the gradient channel. However, they were much weaker compared to stimulation with TNF-α.

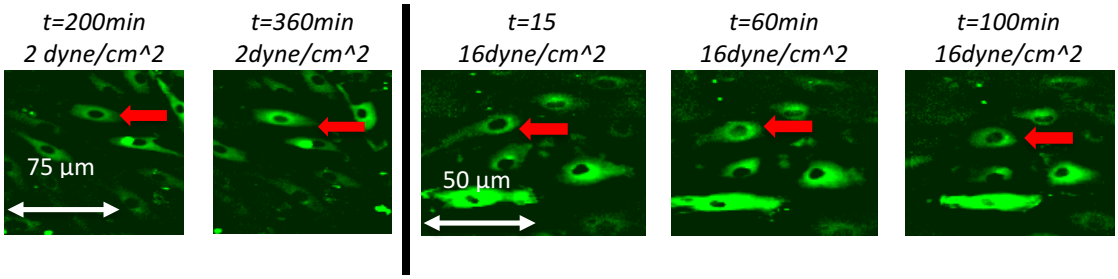

Figure 141: HUVECs experiencing different shear stress magnitdues within the shear stress gradient. HUVEC exposed to a low shear stress (2 dyne/cm^2) showed a slight increase in nuclear GFP-RelA intensity at 360 minutes. HUVEC exposed to a high shear stress (16 dyne/cm^2) had a slightly increased nuclear GFP-RelA intensity at 60 minutes. HUVECs of interest are highlighted with a red arrow.

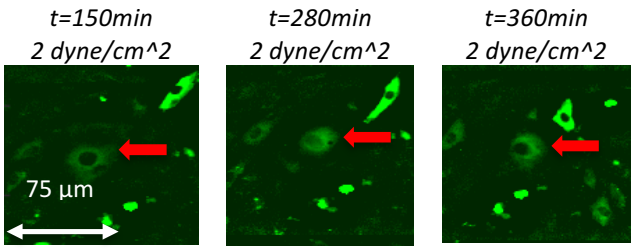

Figure 142: HUVEC exposed to low shear stress (2 dyne/cm^2) within the shear stress gradient experienced a increased nuclear GFP-RelA intensity at 360 minutes.

4.3.2. Max peak analysis with normalisation by time average

In Figure 143.A, all cells are shown as a projected view, where the projection was made according to the intensity axis. Small patches of red can be observed throughout the population.

The temporal nuclear GFP-RelA intensity profiles of 100 cells (randomly picked from each position) are shown in Figure 143.B. Only a few cells experienced a large

change (> 2.5). In Figure 143.C, the maximum peak distribution of all cells within the gradient channel is shown. It appeared that the maximum peaks of each cell most likely occurred early at approximately 60 minutes and late at 330 minutes. The peak distribution tendency of early and late peaks is similar to those found in low and high shear stress experiments. However, the distribution also has similiarities with the distribution under static conditions. This indicates a less strong effect of the shear stress gradient on the NF-κB dynamics within the total population than exposure to uniform flows.

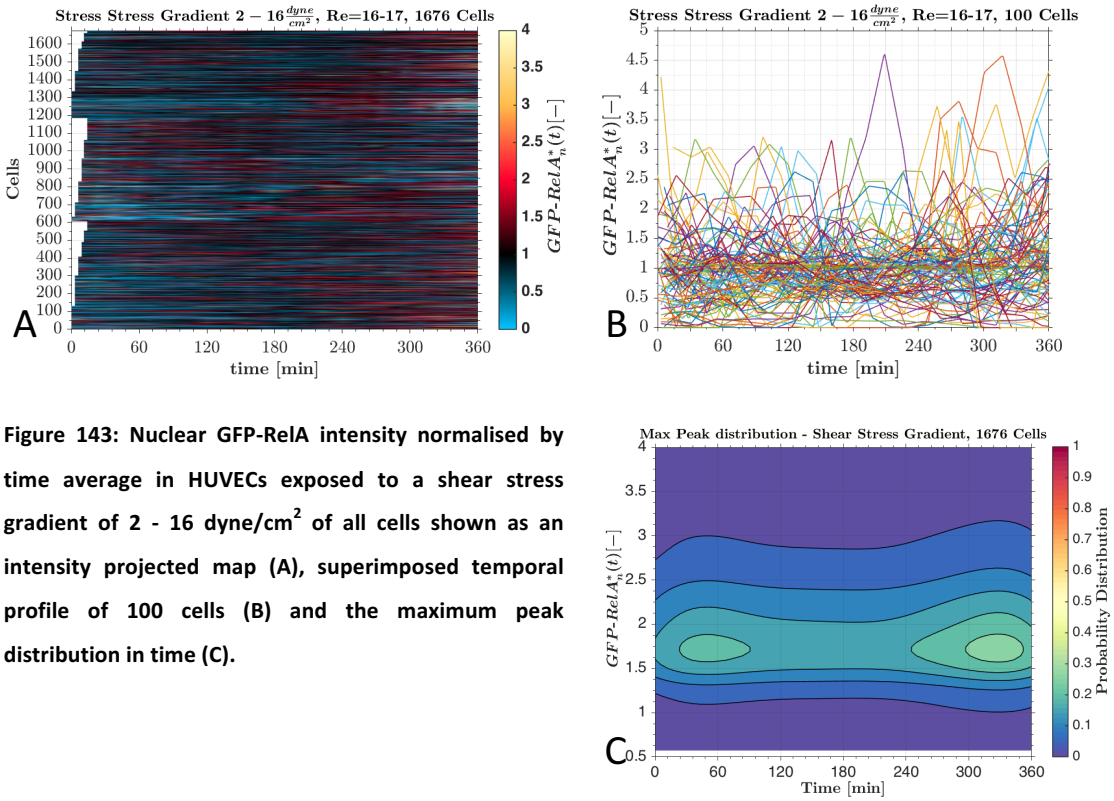

Figure 143: Nuclear GFP-RelA intensity normalised by time average in HUVECs exposed to a shear stress gradient of 2 - 16 dyne/cm^2 of all cells shown as an intensity projected map (A), superimposed temporal profile of 100 cells (B) and the maximum peak distribution in time (C).

4.3.3. Clustering of single cell measurements

Normalisation and clustering of the single cell measurements was carried out in the same manner as for low shear stress (section 4.1.5) and high shear stress. Identification of number of groups was undertaken by visual inspection. Moreover, clustering was attempted using normalisation by time average (main analysis) and

earliest common point (secondary analysis). Results for both methods are presented in the following sections.

In addition, the identified cluster groups with intensity normalised by time average will later be applied to the shear stress induced NF-κB pathway model in chapter 6.

4.3.3.1. Clustering attempts with normalisation by time average – Main analysis

Using Kmeans, five different temporal nuclear translocation groups for the nuclear GFP-RelA intensity signal were identified. These are depicted in Figure 144. The five groups were labelled: Initial activation group (peak at 30 minutes), early activation group (peak at ca. 110 minutes), mid activation group (peak at ca. 220 minutes), late activation group (peak at ca. 345 minutes) and inactive group (small peak at 360 minutes).

The initial activation (8 % of the total cell population) experienced a strong peak directly after onset of flow. The percentage of initial activation cells (Gr.5 in Figure 144.C) remained almost unchanged at all shear stress magnitudes.

The early activation group (16 % of total cell population) peaked at approximately 110 minutes. The percentage of early activation cells (Gr.1 in Figure 144.C) increased by approximately 15 % from low to high shear stress. This suggests that high shear stress magnitudes cause an increased nuclear translocation of GFP-RelA at the early onset of flow.

The mid activation group (20 % of total cell population, peak at 220 minutes) experienced a decrease in population percentage of approximately 10 % on moving from low to high shear stress (Gr.2 in Figure 144.C).

The late activation group (18 % of total cell population, peak at 345 minutes) experienced a decrease in population percentage of approximately 15 % on moving from low to high shear stress (Gr.3 in Figure 144.C). Therefore, this suggests that at low shear stress, more cells experience nuclear translocation between 180 and 360 minutes than at high shear stress. The percentage of the inactive group (Gr.4 in Figure 144.C) increased by approximately 20 % from low to high shear stress, suggesting that less cells were strongly active at a higher shear stress.

In Figure 145, the single cell measurements of the gradient channel were clustered using pulse search with 20 pulses and 1 inactive group (k=21). It was observed that ca. 40 % experienced a high nuclear GFP-RelA peak. These cells experienced peaks almost uniformly distributed in time. This demonstrated that a constant activation of individual cells was triggered in the culture by the shear stress gradient.

In Figure 146, the single cell measurements of nuclear GFP-RelA under low shear stress were clustered using hierarchical clustering. Hierarchical clustering demonstrated the large variability between cells when exposed to a shear stress gradient of 2-16 dyne/cm^2. We find a similar pattern to the pulse search, but a much more distributed arrangement than with Kmeans.

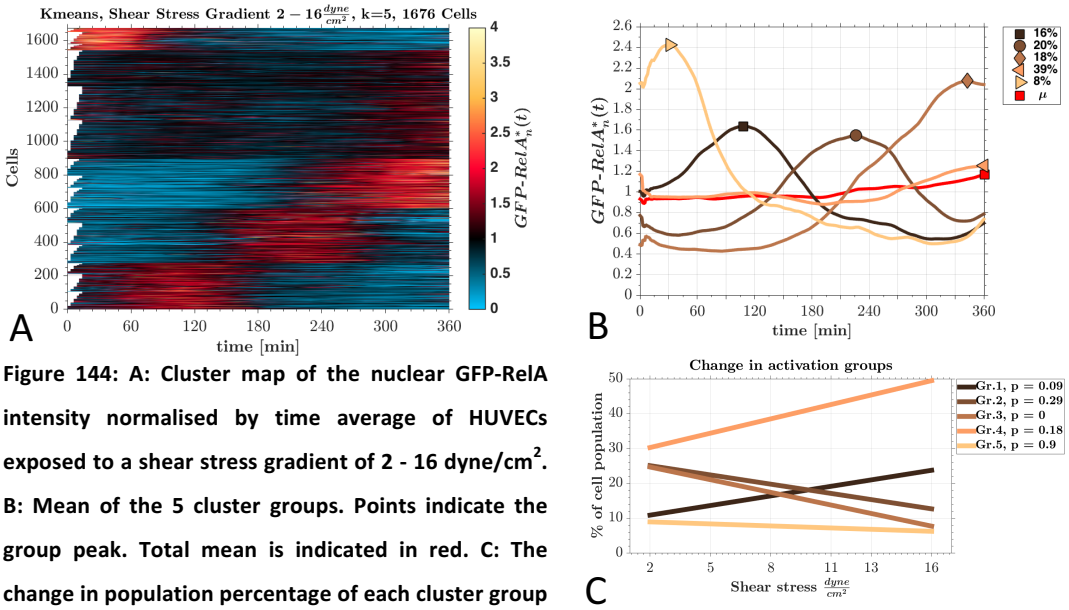

Figure 144: A: Cluster map of the nuclear GFP-RelA intensity normalised by time average of HUVECs exposed to a shear stress gradient of 2 - 16 dyne/cm^2. B: Mean of the 5 cluster groups. Points indicate the group peak. Total mean is indicated in red. C: The change in population percentage of each cluster group at different shear stress positions fitted to a linear regression. P-value is calculated with an anova.

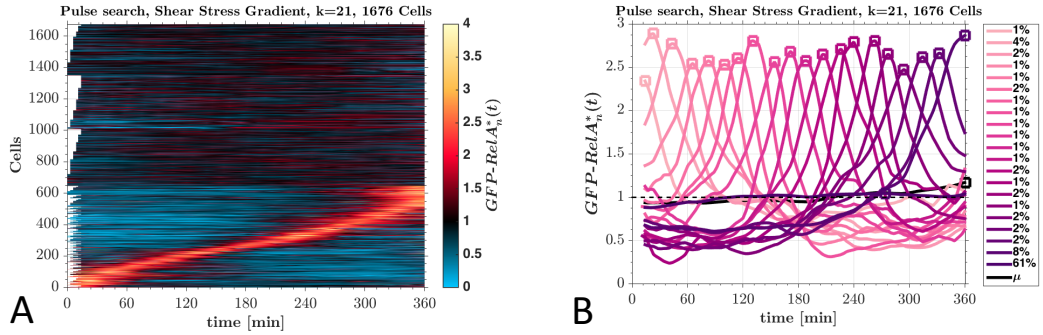

Figure 145: Pulse search(k=21) applied to nuclear GFP-RelA intensity of HUVECs exposed to a shear stress gradient. A: Projected map of the signals sorted with pulse search B: The mean of the pulse search groups.

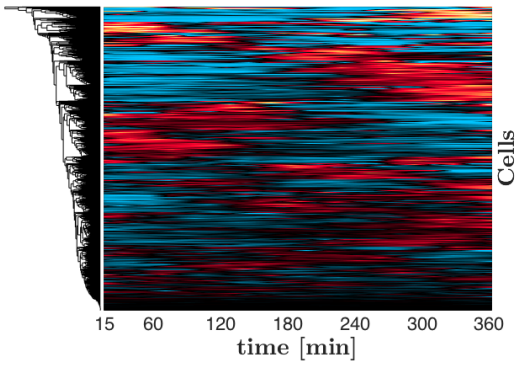

Figure 146: Hierarchical clustering of nuclear GFP-RelA intensity normalised by time average of HUVECs exposed to a shear stress gradient of 2-16 dyne/cm^2.

4.3.3.2. Clustering attempts with normalisation by earliest common time point – Secondary analysis

In Figure 147, the single cell analysis for the gradient channel is shown when normalising each cell by the earliest common time point. In Figure 147.A, the normalised nuclear GFP-RelA intensity of all cells are plotted. An example for 100 cells is shown in Figure 147.D. Figure 147.G shows the mean and standard deviation of all cells when normalised by the earliest common time point.

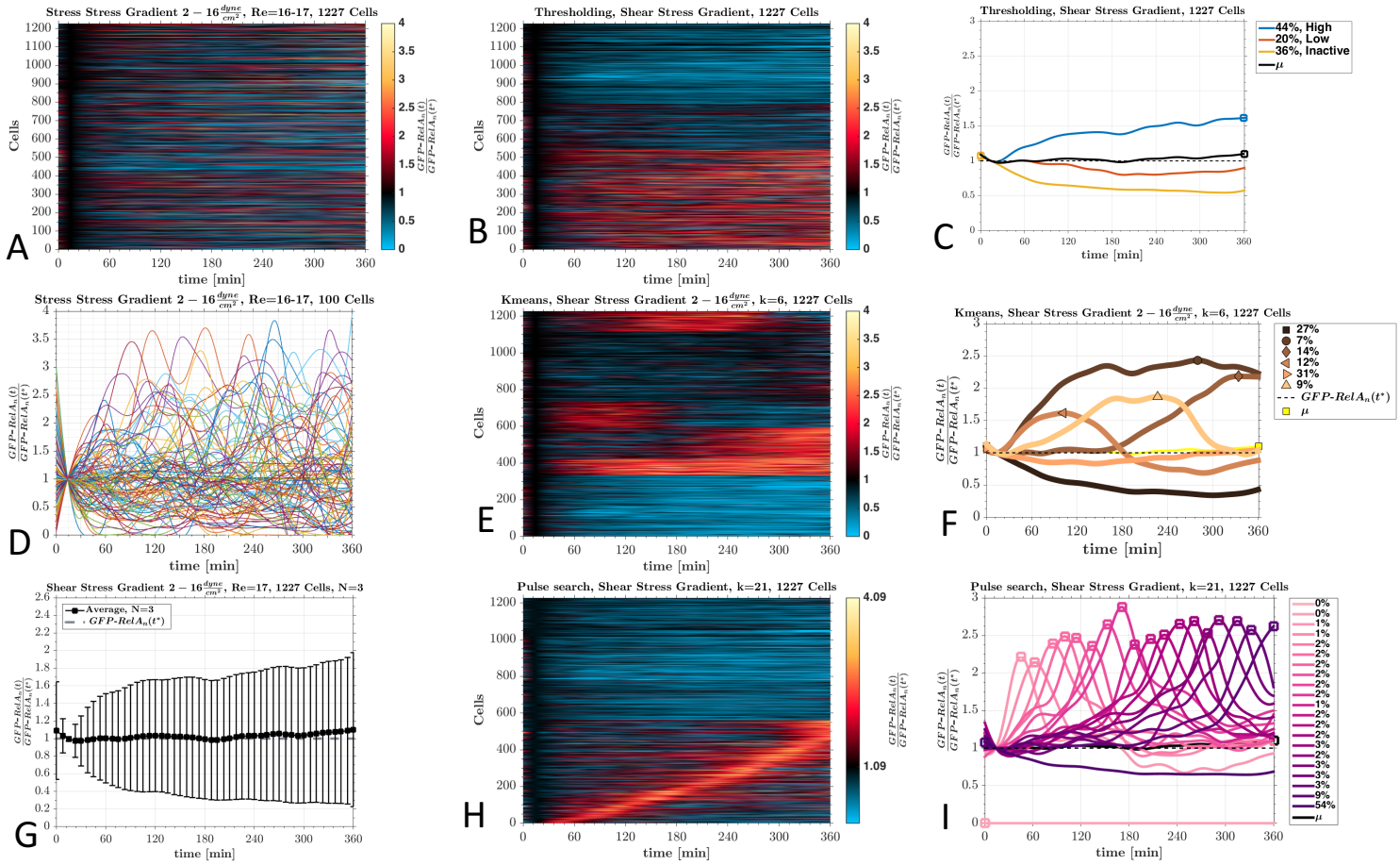

Figure 147: A: Single cell analysis of nuclear GFP-RelA intensity normalised by the earliest common time point (t*=15min) of HUVECs exposed to a shear stress gradient of 2 to 16 dyne/cm^2. A: The nuclear GFP-RelA intensity of all cells recorded. D: Examples of the nuclear GFP-RelA intensity for 100 cells. B: Cells were clustered using thresholding. C: The mean of the thresholding groups. E: Cells clustered using Kmeans. F: The mean of the kmeans clustering groups. G: Mean and standard deviation of the intensity normalised by earliest common time point. H: Cells clustered using pulse search. I: The mean of each pulse group. The squares in the mean plots indicate the peaks, and in the legend the percentage of the cell population per group is given.

In Figure 147.B and C, with thresholding, it was found that a shear stress gradient from 2 to 16 dyne/cm^2 caused high nuclear translocation of GFP-RelA in ca. 45 % of the cells. This is ca. 15 % higher than under static conditions. With Kmeans (Figure 147.E and F), three distinctive peak groups could be identified: An early peak group (90 minutes), and mid peak group (180 minutes) and a late peak group (360 minutes). Morover, another group had a constant high nuclear GFP-RelA intensity.

Using the pulse search (Figure 147.H and I), again a constant activation of a small fragment of cells was found to occur during flow. Moreover, it was identified that 45 % experience a high activation. This observation agrees with the percentage of active cells found with thresholding and Kmeans.

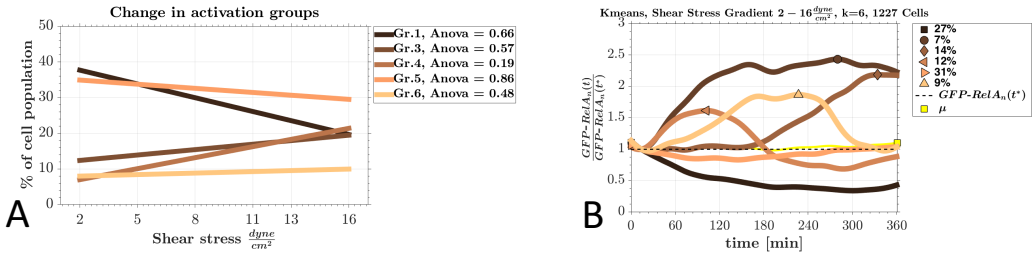

Figure 148: The change in percentage (A) of identified peak groups per shear stress (B).

The change in percentage of the identified groups (groups identified with Kmeans) per shear stress is shown in Figure 148. The early activation group (Gr.4) increased with more than 10 % from low to high shear stress (2 to 16 dyne/cm^2). The mid activation group (Gr.6) did not show much change with increasing shear stress. The late activation group (Gr. 3) showed an increase with less than 10 % with an increasing shear stress. The cells, which are understood to be inactive (Gr.1), appeared to decrease in percentage (20 %) with an increasing shear stress.

In Figure 148, a shear dependency of three distinctive activation groups was found to occur earlier with normalised by time average.

In Figure 149, the means of normalised (by earliest time point) nuclear GFP-RelA intensity at all shear stress magnitudes was interpolated and plotted. This provide a similar plot as shoen in Figure 140, when normalised by the time average. On comparison, small differences can be observed. A stronger early activation at high shear stress is observed when normalisation is carried out by earliest common time point.

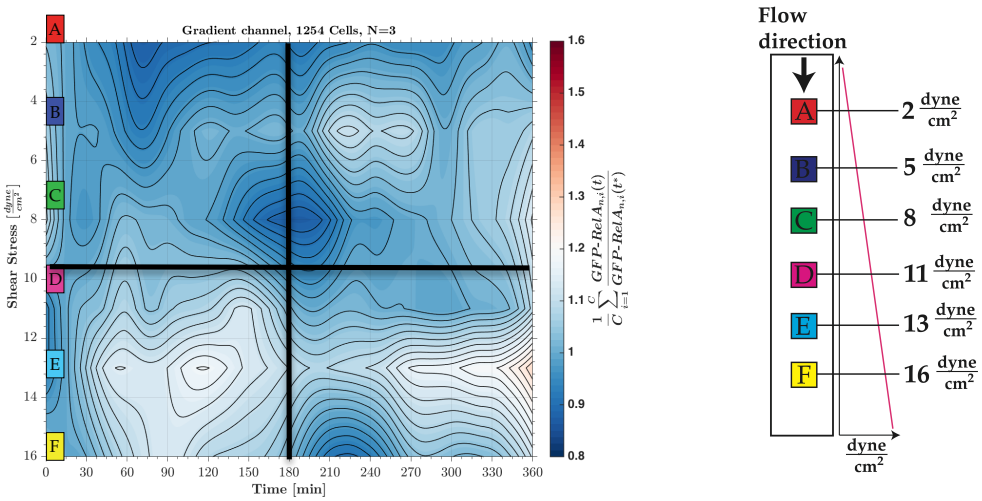

Figure 149: The mean of the normalised by the earliest time point (t*=15min) nuclear GFP-RelA intensity over time for each measured shear stress (2, 5, 8, 11, 13 and 16 dyne/cm^2) were linear interpolated and plotted as a contour map. Each measured shear stress is indicated with a letter and colour that corresponds to the annotation in the schematic diagram on the right. The mean nuclear GFP-RelA intensity is the Z-axis and the colour bar indicates its values.

When normalising by the earliest time point, the change of the nuclear GFP-RelA intensity to a certain time point is considered. To filter out heavy responding cells (predominantly dying or splitting cells), all cells that changed their initial states more than four times were removed. This allowed for analysis of cells with similar expression levels and similar changes in time. Using the refined data, four distinct regions were still observed as indicated in Figure 149. Carrying out normalisation using earliest time point produced a similar plot (differences in intensity) to that found in Figure 140, when normalising by time average. However, normalisation to

an initial time point meant information was lost around this time point. Therefore, normalisation by time average was used as it produced more information for all of the time signals.

4.3.4. Cell movement vs. nuclear GFP-RelA intensity

The nuclei of each cell was tracked over time which is interpreted as the movement/motility of cells during the given experimental conditions. The movements of cells exposed to a shear stress gradient in all three experiments are depicted in Figure 150. The location and shear stress magnitude are colour coded. Accordingly, A, B, C, D, E, and F correspond to 2, 5, 8, 11, 13 and 16 dyne/cm^2. Cells under a shear stress of 2 and 5 dyne/cm^2 moved predominantly in the direction of flow with an average velocity of 0.4 nm/s and 0.6nm/s.

Cells under 8 dyne/cm^2 did not move significantly with the direction of flow, but rather moved predominantly perpendicular to the flow with an average velocity of 0.45nm/s.

Cells under 11, 13 and 16 dyne/cm^2 moved predominantly against the flow direction with a high average velocities of 0.65 nm/s, 0.58 nms and 1.1 nm/s.

In Figure 151, the average movement of cells per recorded position (each position corresponds to a shear stress magnitude) parallel (Figure 151.A) and perpendicular (Figure 151.B) to flow direction are shown. The cells moved in the direction of flow at 2 and 5 dyne/cm^2. At 8 dyne/cm^2, cells only moved marginally (max. 2.5 µm) in the direction of flow. Cells at 11, 13 and dyne/cm^2 moved against the flow. With an increasing shear stress magnitude cells travelled larger average distances against the flow. For example, cells at 11 dyne/cm^2 displaced around 5 µm, cells at 13 dyne/cm^2

moved 12 µm, while at 16 dyne/cm^2 cells moved 20µm against the direction of flow. Consequently, in contrast to low and high shear stress, cells under a shear stress gradient moved with and against the flow direction. This implies that not the monolayer moves but cells move appropriately in response to different shear stress magnitudes.

The directionality ratio under a shear stress gradient was 2.16, which is lower than under low shear stress and static conditions (statistically significant) but higher than under high shear stress. This indicates increased persistence of mobility in a shear stress gradient, but less strong as under uniform high shear stress.

At all shear stress magnitudes, cells moved slightly perpendicular to the direction of flow with a maximum average perpendicular displacement of 7 µm.

In Figure 152, the nuclear GFP-RelA intensity at the cells location, over time, is depicted for all recorded shear stress magnitudes within the gradient channel. The Z-axis corresponds to the nuclear GFP-RelA intensity, while the X and Y-axes are the location coordinates. In channels 1 and 3 more cells could be tracked at lower shear regions. Cells were found to grow better at lower shear regions. Moreover, these positions within the channel had greater height (Better growth environment as more growth medium available). Hence, more variation is observed at low compared to high shear stress positions.

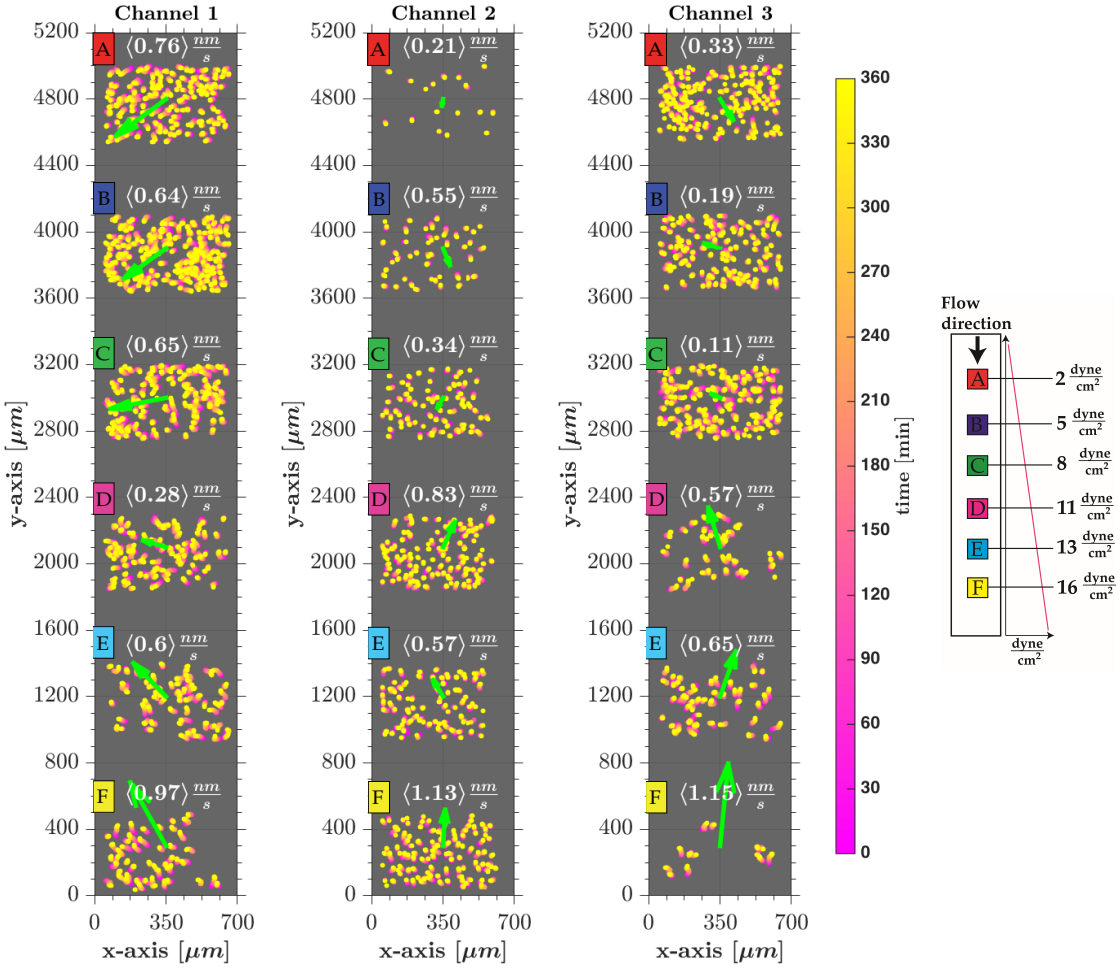

Figure 150: Movement of cells under a shear stress gradient of 2-16 dyne/cm^2. Channels 1-3 have 6 positions (A-F) that correspond to the shear stress magnitudes indicated in the schematic diagram on the right. Each nuclei's temporal location is depicted in pink at 0 minutes and yellow at 360 minutes. The mean cell movement per position is indicated with a green arrow and the value is noted above each position. The flow direction with the corresponding velocities is indicated on the left.

In Figure 153, the probability distribution of the cells displacement *vs.* nuclear GFP-RelA intensity is shown for HUVECs exposed to a shear stress gradient of 2 to 16 dyne/cm^2. The distribution is shown for all shear stress magnitudes recorded. At 2 dyne/cm^2, cells displaced the shortest distance (0-20 μm), but experienced the largest distribution in intensity. As displacement increased with an increasing shear stress, the intensity distribution was more widely spread and less concentrated. At

16 dyne/cm^2, the spread ranged from 0 to 60 µm leading to a more uniform distribution of nuclear GFP-RelA intensity.

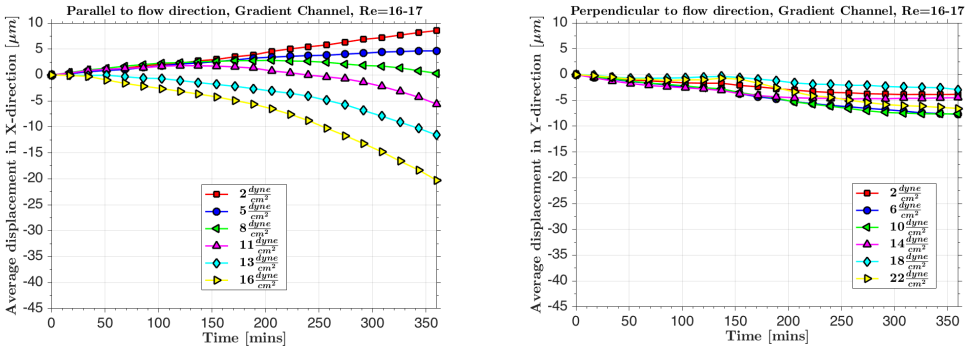

Figure 151: The mean cell movement per shear stress position parallel (A) and perpendicular (B) to the flow direction.

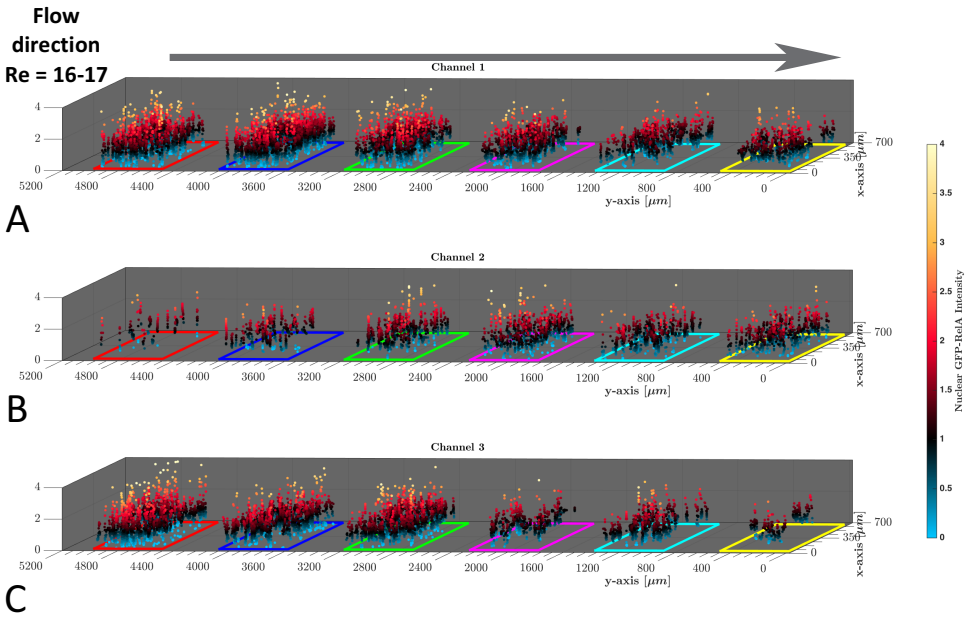

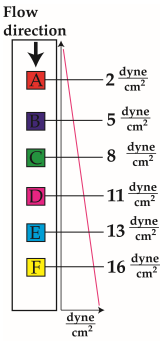

Figure 152: A-C: The nuclear GFP-RelA intensity normalised by time average (z-axis) at the cells location over time for all 5 repeats. The flow direction is from left to right. Location of positions is colour coded with the schematic diagram of the gradient channel (D). Each colour corresponds to a shear stress magnitude within the channel.

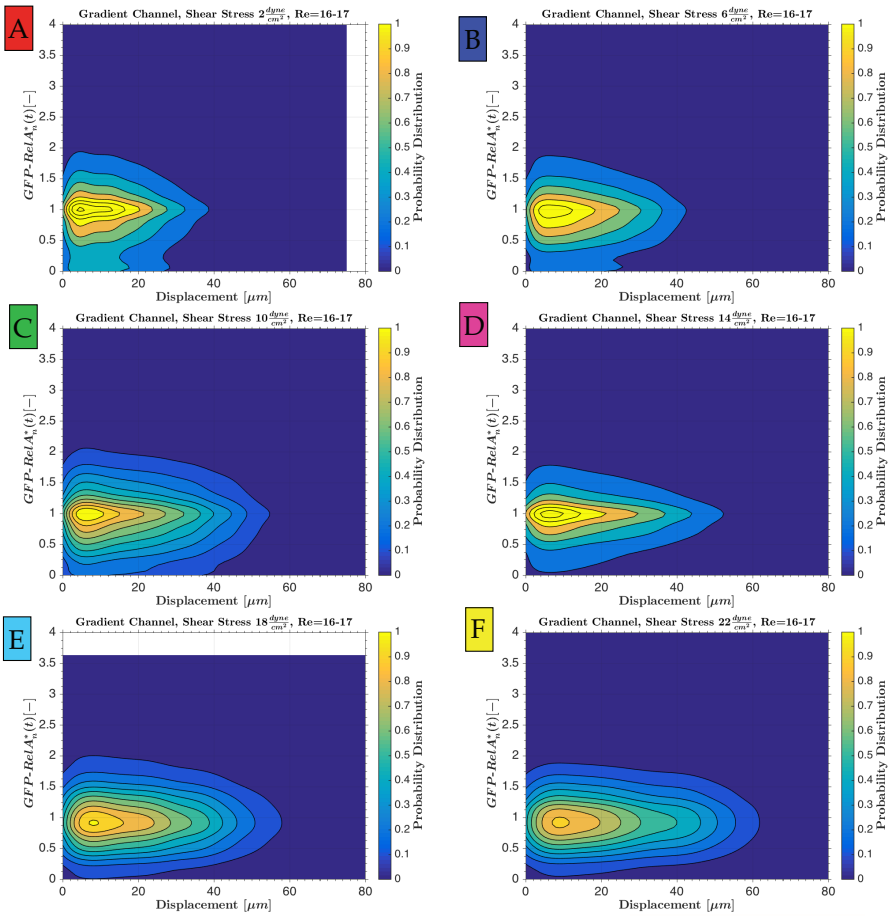

Figure 153: The probability distribution of the cells displacement versus nuclear GFP-RelA intensity normalised by time average for cells exposed to a shear stress gradient of 2 to 16 dyne/cm^2.

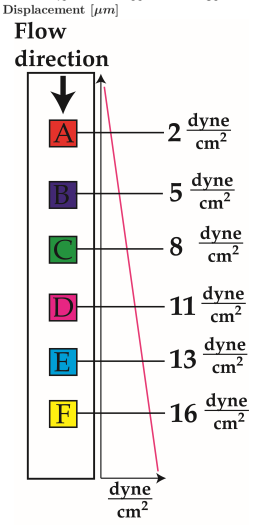

5. Flow Characteristics of the Gradient Channel and Backward Facing Step Channel

Summary: *This chapter presents the flow characteristics of the gradient channel (3D simulation) and a backward facing step channel (2D simulation). First, the numerical methods applied are described for both cases. Then the acquired results are shown. In the results section, grid independence was sought for the gradient channel and the backward facing step channel. For the gradient channel 5 million elements were necessary for grid independence. The outflow pillar was demonstrated to be the most sensitive area. Grid independence of the backward facing step channel was achieved with a relatively coarser mesh (250 000). To validate the step channel, the reattachment zone of the simulation was compared to experimental measurements.*
As expected, the flow velocity profile along the gradient channel portrayed an increasing velocity within the gradient channel. The shear stress at the bottom wall increased gradually after the straight flow development section from 2 to ca. 18 dyne/cm^2 *The y-axis cross-section at the live-cell imaging cross-sections is show. These proved that the shear stress was fully developed 1cm away from the side-walls. Streamlines demonstrate a stable flow throughout the gradient channel. However, the transition from gradient channel to outflow pillar created a jet and a swirling flow. The swirling flow is an indication of high kinetic energies. The straight outflow section prior to transition into the outflow pillar did not allow the swirl flow to affect the linear increasing shear stress.*
The shear stress profile at the bottom wall after the step can be categorised into four zones: Stagnation, recirculation, flow reattachment and developed flow zone. The shear stress profile (0-16 dyne/cm^2*) at Reynolds number 200 was found to be most appropriate for the shear induced NF-κB model.*

5.1. Numerical methods

5.1.1. Gradient channel - Geometry and meshing

The geometry and dimensions of the gradient channel fluid domain are shown in Figure 154. The mesh (non-conforming, Cartesian, with several levels of subdivisions) was created with VisCart (*ESI Group, Paris, France)*. A cross-section of the mesh

domain is shown in Figure 154.D and a magnified view of the beginning of the narrowing cross section in Figure 154.E.

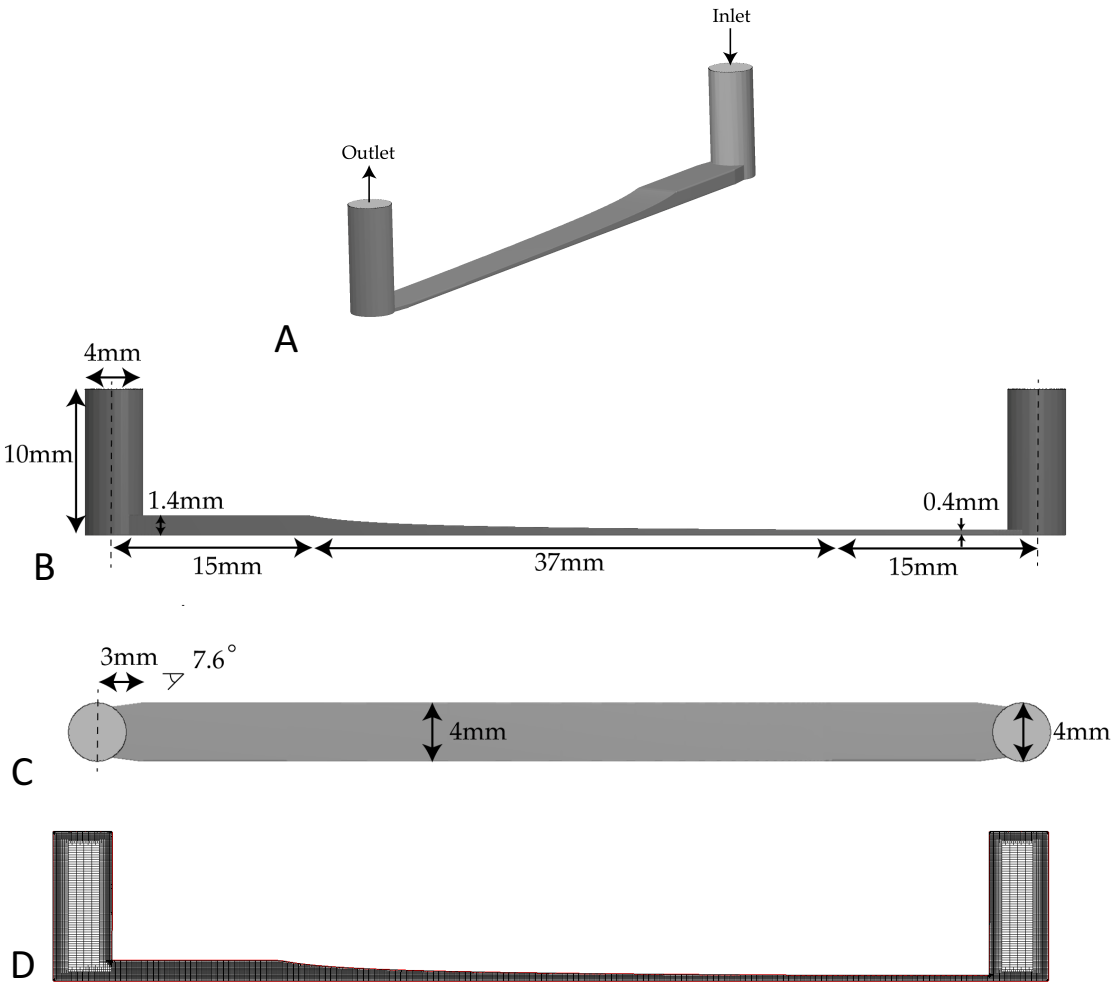

Figure 154: The geometry (A) and dimensions (B and C) of the gradient channel fluid domain. A cross-section of the mesh domain (D). A magnified view of the mesh at beginning of the narrowing cross-section (E).

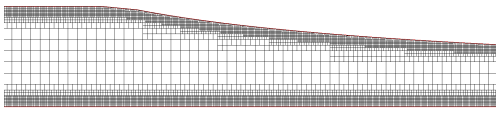

5.1.2. Backward facing step channel – Geometry and meshing

The geometry of the backward facing step channel is depicted in Figure 155 and the mesh of the corner of the sudden expansion is shown in Figure 155.B.

The mesh was made very dense at the sharp corner of the expansion to capture the rapid inertia redistribution patterns created by a sudden expansion.

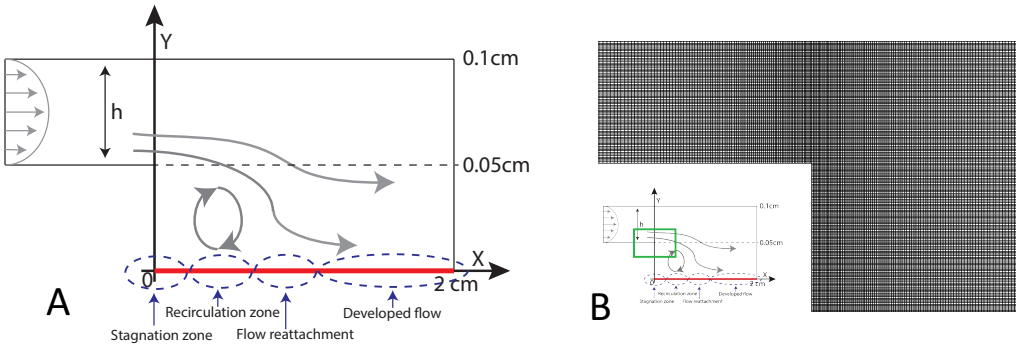

Figure 155: A: The backward facing step channel geometry with dimensions and characteristic flow areas at the bottom wall. B: The mesh at the corner of the sudden expansion. The corner is indicated in the geometry with a green square.

5.1.3. Governing equations, solver and boundary conditions

The fluid flow was governed by the mass conservation (or continuity) equation

$$\frac{\partial \rho}{\partial t} + \nabla \cdot (\rho \vec{u}) = 0 \qquad (36)$$

and the Navier-Stokes equation (conservation of momentum)

$$\rho \left(\frac{\partial \vec{u}}{\partial t} + (\vec{u} \cdot \nabla)\vec{u} \right) = -\nabla \vec{\mathrm{p}} + \mu \nabla^2 \vec{u} \qquad (37)$$

where ρ is the density, $\vec{u}$ the velocity vector (3 dimensional) and $\vec{\mathrm{p}}$ the pressure vector. The commercial software CFD-ACE+ from the ESI Group (*ESI, Paris, France*) was used to solve the governing equations. CFD-ACE+ is based on the finite volume method.

The finite volume method integrates the governing equation over a control volume (The entire flow domain is split into several control volumes as shown in Figure 154.D). A central difference scheme (2nd order accuracy) was applied for spatial discretisation. In addition, CFD-ACE+ uses a blending for the spatial discretisation. Blending includes a certain percentage of upwind discretisation to the central

difference to enhance stability. In this work, the blending was set to a very low value, 0.1 (10% upwind and 90% central difference). This level of blending reduces numerical instabilities without compromising accuracy [160]. The linear equation system of the velocity field was solved with a conjugate gradient squared method (CGS) solver using 50 sweeps and a convergence criterion of 0.0001 [160]. The equation system of the pressure were solved with the algebraic multigrid method (AMG) solver with 50 sweeps and a criterion of 0.1 [160]. Sweeps are the number of solving iterations of the linear equation system and the criterion threshold defines the convergence criteria of the CGS and AMG solver [160]. As no governing equation is giving for pressure [160, 161], CFD-ACE+ uses the Semi-Implicit Method for Pressure-Linked Equations – Consistent (SIMPLEC) scheme to formulate an equation for pressure and to couple it with the velocity (The momentum equations (36) and (37) were solved for the velocity components). The maximum system iterations were set to 2000 and the minimum residual to 10^-18.

The boundary conditions for the gradient channel were: Inlet velocity u = 0.0199 m/s, outlet pressure p = 0 N/m^2 and all remaining walls were non-slip walls. The physical properties of the fluid were set for DMEM +10%FBS at 37 ˚C with μ = 0.000786 Pas and ρ = 1001.13 kg/m^3 [162].

The boundary conditions for the step channel were: Inlet velocity u = 0.4 m/s, outlet pressure p = 0 N/m^2 and all remaining walls were non-slip walls. The physical properties of the fluid were set to μ = 0.001 Pas and ρ = 1000 kg/m^3. For the step channel, it was assumed that water was at room temperature to be able to compare and validate the CFD results with experimental measurements as shown later in the results section.

5.2. Results: Flow characteristics of the Gradient Channel and Backward Facing Step channel

5.2.1. Grid independence

Grid independence was sought for the gradient channel and the step channel. Grid independence is mandatory to prove that the solution is independent of the resolution of a mesh. With this, one can be sure that the numerical flow simulation approximates the flow physics.

5.2.1.1. Gradient Channel

Grid independence results for the gradient channel are shown in Figure 156. The velocity profile at four important cross-sections, specifically: Inlet, converging cross-section, narrow channel outflow and outflow pillar (identified with A, B, C, and D) are plotted for 3 different grids.

The three different grids possessed 800k, 5 million and 22 million mesh elements. Regions of higher inertia and steep changes such as the primary bend from inlet to narrow channel and the outflow from the narrow channel to the outflow pillar were meshed densely. Regions with less inertia and smoother changes were meshed with a lower density of elements. In Figure 156, the velocity profile at point A and B were considered grid independent for all grids in this study. At cross-section C and D, grid independence was achieved with 5 million elements (Relative error between 22M and 5M was < 5%).

The narrow outflow in to the pillar created a jet like outflow with higher inertia forces than at other regions within the channel. However, the main interest was the flow section in the narrowing channel, for which grid independence was achieved for

all grids considered. It was concluded that 5 million mesh elements were sufficient to achieve a grid independent flow simulation.

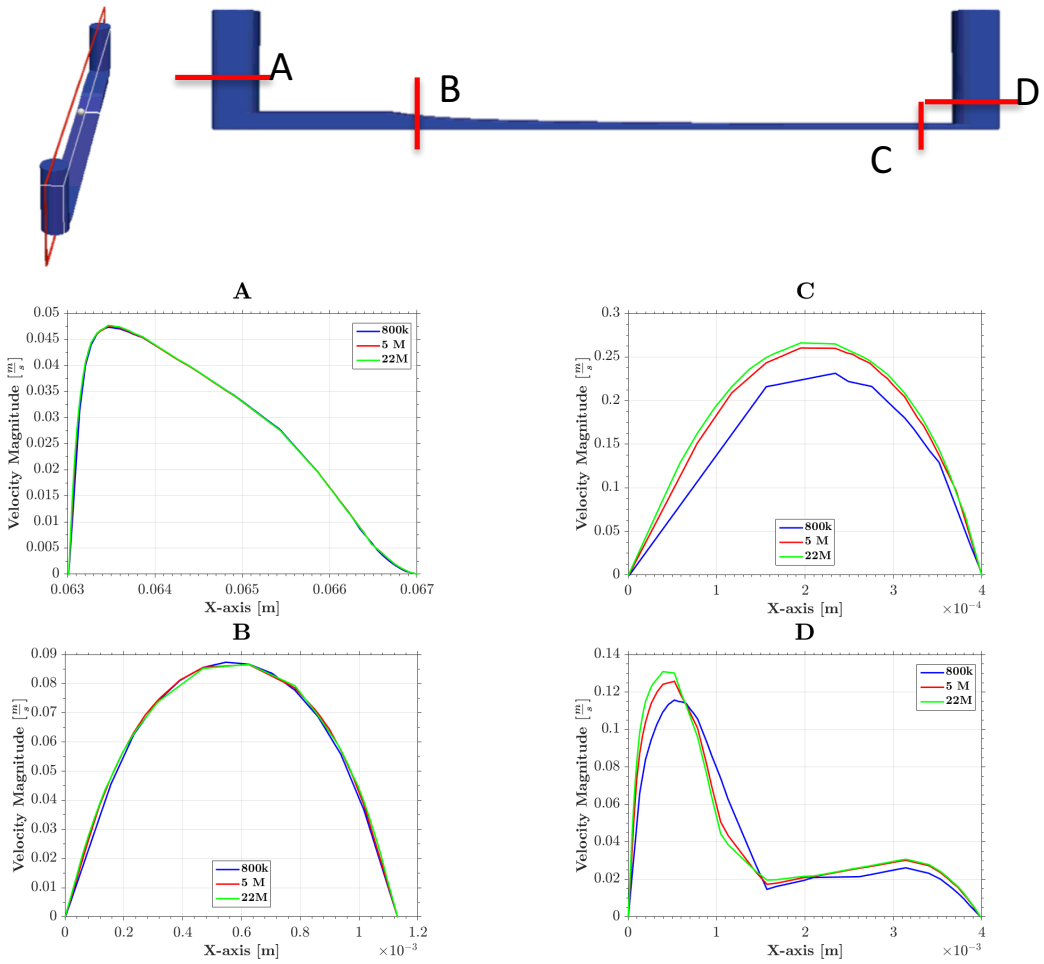

Figure 156: Grid independence study of the gradient channel at 4 different locations: Inlet (A), convergent channel (B), narrowest cross-section outflow (C), and outflow (D).

5.2.1.2. Backward facing step channel

For the backward facing step channel (2D simulation), a grid independent analysis with four grids: 50k, 100k, 250k and 1 million mesh elements, was performed. Grid independence was achieved with a relatively coarse grid of 250k elements.

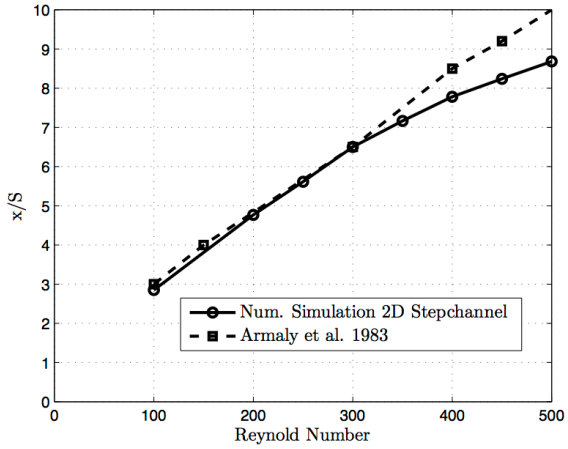

Figure 157: Comparison of reattachment point of the numerical simulation with measurements by Armaly et al. [163]

The simulation results with 250k elements (Figure 157) could be validated against experimental findings from Armaly *et al.* [163] by comparing the comparing the reattachment point (*x* = location with zero velocity, *S* = height of the step). Good agreement of the reattachment point for Reynold numbers between 100-300 was found. Above a Reynolds number 300, the resolution was poor, and additional flow instabilities start to occur which would necessitate transient simulations and/or 3D flow simulations [164] being conducted. In this work, it was proposed that a backward facing step channel with a low Reynolds numbers such as 100-300 would be investigated.

5.2.2. Velocity profile

The velocity profile of the gradient channel of a cross-section along the whole channel is shown in Figure 158. The flow direction is from left to right. The flow develops in the 10cm long straight section before entering the convergent channel. The convergence of the channel height increased the velocity, which peaked at the end of the gradient channel before entering the outflow pillar. The transition from narrow gradient channel to the outflow pillar gave rise to a jet.

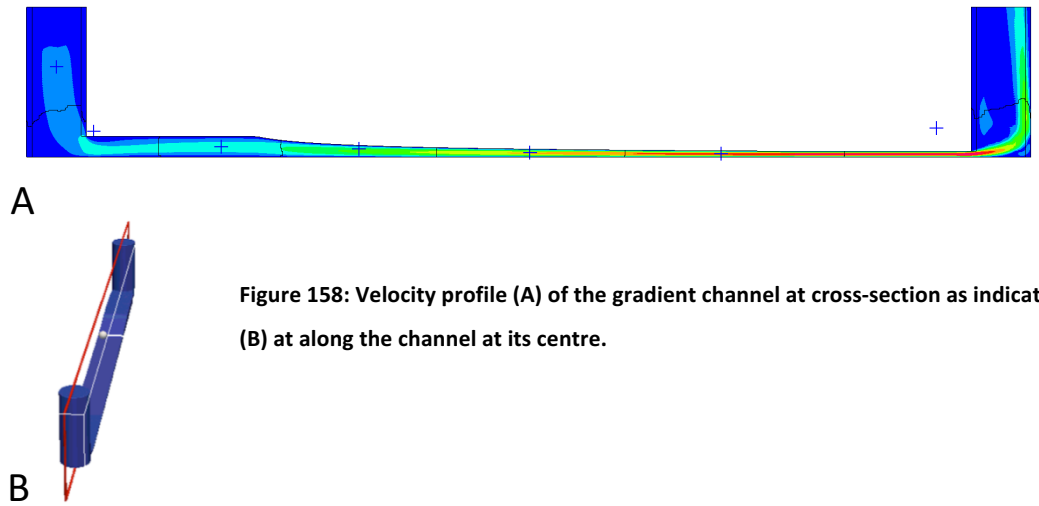

Figure 158: Velocity profile (A) of the gradient channel at cross-section as indicated (B) at along the channel at its centre.

5.2.3. Shear stress profile

In Figure 159, the shear stress profile of the cross-section along the bottom wall of the gradient channel is shown. It shows a gradually increasing shear stress from 15mm until 52mm.

Coloured squares indicate the positions at which the live-cell imaging was recorded. The live-cell imaging was recorded at a shear stress of 2, 5, 8, 11, 13 and 16 dyne/cm^2. The shear stress profiles of the recording position (red, blue, green, purple, cyan and yellow) of the cross-section in the Y-direction are shown. These show the increase in shear stress magnitude, and that at 1 cm away from both the

side-walls (1 and 2.7cm) the shear stress profiles were uniform. Consequently, the recording positions were positioned in the middle of the Y-cross section to ensure a uniform shear stress profile.

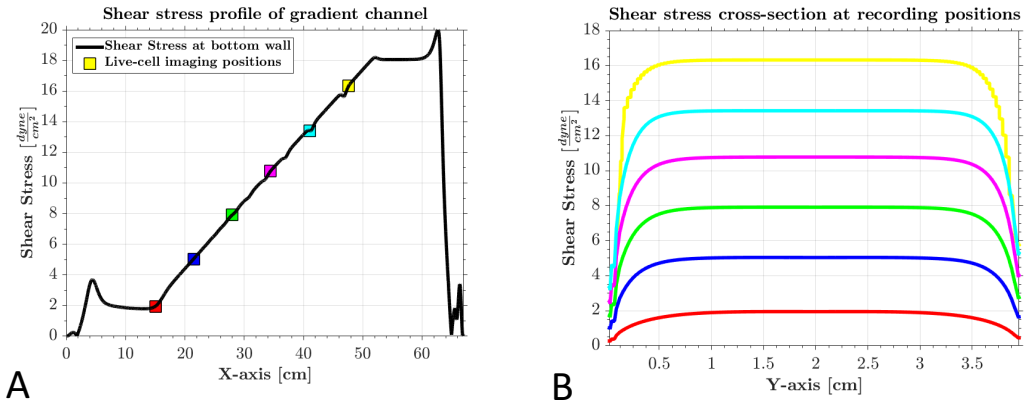

Figure 159: Shear stress profile (A) along the channel at the bottom wall (*z=0cm*) at the middle of the channel (x=2cm). The positions for live-cell imaging are indicated with color-coded square symbols. The shear stress profile along the Y-axis (B) at the bottom wall (z=0cm) for the live-cell imaging positions. Shear stress profiles are colour-coded with the position indicated in A.

5.2.4. Streamlines within the gradient channel

Different views of the streamlines within the gradient channel are shown in Figure 160. Figure 160.A shows the streamlines along the whole channel. The flow enters the gradient channel from the first pillar without major disturbances. Only a small recirculation zone existed at the far bottom left of the pillar (Figure 160.B and Figure 160.C).

The convergence of the channel cross-section increased the flow velocity without causing major variability; streamlines did not show any secondary vortices. The transition from the narrow cross-section to the out-flow pillar caused a jet that created a swirling motion. The jet and swirling motion are shown presented in Figure 160.D and Figure 160.E. The swirl ranges from the bottom to the top of the pillar. However, due to the long (10cm) straight section following the convergent section,

the swirl does not affect the flow in the gradient channel where the measurement of the cells was performed. Hence, the swirl can be regarded as negligible. It is important to guarantee little disturbance within the gradient channel to ensure that cells are only affected by a linear shear stress gradient. Large flow disturbances at the in- and outflow can propagate or penetrate through the channel and may affect the behaviour of the cells and change the conditions they are exposed to.

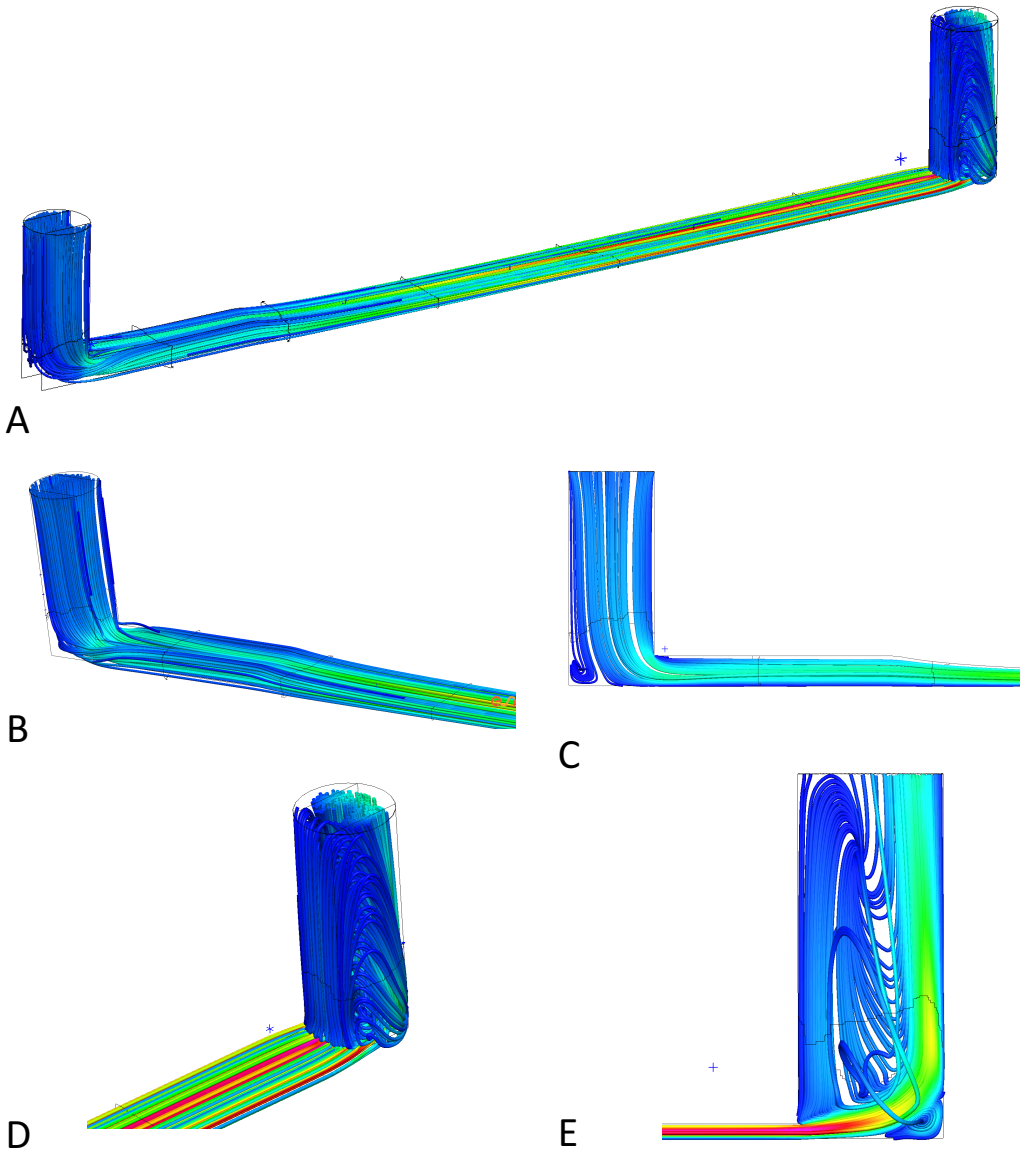

Figure 160: Streamlines of the gradient channel (A), entrance (B and C) and the outlet (D and E).

5.2.5. Backward facing step channel

In Figure 161, shear stress profiles at the bottom wall of the backward-facing step channel at different Reynolds numbers (50 – 250) are shown. The bottom wall of the step channel can be divided into four different regions: Stagnation zone, recirculation zone, flow reattachment and developed flow zone.

With an increasing Reynolds number, the shear stress increased at all zones. Moreover, the increases were largest at the recirculation zone. In this work, the shear profile of interest was found to be at a Reynolds number of 200. At this Re, a shear stress range of 0 to 16 dyne/cm^2 was observed. This range is suitable for the shear induced NF-κB simulation. Measurements were experimentally obtained of the nuclear NF-kB intensity of cells exposed to a similar shear stress range (2-16 dyne/cm^2) in a shear stress gradient channel.

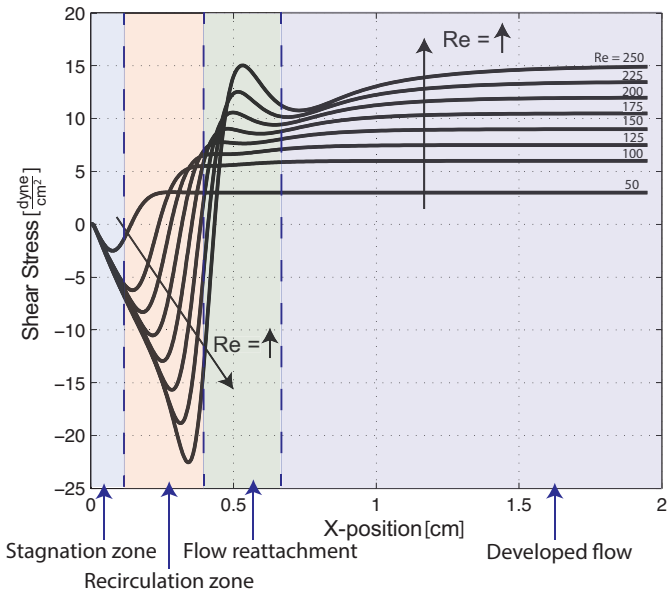

Figure 161: Shear stress profiles of the backward-facing step channel at different Reynolds numbers

6. Modelling the NF-κB Pathway of a Cell Population

Summary: *This chapter presents the modelling effort to predict nuclear NF-κB concentration in a cell population when stimulated with TNF-α or flow. In the first section, the numerical methods of the cell population model are presented. The fundamentals of biochemical reaction kinetics are discussed. Subsequently, the cell population model of the NF-κB pathway triggered by TNF-α is described in detail. Then, the numerical methods used for the ODE system and the protocols for cell population simulations are presented. In the second section, the results of the cell population stimulated with different TNF-α concentrations are shown. In the third section, the modelling addition to simulate shear stress induced NF-κB is shown and relevant results are demonstrated.*

6.1. Numerical methods

6.1.1. Biochemical Reaction kinetics

A chemical reaction transforms a set of substances (reactants) into another set (products). In general, this transformation is reversible and can be distinguished between forward and reverse reactions. The reaction occurs at discrete and fixed ratios, which indicate how much of each substance is needed for the reaction to occur [165]. A general reaction is given as

$$aB + bB \longrightarrow pP \qquad (38)$$

where A and B are reactants and P the product. The stoichiometry coefficients *a, b* and *p* indicate the molar amounts of each substance.

Chemical kinetics defines the rate of a reaction via consumption and production. The reaction rates of the above chemical reaction can be written as,

$$v = \frac{1}{-a}\frac{dA}{dt} = \frac{1}{-b}\frac{dB}{dt} = \frac{1}{p}\frac{dP}{dt} \qquad (39)$$

Using Eq. (35), the change of each substance can be calculated in relation to the reaction rate and the stoichiometric coefficient.

$$\frac{dA}{dt} = -a \cdot \upsilon \qquad (40)$$

$$\frac{dB}{dt} = -b \cdot \upsilon \qquad (41)$$

$$\frac{dP}{dt} = p \cdot \upsilon \qquad (42)$$

Chemical reactions occur if the participants collide or come very close – this depends on the environment and density of the participants. The "Law of Mass-Action" defined by Guldberg and Waage [165] states "that the rate of unidirectional chemical reactions are proportional to the product of the concentration of the reactants to the power of constant exponents." For example, the assumed mass-action kinetics of Eq. (38) can be described as

$$\upsilon = k \cdot A^{n_A} \cdot B^{n_B} \qquad (43)$$

Where k is the proportional rate constant and $n = n_A + n_B$ is the order of the reaction. Generally, the order of reaction is equal to number of molecules involved in the reaction. Mass-action kinetics is an approach for large and vaguely defined reaction networks as in mechanotransduction. Zero, first and second order reactions are listed below as examples:

Zero order reaction (not dependent on any reactant):

$$X \overset{k}{\rightharpoonup} P \qquad (44)$$

$$\upsilon = k \cdot X^0 = k \qquad (45)$$

$$\frac{dX}{dt} = -\upsilon = -k \qquad (46)$$

$$\frac{dP}{dt} = +v = +k \tag{47}$$

First order reaction:

$$A \overset{k}{\rightharpoonup} P \tag{48}$$

$$v = k \cdot A^1 = k \cdot A \tag{49}$$

$$\frac{dA}{dt} = -v = -k \cdot A \tag{50}$$

$$\frac{dP}{dt} = v = k \cdot A \tag{51}$$

Second order reaction:

$$A + B \overset{k}{\rightharpoonup} P \tag{52}$$

$$v = k \cdot A \cdot B \tag{53}$$

$$\frac{dA}{dt} = -v = -k \cdot A \cdot B \tag{54}$$

$$\frac{dP}{dt} = v = k \cdot A \cdot B \tag{55}$$

A multi-reaction system, for example, a reversible process as

$$A \underset{k_2}{\overset{k_1}{\rightleftharpoons}} P \tag{56}$$

is subsequently described with the following system of ordinary differential equation (ODE):

$$\frac{dA}{dt} = -v_1 + v_2 = -k_1 \cdot A + k_2 \cdot P \tag{57}$$

$$\frac{dP}{dt} = v_1 - v_2 = k_1 \cdot A - k_2 \cdot P \tag{58}$$

Describing multiple reactions in the form ODE systems can be extended without limits. Each substance will contain one differential equation, which includes the relevant components of the different reactions in the system. The differential equation of a substance in a system with *r* reactions is given as:

$$\frac{dS_n}{dt} = \sum_{i=1}^{r} \lambda_i \nu_i \qquad (59)$$

λ_i is the stoichiometric coefficient of S_n in reaction i, and ν_i the corresponding reaction rate.

The first approach to describe enzymatic reactions was presented by Michaelis and Menten [166]. The authors proposed the establishment of a rapid equilibrium between enzyme and substrate. A simple enzyme reaction of substrate S and enzyme *E* to a product *P* can be described as follows:

$$S + E \underset{k_{-1}}{\overset{k_1}{\rightleftarrows}} ES \xrightarrow{k_2} E + P \qquad (60)$$

where k_1 and k_{-1} are reaction constants, k_2 is the catalytic constant. For example, the time dependency of [ES] expressed in equation form is given as

$$\frac{dES}{dt} = k_1 \cdot E \cdot S - k_{-1} \cdot ES - k_2 \cdot ES \qquad (61)$$

At steady state $\frac{dES}{dt} = 0$, the concentration of the intermediate ES complex is constant. The equation can be rearranged to give

$$K_M = \frac{k_{-1} + k_2}{k_1} \qquad (62)$$

$$E = ES \cdot \frac{K_M}{S} \qquad (63)$$

Where the concentration of the enzyme is constant

$$E = E_t - ES. \qquad (64)$$

Therefore, the mass kinetics of the product *P* from the enzyme reaction are given as

$$v = \frac{dP}{dt} = k_2 \cdot ES = k_2 \cdot E_t \frac{S}{K_M + S} \quad (65)$$

$k_2 \cdot E_t = v_{max}$ is often described as the maximal velocity, which is mostly used in modelling biochemical processes in which the exact mechanism are unknown [165]. However, this is only applicable if the enzyme concentration is contant (requires substrate in large excess), which is rarely the case in signal transduction [165]. If the substrate concentration equals K_M, the reaction velocity is equal to half its maximal velocity.

6.1.2. Cell population model of the NF-κB pathway

The overarching goal of the modelling effort undertaken in this dissertation was to simulate the NF-κB pathway of an entire cell population in response to a stimulus. The cell population model is schematically shown in Figure 162.

Due to the naturally occurring heterogeneity in a cell population [85], differences in cell shape, surface receptors, cell orientation and cell life cycles may be present. We have developed a methodology based on a Monte Carlo technique that addresses heterogeneity and thus captures each individual cell response. For the heterogeneity, only extrinsic noise that influences each cell's individual activation and reaction rates of certain biochemical processes was considered [167] [168].

We hypothesised that all cells have the same amount of surface receptors, *M*. A stimulus activates the surface receptors. However, the number of activated receptors is defined by the intensity of the stimulus. This variation of activated receptors per cell of a population is represented by a Gaussian normal distribution. The use of a Gaussian normal distribution is aimed at representing cell

heterogeneity. Heterogeneity is defined herein solely by the number of activated surface receptors, which is per se a simplification of the total external noise such as cell size, state of cell and measurable properties.

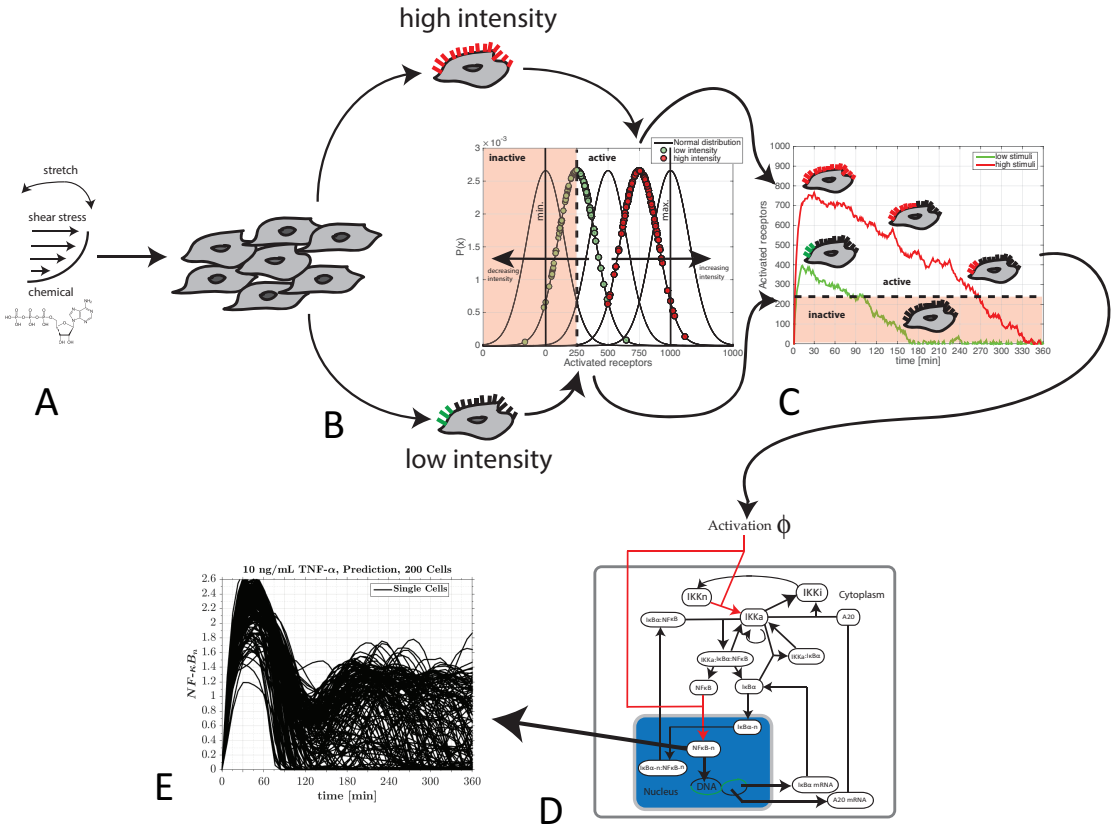

Figure 162: Schematic of the cell population model. A) Cells are stimulated by TNF-α or shear stress. B) The stimulus activates surface receptors of each cell. Due to differences of cells in a population, the number of activated receptors per cell varies. The number of activated receptors is a random number of a Gaussian normal distribution. The intensity of the stimulus defines the mean of the normal distribution. High intensity defines a high mean, while low intensity implies a low mean. Based on a random seed, we select from the stimulus-depended distribution the number of initially activated receptors per cell. C) The number of activated receptors possesses a temporal behaviour with initial delay, random in- or activation, fast and slow decay. A threshold *a* defines if a cell is activated or not. In other words, if a cell has less than *a* receptors activated, it is inactive. If more than *a* receptors are activated, the cell is active and the NF-κB pathway is triggered. D) The NF-κB signalling pathway with reaction rate *φ* which is a function of the activated receptors. E) The nuclear NF-κB concentration of a cell population of 200 cells stimulated with 10 ng/mL TNF-α.

The stimulus intensity defines the mean of such a normal distribution. For example, if cells are exposed to high TNF-α concentration then the mean of the receptor activation Gaussian normal distribution will be high. If the TNF-α concentration is

low, the mean of the normal distribution will be low. Random numbers are then selected from the normal distribution to define the initially activated receptors of each cell. The activated receptors have a temporal behaviour including initial delay, random in- or activation, fast and slow decay (described in detail in 6.1.3.).

In addition, a threshold function was defined, such that a cell only gets activated if more surface receptors are activated than a pre-defined threshold *a*. If less than *a* surface receptors are activated, the cell remains inactive. Active defines that the NF-κB pathway is triggered with the activation rate $\phi(t)$ larger than zero. ($\phi(t)$ is a function of activated surface receptors). Inactive cells imply the pathway is not initiated and the activation rate $\phi(t)$ is equal to zero. The NF-κB pathway was then calculated for each cell with each cells individual activation rate *φ*. An example of the nuclear NF-κB concentration for 200 cells stimulated with 10 ng/mL TNF-α is shown in Figure 162.E.

6.1.3. Receptors activation

The temporal change in activated receptors of each cell *i* was defined as:

$$r_i(t) = tanh\left(\frac{1}{T_{Delay} \cdot w_{Delay}}\right)\left(1 - k_C \cdot tanh\left(\frac{1}{T_{FDecay} \cdot w_{FDecay}}\right)\right)\left(X_i + k_L \cdot w_L - e^{\frac{t}{T_{SDecay}}}\right) \quad (66)$$

The receptor activation equation approximates the binding of free TNF-α molecules to TNFR1 [95, 96].

- Initial delay: $\tanh\left(\frac{1}{T_{Delay} \cdot w_{Delay}}\right)$, with delay time T_{Delay} and a random number $w_{Delay} \in \{0, \dots, 1\}$

- Fast decay: $1 - k_c \cdot \tanh\left(\frac{1}{T_{FDecay} \cdot w_{FDelay}}\right)$, with decay time T_{Fdecay} , k_c is a constant and a random number $w_{Fdecay} \in \{0, \dots, 1\}$. The fast decay was included due to suggestion by Cheong *et al.* [86] that IKK activation has a quick decay after initial stimulation.
- Initially activated receptors: The number X_i is randomly picked for each *i-th* cell from the Gaussian normal distribution $P_i\left(b_i, \mu(t)\right)$ with a mean as a function of stimuli intensity $\mu(t)$. The Gaussian normal distribution and X_i are given a

$$P_i\left(b_i, \mu(t)\right) = \frac{1}{\sigma\sqrt{2\pi}} e^{\frac{-\left(b_i - \mu(t)\right)^2}{2\sigma}} \quad (67)$$

$$b_i = \left\{ b_i \in \Re, -\frac{M}{2} \leq b_i \leq \frac{3M}{2} \right\} \quad (68)$$

$$\mathrm{X_i} = \begin{cases} X_i = 0 & b_i < 0 \\ X_i \in P_i & 0 \leq b_i \leq M \\ X_i = M & b_i > 0 \end{cases} \quad (69)$$

$P_i(b_i, \mu(t))$ is the receptor activation probability, σ the standard deviation, and *M* is the total number of receptors of each cell. b_i is the span of the normal distribution and X_i is the randomly chosen number of activated receptors. Note: If X_i is chosen where b_i is smaller than zero then X_i is zero. If X_i is chosen where b_i is greater M then X_i is equal to *M*.

- Random walk: A random number picked from $w_L \in \{-1,0,1\}$
- Slow decay: $-e^{\frac{t}{T_{SDecay}}}$ is a natural decay function with slow decay time T_{Sdecay}.

6.1.4. TNF-α stimulation

The stimuli intensity $\mu(t)$ when stimulated with TNF-α is given as

$$\mu(t) = \alpha \cdot TNF^2 + \beta \cdot TNF + \gamma, \quad (70)$$

where *TNF* is the TNF-α concentration. The parameters used for this equation were $\alpha = -10.9635, \beta = 267.1747$ and $\gamma = 130.2175$.

6.1.5. IκBα-NFκB signaling pathway

The NF-κB pathway is described schematically in Figure 160. IKK has three states: Neutral, active and inactive. Active IKK phosphorylates IκBα, of the IκBα-NFκB complex, and causes ubiquitination of IκBα. This unbinds NF-κB, which can then freely travel into a nucleus. Nuclear translocated NF-κB binds to DNA and transcribes new IκBα and A20. The transcribed IκBα and A20 can then synthesise to form proteins in the cytoplasm. Subsequently, the newly synthesised cytoplasmic IκBα proteins bind again to form NF-κB and inhibit its function and mobility. Newly synthesised A20 causes the inactivation of IKK. Therefore, the NF-κB pathway is a negative feedback loop [75, 80].

In this work, the mathematical model of the NF-κB pathway described by Lipniacki *at al.* [80] was implemented in the cell population model. Moreover, the model was extended by defining a new activation scale $\phi_i(t)$ for each cell

$$\phi_i(t) = \begin{cases} \dfrac{r_i(t) - a}{M - a}, & r_i(t) > a \\ 0, & r_i(t) \leq a \end{cases} \quad (71)$$

Where *a* is a threshold. In cases were the number of activated receptors $r_i(t)$ is lower than the threshold a, the activation scale is zero. If the activated receptors $r_i(t)$ are above the threshold a, the activation scale is the rate of activated receptors over the

maximum number of receptors ***M***. Therefore, if the number of activated receptors is above a, the cell is activated. If the number is below *a*, the cell is inactive.

Using the activation scale, the reaction rates in the IκBα-NF-κB signaling pathway were proportioned. First, the IKK activation rate was scaled with the above defined scale $\phi_i(t)$. This approach was adopted based on the suggestion by Cheong *et al.* [86] that the IKK activation has a temporal dynamic with a sharp decaying curve. Moreover, Turner *et al.* suggested modification of the IKK activation with a decay function that includes a random walk. In this work, the activation rate of IKK was scaled proportional to the number of activated surface receptors as described in Equations (66) and (71). Therefore, the activation rate of IKK was affected by the stimuli intensity, fast and slow decays, a random walk and a threshold cut-off.

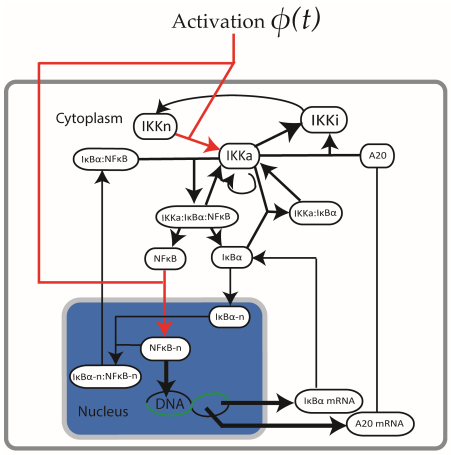

Figure 163: Schematic of the NF-κB pathway with a cell. The reaction rates that are influenced by activated receptors $\phi_i(t)$, the IKK activation and the nuclear import of NF-κB are highlighted in red.

Second, we have scaled the nuclear import of NF-κB proportional to the number of activated receptors. This allowed the establishment of a nuclear NF-κB peak that is proportional to the stimuli. The nuclear import rate was scaled based on the assumption that the nuclear transport of NF-κB facilitated by Importin-α3 and

Importin-β4 is a TNF-α influenced mechanism [169, 170]. Other studies have used stochastic models to reduce the nuclear NF-κB amplitude as the probability of dissection and association decreases with stimuli intensity [89]. However, in this work the aim was to simplify the model to a deterministic model by using extrinsic noise only. In scaling the reaction rate of nuclear import of NF-κB, the nuclear NF-κB peaks could be reduced proportional to the stimuli. Including this feature, allowed for qualitative reproduction of the live-cell measurements of transfected HUVECs exposed to TNF-α and shear stress.

The receptor dependent reaction rates of the NF-κB model are:

- The IKK activation rate caused by TNF-α

$$k_1 = 0.5163 \cdot \phi_i(t) \quad (72)$$

- Nuclear import rate of NF-κB

$$i_1 = 0.0026 \cdot \phi_i(t) \quad (73)$$

All reaction rate constants were based on the work of Lipniacki *et al.* [80]. Moreover, these were extended with the activation scale $\phi_i(t)$ and fitted to nuclear GFP-RelA measurements presented in Chapter 3. The full set of all biochemical reactions of the IkBa-NFkB signalling pathway [80] are:

- The neutral state of IKK:

$$\frac{d}{dt} IKK_n(t) = k_{prod} - k_{deg} \cdot IKK_n(t) - k_1(t) \cdot IKK_n(t) \quad (74)$$

- The activation of IKK:

$$\frac{d}{dt}IKK_a(t) = k_1(t) \cdot IKK_n(t) - k_3 \cdot IKK_a(t) - k_2(t) \cdot IKK_a(t) \cdot A_{20}(t) - k_{deg} \cdot IKK_a(t) - a_2 \cdot IKK_a(t) \cdot I\kappa B\alpha(t) + \mathrm{t}_1(t) \cdot IKK_a I\kappa B\alpha - \mathrm{a}_3(t) \cdot IKK_a(t) \cdot I\kappa B\alpha \mathrm{NF}\kappa B(t) + t_2(t) \cdot IKK_a I\kappa B\alpha \mathrm{NF}\kappa B(t) \quad (75)$$

- The inactivation of IKK:

$$\frac{d}{dt}IKK_i(t) = k_3(t) \cdot IKK_a(t) + k_2(t) \cdot IKK_a(t) \cdot A_{20}(t) - k_{deg} \cdot IKK_i(t) \quad (76)$$

- Active IKK and IκBα complex that degrades IκBα:

$$\frac{d}{dt}IKK_a I\kappa B\alpha(t) = a_2(t) \cdot IKK_a(t) \cdot I\kappa B\alpha(t) \cdot -\mathrm{t}_1(t) \cdot IKK_a I\kappa B\alpha(t) \quad (77)$$

- Active IKK association with the IκBα-NFκB complex:

$$\frac{d}{dt}IKK_a I\kappa B\alpha \mathrm{NF}\kappa B(t) = a_3(t) \cdot IKK_a(t) \cdot I\kappa B\alpha \mathrm{NF}\kappa B(t) - t_2(t) \cdot IKK_a I\kappa B\alpha \mathrm{NF}\kappa B(t) \quad (78)$$

- The unbound cytoplasmic NFκB:

$$\frac{d}{dt}\mathrm{NF}\kappa B = c_{6a} \cdot I\kappa B\alpha \mathrm{NF}\kappa B(t) - a_1 \cdot \mathrm{NF}\kappa B(t) \cdot I\kappa B\alpha(t) + \mathrm{t}_2(t) \cdot IKK_a I\kappa B\alpha \mathrm{NF}\kappa B(t) - i_1(t) \cdot \mathrm{NF}\kappa B(t) \quad (79)$$

- Unbound nuclear NFkB:

$$\frac{d}{dt}\mathrm{NF}\kappa B_n = i_1(t)\cdot k_v\cdot \mathrm{NF}\kappa B(t) - a_1\cdot I\kappa B\alpha_{\mathrm{n}}(t)\cdot \mathrm{NF}\kappa B_n(t) \quad (80)$$

- Inhibitor A20 protein:

$$\frac{d}{dt}A_{20}(t) = c_4\cdot A_{20mRNA}(t) - c_5\cdot A_{20}(t) \quad (81)$$

- A20 mRNA:

$$\frac{d}{dt}A_{20mRNA}(t) = c_2 + c_1\cdot \mathrm{NF}\kappa B_n(t) - c_3\cdot A_{20mRNA}(t) \quad (82)$$

- Unbound IkBa protein:

$$\begin{aligned}\frac{d}{dt}I\kappa B\alpha(t) = {} & -a_2(t)\cdot IKK_a(t)\cdot I\kappa B\alpha(t) - \mathrm{a}_1(t)\cdot I\kappa B\alpha(t)\cdot \mathrm{NF}\kappa B(t)\\ & + c_{4a}\cdot I\kappa B\alpha_{mRNA}(t) - c_{5a}\cdot I\kappa B\alpha(t) - \mathrm{i}_{1\mathrm{a}}\cdot I\kappa B\alpha(t)\\ & + \mathrm{e}_{1\mathrm{a}}\cdot I\kappa B\alpha_{\mathrm{n}}(t)\end{aligned} \quad (83)$$

- Unbound nuclear IkBa protein:

$$\begin{aligned}\frac{d}{dt}I\kappa B\alpha_{\mathrm{n}}(t) = {} & -a_1(t)\cdot I\kappa B\alpha_{\mathrm{n}}(t)\cdot \mathrm{NF}\kappa B_n(t) + i_{1a}\cdot k_v\cdot I\kappa B\alpha(t) - \mathrm{e}_{1\mathrm{a}}\\ & \cdot \mathrm{k}_{\mathrm{v}}\cdot I\kappa B\alpha_{\mathrm{n}}(t)\end{aligned} \quad (84)$$

- IkBa mRNA:

$$\frac{d}{dt}I\kappa B\alpha_{mRNA}(t) = c_{2a} + c_{1a}\cdot \mathrm{NF}\kappa B_n(t) - c_{3a}\cdot I\kappa B\alpha_{\mathrm{mRNA}}(t) \quad (85)$$

- Cytoplasmic IkBaNFkB complex:

$$\frac{d}{dt} I\kappa B\alpha \mathrm{NF}\kappa B(t) = a_1(t) \cdot I\kappa B\alpha(t) \cdot \mathrm{NF}\kappa B(t) \cdot -c_{6a} \cdot I\kappa B\alpha \mathrm{NF}\kappa B(t) - a_3(t) \cdot IKK_a(t) \cdot I\kappa B\alpha \mathrm{NF}\kappa B(t) + e_{2a} \cdot I\kappa B\alpha_{\mathrm{n}} \mathrm{NF}\kappa B_n(t) \quad (86)$$

- Nuclear IkBaNFkB complex:

$$\frac{d}{dt} I\kappa B\alpha_{\mathrm{n}} \mathrm{NF}\kappa B_n(t) = a_1(t) \cdot I\kappa B\alpha_{\mathrm{n}}(t) \cdot \mathrm{NF}\kappa B_n(t) - e_{2a} \cdot k_v \cdot I\kappa B\alpha_{\mathrm{n}} \mathrm{NF}\kappa B_n(t) \quad (87)$$

Table 5: Parameter with * were fitted, for the others the references are indicated.

Reaction rate	K_v [80]	C_1 [80]	C_2 [80]	C_3 [80]	C_4 [80]	K_{prod}*	K_{deg}*
value	5	5e-7	0	0.004	0.5	2.62e-5	1.2e-4
Reaction rate	A_1*	C_{1a}*	C_{2a}*	C_{3a}*	C_{4a}*	C_{5a}*	C_{6a}*
value	0.5026	3.23e-7	0	4..7e-4	0.4814	1.14e-4	1.77e-5
Reaction rate	E_{2a}*	i_{1a}*	E_{1a}*	k_2*	a_2*	a_3*	t_1 [80]
value	0.0105	0.001	4.9e-4	0.0918	0.2089	1.152	0.1
Parameter	t_2*	k_3*	T_{delay}	k_C	T_{FDecay}	k_L	T_{SDecay}
value	0.1064	0.0016	7	0.65	46.125	50	307

All constant parameters are provided in Table 5.The parameters were fitted using *fminsearch* in *Matlab* (*MathWorks, Natick, Massachusetts, US*), employing a simplex search method by Lagarias *et al.* [171]. Within the search method, the minimum error between model and experiment was found using a simple error calculation:

$$\varepsilon = \sqrt[2]{S_{Model} - S_{Experiment}} \quad (88)$$

Arbitrary units were used for the model and the experiments, and the curves were fitted until they reached a qualitative similar shape.

6.2. Numerical methods for ordinary differential equations

Several numerical methods exist to solve ordinary differential equations (ODE). The most common methods are explicit and implicit Euler, Runge-Kutta of 2nd and 4th order, and Backward Differentiation Formula methods. However, when dealing with stiff differential equations implicit methods demonstrate a higher stability and are computationally less expensive [172-174].

The ODE system described in Chapter 0 has stiff characteristics. Stiffness occurs due to sudden activation or inactivation of IKK caused by the activation scale $\phi(t)$. In this work the ODE systems were solved in *Matlab* using an implicit Runge-Kutta formula coupled with a 2nd order backward differentiation formula (TR-BDF2, *ode23tb*), which is suitable for stiff differential equations [175, 176].

6.2.1. Cell population simulation protocol

1) Calculate activated receptors over time for each cell for static conditions with $\mu = 78$.
2) Run the cell population model with input $\phi(t) = 0$, for 100 hrs. Initial conditions were $I\kappa B\alpha \mathrm{NF}\kappa B(0) = 0.06$, all other variables were zero at time t=0.

3) Use steady state conditions from step 2 as input conditions. Run the cell population model for 360 minutes with the static conditions receptors activation sacle $\phi(t)$.
4) Use end state of the static condition simulations as an input condition for the real simulation. This allows for simulation of cells that are initially in different activation states.
5) Run the cell population model with end results from step 3 and assign to each cell its activation rate $\phi(t)$ for the desired case (TNF-α or flow). The time span was set to 360 minutes with a time step of 0.5 minutes.

6.3. Results: Modelling NF-kB activation in a cell population stimulated with TNF-α

Summary: *This section presents the modelling results for the NF-κB pathway prediction in a cell population when stimulated with TNF-α. First, it was demonstrated that the cell activation threshold of the population model defines a Hill function. Second, it was identified that scaling the nuclear import affects the nuclear NF-κB concentration the most. Thus, additional scaling of the nuclear import rate together with the initial trigger scaling of the IKK activation was undertaken. The population model was then illustrated for a population of 200 cells under four different conditions: Stimulation with 1, 10 and 100 ng/mL TNF-α and under static conditions. Predication of the NF-κB pathway in cell populations exposed to different TNF-α concentrations and under static conditions were compared with live-cell imaging measurements and immunohistochemistry. Predictions of single cell dynamics were found to be in agreement with live-cell measurements, while differences between IHC were observed. The cell population model can be used to reproduce the large heterogeneity observed under static conditions. Synchronisation of the NF-κB pathway within a cell population was observed to decrease when lowering the TNF-α concentration.*

6.3.1. The activation threshold defines a Hill function

A cell is only activated if more receptors are activated than the defined threshold *a.* The initial number of activated receptors was selected using a random number generator employing a Gaussian normal distribution $P_i\left(b_i, \mu(t)\right)$ with mean $\mu(t)$. In Figure 164, the percentages for initially activated cells (points) are shown for four different thresholds (*a*= 100, 200, 500 and 750) of a population of 100 cell as a function of the mean $\mu(t)$. The mean μ was set to be proportional to the stimulus strength, which was the concentration of TNF-α or the shear stress magnitude. The percentage of activated cells as a function of the mean $\mu(t)$ was observed to behave like a Hill function (straight lines in Figure 164).

A Hill function based on the mean $\mu(t)$ of the Gaussian distribution can be defined as:

$$V(\mu) = V_{max} \frac{\mu(t)^n}{K^n + \mu(t)^n} \quad (89)$$

where V_{max} is the maximum activation rate (100%), K the Hill constant, n the Hill coefficient and $\mu(t)$ the mean of the activated receptors/Gaussian distribution. In this work, the Hill coefficient n was observed to be proportional to the threshold a.

Tay *et al.* [95] previously measured that the number of activated cells increase with increasing TNF-α concentration. They defined a Hill function with Hill coefficient 1.5. For the cell population simulation, a threshold of *a*=200 was chosen. This approximately corresponds to a Hill function coefficient of *n*=2.5 with K=190.

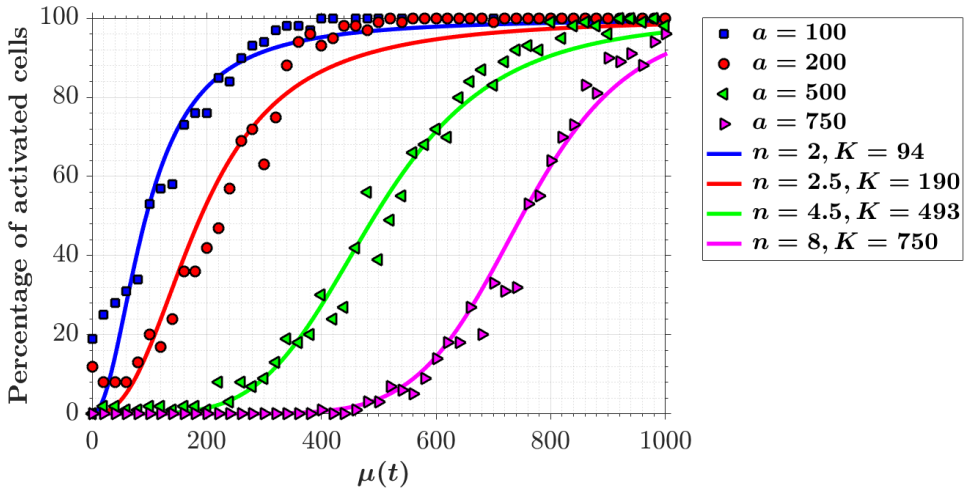

Figure 164: The percentage of activated cells as a function of the mean $\mu(t)$ of the Gaussian normal distribution $P_i(b_i, \mu(t))$ for four different thresholds (points - left to right, *a*=100,200, 500 and 750) compared with the Hill function of four different Hill constants (lines - n=2, 2.5, 4.5 and 8).

6.3.2. Receptors and cell activation

The temporal behaviour of the receptor activation (Eq. (66)) and the activation of cells with a threshold *a*=200 for a cell population of 200 cells are illustrated for four

cases: Stimulation with 3 different TNF-α concentrations (100, 10, 1 ng/mL) and under static conditions. The receptor activation and cell activation for each of the four cases are presented in Figure 165.

In Figure 165.A-C, the intensity of the TNF-α concentrations defines how many receptors were initially activated. The higher the TNF-α concentration, the larger the number of activated receptors. An initial activation jump was followed by fast decay that stabilised after ca. 60 minutes. Thereafter, a slow decay decreased the number of activated receptors. In addition, at every time step, receptors were activated or inactivated randomly by definition of a random walk. The random walk becomes dominant after stabilisation of the fast decay (ca. 60 minutes).

The number of activated receptors under static conditions are shown in Figure 165.D. Under static conditions, the random walk is dominant and is responsible for cell activation. The number of activated cells for each of the four cases is shown in Figure 165.E-H. The threshold was set to 200. Consequently, more than 200 receptors must be activated to activate a cell (Once a cell is activated the NF-κB pathway is triggered).

On stimulation with 100 ng/mL TNF-α (Figure 165.E), all 200 cells were initially activated. Following 60 minutes, the number of activated cells decreased linearly. On stimulation with 10 ng/mL TNF-α (Figure 165.F), all 200 cells were initially activated. However, the number of activated cells started to decrease linearly after 5 minutes.

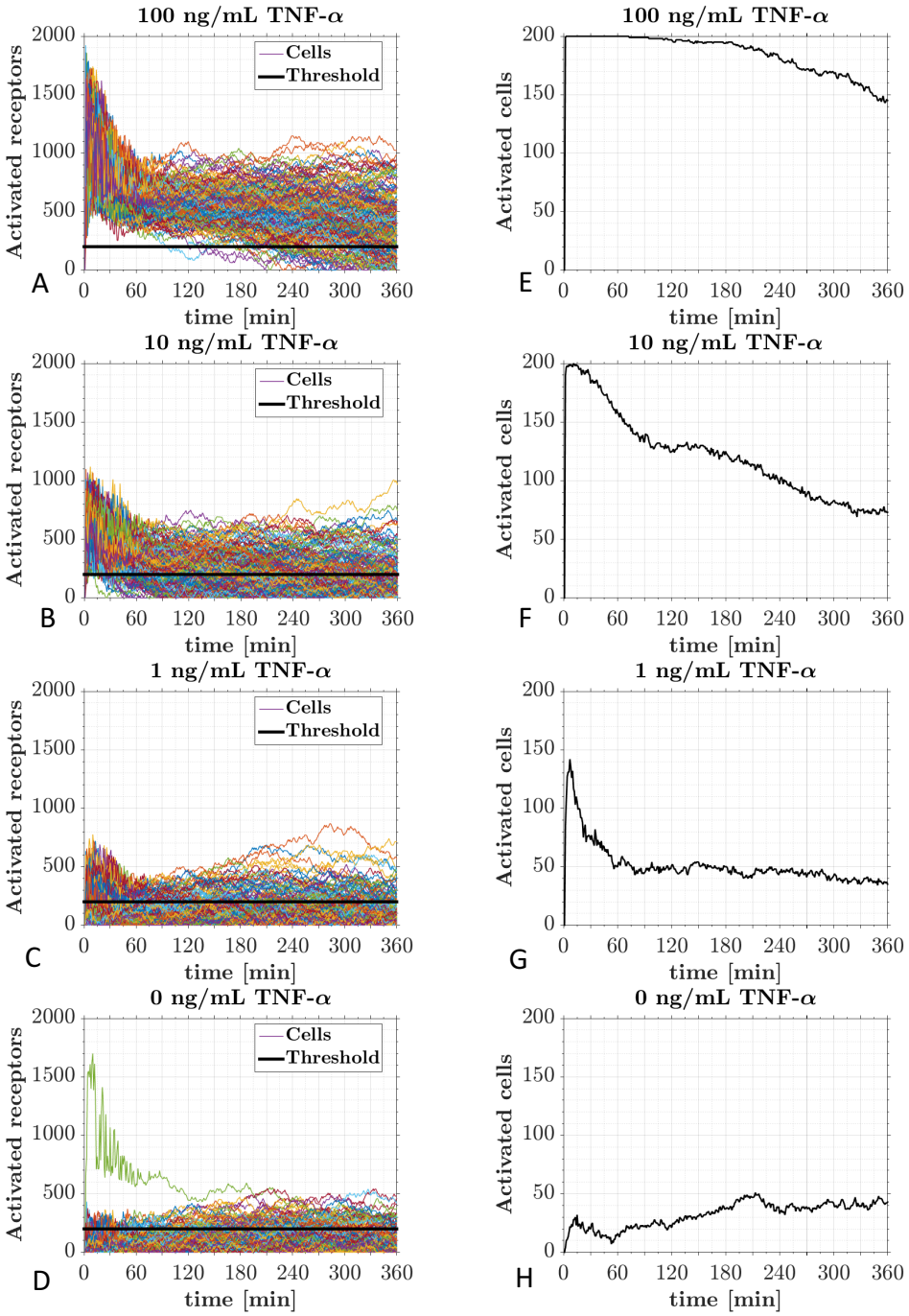

Figure 165: The temporal behaviour of activated receptors (A-B) and the number of activated cells (E-H) (threshold = 200) under 4 different conditions: 100 ng/mL TNF-α (A, E), 10 ng/mL TNF-α (B, F), 1 ng/mL TNF-α (C, G), and static conditions (D, H).

On stimulation with 1 ng/mL TNF-α (Figure 165.G), only 120 cells were initially activated. The number of activated cells proceeded to rapidly decline to ca. 50, were the number remained stable. Under static conditions (Figure 165.H), the number of active cells varied from 10 to approximately 50, with a tendency of higher activation

towards the end of the experiments. Activation under static conditions was only possible due to random activation or inactivation of receptors.

6.3.3. Scaling nuclear NF-κB proportional to the stimuli TNF-α

To justify the choice to scale the activation rate of IKK and the nuclear import of NF-κB, all system parameters were screened for the effect of scaling $\phi_i(t) = 0.1, 0.2, 0.3 \dots, 2$, and the effect of cutoff $\phi_i(t) = 0$ or 1. In Figure 166, the standard deviation of the maximum nuclear NF-κB peak (major peak at 30 minutes) when scaling the parameters from 1-200% (Figure 166.A) and switching on or off (Figure 166.B) are presented. By scaling the parameter from 1-200%, only *i1* was shown to have a strong influence. Parameter *i1* is responsible for the nuclear import of NF-κB. Switching the reaction rates on or off resulted in more parameters showing significant effects on the nuclear NF-κB peak. These parameters were: k1 (activation by TNF-α), kprod (neutral IKK production rate), a3 (IKK association with IκBαNF-κB), t2 (degradation of IKK-IκBαNFκB), i1 (nuclear import of NF-κB), e2a (nuclear export of NF-κB), i1a (nuclear import of IκBα), c1 (transcription of IκBα) and c3 (degradation of IκBα mRNA). This revealed that switching on and off of these reactions (or blocking or knocking out) can strongly influence the nuclear translocation of NF-κB. For simplicity, only two reaction rates were scaled and switched on by the activation scale. These were the nuclear import of NF-κB (i1) and the activation rate of IKK (k1). By scaling the nuclear import of NF-κB, the nuclear NF-κB peak was proportioned to the stimuli intensity. By scaling the activation rate of IKK, the NF-κB pathway was triggered.

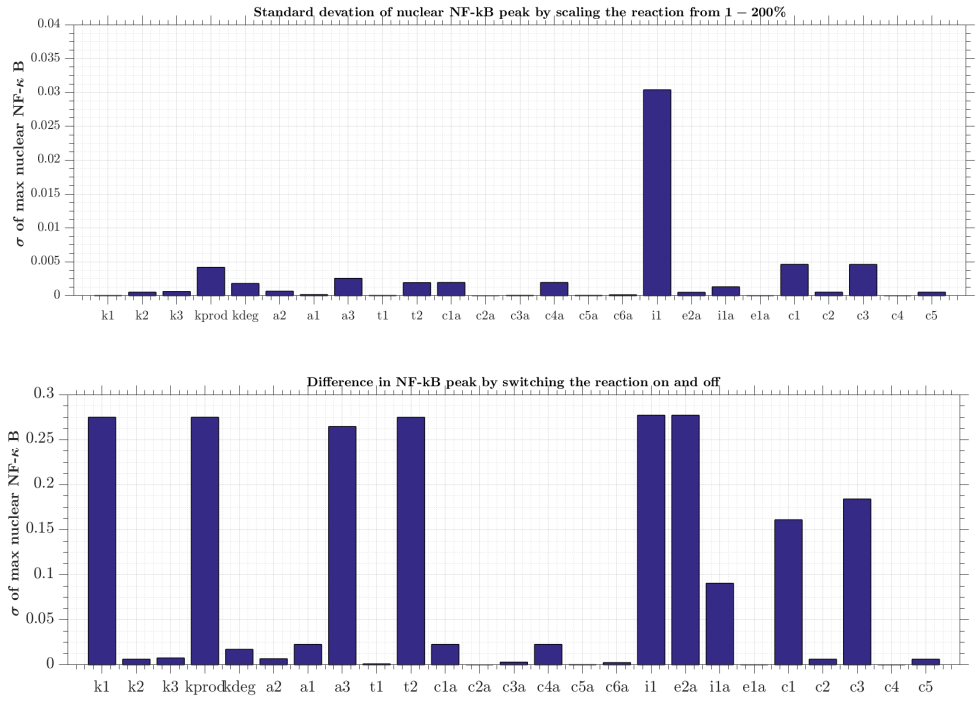

Figure 166: The standard deviation of change in nuclear NF-κB peaks when scaling the reaction rate parameters from 1 to 200% (A) and the difference in nuclear peak by switching the reaction from on to off (B).

6.3.4. Cell population read outs

The cell population model was illustrated with a population of 200 cells for four different cases: 100, 10 and 1 ng/mL TNF-α and under static conditions. The model parameters were fitted to the population response to 10ng/mL TNF-α in arbitrary units. The stimuli intensity was then amended to qualitatively match the nuclear translocation to lower and higher TNF-α stimuli.

The results of the cell population model are presented with the following quantities extracted from the model:

- The total nuclear NF-κB concentration normalised by time average:

$$\mathrm{NF}\kappa B_{Nuc}(t) = \frac{\mathrm{NF}\kappa B_n(t) + I\kappa B\alpha\mathrm{NF}\kappa B_n(t) + E}{\langle \mathrm{NF}\kappa B_n(t) + I\kappa B\alpha\mathrm{NF}\kappa B_n(t) + E \rangle} \quad (90)$$

Where E = 0.035 is an included measurement noise to allow normalisation of inactive cells and mimic experimental conditions.

- The total cytoplasmic IκBα concentration:

$$I\kappa B\alpha_{Cyto}(t) = IKK_a I\kappa B\alpha(t) + IKK_a I\kappa B\alpha \mathrm{NF}\kappa B(t) + I\kappa B\alpha(t) + I\kappa B\alpha \mathrm{NF}\kappa B(t) \quad (91)$$

- And the active IKK concentration:

$$IKK_{Activated} = IKK_a + IKK_a I\kappa B\alpha(t) + IKK_a I\kappa B\alpha \mathrm{NF}\kappa B(t) \quad (92)$$

The nuclear NF-κB concentration was normalised using the time average (for comparison with live-cell imaging experiments), while active IKK and IκBa are provided in arbitrary concentration units. Each quantity is depicted for every case with a cluster map and a population mean, which includes the standard deviation. The maps were clustered by applying Kmeans with 5 groups. All quantities of the NF-κB pathway for the four different cases are shown in the Appendix (Figure 196, Figure 197, Figure 198, Figure 199).

6.3.5. Nuclear NF-κB concentration - Population maps

100 ng/mL TNF-α: In Figure 167.A, the cluster map shows that, at a very high TNF-α concentration, all cells experienced a high nuclear NF-κB concentration after 30 minutes. Moreover, all the cells were initially well synchronised. Differences in synchronisation began to occur following the decrease of the peak. A small percentage of cells experienced lower concentrations from 120 minutes onwards. This was due to slow decay and random activation or inactivation of surface receptors. The simulation cluster map (Figure 167.A) is in close agreement with the

experimental measurement of nuclear GPF-RelA intensity when stimulated with 100 ng/mL TNF-α (Figure 167.E).

10 ng/mL TNF-α: In Figure 167.B, all cells peaked between 30 and 60 minutes. The groups showed variations in their temporal profile beyond the initial peak. Moreover, they decreased to a very low nuclear NF-κB concentration at 90 minutes (early) or at 300 minutes (late), or they decreased and experienced random activation (only very few). These results were in good agreement with measurement of nuclear GFP-RelA intensity when stimulated with 10 ng/mL TNF-α (Figure 167.F)

1 ng/mL TNF-α: Figure 167.C shows the cluster map when stimulated with a low TNF-α concentration. Two groups revealed late peaks (around 200 and 300 minutes). This was due to random activation of cells. A large group peaked between 30 and 120 minutes but this was moderate compared to results for the higher TNF-α concentrations. Most cells experienced weak or no nuclear NF-κB concentration

Static conditions – 0 ng/mL TNF-α: In Figure 167.D, most cells remained inactive. A few cells had an initial high nuclear NF-κB concentration (due to initial conditions). 3 small groups experienced random activation and thus experienced nuclear NF-κB peaks at around 180, 240 and 330 minutes. The random activation of cells (population model) was comparable with the random activation observed with live-cell imaging under static conditions. The groups might not be identical, but the heterogeneity of the population could be approximated with population modelling.

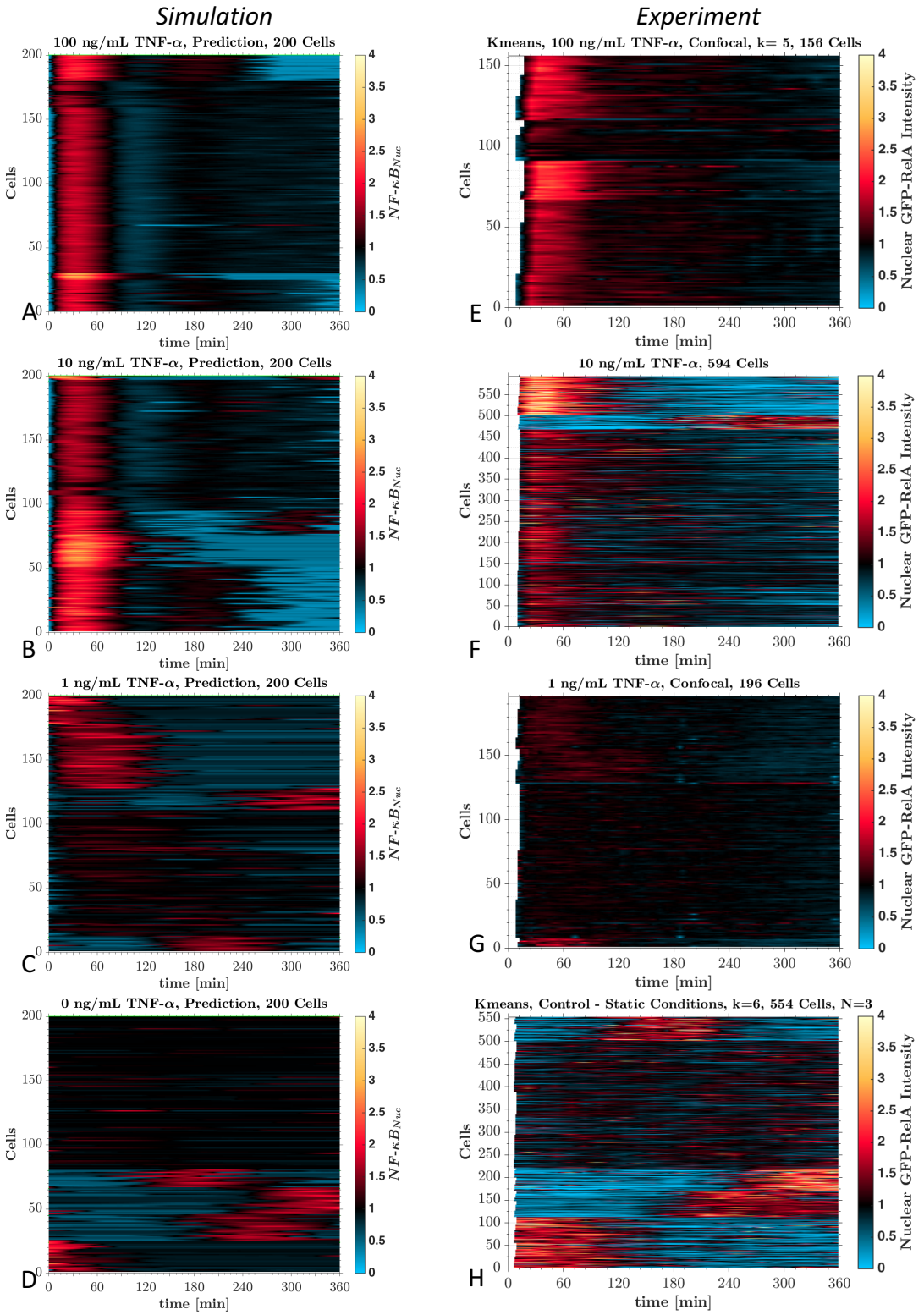

Figure 167: Comparison of cell population simulation (A, B, C, D) and experiment (E – confocal, F – wide-field, G – confocal, H – wide-field). The cluster maps of nuclear NF-κB concentration when stimulated with 100 ng/mL TNF-α (A, D), 10 ng/mL TNF-α (B,E), 1 ng/mL TNF-α (C,F) and under static conditions (D,H).

6.3.6. Populations means

100 ng/mL TNF-α: In Figure 168.A, the population mean with standard deviation is shown for 200 cells stimulated with 100 ng/mL TNF-α. All cells were well synchronised. The standard deviation increased from 180 minutes onwards. This was due to the programmed decay of the activated receptors, which caused cells to desynchronise. The simulation mean was found to agree with the mean of the experimental observation (Confocal measurements - Figure 168.E). However, the simulation showed a stronger oscillation. The oscillation might have been lost in the experiment due to the measurement of noise.

10 ng/mL TNF-α: In Figure 168.B, the total mean of the population peaked at 30-40 minutes. This peak was slightly off (ca. 5 min) in comparison with the experiment. The standard deviation was larger compared to the 100ng/mL TNF-α case. This indicates an increased loss of synchronisation. An even larger standard deviation was observed in the experimental measurements (Figure 168.F).

1 ng/mL TNF-α:. In Figure 168.D, the mean of the cell population for a low TNF-α concentration showed a small peak at 60 minutes that gradually decreased until 360 minutes. The standard deviation was large throughout the simulation, indicating that cells were out of phase. Agreement between the population model and live-cell measurments was found (Figure 168.G).

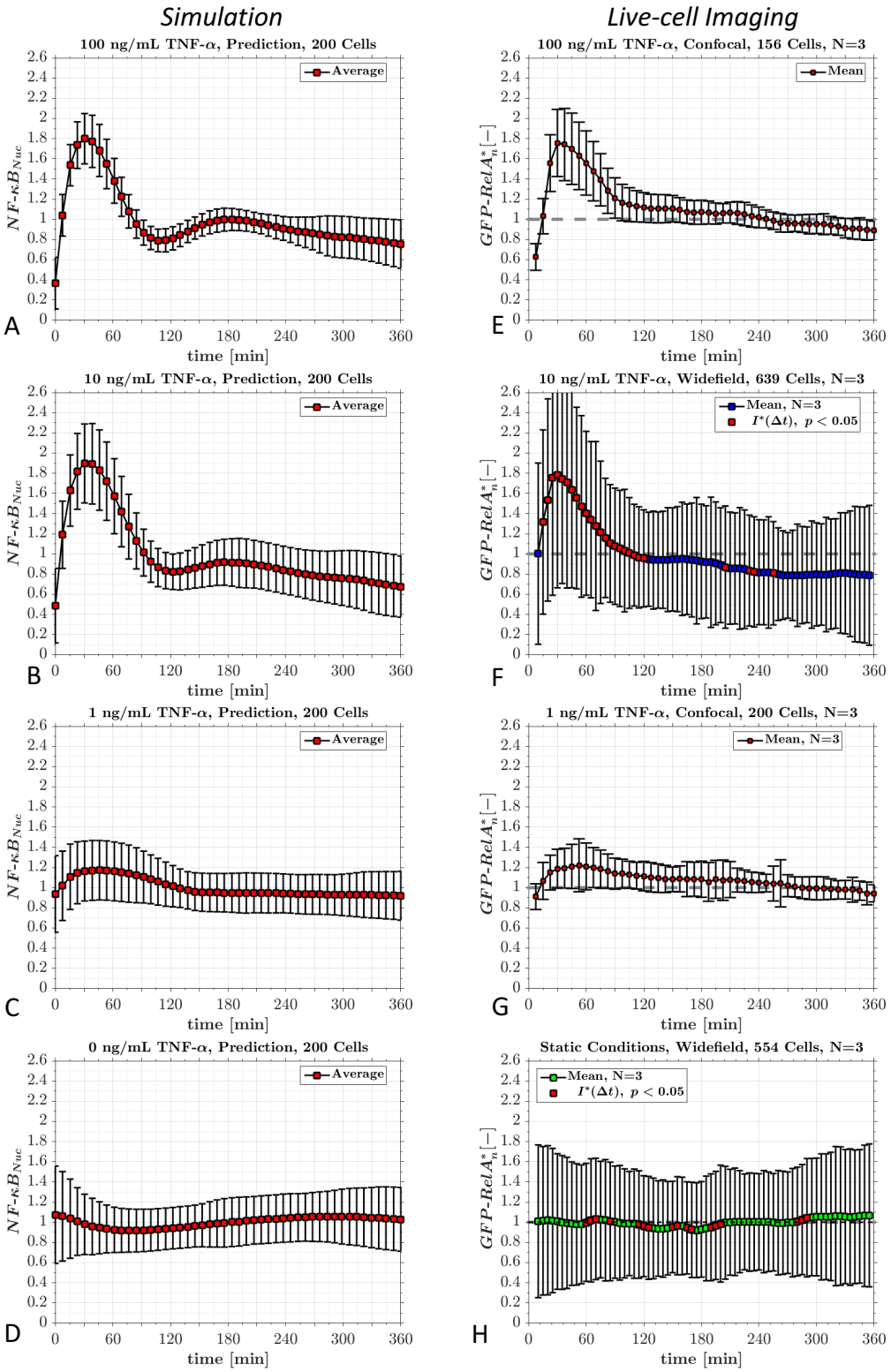

Figure 168: Comparison of cell population simulations (A, B, C, D) and experiment (E – confocal, F – wide-field, G – confocal, H – wide-field). The mean of the nuclear NF-κB concentration and GFP-RelA intensity when stimulated with 100 ng/mL (A, D), 10 ng/mL (B, E), and 1 ng/mL TNF-α (C, F) and under static conditions (D, H).

Static conditions – 0 ng/mL TNF-α: Under simulated static condtions (Figure 168.D) the mean of the nuclear NF-κB concentration hovered about its initial value. This standard deviation was due to random activation of cells. The random activation created heterogeineity as was observed in measurments of transfected cells under static conditions (Figure 168.H).

6.3.7. Nuclear NF-κB population mean compared to immunohistochemistry measurements

In Figure 169.A and C, the simulation of 10 ng/mL TNF-α is compared with immunohistochemistry measurements.

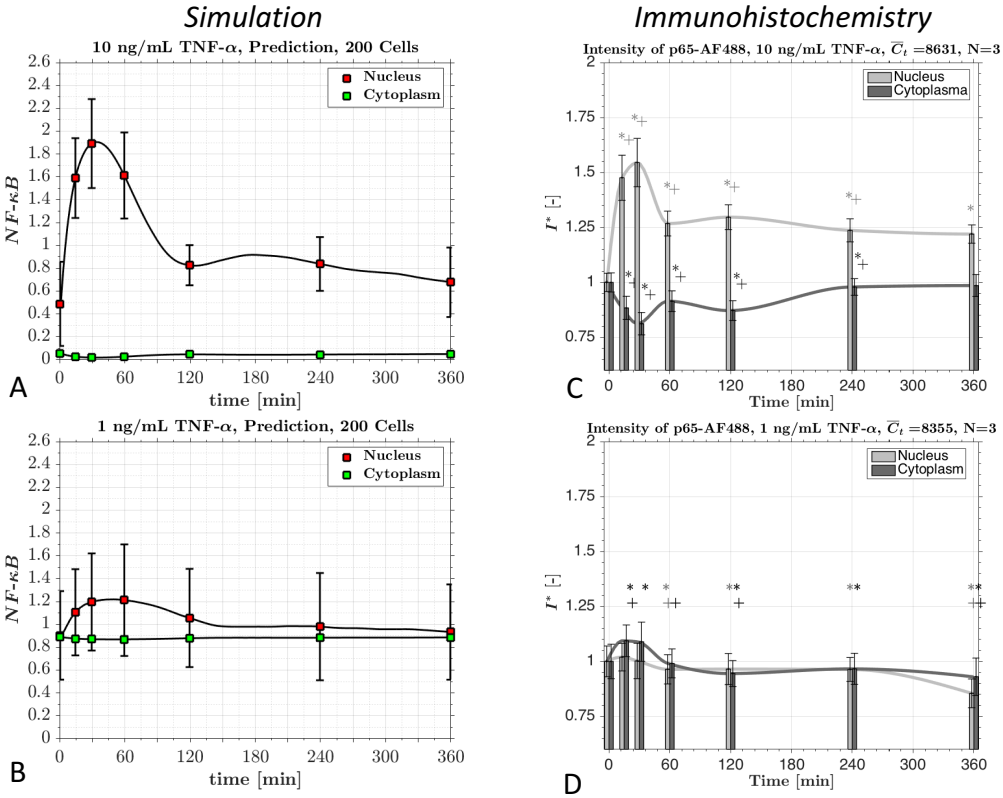

Figure 169: Comparison of cell population simulation (A, B) with immunohistochemistry (C,D) when stimulated with 10 and 1 ng/mL TNF-α

The general trend observed in immunohistochemistry was confirmed. However, IHC showed a stronger drop of nuclear p65 at 60 minutes than was observed in the

simulation. This was due to the fitting of the model to live-cell imaging observations, which has the same disagreement with IHC.

In Figure 169.B and D, the simulation of 1 ng/mL TNF-α is compared with the immunohistochemistry measurements. IHC showed that 1ng/mL TNF-α caused a drop in nuclear p65 concentration from 60 minutes onwards. This was vaguely comparable with the simulated NF-κB peak at 30 and 60 minutes.

6.3.8. Activation of IKK (phosphorylation of IKK)

100 ng/mL TNF-α: Figure 170.A depicts the cluster map of the temporal activated IKK concentration after stimulation with a very high TNF-α concentration. All the cells were found to respond in a well synchronised fashion. Moreover, activated IKK peaked early at around 5-10 minutes. In Figure 170.E, the total population mean of activated IKK shows an early peak. This was followed by a sharp decline and consequently a low concentration.

10ng/mL TNF-α: In Figure 170.B, the cluster map of the temporal activated IKK concentration in response to 10ng/mL TNF-α response is shown to be very similar to the 100 ng/mL TNF-α case. An early but lower peak at 5-10 minutes was followed by a sharp decline (Figure 170.F). The mean of activated IKK can be compared with immunohistochemistry measurement in Figure 170.I. Immunohistochemistry measured a peak at 15 minutes indicating early activation of IKK.

1 ng/mL TNF-α: At low TNF-α concentration, most cells still experienced a strong early IKK activation (Figure 170.C). The simulation predicts that few cells were randomly activated. The limited number of small white dots in the cluster map indicates random activation of IKK.

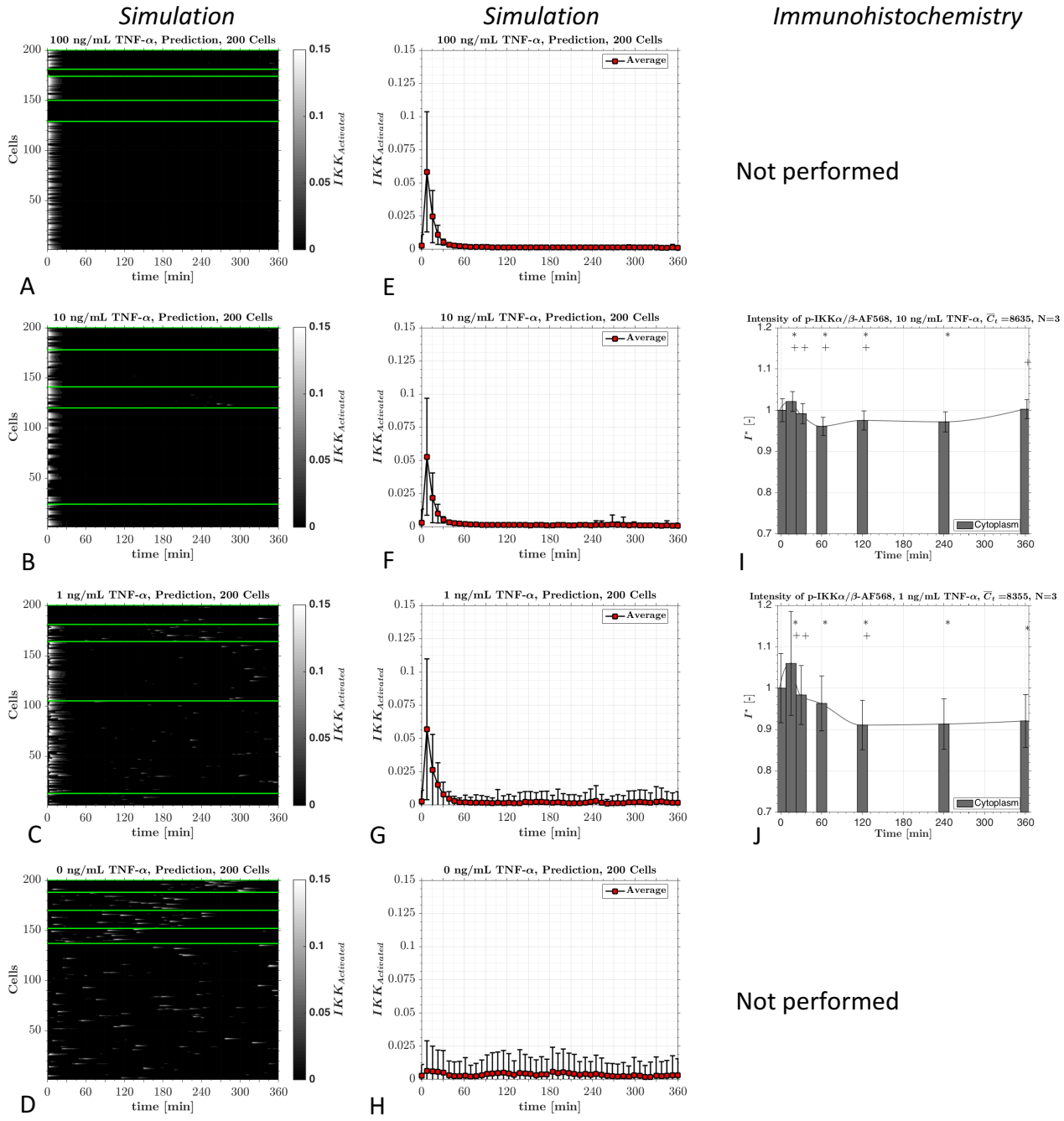

Figure 170: Cell population simulation (200 cells) when stimulated with 100 ng/mL (A, E), 10 ng/mL (B, F, I), 1 ng/mL TNF-α (C, G, J) and under static conditions (D, H). The left column (A-D) shows the temporal profile of active IKK of all cells grouped and mapped. The middle column (E-H) shows the total population average of active IKK with its standard deviation. The right column (I and J) shows immuhistochemistry of nuclear and cytoplasmic phorphosrylated IKKα/β (active IKK).

Immunohistochemistry of HUVECs stimulated with 1 ng/mL TNF-α revealed an early peak followed by a gradual decrease up to 120 minutes. Thereafter, the system plateaued (Figure 170.J). This indicates an early activation of IKK low TNF-α concentration.

Static conditions – 0 ng/mL TNF-α: In Figure 170.D, cells in static conditions are shown to experience random IKK activation. The cluster map shows that activation of IKK is randomly distributed (small white dots). If IKK is activated, it peaks and then gradually decreases. In Figure 170.H, the total population mean shows a large standard deviation, which is due to random activation of cells.

6.3.9. IκBα ubiquitination and transcription

100 ng/mL TNF-α: The cluster map of the temporal total cytoplasmic IκBα concentration of all 200 cells is depicted in Figure 171.A. All cells experienced a minimum at around 15 - 30 minutes (black). This minima was followed by a local peak at 90 minutes, which again decreased to a local minimum at 180 minutes. Then the concentration gradually increases until 360 minutes. In Figure 171.E, the total population mean is shown. The standard deviation is shown to increase over time. This indicates a loss of synchronisation.

10 ng/mL TNF-α: In Figure 171.B, all cells are shown to drop to a low IκBα concentration after 15 minutes. This was followed by an increase in concentration after 30 minutes. The concentration was then found to peak around 90 minutes, followed by a decrease and slightly rise. Each group reacted to each other leading to noise. In Figure 171.F, the total population mean shows the minimum at 15 min and local maximum at 90 min. However, the standard deviation is large because of the

increased level of noise (less synchronisation). The immunohistochemistry of IκBα showed a drop of concentration at 30 and 120 minutes. However, this was not in agreement with the simulation (drop at 15 minutes). As a large number of unspecific bindings of the IκBα antibody were observed in the immunohistochemistry, this measurement was considered inaccurate and was not capable of validating the model. However, it was still able to demonstrate a drop in IκBα concentration in response to 10 ng/mL TNF-α.

1 ng/mL TNF-α: In Figure 171.C, only a few cells experienced a drop in IκBα during 15-60 minutes. The IκBα concentration wsa then shown to rise again. A large percentage of the cells were inactive. Therefore, they did not show a significant drop or change in IκBα concentration. In Figure 171.G, the total population mean reached a minimum at 30 minutes. It then increased to a high level at 120 minutes. The standard deviation was found to be large due to unsynchronised cells.

Similar to the 10 ng/mL TNF-α, immunohistochemistry showed a small but significant drop at 120 minutes. However, due to unspecific binding the immunohistochemistry of IκBα was not usable to validate the model.

Static conditions – 0 ng/mL TNF-α: Under static conditions (**Figure 171**.D, most cells were found to be inactivated. However, those that had random activation experienced a drop in IκBα concentration (black spots). **Figure 171**.H shows the total population mean of the cytoplasmic IκBα concentration. The mean remained steady at its initial state with a large standard deviation throughout the simulation pointing to bad synchronisation.

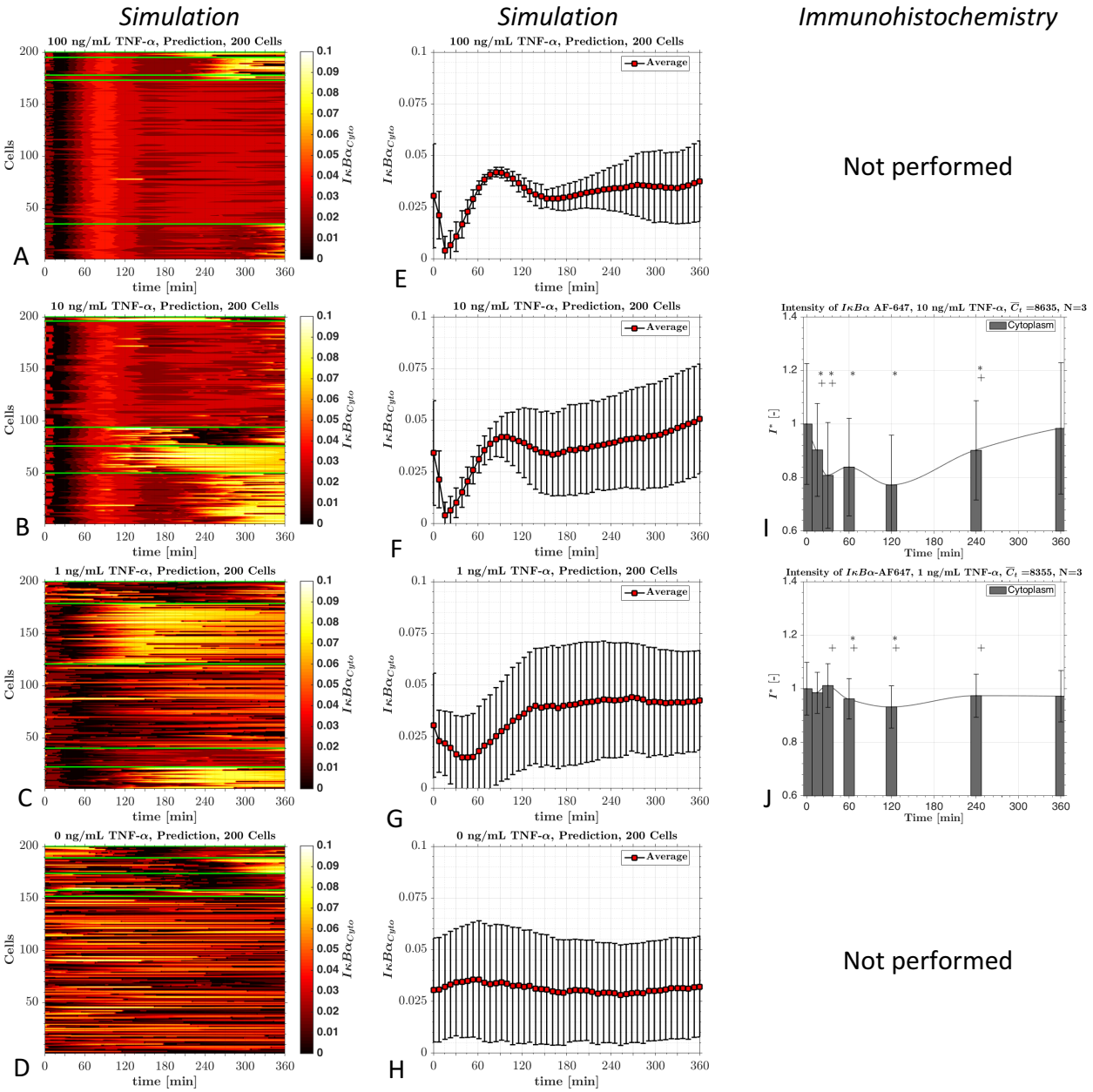

Figure 171: Cell population simulation (200 cells) when stimulated with 100 ng/mL (A, E), 10 ng/mL (B, F), 1 ng/mL TNF-α (C, G) and under static conditions (D, H). The left column (A-D) shows the temporal profile of active IKK of all cells grouped and mapped. The right column (E-H) shows the total population average of active IKK with its standard deviation.

6.4. Modelling of the NF-κB Pathway of a Cell Population in Response to Shear Stress

Summary: *This section presents a modelling effort to predict the nuclear NF-κB concentration in a cell population exposed to different shear stress environments. Cells exposed to shear stress were categorised into 5 NF-κB activation groups. The 5 groups are: Initial activation, early activation, mid activation, late activation and inactive cells. Each group corresponds to a shear dependent percentage of cells. The shear dependent percentages were based on experimental observations made with the gradient channel in chapter 4. We reproduced the cluster map features of the nuclear GFP-RelA intensity of cells exposed to a shear stress gradient of 2-16* dyne/cm^2 *with the shear induced NF-κB cell population model qualitatively well. The model revealed shear dependent dynamics of proteins involved in the NF-κB pathway, and most crucially active IKK and IκBα are presented. The model predicts late nuclear NF-κB concentrations under low shear, while high shear stress caused a larger early activation. IKK was more active throughout the simulation at low shear stress, while at high shear stress only an early significant activation occurred. The cell population model for cells exposed to a shear stress profile at the bottom wall of a backward facing step channel was illustrated. The model predicted a high nuclear NF-κB concentration of the population at the recirculation zone occurring after 90 minutes that dropped again within 30 minutes. The modelling effort of shear induced nuclear translocation of NF-κB suggest that the nuclear NF-κB concentration in endothelial cells is affected by shear stress and might be non-linear in time.*

A modelling effort to predict the moderate changes observed in nuclear GFP-RelA intensity in HUVECs exposed to a shear stress gradient is presented. The model is based on identified Kmeans groups found in the single cell measurements (normalised by time average) in the gradient channel depicted in Chapter *4*. Five groups were identified: Initial activation, early activation, mid activation, late activation and inactive cells. The grouping was considered as an approximation of how nuclear translocation of GFP-RelA in single cells exposed to shear stress may occur. As will be demonstrated, reproduction of such groups was achieved reasonable well. The prediction of nuclear NF-κB in cells exposed to a gradient

channel was qualitatively in good agreement with experimental observations. However, this modelling effort was based on visual inspected grouping of activation groups. Therefore, the presented link between shear stress and NF-κB activation provides a suggestion of how such complex systems could be predicted.

6.4.1. Model assumptions of the shear stress induced NF-κB activation

- Receptor based IKK activation mimics shear induced NF-κB activation via Flk-1, integrins, AKT and PI3K [105].
- Randomness in receptor activation mimics cell heterogeneity including factors such as: cell size, cell state and orientation
- Model parameters are assumed to be independent of stimuli and are based on TNF-α observations.
- Number of activation groups were identified with Kmeans by visual inspection
- Kmeans were performed with the nuclear GFP-RelA intensity normalised by the time average
- Relationships between activation groups and shear stress were fitted based on experimental measurements within a gradient channel (Chapter 4) to a linear regression (initial, mid, late) or second order polynomial regression (early activation group).

6.4.2. Shear stress dependent stimulation of the NF-κB pathway

In cases were flow was the stimulus of receptor activation, it was assumed that flow activated through PECAM-1, VEGF2, integrin and Flk-1 via AKT and PI3K the IKK, and the NF-κB pathway [105] [107]. This complex signalling pathway was simplified by applying the same receptor activation profile as defined for the TNF-α. It was assumed that flow activates a certain number of receptors that trigger the NF-κB pathway in a similar manner to TNF-α. Using this approach, the link between flow

and activation of NF-κB was shortened and simplified. An attempt to define a more in detail signalling model of the shear induced NF-κB pathway via PI3K, AKT and IKK is schematically presented in section 6.5.

The shear induced NF-κB stimulated model parameters were based on the model fitting to TNF-α. This assumed that the NF-κB pathway has a universal dynamic (independent of stimuli). The intensity of the flow stimuli was accordingly tailored, and each activation group experienced a stimulus comparable with 1-5 ng/mL TNF-α.

Five groups that experience different time dependent stimuli intensities $\mu(t)$ were defined. The number of cells per groups was shear stress dependent.

- Case 1 - Inactive cells:

$$\mu_R(t) = 27, R = 1,2,3, \dots, R_{max}(\tau) \quad (93)$$

  Cells remain inactive (but can experience random activation) throughout the experiment. The total number of inactive cells is $R_{max}(\tau)$.

- Case 2: Initial activation group:

$$\mu_A(t = 0) = 1090, A = 1,2,3, \dots, A_{max}(\tau) \quad (94)$$

  Cells experience activation at 0 minutes. The total number of initial activation cells is $A_{max}(\tau)$.

- Case 2: Early activation group:

$$\mu_B(t) = \begin{cases} 788, & 15 + \xi_B < t < 360 \\ 27, & t < 15 + \xi_B \end{cases} \quad (95)$$

$$B = 1,2,3, \dots, B_{max}(\tau) \quad (96)$$

ξ_B is a random number picked from $\xi_B \epsilon \{0, \dots, 60\}$. Cells experience random activation between 15 and 75 minutes. The total number of early activation cells is $B_{max}(\tau)$.

- Case 3: Mid activation group:

$$\mu_C(t) = \begin{cases} 677, & 110 + \xi_C < t < 360 \\ 27, & t < 110 + \xi_C \end{cases} \quad (97)$$

$$C = 1,2,3, \dots, C_{max}(\tau) \quad (98)$$

ξ_C is a random number picked from $\xi_C \epsilon \{0, \dots 90\}$. Cells experience random activation between 125 and 215 minutes. The total number of mid activation cells is $C_{max}(\tau)$.

- Case 4: Late activation group:

$$\mu_D(t) = \begin{cases} 778, & 235 + \xi_D < t < 360 \\ 27, & t < 235 + \xi_D \end{cases} \quad (99)$$

$$D = 1,2,3, \dots, D_{max}(\tau) \quad (100)$$

ξ_D is a random number picked from $\xi_D \epsilon \{0, \dots 90\}$. Cells experience random activation between 245 and 335 minutes. The total number of early activation cells is $D_{max}(\tau)$.

The total number of cells in each group sums the total number of cells of the population. Thus, with *E* as the total number of cells in the population, we can write:

$$\frac{1}{E}\Big(A_{max}(\tau) + B_{max}(\tau) + C_{max}(\tau) + D_{max}(\tau) + R_{max}(\tau)\Big) = 1 \quad (101)$$

The number of cells of each activation group was shear dependent. The percentage of cell population $(\frac{A_{max}}{E}, \frac{B_{max}}{E}, \frac{C_{max}}{E}, \frac{D_{max}}{E})$ vs. shear stress is depicted in Figure 172. The shear dependency of the groups was based on observation made with the gradient channel experiments (Chapter 4).

Each group's cell number can be written as an empirical function of shear stress:

$$\frac{A_{max}(\tau)}{E} = -0.11935 \cdot \tau + 9.3632 \quad (102)$$

$$\frac{B_{max}(\tau)}{E} = 0.0821 \cdot \tau^2 - 0.5485 \cdot \tau + 13.7780 \quad (103)$$

$$\frac{C_{max}(\tau)}{E} = -0.8862 \cdot \tau + 26.8841 \quad (104)$$

$$\frac{D_{max}(\tau)}{E} = -1.2120 \cdot \tau + 27.1389 \quad (105)$$

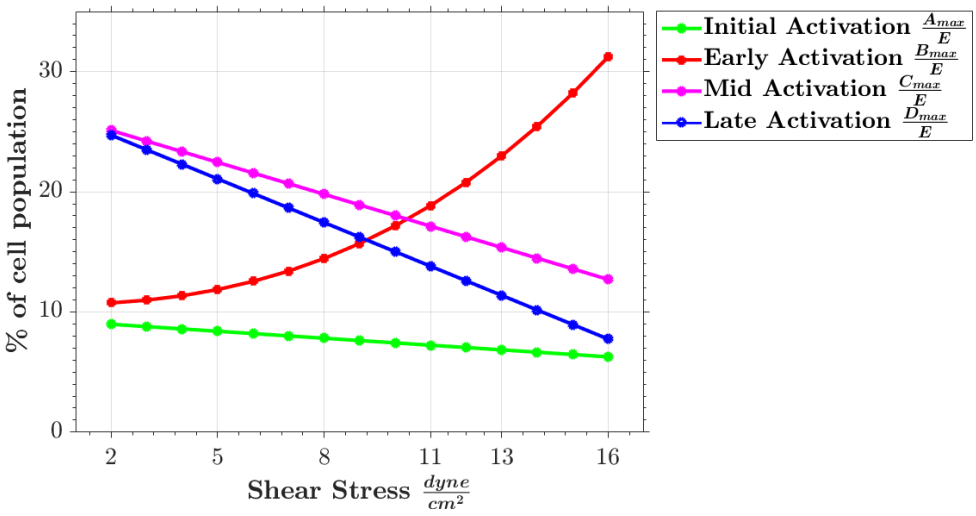

Figure 172: The shear stress dependency of the activation groups based on the measurement of the nuclear GFP-RelA intensity of cells exposed to a shear stress gradient (Chapter 6).

The time dependent stimuli intensity of each cell was then fed into a receptor activation equation (Eq.(66)) and the NF-κB pathway, as described in section 0, was calculated for each cell.

6.4.3. Initial, early, mid and late activation groups

Based on experimental observations of nuclear translocation of GFP-RelA in a shear stress gradient (Chapter 4), the flow triggers for each of the four groups at four different time ranges could be defined. The time ranges are: Initial activation (0 min), early activation range (15 – 75 min), mid activation range (110 – 150 min) and late activation range (275 – 335 min).

During each time span a certain percent of cells were activated. Inactive cells also experience random activation. Based on experimental observations in a shear stress gradient (2-16 dyne/cm^2) (Chapter 4), a mean percentage for each group was defined for 1500 cells within the shear stress gradient as shown in Table 6**Error! Reference source not found.**.

The temporal changes of activated receptors for 1500 cells based on the activation groups defined in Table 6 are depicted in Figure 173.A. The time range for the four activation groups is indicated: initial (green) early (red), mid (magenta) and late (blue). A constant high activation of receptors throughout the 360 minutes was observed.

Table 6: Time range and percentage of total population of activation groups

	Time span [min]	**% of total population**
Initial Activation Range:	0	$\frac{A_{max}}{E} = 0.10$
Early Activation Range:	15 – 75	$\frac{A_{max}}{E} = 0.2$
Mid activation range:	110 – 200	$\frac{B_{max}}{E} = 0.2$
Late activation range:	235 – 325	$\frac{C_{max}}{E} = 0.2$
Inactive with random activation:	0 – 360	$\frac{R_{max}}{E} = 0.3$

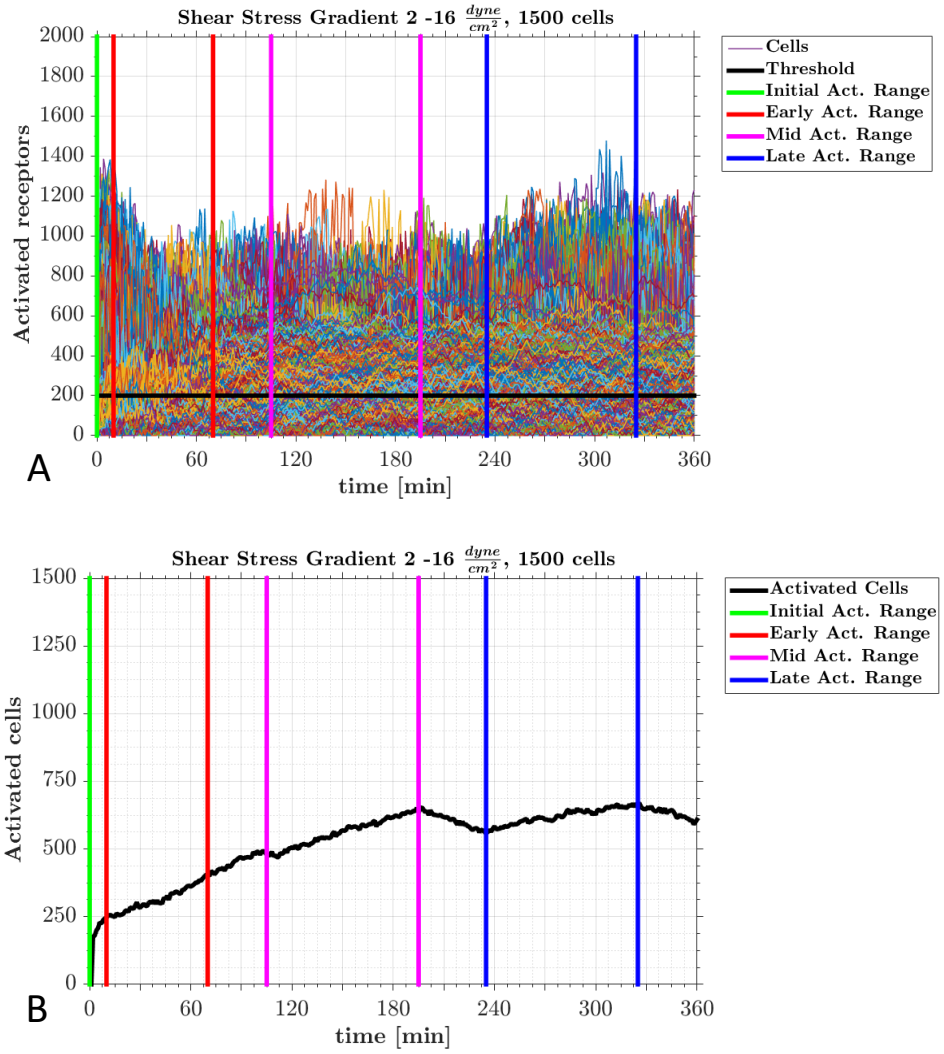

Figure 173: A: The activation profile of 1500 cells in a shear stress gradient. Cells were activated at 3 different time ranges: early (15 – 75 min, red), mid (120 - 180 min, blue) and late (250 – 330 min, green) activation. The threshold is indicated at 200 cells. B: The number of activated cells with indicated activation ranges.

In Figure 173.B, the number of activated cells in a cell population exposed to a shear stress gradient of 2 – 16 dyne/cm^2 for 360 minutes using the mean percentages from Table 6 are shown. The number of activated cells increases linearly until approximately 190 minutes. From 190 minutes onwards, the number of activated cells remains around 600.

6.4.4. Cell population read outs

The results of the shear induced NF-κB population model are presented with the following quantities extracted from the NF-κB pathway model depicted in section 0:

- The total nuclear NF-κB concentration normalised by time average:

$$\mathrm{NF}\kappa B_{Nuc}(t) = \frac{\mathrm{NF}\kappa B(t) + I\kappa B\alpha\mathrm{NF}\kappa B_n(t) + E}{\langle \mathrm{NF}\kappa B(t) + I\kappa B\alpha\mathrm{NF}\kappa B_n(t) + E \rangle} \quad (106)$$

Where *E*=0.035 is an included measurement noise to allow normalisation of inactive cells and mimic experimental conditions.

- The total cytoplasmic IκBα concentration:

$$I\kappa B\alpha_{Cyto}(t) = IKK_a I\kappa B\alpha(t) + IKK_a I\kappa B\alpha\mathrm{NF}\kappa B(t) + I\kappa B\alpha(t) + I\kappa B\alpha\mathrm{NF}\kappa B(t) \quad (107)$$

- And the active IKK concentration:

$$IKK_{Activated}(t) = IKK_a + IKK_a I\kappa B\alpha(t) + IKK_a I\kappa B\alpha\mathrm{NF}\kappa B(t) \quad (108)$$

The nuclear NF-κB concentration was normalised using the time average (for comparison with the live-cell imaging experiments), while active IKK and IκBα were giving in arbitrary concentration units.

6.4.5. NF-κB pathway in a cell population exposed to a shear stress gradient of 2 – 16 dyne/cm^2.

The NF-κB pathway cell population model was run for 1500 cells exposed to a shear stress gradient of 2 - 16 dyne/cm^2 with the mean group percentages reported in Table 6. The model parameters were fitted to the peaks and the percentage of peak groups correspond to the experimental results of the nuclear GFP-RelA intensity

observed in a gradient channel as reported in Chapter 4. The nuclear NF-κB concentrations of all cells are mapped in Figure 174.A. Each groups mean and peak are plotted in Figure 174.B. The map, means and peaks can be directly compared with the experimental results (Figure 174.C and Figure 174.D).

In Figure 174.A, the cell population model calculated four peaks (red regions). These are comparable with the peaks observed in the experimental results in Figure 174.C. The peaks include a small initial activation peak, followed by three large peaks at time intervals of approximate 110, 210 and 345 minutes. The inactive group remained close to 1, with a few random nuclear translocations of NF-κB. In the experiment, the defined inactive group was found to experience a slight increase in nuclear GFP-RelA from 300 to 360 minutes.

In Figure 174.B, the peaks of the groups occur at approximately 30, 110, 210 and 345 minutes. The inactive group (30%) remained close to 1. Similar trends of the peaks were observed in the experiments (Figure 174.D)

In Figure 175, cell population simulation results of the temporal profiles of phosphorylated IKK and cytoplasmic IκBa of 1500 cells exposed to a shear stress gradient are shown as a map (Figure 175.A and C) and the mean of each cluster group (Figure 175.B and D).

The four active groups, showed four distinctive phosphorylated IKK peaks. The initial activation group had a strong IKK activation. This was due to defined synchronised activation of the initial activation group. The early, mid and late activation group had flat (like a flat hill) activation peak disturbed over the defined time ranges of each group. The inactive group experienced a small IKK activation at around 30 minutes, which then remained at a low level.

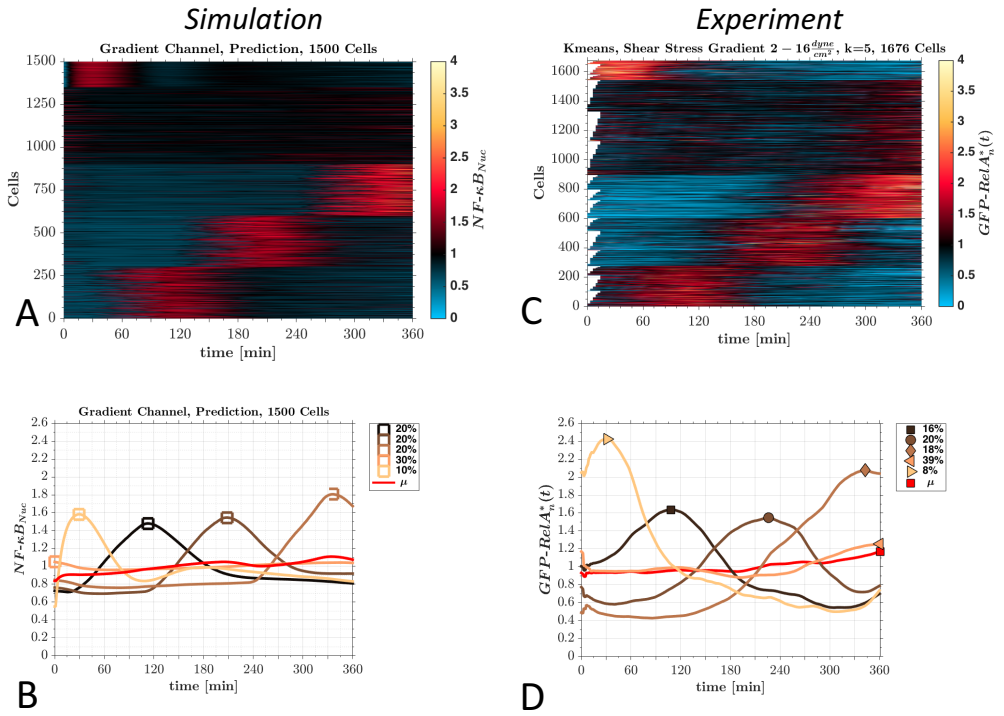

Figure 174: A: Cluster map of the predicted temporal nuclear NF-κB concentration (A) and measured nuclear GFP-RelA intensity (C) of a cell population exposed to a shear stress gradient of 2-16 dyne/cm^2. Means of the predicted temporal nuclear NF-κB concentration (B) and measured nuclear GFP-RelA intensity (C) of each cluster group. The total mean is indicated in red. The peaks of each group and the percentages of the total population are indicated.

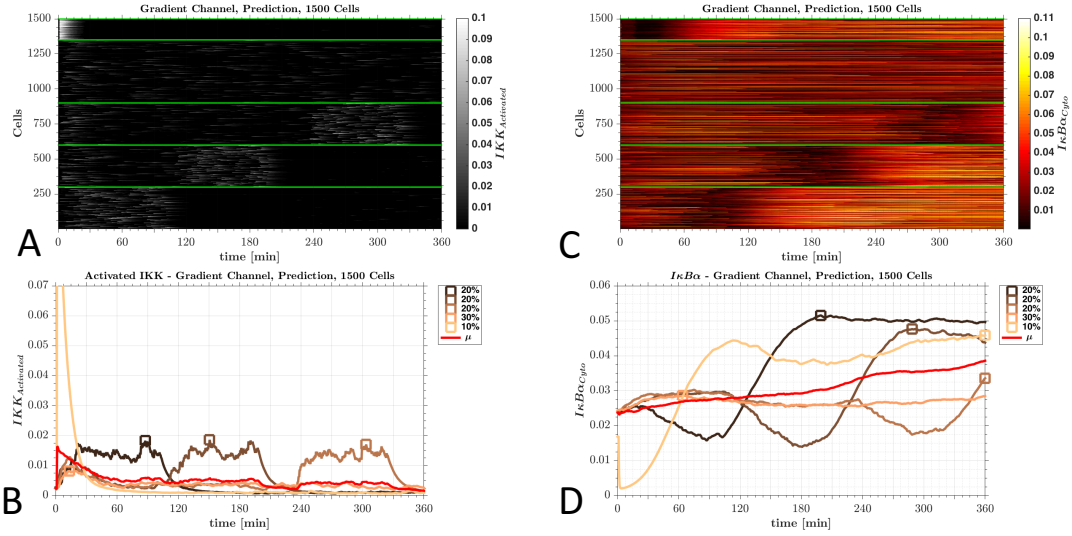

Figure 175: Cluster map of the temporal activated IKK(A) and IκBα (C) concentration of 1500 cells exposed to a shear stress gradient (2 – 16 dyne/cm^2). Means of the temporal activated IKK(B) and IκBα (D) concentration of each clustered group and the total mean (red). In addition, the peaks of each group and the percentages of the total population are indicated.

The cytoplasmic IκBα concentration of the groups behaved in a similar fashion. The initial activation group experienced an initial sharp drop of IκBα that recovered quickly after 60 minutes. The early, mid and late activation groups experienced a mild but wide drop of IκBα with local minima at 90, 180 and 300 minutes. The inactive cells remained close to their initial value with little change in their IκBα concentrations.

6.4.6. Prediction of shear dependent nuclear translocation of NF-κB

The effect of each individual shear stress magnitude on the nuclear translocation of NF-κB was calculated. This was achieved by changing the percentage of each activation group based on observations of the gradient channel experiments (Chapter 4) and as defined in section 6.4.2. The change of percentage of each activation group was fitted to a linear or polynomial regression curve as shown earlier.

We simulated the shear induced cell population model at shear stress magnitudes of 1-16 dyne/cm^2 with 300 cells at each shear stress magnitude.

Accordingly, the total cell population was 16x300 = 4800 cells. In Figure 176.A, the population mean of the nuclear NFκB concentration for all shear stress magnitudes 1-16 dyne/cm^2 (interpolated between magnitudes) are plotted as a contour map and can be directly compared with the experimental results shown in Figure 176.B. The predicted contour map in Figure 176.A can be divided into four regions:

- *Low early translocation*: Time: 0 -180 minutes and 0 – 9/10 dyne/cm^2.
- *Medium-High early translocation*: Time: 0 -180 minutes and 10 – 16 dyne/cm^2.

- *High late translocation*: Time: 180 – 360 minutes and 0 – 10 dyne/cm^2.
- *Medium late translocation*: Time: 180 – 360 minutes and 10 – 16 dyne/cm^2.

These four regions are in qualitative agreement with the experiments shown in Figure 176.B. Some differences in the four regions between prediction and experiment were found. These include low concentration at early low shear stress or increased concentration at 360 minutes. Nevertheless, the prediction could predict closely the major trends observed within the four shear stress boxes.

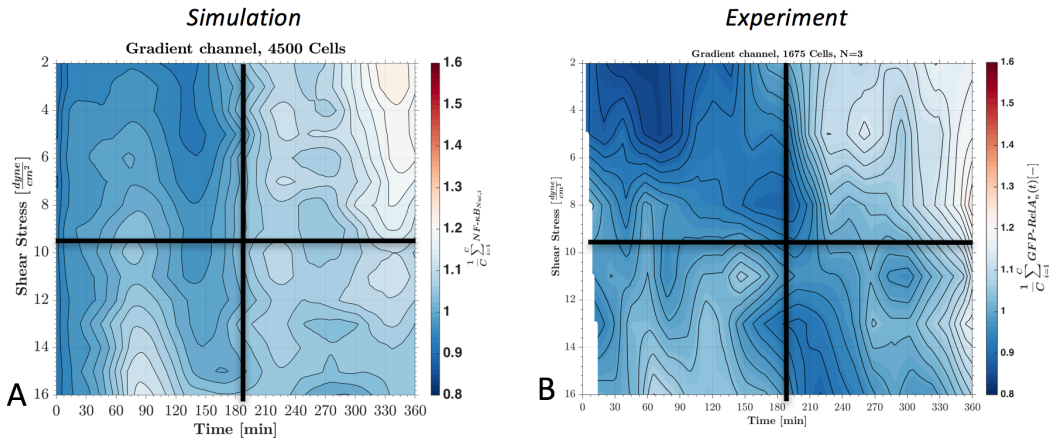

Figure 176: A: Cell population simulation results: The mean of nuclear NF-κB concentration of 300 cells at shear stress 1-16 dyne/cm^2 displayed as a contour map. B: experimental results: The mean nuclear GFP-RelA intensity measured at 2, 5, 8, 11, 13 and 16 dyne/cm^2 (values in-between were interpolated).

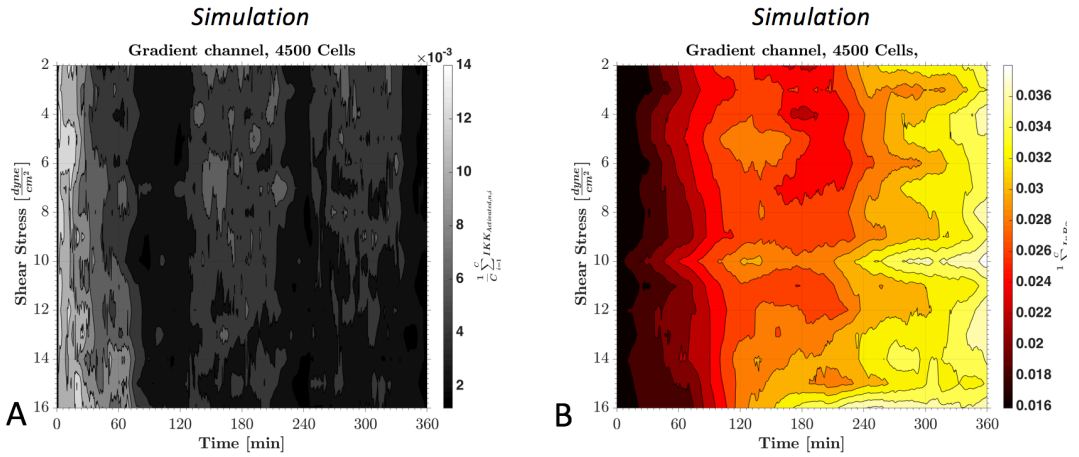

Figure 177: Cell population results of the mean of activated IKK (A) and cytoplasmic IκBα (B) at shear stress magnitudes of 1-16 dyne/cm^2.

In Figure 177, the contour maps for the interpolated total population mean of activated IKK (Figure 177.A) and cytoplasmic IκBα (Figure 177.B) for all shear stress magnitdues are shown. A high IKK activation occurred between 0 and 60 minutes at all shear stress magnitudes. Subsequently, the activation dropped and reached a minimum around 90 minutes. Between 120 and 180 minutes a second but less strong activation occurred at all shear stress magnitudes with a fading tendency towards high shear stress magnitudes. Between 240 and 360 minutes, a third IKK activation occurred, this time, the activation was noticeably stronger at lower shear stress magnitudes. In Figure 177.B, the cytoplasmic IκBα concentration experienced a low concentration from 0 to approximate 90 minutes at all shear stress magnitudes. The IκBα concentration rose at all shear levels, with a slight tendency of more IκBα production at higher shear stress magnitudes.

6.4.7. Low and high shear stress prediction

The cell population stimulated with shear stress confirmed the similar trends observed in a gradient channel as demonstrated in Figure 177. Hence, individual shear responses can be examined and compare with experiments.

In Figure 178, the cell population results of the total population mean of nuclear NF-κB concentration for cells exposed to a low and high shear stress (2 and 16 dyne/cm^2) are compared with experimental findings in the gradient channel and the straight Ibidi channel. At low shear stress, the cell population simulation predicted an increasing nuclear NF-κB concentration with local peaks at 190 and 350 minutes. This is comparable to the observation at low shear stress made in the gradient

channel. The measurements in the straight Ibidi channel showed a similar trend of an increase in nuclear GFP-RelA when exposed to a uniform low shear stress.

The population model predicts that cells exposed to a high shear stress, experience a flatter nuclear NF-κB profile. The flat profile includes a small early bump at 90 minutes that is comparable to small increases observed at high shear stress in the gradient channel and within the straight uniform flow channel. In general, low shear stress appeared to increase the nuclear NF-κB concentration within 360 minutes exposure to low shear stress, while at high shear stress the mean of nuclear NF-κB appeared more affected within the first 120 minutes.

The cell population simulation results of the total population mean of activated IKK and cytoplasmic IκBα for cells exposed to a low and high shear stress (2 and 16 dyne/cm^2) are depicted in Figure 179.

The activation of IKK at low show shear stress showed small peaks at 0, 60, 180 and around 300 minutes. This was due to the defined activation groups. At the peaks the standard deviation of IKK is large indicating high heterogeneity at the activation point. On the contrary, high shear stress caused a stronger IKK activation between 0 and 60 minutes, followed by a weaker activation. Thus, the simulation revealed that low shear stress caused more IKK activation distributed in time, while high shear stress only triggered an early strong activation of IKK.

At low shear stress, the cytoplasmic IκBα concentration experienced two drops at 30 and 180 minutes. High shear stress only caused an early drop between 0 and 90 minutes. Thereafter, it rose to a higher level. In both cases, the IκBα concentration of the population was highly heterogenic, which is reflected in the larger standard deviation.

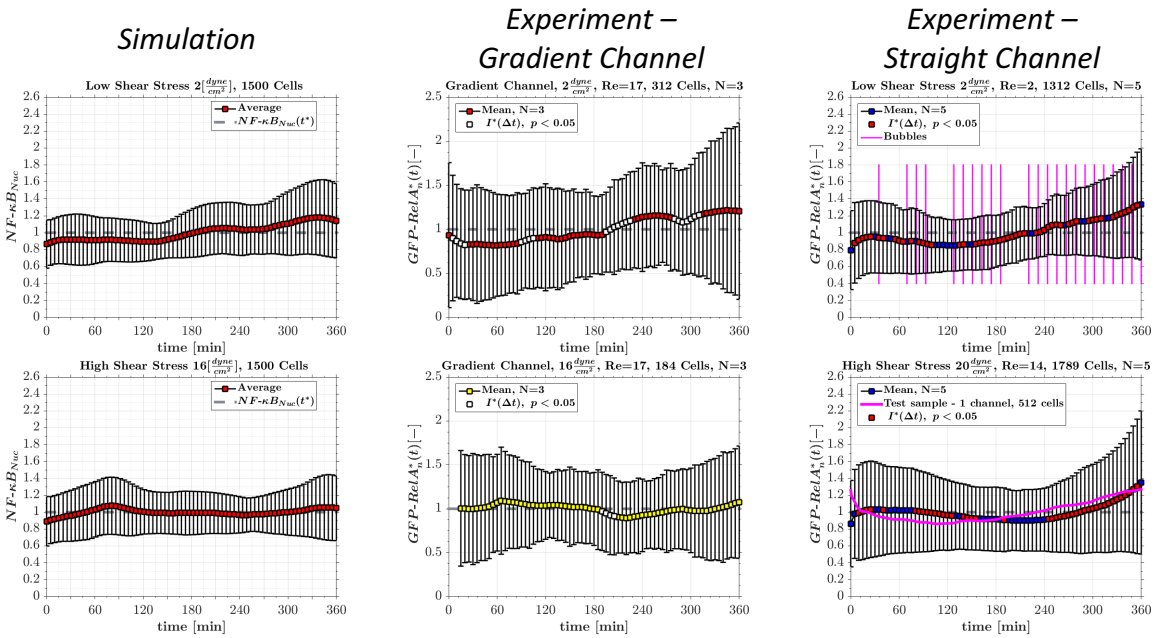

Figure 178: Comparison of low and high shear stress results of the cell population simulation, gradient channel and straight channel experiments.

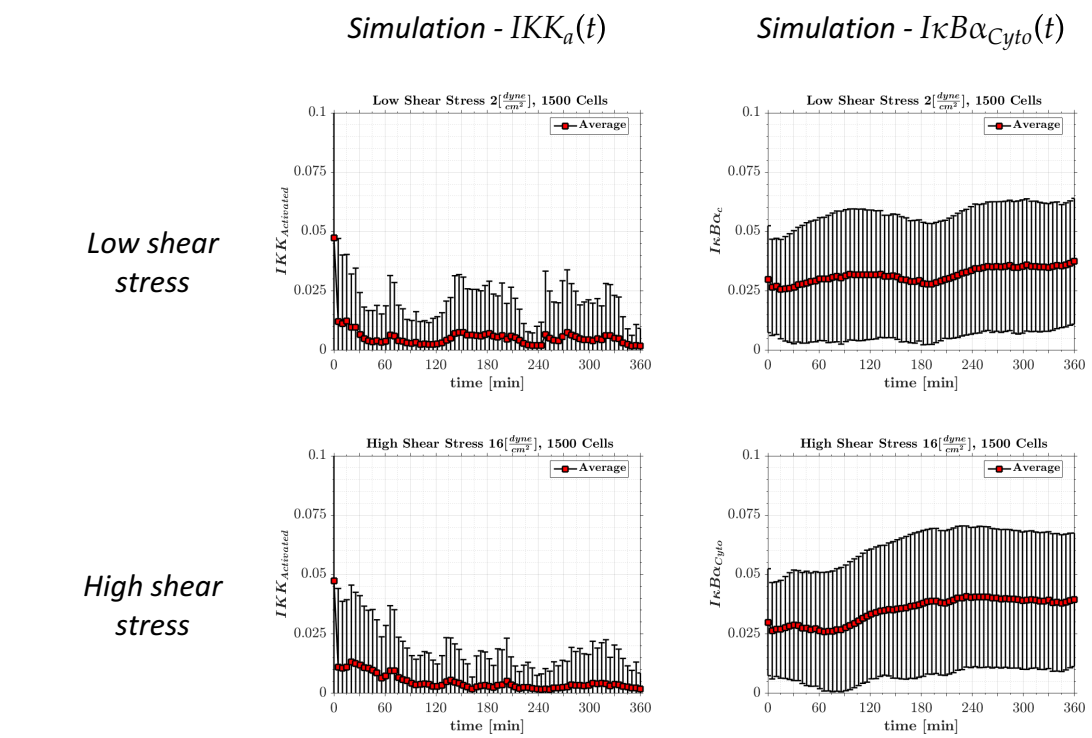

Figure 179: Cell population results for active IKK and cytoplasmic IκBα for low and high shear stress (2 and 16 dyne/cm^2).

6.4.8. Backward facing step channel prediction

The cell population model was exemplified at the bottom wall of a backward facing step channel with a Reynolds number of 200. The backward facing step was analysed to apply the nuclear GFP-RelA dynamics observed in the gradient channel to a more complex flow field. The aim was to gain insight with the mathematical model about how nuclear translocation of GFP-RelA is effect under such conditions.

The nuclear NF-κB, activated IKK and cytoplasmic IκBα concentration at the bottom wall of the step channel are shown Figure 180, Figure 181 and Figure 182.

In Figure 180, Figure 181 and Figure 182 the shear stress profile along the bottom wall (A), the total population mean and active cell only mean of nuclear NF-κB concentration (Figure 180.B and C), cytoplasmic IκBα (Figure 181.B and C) and activated IKK (Figure 182.B and C) are plotted. Each point indicated in the shear stress profile corresponds to 300 cells simulated with the cell population model at the corresponding shear stress magnitude. The 300 cells were then averaged for the whole population or the active cells only. Four flow regions (stagnation zone, recirculation zone, flow reattachment and developed flow) of the backwardfacing step channel will be discussed for NF-κB, IκBα and active IKK.

Stagnation zone effect on nuclear NF-κB (Figure 180): At the stagnation zone (Low shear stress values of 0 to 5 dyne/cm^2), cells experienced an increase in nuclear NF-κB concentration only towards the end of the simulation (360 minutes).

Recirculation zone effect on nuclear NF-κB (Figure 180): At the recirculation zone the shear stress ranges from 0 to 16 dyne/cm^2 and includes a positive and negative shear stress gradient (0 to 16 dyne/cm^2 and 16 to 5 dyne/cm^2). At recirculation zone,

cells experienced a high nuclear NF-κB concentration early at approximately 90 minutes, with the highest nuclear NF-κB concentration occurring at 16 dyne/cm^2. Subsequently, the concentration dropped and remained relatively low throughout the simulation. This suggests that disturbed flows (recirculation flows) result in an increased nuclear NF-κB concentration within 90 minutes. The same trend was observed for the active cells.

Flow reattachment effect on nuclear NF-κB (Figure 180): At the flow reattachment zone, the flow re-established a rectangular channel flow profile. This included a shear stress gradient from 0 to 12 dyne/cm^2 spread over 1mm and an adaption length of 6mm with 10 – 12 dyne/cm^2.

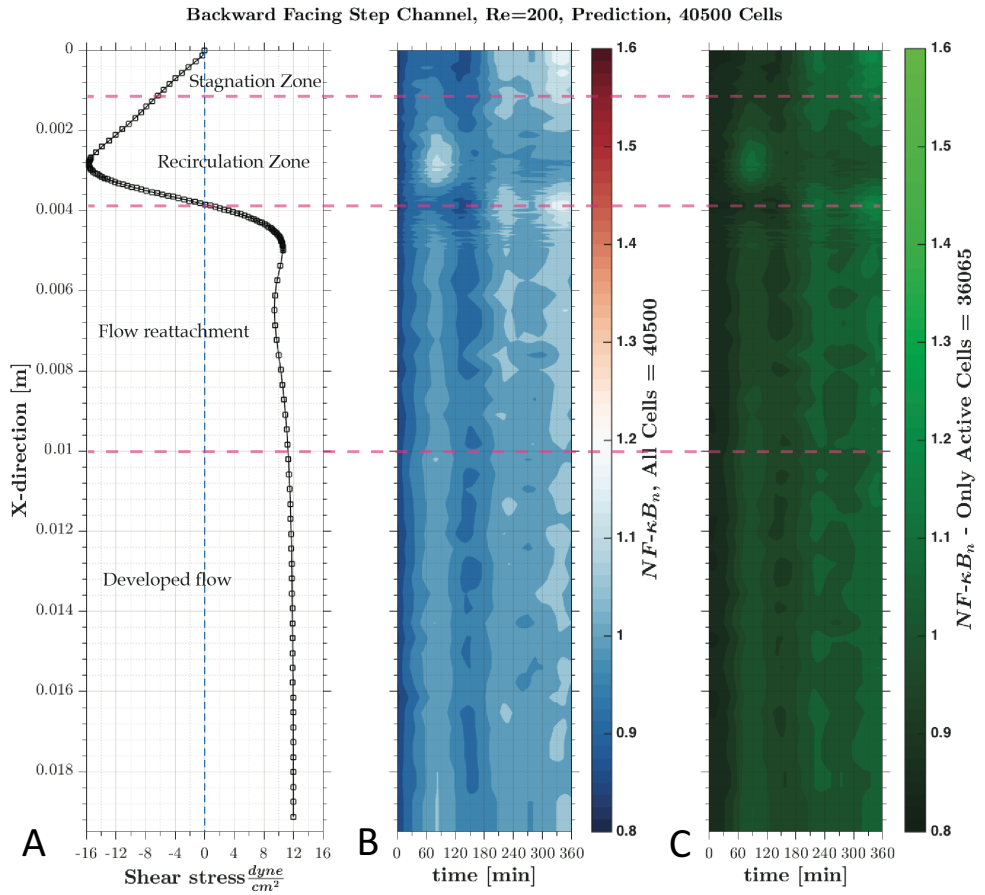

Figure 180: The shear stress profile along the bottom wall of the step channel (A). The total mean of the nuclear NF-κB concentration along the bottom wall of the step channel for 360 minutes (B). The mean of only active cells along the bottom wall of the step channel (C).

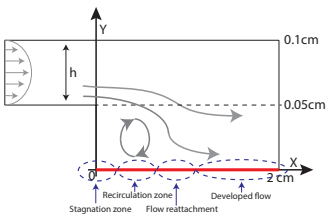

Directly after the recirculation zone and at the beginning of the flow reattachment, cells experienced only an increase of nuclear NF-κB concentration from 180 minutes onwards. For 5 to 12 dyne/cm^2, all cells experienced a medium-high nuclear NF-κB concentration at 90 minutes. This was followed by a decrease and a high concentration at 360 minutes. The active cells showed a similar trend.

Developed flow effect on nuclear NF-κB: At the developed flow area, the flow reached a fully developed state in a rectangular channel flow profile and the shear

stress remained constant at 12 dyne/cm^2. Therefore, the nuclear NF-κB concentration has the same trend along the section. A medium-high concentration at 90 minutes was followed by a decrease. A subsequent increased concentration occurred from 180 minutes onwards. The active cells were found to have the same trend as the total mean.

Effect of a backward facing step channel on the IKK activation (Figure 181**):** A high activation of IKK occurred after onset of flow at all shear stress magnitudes throughout the channels. The initial high activation dropped quickly until 60 minutes. A second “wave” of IKK activation was observed from 120 to 200 minutes, with stronger activation at the stagnation zone, flow reattachment and developed flow sections. The recirculation zone showed no second IKK activation for very high shear stress magnitudes. A third “wave” of IKK activation occurred at 240 to 330 minutes. This time the IKK activation was weaker throughout, but strongest at the stagnation zone and at the beginning of the flow reattachment (reattachment point).

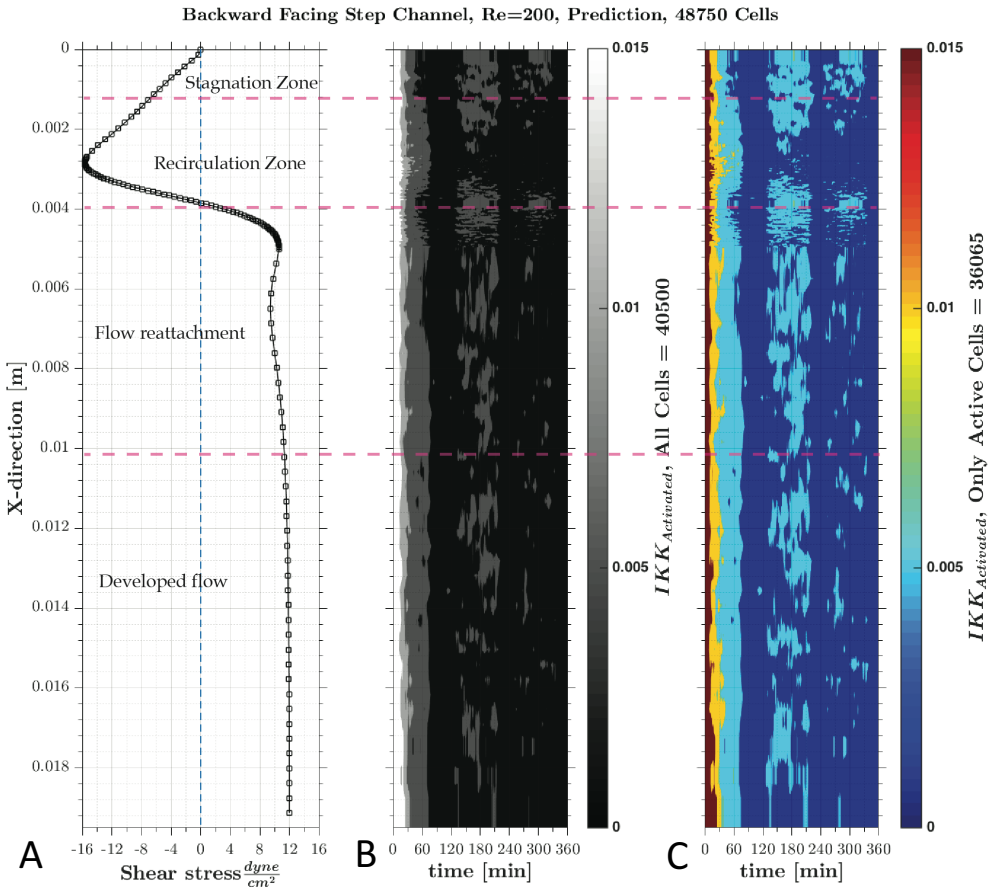

Figure 181: The shear stress profile along the bottom wall of the step channel (A). The total mean of the active IKK concentration along the bottom wall of the stepchannel for 360 minutes (B). The mean of only active cells of the active IKK concentration along the bottom wall of the step channel (C).

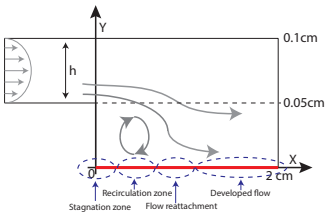

Effect of a backward facing step channel on the IκBα concentration (Figure 182): The model predicts a drop in the IκBα concentration at all shear stress magnitudes from 0 to 30 minutes. IκBα then increased at all channel positions. The strongest production of IκBα from 120 minutes onwards was observed at the recirculation zone. The production was weaker at the stagnation zone and at the beginning of the flow reattachment. The developed flow area experienced a strong production of IκBα from 180 minutes onwards.

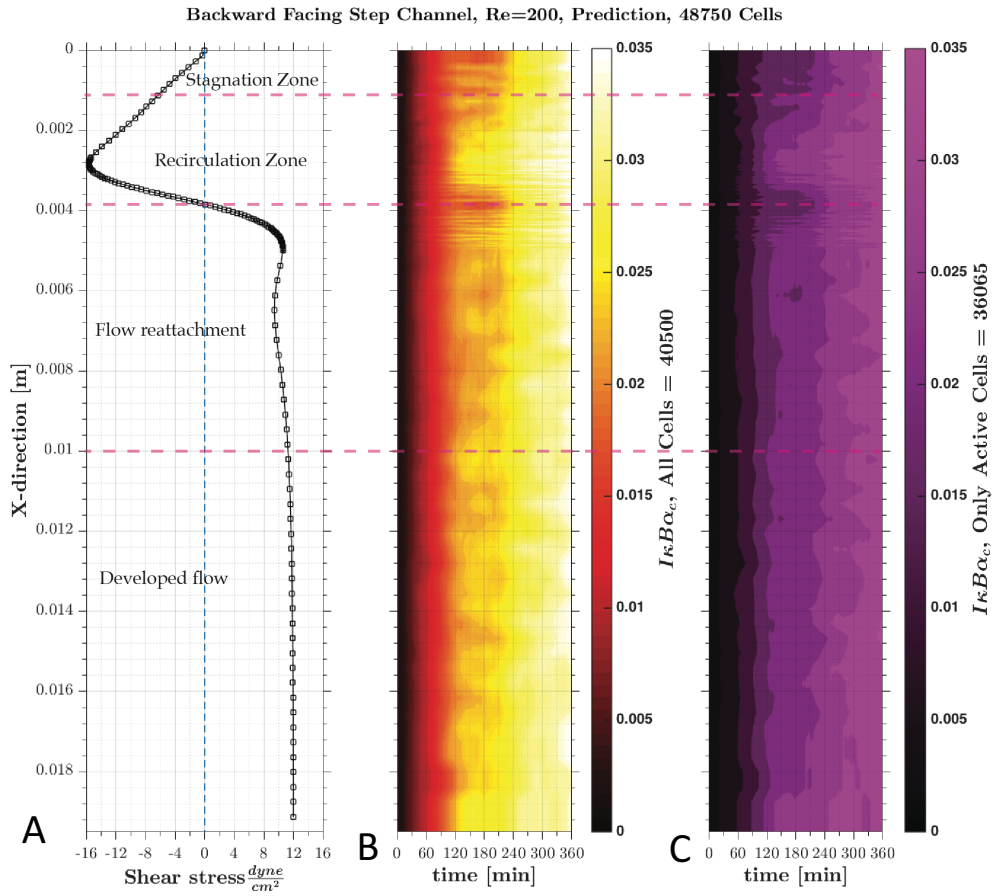

Figure 182: The shear stress profile along the bottom wall of the channel (A).The total mean of the cytoplasmic IκBα concentration along the bottom wall of the stepchannel for 360 minutes (B). The mean of the only active cells cytoplasmic IκBα along the bottom wall of the step channel (C).

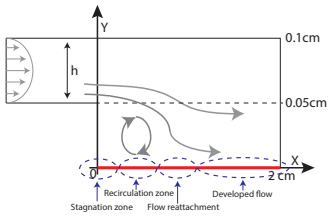

In Figure 183, the concentration of NF-κB, active IKK and IκBα throughout the channel are plotted at different time points (90, 180 and 360 minutes). This illustration demonstrates the complexity of the system and the difficulty of understanding the signalling when only capturing a limited number of time points. At the recirculation zone and flow attachment point, the NF-κB concentration experienced strong non-linear local and temporal changes. This was also the case for IKK activation at the recirculation and flow attachment. Only the IκBα concentration

appeared to be more linear as it showed an increasing concentration in time at all positions within the channel.

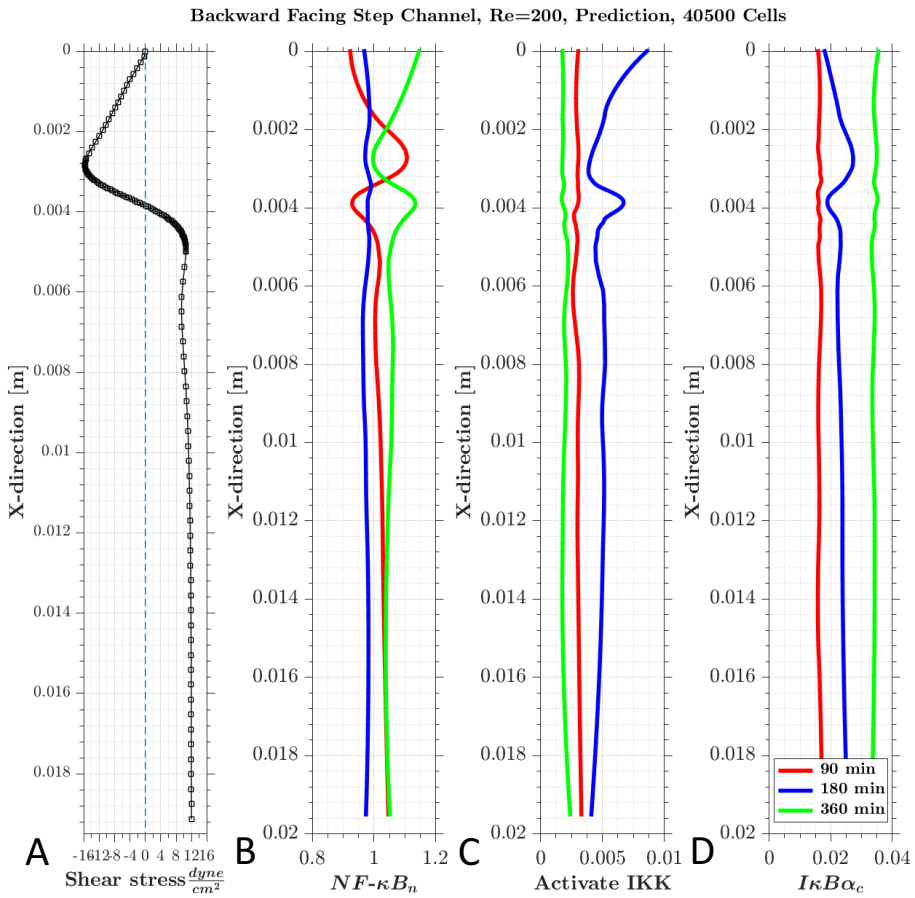

Figure 183: The shear stress profile along the bottom wall of the step channel (A). The NF-κB (B), active IKK (C) and IκBα (D) concentration throughout the channel at three different time point (90, 180 and 360 minutes).

6.5. Proposal for an extended NF-κB model

We propose an extended biochemical model that links wall shear stress to the activation and nuclear translocation of NF-κB. The WSS-PI3K-AKT-NFkB model is depicted in Figure 184.

The model is based on proposed pathways by Wang et al. [104, 105]. Wall shear stress is sensed by integrins, transmited via FAK and Src kinases (focal adhesion and actin cytoskeleton) to activate Flk-1 [105]. In addition, it is hypothesis that PECAM-1

sense shear stress and activates - in the presence of VE-cadehrin - Flk-1 [17]. Flk-1 can be chemically activated by VEGF (VEGF121, VEGF161) [104, 177]. Activated Flk-1 triggers (via Cbl) the phosphorylation of PI3K (It is currently believed that the mechanical and chemical stimuli converge at Flk-1 [104]). Phosphorylated PI3K then activates AKT, which triggers the activation of IKK. Active IKK promotes the degradation of IκB, which inhibits NF-κB. Due do degradation of IκB, NF-κB unbinds from the IκB-NF-κB complex. Free NF-κB can travel into the nucleus, where it causes transcription of inflammation specific genes. Most importantly, it transcribes IκB and thus renews the lost IκB, which binds to free NF-κB and inhibits it and consequently stops it travelling into the nucleus.

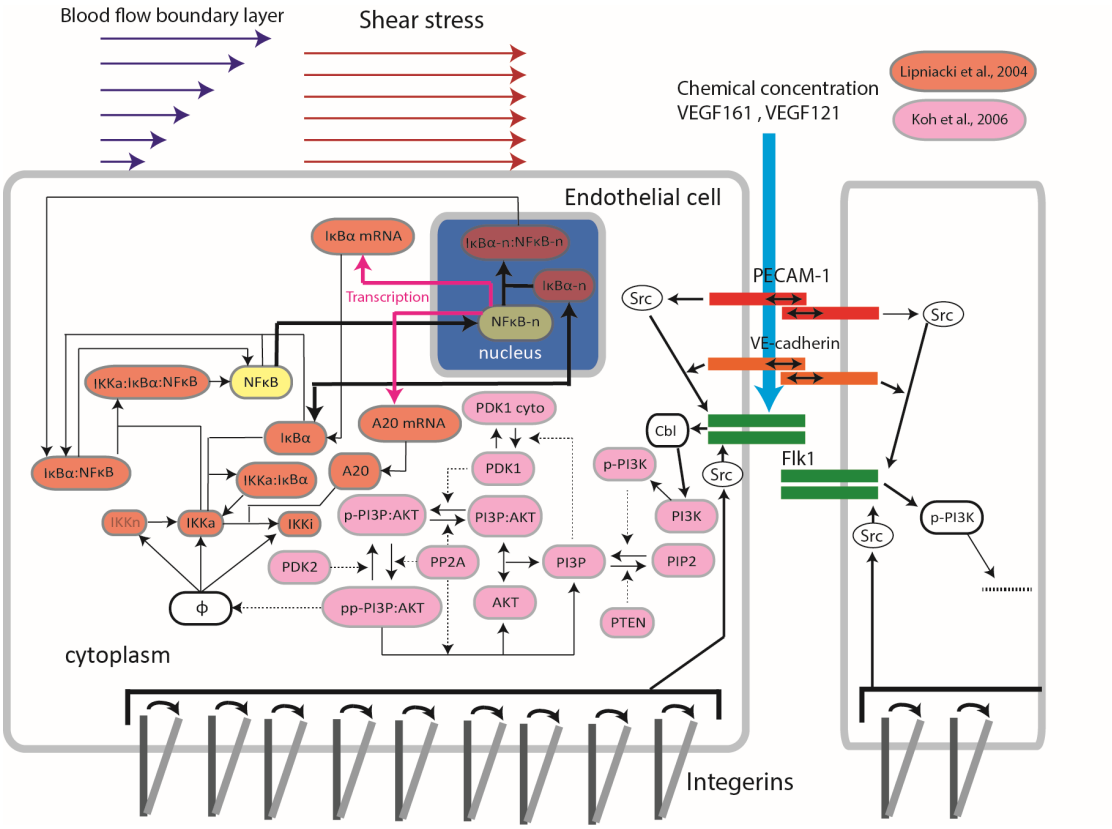

Figure 184: Proposed mechanotransduction pathway for shear stress induced nuclear translocation of NF-κB. The model is a combination the modelling effort by Lipniacki *et al.* [80], Koh *et al.* [178], Koo *et al.* [179] and Go *et al.* [180].

In order to model the bio-chemical reactions, the WSS-PI3K-AKT-NF-κB model can be divided into two pathway parts: The first pathway describes the shear stress dependent activation of AKT via PI3K. The second pathway describes the NF-κB activation and translocation induced by activated AKT.

In the first part, the activation (phosphorylation) of PI3K by shear stress with an empirical formula is described based on observations by Go *et al.* [180]. Once PI3K is phosphorylated, it causes a reaction chain to activate AKT. This reaction chain has been described by by Koh *et al.* [178] and Koo *et al.* [179]. It is constructed as follows: Activated PI3K in combination with PIP2 and PTEN phosphorylates PIP3. Phosphorylated PIP3 attracts AKT towards the plasma membrane and PDK1 causes the first phosphorylation of AKT. In addition, PDK2 (a so far unknown kinase) phosphorylates AKT, making it double phosphorylated. The double phosphorylated AKT serves as input signal that activates the IKK complex.

The second pathway describes the NF-κB activation induced by activated AKT [80]. AKT would be handled as the trigger signal for IKK activation and the same model as described in Chapter 6.1.5 would be applied.

7. Discussion of Key Findings, Limitations and Further Work

7.1. HUVECs expressing GFP-RelA and H2B-mCherry stimulated with TNF-α confirm the same temporal nuclear translocation of GFP-RelA as endogenous p65 in non-transfected HUVECs

This work demonstrates for the first time the nuclear translocation of GFP-RelA of a large cell population in HUVECs in real time. HUVECs transfected with two plasmids (H2B-mCherry and GFP-RelA) were successfully grown. Despite the toxicity of plasmids, confluent cultures with a transfection efficiency of ca. 80-90 % were maintained. Expressing HUVECs were stimulated with different TNF-α concentrations and the nuclear translocation was measured with either a confocal or a wide-field microscope. An increase in nuclear translocation of GFP-RelA was observed with increasing TNF-α concentration. These findings were confirmed with immunohistochemistry experiments. A main concern was that the inserted plasmid GFP-RelA reacts differently than the endogenous p65. However, with the observed agreement between immunohistochemistry and live-cell imaging experiments, it was concluded that the GFP-RelA reflects the endogenous p65 temporal dynamics. Stimulation with 100 and 10 ng/mL TNF-α resulted in a major peak at 30 minutes. This was followed by a drop and slight local peak at 120 minutes, which then decreased again. It was observed that most cells were synchronised at the major peak but subsequently lost synchronisation. These observed characteristics agree

well with studies of live-cell imaging of NF-κB in several different cell types (p65 knock out or in) [92, 95, 96, 99, 100, 181].

Measuring nuclear translocation of GFP-RelA optimises the experimental time needed in comparison with immunohistochemistry. While immunohistochemistry requires fixing and staining at each time point, live imaging cells can be recorded in a time interval of 2-10 minutes and can capture the full dynamics in one experiment. However, there is several technical obstacles to overcome. These include the accuracy and speed of the camera, and photo bleaching of the fluorescents tags. During trial and error experiments, GFP-RelA expressing cells were imaged live with a confocal microscope every 2.5 minutes at a high resolution with a high laser power. The cells exploded after approximately one hour as shown in Figure 185. This was probably due to the high energy created by the laser on the expressed GFP molecules within the cells, which might be highly toxic. The LED lamps of the wide-field microscope were weaker and less toxic for the cells. However, to avoid photo bleaching and reduce the toxicity of GFP we set the imaging time interval between 10 and 15 minutes

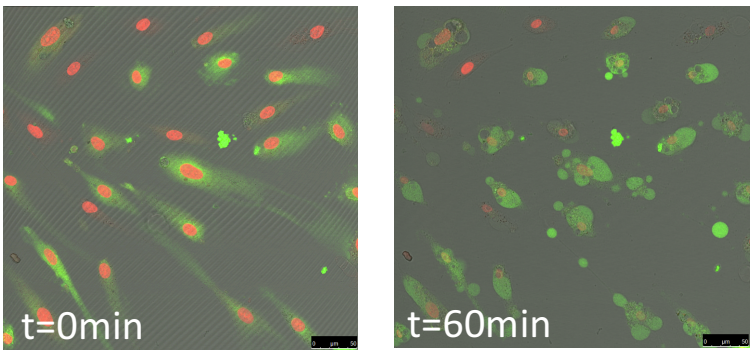

Figure 185: HUVECs expressing GFP-RelA and H2B-mCherry "exploded" after approximating one hour of imaging with a high laser power at time interval of 2.5 minute.

7.2. Lowering the TNF-α concentration resulted in a reduction of nuclear translocation of GFP-RelA, activation and synchronisation of cells.

When stimulated with a very high TNF-α concentration (100 ng/mL) all cells were activated, synchronised and had a high nuclear GFP-RelA intensity that peaked at around 30-45 minutes. With a decreasing TNF-α concentration, the major peak at 30 minutes was found to decrease, as did the number of activated cells and the level of synchronisation. With immunohistochemistry, the decrease in peak at 30 minutes of the endogenous p65 when stimulated at different TNF-α concentrations could be confirmed. Similar observations have been made by Tay *et al.* [95] and Zambrano *et al.* [99, 100]. They used p65-knockout cells with an inserted RelA plasmid. They also observed moderation of nuclear translocation of GFP-RelA and less active cells when lowering TNF-α concentrations. In this work, it was not possible to knockout human endothelial cells and thus RelA was overexpressed with an inserted GFP-RelA plasmid. However, the same trends were still observed with overexpression of RelA. Nelson *et al.* [81] found a similar nuclear GFP-RelA temporal dynamics in transfected HeLa cells (endogenous and plasmid RelA) when treated with 10 ng/ml TNF-α. Their finding showed that overexpression of GFP-RelA can reproduce the dynamics of nuclear translocation of NF-κB. This is in agreement with the HUVECs observations in this work.

7.3. Spontaneous nuclear translocation of GFP-RelA occurs in static conditions

In this work, we observed that many cells (approximate 50%) experience spontaneous nuclear translocation of GFP-RelA under static conditions. It was expected that unstimulated cells would show an unchanged nuclear GFP-RelA signal

in time. However, this was not the case. Many cells experienced spontaneous nuclear translocation of GFP-RelA and were randomly distributed in time. Plotting the distribution of the maximum peaks under static conditions showed that the cells were very uniformly distributed in time (with slight tendency of early and late accumulation). Therefore, it appeared as if the nuclear GFP-RelA concentration was at a different state in every single cell or every single cell was out of phase. Moreover, it was difficult to identify the number of active or inactive cells in the large heterogeneity. The applied clustering methods required manual intervention to find a unique solution of activation groups. Zambrona *et al.* [99] observed that 15 % of cells had a significant spontaneous activation and after 15 hours of experiment, a total of 70 % showed spontaneous activation. Using Kmeans clustering, it was identified that approximately 50 % of cells experienced spontaneous activation. Hence, there is clear evidence of several spontaneous nuclear translocations of NF-κB occurring under static conditions. However, more research is required to quantify exactly the dynamics and percentage of such spontaneous translocation under static conditions.

7.4. Uniform low shear stress increases nuclear translocation of GFP-RelA

The mean of GFP-RelA and H2B-mCherry expressing HUVECs exposed to a low shear stress experienced an early small bump in nuclear GFP-RelA intensity (15-60 minutes). Subsequently, the intensity had a local minimum at 120 minutes from which it gradually increased until 360 minutes. Technical limitations of the experimental setup created the accumulation of bubbles in the silicon connection tubes. These bubbles were randomly released due to the low flow rate. At some

positions the nuclear GFP-RelA intensity was found to increase dramatically after bubble detection. Consequently, the increase in nuclear GFP-RelA intensity from 180 minutes onwards could be due to the number of passing bubbles. Mohan *et al.* [108] measured that the DNA binding activity in HAECs of NF-κB is elevated due to low shear stress at 30, 120 and 360 minutes. Measurements undertaken in this work, showed an increased nuclear GFP-RelA intensity at 30 minutes, a decreased concentration at 120 minutes and an elevated intensity at 360 minutes. It is questionable how the DNA-binding activity is related to the NF-κB concentration in the nucleus. Ganguli *et al.* [102] has shown that shear stress elevated nuclear eGFP-RelA expression within 60 minutes, which is comparable with the early bump measured in experiments carried out herein. Another study [182] showed an increase in phosphorylation of p65 after exposure to low shear stress at 60, 120 and 180 minutes.

7.5. Uniform high shear stress affects nuclear translocation of GFP-RelA

GFP-RelA and H2B-mCherry expressing HUVECs exposed to a high shear stress of 20 dyne/cm^2 showed a different dynamic than under uniform low shear stress. The mean of nuclear GFP-RelA intensity appeared to elevate and peak at 60 minutes. This reached a local minimum at 240 minutes. From 240 minutes, the intensity gradually increased up to 360 minutes. Comparing the maximum peak distribution of high shear stress with static conditions, a stronger accumulation of maximum peaks at 60 minutes and 360 minutes can be observed. The early accumulation of peaks may indicate an improved synchronisation of cells due to high shear stress when compared with static conditions.

The large increase of nuclear GFP-RelA intensity from 240 minutes onwards is thought to be due to cells undergoing apoptosis and cell division, which were not excluded from the tracking algorithm. At high flow rates, no bubble accumulation was observed within the silicon tubes. Passing bubbles might only have occurred at the beginning of the experiment when the flow was switched on. The effect of bubbles on the nuclear translocation of GFP-RelA under high shear stress or at high flow rates at later time points can be excluded. Therefore, incorporating cells in unhealthy states from 240 minutes may have increased the mean intensity based on limitation of the tracking algorithm. This might have also occurred in the uniform low shear stress experiment.

Previous studies [108] showed that high shear stress lead to increased DNA-binding activity of NF-κB in HAECs after 30 minutes. Subsequently, this was found to decrease below static conditions at 360 minutes. Increased NF-κB binding activity induced by shear stress after 30, 60, 90 and 120 minutes was also observed in BAECs [110]. A further study [106] demonstrated that high shear stress (15 dyne/cm^2) induced nuclear translocation of p65 in HUVECs with a peak occurring at 30 minutes (studied only from 0 to 240 minutes). Accumulation of p50-p65 heterodimers was observed after exposing BAECs for 60 minutes to 10 dyne/cm^2 [109]. A strong increase in nuclear p65 concentration was demonstrated in BAECs exposed to 12 dyne/cm^2 for 120 minutes [105]. The measurements carried out n this work showed a slight increase of nuclear GFP-RelA intensity in HUVECs at 60 minutes when exposed to 20 dyne/cm^2. The observations by Hay *et al.* [106] are closest to these findings (both studies used HUVECs). In comparison with other endothelial cell lines, it appears that BAECs experience a much stronger nuclear translocation of p65 under

high shear stress than what is observed in HUVECs. Therefore, repeating the current set of experiments with human aortic endothelial cells might show a stronger effect for nuclear translocation. Furthermore, repeating the experiments with HAECs would be more physiological relevant and may reveal more details in regards to shear induced translocation of p65 in the human vasculature.

7.6. Indication of differences in the temporal nuclear translocation of GFP-RelA at different shear stress magnitudes within a shear stress gradient

The mean of all cells tracked within the gradient channel showed little change within the first 180 minutes. Following 180 minutes, the intensity of nuclear GFP-RelA appeared to increase slightly up to 360 minutes. In all the flow experiments carried out, an increase in GFP-RelA intensity was observed after 360 minutes of the onset of flow. Consequently, it must be questioned whether this effect arises due to a technical issue (limitation of tracking algorithm or healthy state of cells) or is real nuclear translocation. On examining each individual shear stress magnitude position within the gradient channel, small differences in the temporal nuclear GFP-RelA intensities can be observed. These differences appeared (only very weak) at shear magnitudes of 2, 5 and 8 dyne/cm^2. Moreover, the nuclear GFP-RelA intensity increased only from 180 minutes onwards. At high shear stress magnitudes (13 and 15 dyne/cm^2) a small peak was noticeable at 60 to 120 minutes. Examining the interpolated map of all nuclear GFP-RelA means of each shear position, this could be split into four regions: Early low shear (2-10 dyne/cm^2, 0 to 180 min), early high shear (10-16 dyne/cm^2, 0 to 180 min), late low shear (2-10 dyne/cm^2, 180 to 360 min) and late high shear (10 -12 dyne/cm^2, 180 to 360 min).

While the early low shear region experienced little change, the early high shear region experienced an increased nuclear GFP-RelA intensity. Moreover, in the late low shear region the nuclear GFP-RelA intensity increased and was higher than in the late high shear region. However, all cells showed a high nuclear GFP-RelA intensity at 360 minutes. It was previously reported that the nuclear p65 concentration in HAECs exposed to a shear stress gradient of 0 to 16 dyne/cm^2 including 1 ng/mL TNF-α in the medium was elevated at 9 to 16 dyne/cm^2 after 60 minutes [183]. It is unclear how strong an effect the addition of TNF-α had on the flow. Hence, comparison with the literature study is difficult. A further study [111] demonstrated that a gradient created by a step channel caused higher nuclear p66 concentration at areas of higher shear stress (disturbed flow areas) after 30 minutes of flow exposure. A second step channel study [112] showed a 1.5x increase in nuclear p65 concentration in HAECS at the disturbed flow area (high shear stress area) for a flow exposure of 24 hours.

However, the observations in this work provide evidence that the temporal nuclear translocation of GFP-RelA or NF-κB in HUVECs is different at low and high shear stress in a shear stress gradient. Moreover, to the best knowledge of the author this was the first study investigating the nuclear translocation of GFP-RelA in HUVECs exposed to a shear stress gradient with live-cell imaging.

7.7. Heterogeneity of nuclear GFP-RelA under static conditions is weakly synchronised by shear stress

A large heterogeneity in nuclear GFP-RelA intensity of cells under static conditions has been observed in this work. In contrast, cells stimulated with a high TNF-α

concentration synchronised and showed a bundled peak of nuclear GFP-RelA intensity at 30 minutes. One of the aims in this work was to identify nuclear GFP-RelA peaks occurring under static conditions. However, this aim was never acheived. Performing Kmeans with gap statistics did not identify a unique number of clusters. Moreover, the use of different normalisation methods did not improve the cluster evaluation.

It appears that cells under static conditions have a very noise temporal GFP-RelA profile and some experience random translocation. Attempts to place all the different temporal profiles into groups would only be possible by aligning them in time. This means, one must identify peaks and shift them along the time axis until they align with similar peaks/signals. Numerically, this is an extremely difficult task. Moreover, it is made more complicated by having a noisy signal such as those found in this work. An attempt to align cells according to time only partially succeeded. Such a temporal alignment would require much testing and verifications. It was still approximately concluded using Kmeans that a fraction of cells (ca. 50 %) experienced random nuclear translocation of GFP-RelA under static conditions. However, how many cells experienced spontaneous nuclear translocation and when and how strong the translocation is, was not easily identified.

A more suitable measure was the maximum peak distribution of the population. The maximum nuclear GFP-RelA peak distribution under static conditions was almost uniform. This indicated a large heterogeneity of cells state and high noise ratio of the measurments.

In Figure 186, the correlations of the maximum peak distirubtion (in time only) between all experiments and static conditions are shown. The correlation between

the maximum peak distribution of TNF-α and static conditions shows a low negative value (-0.2), indicating poor correlation. As observed previously, TNF-α synchronised cells and resulted in a clear nuclear GFP-RelA peak at 30 minutes. Therefore, the poor correlation to the almost uniformly distributed maximum peaks under static conditions can be interpreted as an indicator for strong nuclear translocation and improved synchronisation.

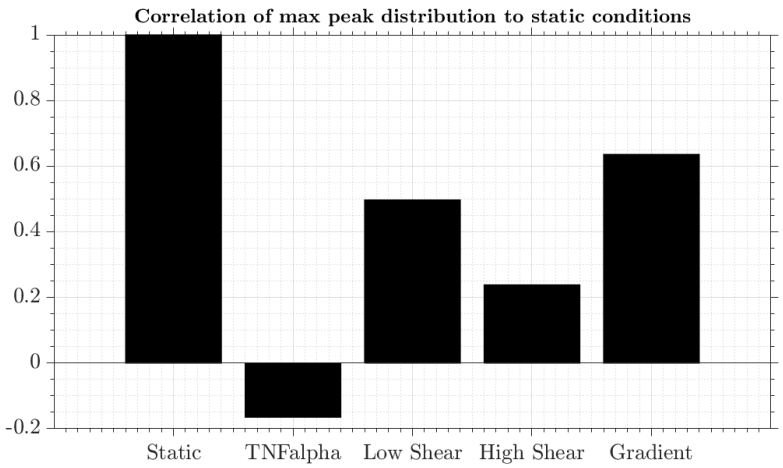

Figure 186: Correlation coefficient of maximum peak distribution (in time only) between each experiments and static conditions

When flow was the stimuli (low, high or shear gradient), translocation increased slightly and synchronisation of cells may have improved as the correlation values dropped (Figure 186). High shear stress affected the cells the most. This resulted in poor correlation of the positive peaks (0.2). This suggests that high shear stress affected the nuclear translocation and synchronisation improved. Cells exposed to low shear stress had a medium correlation (0.5), suggesting that low shear only had a weak effect on cells. The correlation to the shear stress gradient was even higher (0.6). This indicates that the total population was inadequately syncrhonised and the nuclear GFP-RelA intensities were similarly distributed as under static conditions. Alternativley, it could be argued that due to the flow conditions noise had been

reduced (dirt was removed and constant fresh media was flowing over the cells). Hence, the signal was clearer and differences in maximum peak distribution occured. In general, shear stress did not produce a clear synchronisation and peak as observed with TNF-α. Hence, this work questions how strong the mechanical transduction effect of flow really is on the nuclear translocation of NF-κB.

7.8. In a shear stress gradient, cells move with or against the flow direction towards a "favourable" shear stress

It was observed that under uniform low shear stress, cells moved very slowly in the direction of the flow. Whereas, under uniform high shear stress cells moved faster (average displacement of 0.26 nm/s) and in the direction of the flow. This was expected. Moreover, it appears as if the flow was "pushing" cells in the flow direction. However, it was observed that cells in a shear stress gradient did not move in the flow direction. In the gradient channel at low shear stress magnitudes (2 and 5 dyne/cm^2), cells moved slightly in the direction of the flow. However, at 8 dyne/cm^2 this changed, and the cells decreased their movement in the direction of flow and increased their movement perpendicular to flow direction. At even higher shear stress magnitudes (11, 13 and 16 dyne/cm^2), cells moved in the direction opposite to the flow. This observation does not agree with the movement under uniform flow and high shear stress. It appears that cells tend to move towards a favourable shear stress condition. Hence, there must be some underlying mechanism that allows cells to sense shear stress and communicate with each other. Two possibilities may include:

1. Cells move randomly and if random movement is in their favour they continue to move in this direction
2. Cells in a favourable shear stress release chemicals that travel via convective transport and are sensed downstream by other cells. This way, the cells at 8 dyne/cm^2 would have released a chemical that was sensed by cells at higher shear positions which informed them to move back (against the flow). Cells at low shear stress did not get this information from cells at the favourable shear stress and thus move (or are pushed) in the flow direction.

It was reported with IHC that, in a shear stress gradient produced by a step channel, cells migrate away from the reattachment zone (migration from low to high shear stress) [184]. Time lapse recording [185] of HUVECs exposed to a disturbed flow area (backward facing step channel) revealed that cells migrate away from high shear stress in both direction with and against the flow. Another study [140] has reported that BAECs are more aligned following 24 hours exposure to a positive shear stress gradient at lower shear stress magnitudes. After 36 hours, cells were not aligned throughout the positive shear stress gradient. Interestingly, they demonstrated that cells in a negative shear stress gradient are all well aligned after 36 hours of shear stress. However, the study did not reveal movement of cells (IHC), hence it can only be guessed that alignment is closely related with cell movement against or with the flow direction. Several other studies have shown that different shear stress gradients enhance or hinder EC alignment to the flow direction [140, 186-191]. This points to a complex mechanism of cell mobility in shear stress gradients. A recent study [192] demonstrated by tracking HMVECs that cells migrate against the flow direction in a shear stress gradient created by an impinging flow. This could confirm the findings of

this work that endothelial cells migrate against the flow direction at high shear stress magnitudes within the gradient channel. A further study demonstrated that in rat aortas Dil-labeled endothelial cells migrated within 3 weeks towards the heart and not in the direction of the blood flow. This in-vivo study further suggests cell migration against the flow direction at high shear stress [193]. A further study demonstrated that porcine aortic endothelial cells indicate morphological adaptions in planar cell polarity related to shear stress and direct in flow direction [194].

In addition, it has been reported that breast carcinoma line (MDA-MB-231), a cancer cell line, migrates in the flow direction at low shear stress, and migrates against the flow direction at high shear stress magnitudes [195].

Additionaly, persistence of mobility increased with superimposed shear stress. While low shear stress had little but noticeable effect, high shear stress and a shear stress gradient showed a strong effect on the cell mobility and increased directional persistence.

There is evidence that cells move away from high shear stress towards a lower “favourable” shear stress. This phenomenon can only be explained using the two points listed above. It is suggested that further study of the the phenomenon of endothelial cell movement against the flow direction is required, as it may shed insight in disease inception or progression in areas with high shear stress gradients or flow disturbance.

7.9. Simulation of cell heterogeneity approximates live-cell imaging measurements

The cell population model qualitatively predicted the nuclear NF-κB in response to different TNF-α concentration to be close to the measurement of nuclear GFP-RelA in HUVECs stimulated with different TNF-α concentrations. In this work, the deterministic NF-κB model by Lipniacki *et al.* [80] was extended by scaling the IKK activation rate and the nuclear import rate of NF-κB with extrinsic noise on a single cell basis. Each single cell experienced a random activation based on a stimulus dependent Gaussian distribution. The aim was to mimic cell heterogeneity within a population by stimulating each cell individually.

An activation scale was defined to proportion the IKK activation rate and the nuclear import rate. The activation scale is a function of activated surface receptors. The number of activated surface receptors is initially proportional to the TNF-α dosage. The surface receptors then experience a defined fast and slow decay. In addition, surface receptors experience extrinsic noise due to random inactivation or activation. Moreover, a threshold function cuts off the activation if the number of surface receptors drops below a certain threshold. The threshold defines the percentage of active cells per population.

The number of activated cells followed a hill function, which is comparable to other modelling approaches [83, 95, 96]. Therefore, the activation scale modifies the IKK activation rate and the nuclear import of NF-κB according to the stimulus intensity, and if the stimulus intensity is too low (surface receptors below the threshold) these reaction rates are cut off.

The approach applied in this work is comparable to the model of Turner *et al.* [96]. However, to match the obtained experimental observation, scaling of the IKK activation rate and the nuclear import of NF-κB was necessary. Inclusion of these adjustments allowed for the reproduction of a proportional decrease in nuclear NF-κB peak with a decreasing stimulus. This suggests that the nuclear import might be altered according to the stimulus intensity. Therefore, it may be possible to control the immune response of cells by altering the nuclear import of NF-κB. This can be achieved by editing Importin molecules (Importin-α3 and Importin-α4), which are responsible for shuttling molecules between nucleus and cytoplasm. Importins concentration could be increased or their functions blocked. Thus, creating favourable nuclear NF-κB conditions.

In addition, the prediction of active IKK at different TNF–α concentrations, by the model, is in agreement with measurements of phosphorylated IKK when stimulated with different TNF-α concentrations [86] and the IHC measurements when stimulated with 10 and 1 ng/mL TNF-α as performed in this work.

Furthermore, cells at rest were simulated with the inclusion of spontaneous nuclear translocation of NF-κB. In doing so, similarities of standard deviations (simulation and measurements) demonstrated that spontaneous nuclear translocation of NF-κB exists when cells are under static conditions.

7.10. *In-silico* modelling of shear stress activated NF-κB provides insight on the NF-κB pathway dynamics in flow environments

Mimicking nuclear translocation of GFP-RelA in HUVECs with an in-silico model was targeted based on identified activation of groups within the gradient channel. Four

different activation groups were identified using the Kmeans clustering method. However, it must be considered that the clustering solution is not unique and that the groups are more of a guess than a proven value. However, the four activation groups (initial, early, mid and late) could be used to closely reproduce the temporal nuclear translocation of GFP-RelA observed within a shear stress gradient. The groups peaked at 30 minutes (initial), 90 minutes (early), 180 minutes (mid) and 360 minutes (late). The number of cells per group changed according to the shear stress magnitude. The change in the number of cells was based on a linear (initial, mid and late) or polynomial (early) regression curve obtained from measurements within the gradient channel. The shear stress induced NF-κB model with a shear stress profile in a backward facing step channel was exemplified in this work. The sudden expansion of the backward facing step channel created a recirculation zone (disturbed flow area) before the flow reattached and redeveloped into a uniform flow further downstream. The model used in this work predicts that HUVECs in the recirculation zone experience a high nuclear NF-κB concentration at 60 to 120 minutes. A previous study reported an elevated nuclear NF-κB concentration at disturbed flow areas within a step channel after 30 minutes [111]. Others reported a 1.5x elevated nuclear p65 concentration in the disturbed flow area after a sudden expansion after 24 hours [112]. The current model predicts that cells at the recirculation zone (disturbed flow area) experience the highest nuclear translocation of NF-κB but with a peak at 60 minutes. Furthermore, at 360 minutes NF-κB is predicted to be elevated at all locations, except at the recirculation zone which has low concentrations.

Considering that the identified groups are based on an assumption, this still allowed for the prediction of an elevated nuclear NF-κB concentration within the disturbed

flow area early after onset of flow. However, considerably more research is needed to validate the grouping of temporal nuclear translocation and to produce an accurate model of how nuclear translocation of NF-κB within endothelial cells occurs under shear stress.

7.11. Limitations and further work suggestions

7.11.1. Immunohistochemistry

The limitations of immunohistochemistry of TNF-α experiments include the inability to track individual cells, one experiment per time point, and long experimental times (fixing, staining and imaging = 2-3 days).

Staining of p65 worked well and the results were found to be in agreement with the literature. Staining for phosphorylated IKK was difficult as the signal was very weak. However, careful analysis of the images allowed for the observation of a trend for IKK at different TNF-α concentration similar to that found by Cheong *et al.* [86]. Unfortunately, IκBα lead to a large amount of unspecified binding. The image analysis of IκBα stains was difficult as the images were very bright. Subsequently, there is a lack of confidence in the accuracy of IκBα measurements obtained in this work. However, they did show a decrease of cytoplasmic IκBα concentration when stimulated with TNF-α, which was inconsistent with findings in the literature [75]. Hence, it is suggested that alternatives for an IκBα antibody are sort, as the one used (IκBα (H-4) Alexa Fluor 647) in this work was not well suited to HUVECs.

7.11.2. Live-cell imaging

A major limitation of this work is the choice of cell type. HUVECs were choosen due to their low cost and relatively simple maintance. As this was a first study about live measurement of NF-κB under flow conditions, HUVECs were ideal to perform system validation. The system developed in this study could be easily further investigated using any other cell type such as human aortic endothelial cells which would be more physiological relevant.

A further limitation of the study is the experiment time, which was only 6 hours. A short time was chosen to study initial responses from static to flow and the short time was found appropriate to validate such experimental systems. Ideally, longer flow exposure times should be studied. For example, cells exposed to flow for 24 hours up to one week.

The flow model (straight and gradient channel) contains the limitation of only being perfused with a unidirectional steady flow. Realistic physiological flow conditions are pulsatile. Hence, repeating experiments with pulsatile flow profile would increase the physiological relevance of such a study. However, in order to verify and test the system, uniform and steady flow were preferred before moving forward to more complex flow profiles. In addition, more realistic artery geometries (straight and gradient channel are very abstract assumptions) would mimic more realistic physiological flow conditions.

Many other technical limititations arose during this dissertation. It was difficult to record the time point zero (equivalent to static conditions) for all positions to make a comparison from static to flow conditions in one experiment. This was due to dead cells, dirt and other particles within the channel that disturbed the imaging process.

This cell culture noise caused the autofocus to catch cells at different Z-locations, influenced the background and changed the overall intensity of the image. Once the flow was turned on, the “dirt” within the channel was flushed out within 1-3 minutes. It was found incorrect to first flush the chamber for 1-3 minutes and then record within 10-15 minutes all positions under static conditions, and then to finally turn on the flow. This process would have changed the initial conditions to a pulse of shear, followed by static conditions and a second pulse of flow for 360 minutes. In addition, cells immediately changed shape and most importantly flattened when the flow was turned on. It is possible that the change of nuclear GFP-RelA intensity between the first two time points of the low shear stress experiments are due to disturbed fluorescent particles that are disappearing. Under high flow rates (high shear and shear gradient), this appeared less problematic. The change of intensity when recorded first under static conditions and then under flow caused a drop or increase of ca. 25-50 % in intensity as shown in Figure 187. To our knowledge, TNF-α requires 30 minutes to reach the peak of nuclear p65 after TNF-α stimulation. Therefore, an immediate change of intensity from control to flow conditions does not reflect the real case. Thus, comparing the cells nuclear GFP-RelA intensity with the conditions before flow was not possible using this setup.

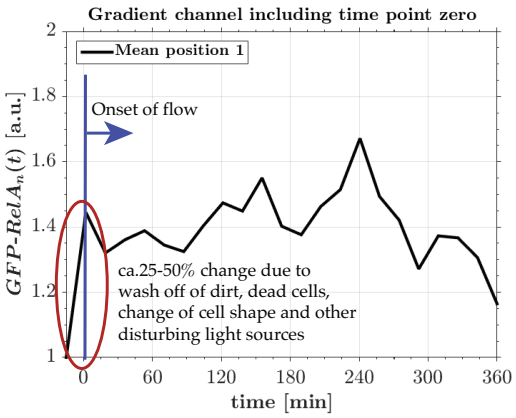

Figure 187: Intensity error between static conditions and flow conditions.

In addition, the sample moved once the valves had been opened. Thus the trajectory of several cells was lost or in the worst case, the microscope was at a new position. Therefore, the valves had to be opened before starting the experiment and opening of the valves resulted in media flowing through the pipes due to hydrostatic pressure differences created by the setup.

Another limitation was photo bleaching of the GFP and mCherry signal. The intensity of the fluorescence decreased within the 6 hours. Post-processing of the images as explained in paragraph 2.18. was carried out to try correct for the bleaching. Due to the frequent reoccurence of picture acquisition (between 7 and 15 minutes), cells experienced high light exposure and photobleaching, which was very present. A reduction of photobleaching effects would be desirable.

In general, this setup was fragile and prone to the users movements and experimental skills. Two flow dampers and the reservoir had to be placed inside the heating box of the wide-field microscope. The heating box was not built to support such elements. Therefore, the box was extremely packed and very careful handling of the perfusion elements was required. Many experimental attempts failed due to accidental dropping of the reservoir (glass broken and huge spillage), or accidental

unplugging of connectors to the flow chambers (liquid flew out and the sample was no longer sterile).

Therefore, before repeating these experiments a solid stand-alone perfusion system with a built in microscope was suggested and built. The system should include high quality disposable channels, precision control of flow rates with minimal peristaltic pump noise and a sterile pressure and flow sensor. Furthermore, non-uniform illumination should be reduced by using only high precision glass for the cells to be grown on. It was also suggested to first flush the sample for 5 minutes at high shear stress to remove all dirt and create a clean environment. Following the initial flushing, it is recommended to let the cells rest for 6 hours to guarantee steady state. Based on findings from this research group, cells recover after ca. 6 hours of TNF-α stimulation. Following 6 hours of initial flushing, the pump could be turned on and the effect of flow recorded. Using this approach it will hopefully be possible to compare the effect of flow to static conditions in one experiment. However, there may still be issues: the cell shape may change and the stagnant media might bleach and change the intensity. Thus, there is still the probability of intensity changes once the pump is turned on.

In terms of space, it would be ideal if the microscope and tissue culture lab are in the same room. In this work, preparation of the samples was carried out in the tissue culture lab and then the whole equipment was carried ca. 10 minutes across campus to a different building. This included taking an elevator and opening several doors. It was a strong concern that the walking movements may affect the cells. However, the cells always appeared fine on arriving at the microscope by showing a black nucleus (no GFP-RelA in the nucleus).

Furthermore, a better transfection method than electroporation should be used. Viral transfection might be more suitable. It would be ideal to add a third plasmid to tag VE=Cadherin. With a fluorescent tagged VE-Cadherin plasmid, an individual would be able to colour the cytoplasm and define the cytoplasmic area. In addition, having a defined cytoplasmic area would allow for the measurement of cytoplasmic changes. This would be very useful to see if flow increases with cytoplasmic p65 concentration and by how much in respect to the nucleus. Given the fact, that it was not very difficult to insert two plasmids into HUVECs using electroporation, the addition of a third plasmid would not be too great a challenge A further idea would be to create a stable cell line with expressing fluorescence tagged VE-Cadherin and H2B-mCherry. These could allow for continuous measurement of the cytoplasmic and nuclear concentrations of any inserted fluorescent protein. Ideally, this could be applied to CRISPR and allow editing of the endogenous p65 and VE-cadherin with fluorescent tags. Moreover, knocking out p65 and VE-Cadherin before inserting them would be a great idea. This would rule out “traffic jams” between expressed plasmid molecules and endogenous molecules.

It is suggested that one measure live the nuclear translocation of GFP-RelA in many different flow enviroments. This includes curvature, channel with a small hole to mimick an aneurysm, or maybe build a 3D artery phantom and measure cells in a 3D structure.

Once data is recorded, data analysis is a further challenge and requires the most advanced machine learning methods. Therefore, data analysis of high throughput studies using smart clustering methods is suggested. Such methods exist and have been applied here. However, they could be extended and improved significantly to

match the type of analysis required for live-cell imaging data. (Live-cell imaging is very noisy and requires good filtering and specific search algorithms.). Furthermore, a universal normalisation method should be sought. One that is capable to compare all sorts of experiments. Moreover, the tracking software should be further developed to ensure that the maximum number of cells can be tracked in time and cells in apoptosis and cell division are clearly removed. In this work ca. 30 % of the recorded cells were rejeted.

7.11.3. *In-silico* NF-κB population model

The population model was based on a receptor activation curve, which was derived from experimental observations within the literature. Therefore, the receptor activation curve is an assumption, and more precise investigation of the receptor dynamics is needed to accurately represent such a mechanism. Randomness in receptor activation was assumed, which allowed spontaneous activation of NF-κB and a close reproduction of the cells dynamics under static conditions. Further investigation to understand what causes such random activation and how it can be controlled may be of interest. The nuclear import rate of NF-κB was made proportional to the TNF-α concentration to achieve the observed reduction of nuclear NF-κB in relation to TNF-α. There might be another undiscovered mechanism that influences the proportionality of TNF-α and nuclear import, which could be added as an additional module to the model.

The shear stress NF-κB model was based on five visually identified cluster groups obtained with Kmeans. Further research needs to be carried out to prescicely characterise all possible temporal reaction groups of cells. This could then allow

precise modelling of all subgroups. Furthermore, longer measurement durations would be ideal to define a model for a much longer time frame with the focus to predict chronic conditions. Ideally, several experiments should be conducted in future to investigate live the translocation of NF-κB in various flow enviroments (backward facing step channel, curvature, flow over a small hole to mimic an aneurysm). These studies could then be compared to the NF-κB population predictions, which may allow for the description of a universal shear induced NF-κB model.

8. Conclusions

In this dissertation, the single cell dynamics of GFP-RelA in HUVECs exposed to different stimuli was investigated. To achieve this, several steps were undertaken from experimental design, biological validation, data analysis and numerical prediction of the observations.

An experimental setup that can capture the NF-κB dynamics in vascular endothelial cells was demonstrated. Successful transfection of a large population of HUVECs with two plasmids, GFP-RelA and H2B-mCherry, was carried out. GFP-RelA was used as a reporter plasmid of the endogenous RelA (p65 or NF-κB). H2B-mCherry coloured the DNA and allowed identification of the nuclei area within a cell. A large fraction of a population was recorded using a wide-field or confocal microscope by exposing the expressing cells to LED lamps or lasers of different wavelengths (GFP and mCherry). More than 1000 cells with a time interval of 5 to 10 minutes were recorded per experiment. Computationally expensive post-processing was required to capture the nuclear GFP-RelA intensities. Cells were tracked throughout time frames and the nuclear GFP-RelA intensity could be measured for each individual cell.

Expressing HUVECs were found to experience a huge heterogeneity and each cell had a different intensity of GFP-RelA. Hence, single cells had to be normalised to a common mean. However, normalisation proved troublesome. Normalisation by the time average was found to be most suitable as it allowed for distinction between strong and weak activated cells.

Expressing HUVECs were exposed to different TNF-α concentrations. Stimulated with high TNF-α concentrations, nuclear GFP-RelA peaked at 30 minutes, followed by a drop and a reoccurring local maximum at 120 to 180 minutes. The amplitude of nuclear GFP-RelA peak at 30 minutes decreased with decreasing TNF-α concentrations. The temporal nuclear GFP-RelA intensity was validated by performing immunohistochemistry of non-transfected HUVECs by staining for p65 at various time points.

Following confirmation of the plasmid dynamic, transfected HUVECs were exposed to different flow environments. A perfusion system was built to ensure steady laminar shear stress. The flow was driven using a peristaltic pump. The flow channel was decoupled using two custom-made flow dampers. The flow dampers reduced the peristaltic pump flow oscillation to a minimum. In addition, a reservoir was manufactured to guarantee absolute sterility with a filtered gas exchange.

Transfected cells were exposed to three flow environments: Uniform low and high shear stresses, and to a shear stress gradient. To create uniform low and high shear stresses commercially available straight cell culture suitable flow chambers were used. To create a shear stress gradient, a gradient channel was manufactured. The gradient channel had the characteristics of a linear increasing shear stress from 2 to 16 dyne/cm^2.

Cells exposed to a uniform low shear stress experienced a change in nuclear GFP-RelA intensity with an early bump and a linear increment from 240 minutes onwards. Exposure to uniform high shear stress, appeared to marginally increase nuclear GFP-RelA intensity in the initial early phase (0-120 minutes). The cells then experienced a high increase from 240 minutes onwards. In the gradient channel, cells were

recorded at 6 different shear stress magnitudes (2, 5, 8, 11, 13 and 16 dyne/cm^2). While the overall shear stress gradient had little effect on the nuclear GFP-RelA intensity over time (intensity increased only slightly after 180 until 360 minutes), the nuclear GFP-RelA intensity at different shear stress magnitudes showed marginal differences. It appeared that cells at higher shear magnitudes experienced an increased nuclear translocation of GFP-RelA from 0 to 180 minutes in comparison to low shear stress magnitudes positions within the gradient channel. Following 180 minutes, the nuclear GFP-RelA intensity appeared to increase until 360 minutes for both low and high shear stress. Hence, it is believed that nuclear translocation of GFP-RelA is different in cells exposed to low and high shear stress, with greater translocation occurring earlier at high shear stress. However, more validation is required to clearly identify the different temporal effects of low and high shear stress on the nuclear translocation of NF-κB in vascular endothelial cells.

In the second part of the thesis, a simulation to predict nuclear translocation of NF-κB in a cell population was developed. The simulation considers heterogeneity of the population by activating each cell with a stimulus picked randomly from a Gaussian distribution. Moreover, cells were only activated if the stimuli were strong enough. The cell population model could reproduce a close approximation of the population heterogeneity observed in the live-cell measurements of HUVECs expressed at different TNF-α concentrations. Most importantly, reproduction of a close approximation of spontaneous nuclear translocation of NF-κB in cells under static conditions was achieved. Hence, the simulation confirms single cell heterogeneity and spontaneous activation of NF-κB under static conditions. Furthermore, this work aimed to reproduce the small differences of nuclear GFP-RelA translocation in the

shear stress gradient. Single cell measurements from the gradient channel were clustered into 6 different groups by applying Kmeans. Consideration that the numbers of groups were not finite and a vague approximation of activation groups within the cell population when exposed to a shear stress gradient was applied. However, by defining shear dependent percentages of activation groups, close reproduction of the temporal profiles of nuclear GFP-RelA intensities observed within the gradient channel was achieved.

Overall, the presence of a large heterogeneity of the nuclear GFP-RelA concentration in single cells within a population was demonstrated. TNF-α is a strong enough stimulus to synchronise all cells to a common frequency. In comparison, flow is too weak a stimulus to fully synchronise the nuclear shuttling of GFP-RelA as seen with TNF-α. The population mean of the nuclear GFP-RelA intensity was only weakly affected by uniform low and high shear stress and a shear stress gradient, in comparison to static conditions. The observations from this dissertation question the statement, “If shear forces are a main promoter of inflammatory responses in endothelial cells”. The effects of flow on nuclear translocation of NF-κB in HUVECs were shown to be remarkably weaker than with TNF-α stimulation.

9. Conferences

9.1. Attended conferences:

- Baeriswyl, D, Krams, R, Ventikos, Y. (2017) **Impact of flow on the nuclear translocation of NF-κB**, 5th International Conference on Computational and Mathematical Biomedical Engineering, Pittsburgh, USA

- Baeriswyl, D, Krams, R, Ventikos, Y. (2017) **Nuclear translocation of NF-κB in a Shear Stress Gradient**, 5th International Conference on Computational and Mathematical Biomedical Engineering, Pittsburgh, USA

- Baeriswyl, D, Krams, R, Ventikos, Y. (2016) **Impact of flow on the nuclear translocation of NF-κB**, 11th International Symposium on Biomechanics in Vascular Biology and Cardiovascular Disease, Atlanta, USA.

- Baeriswyl, D, Krams, R, Ventikos, Y. (2015) **Activation and nuclear translocation of NF-κB in vascular endothelial cells exposed to shear stress - live cell imaging and mathematical modelling**. 4th International Conference on Computational and Mathematical Biomedical Engineering, Paris, France

- Baeriswyl, D, Krams, R, Ventikos, Y. (2015) **Live-cell imaging and mathematical prediction of nuclear NF-κB concentration in vascular endothelial cells exposed to shear stress**. 9th European Solid Mechanics Conference, Leganés-Madrid, Spain

- Baeriswyl, D, Krams, R, Ventikos, Y. (2015) **Activation and nuclear translocation of NF-κB in vascular endothelial cells exposed to shear stress – Live cell imaging and mathematical prediction**, 10th International

Symposium on Biomechanics in Vascular Biology and Cardiovascular Disease, Rotterdam, Netherlands

- Baeriswyl, D, Ventikos, Y. (2014) **The impact of flow on NF-κB, MMPs and CAMs activity in endothelial cells: Insights from coupling cell signalling with fluid dynamics.** 9th International Symposium on Biomechanics in Vascular Biology and Cardiovascular Disease, Montreal, Canada.

- Baeriswyl, D, Ventikos, Y. (2014) **A mathematical model of inflammation in endothelial cells upon exposure to shear stress - Numerical simulation of the production of NF-κB, MMPs and cell adhesion molecules in different flow environments**. 7th World Congress of Biomechanics, Boston, Massachusetts, USA.

- Baeriswyl, D, Ventikos, Y. (2014) **The effect of hemodynamics on inflammatory responses in endothelial cells.** Medical Engineering Centres Annual Meeting and Bioengineering14, London, UK

Appendix

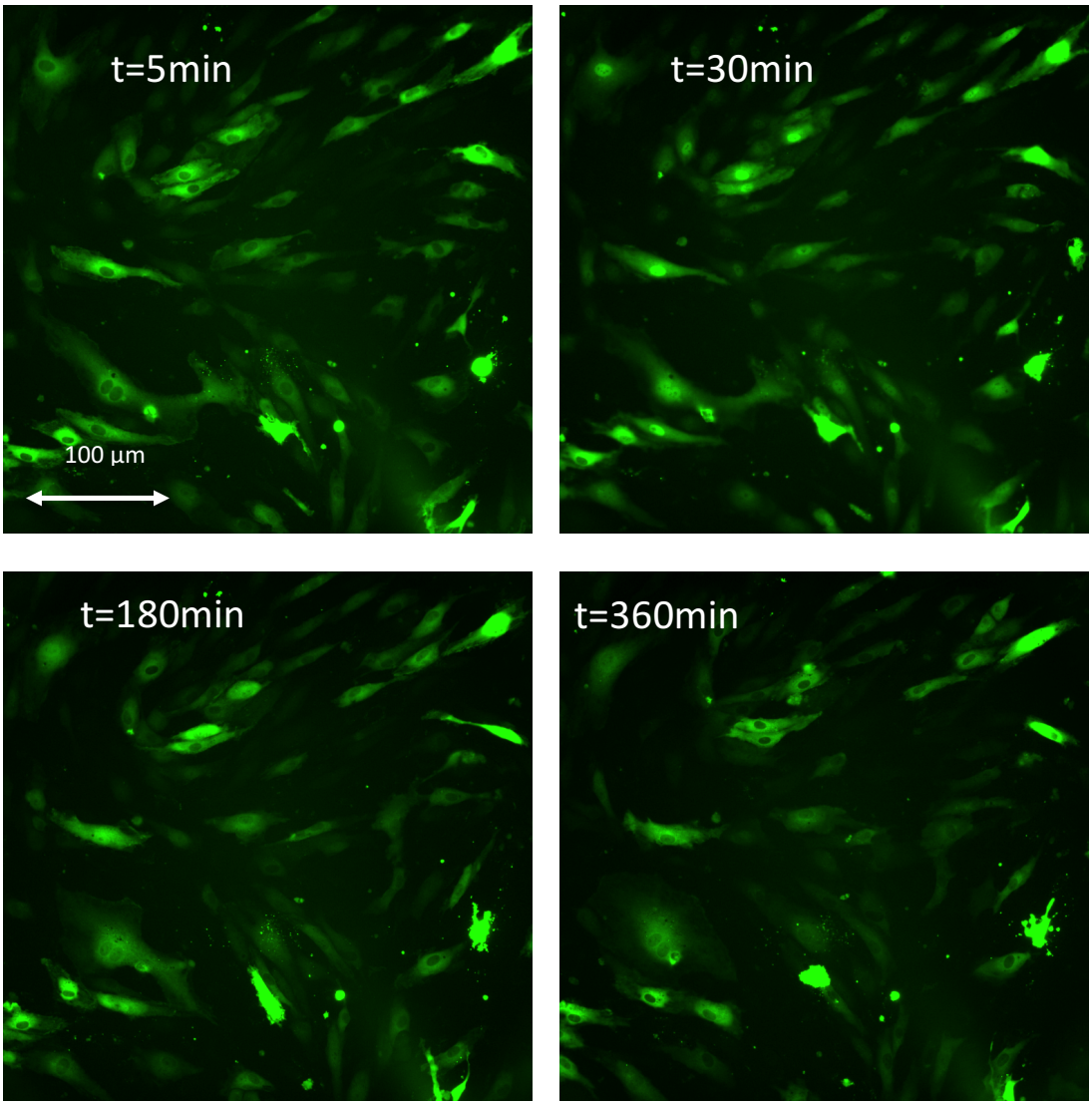

Figure 188: Contrast enhanced images of HUVECs expressing GFP-RelA stimulated with TNF alpha 10ng/mL TNF-α

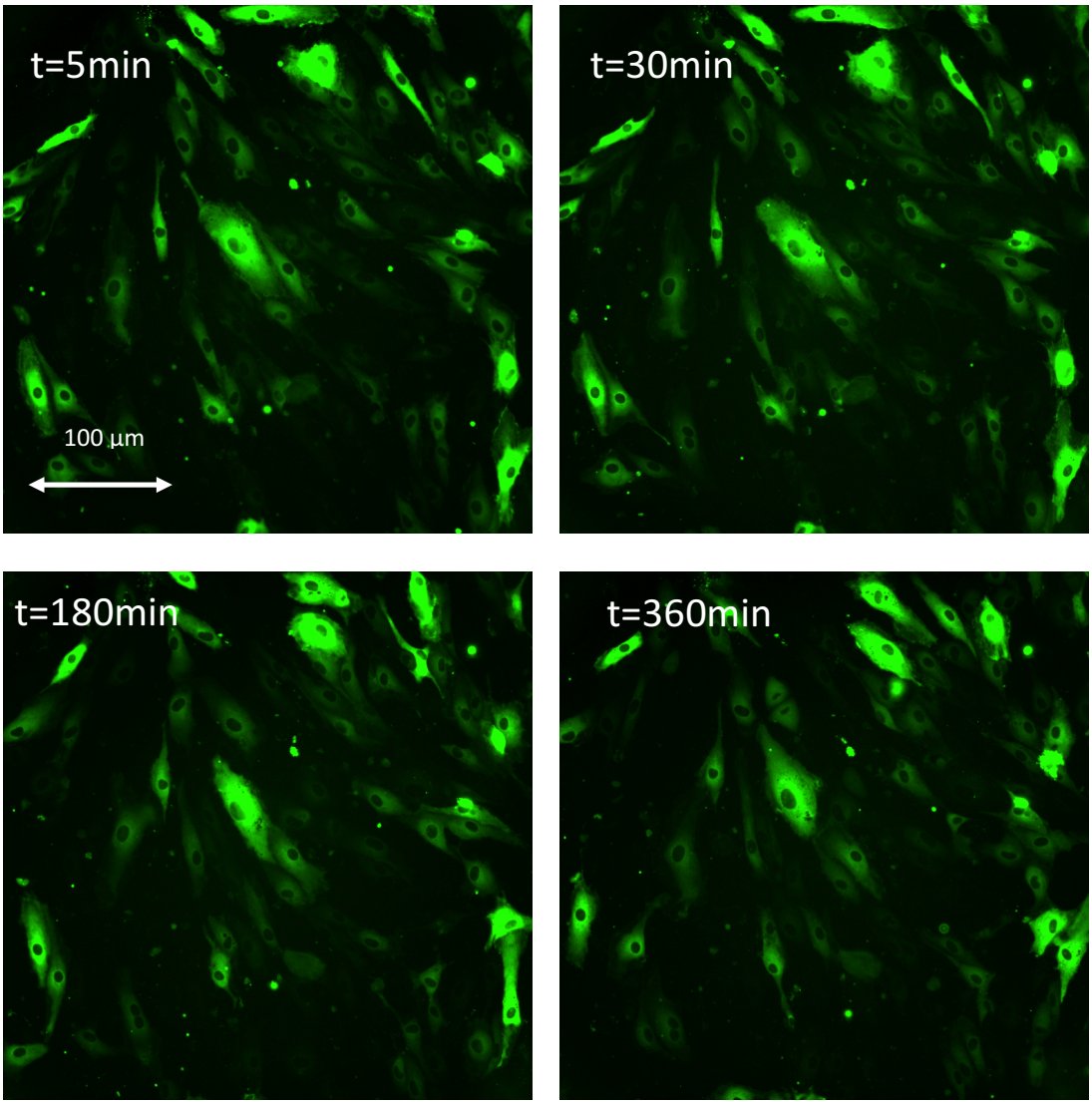

Figure 189: Contrast enhanced images of HUVECs expressing GFP-RelA under static conditions.

2 dyne/cm^2 within a shear stress gradient (2 – 16 dyne/cm^2)

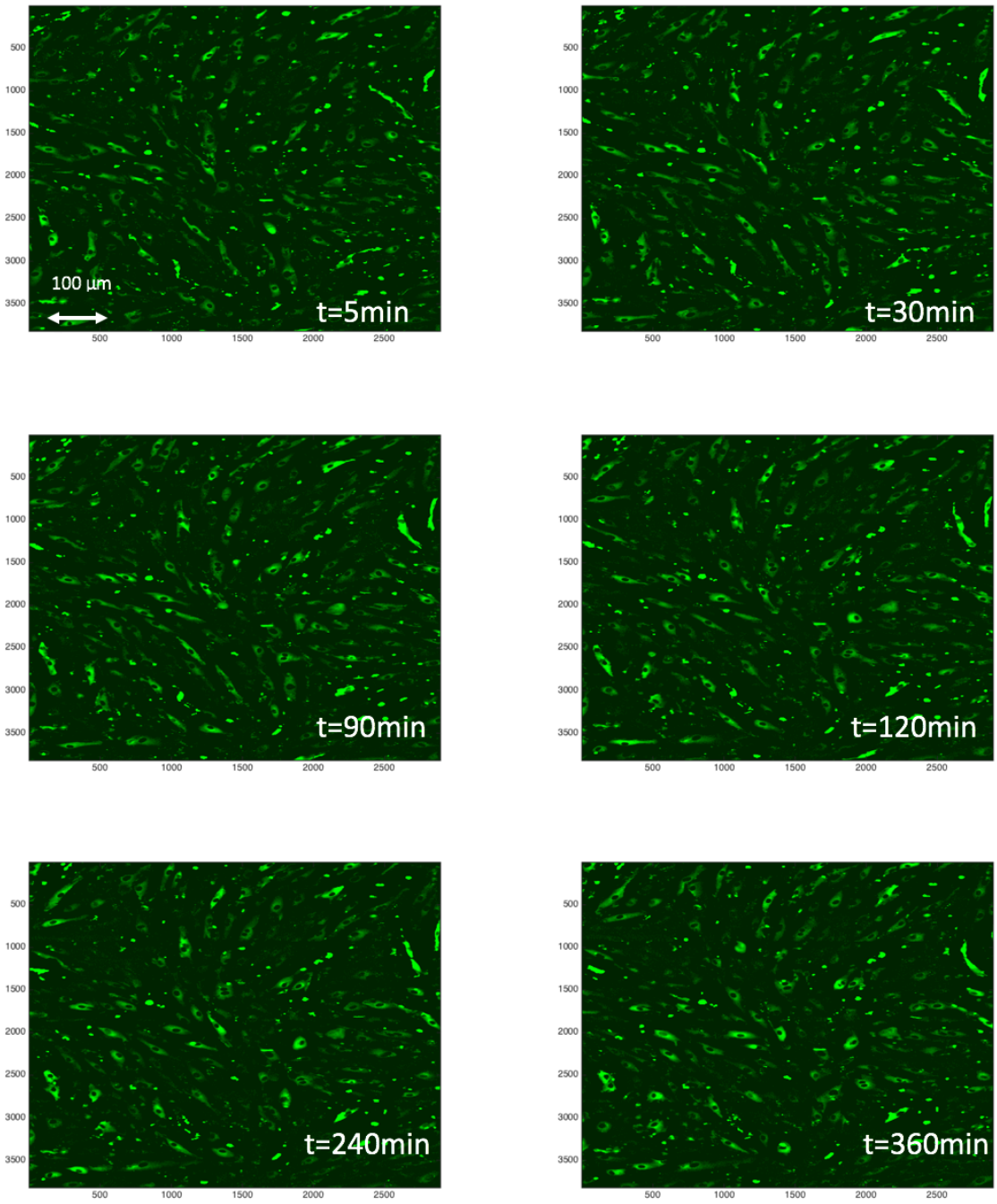

Figure 190: HUVECs expressing GFP-RelA exposed to 2 dyne/cm^2 within a shear stress gradient (2-16 dyne/cm^2)

5 dyne/cm^2 within a shear stress gradient (2 – 16 dyne/cm^2)

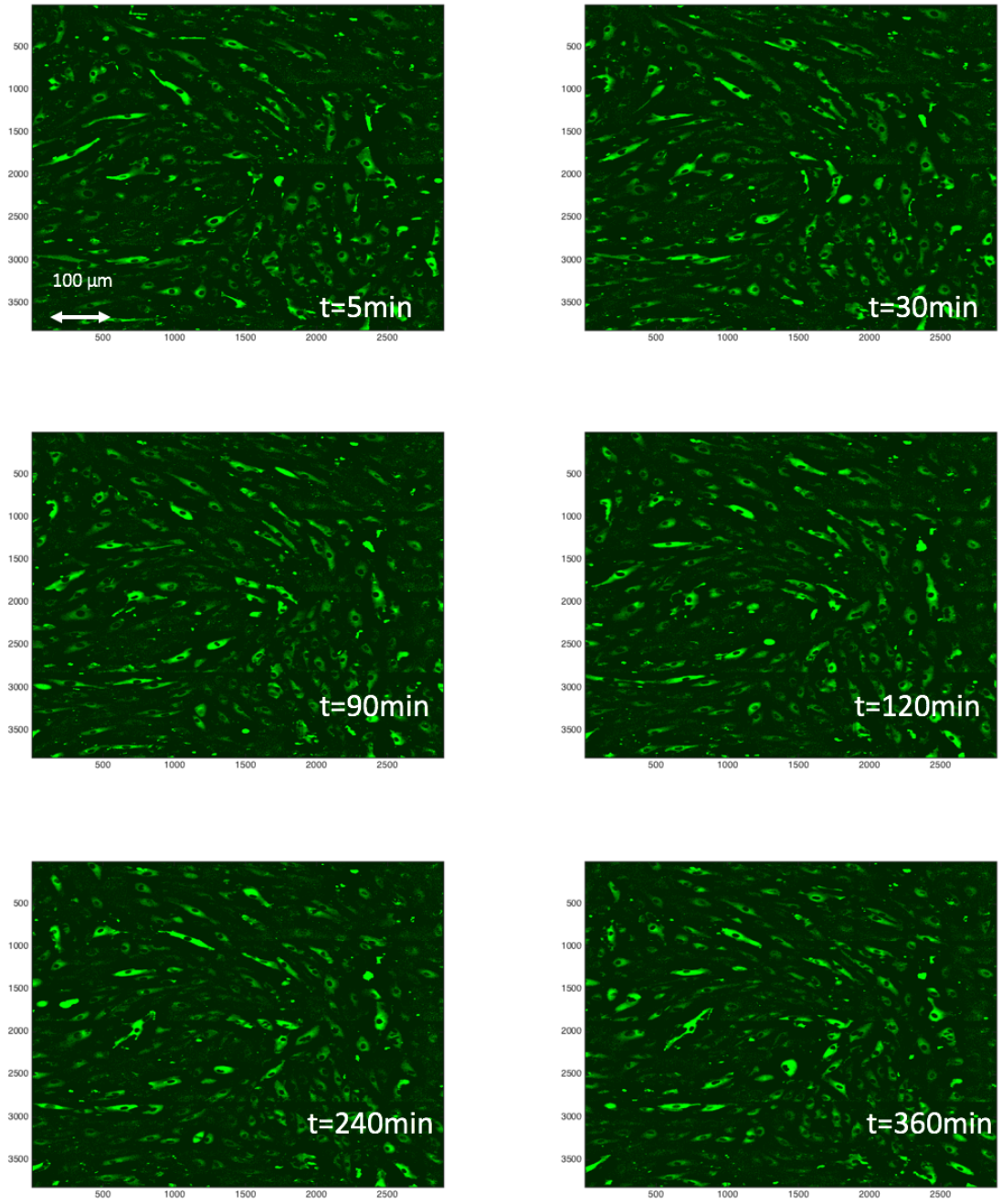

Figure 191: HUVECs expressing GFP-RelA exposed to 5 dyne/cm^2 within a shear stress gradient (2-16 dyne/cm^2)

8 dyne/cm^2 within a shear stress gradient (2 – 16 dyne/cm^2)

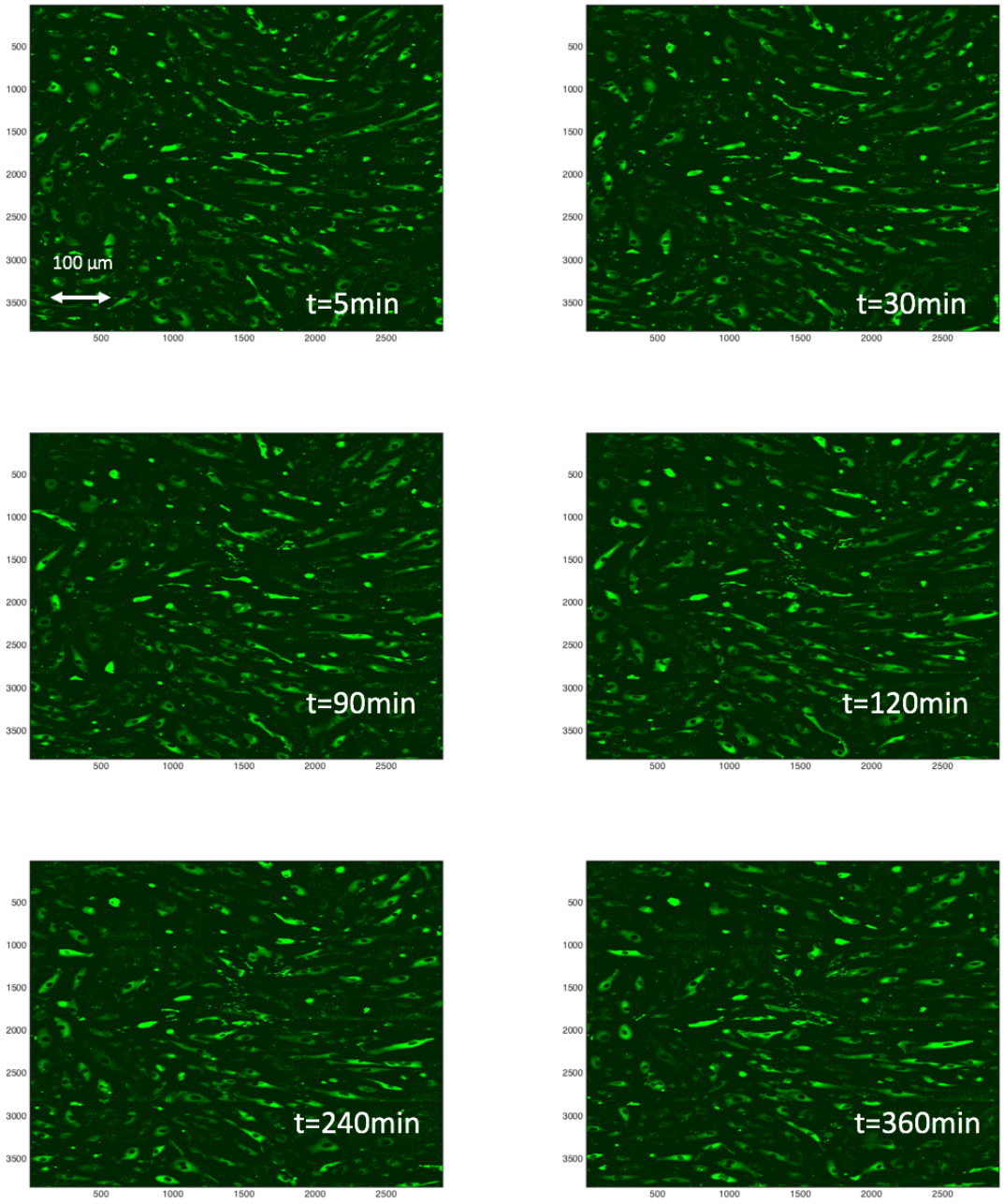

Figure 192: HUVECs expressing GFP-RelA exposed to 8 dyne/cm^2 within a shear stress gradient (2-16 dyne/cm^2)

11 dyne/cm^2 within a shear stress gradient (2 – 16 dyne/cm^2)

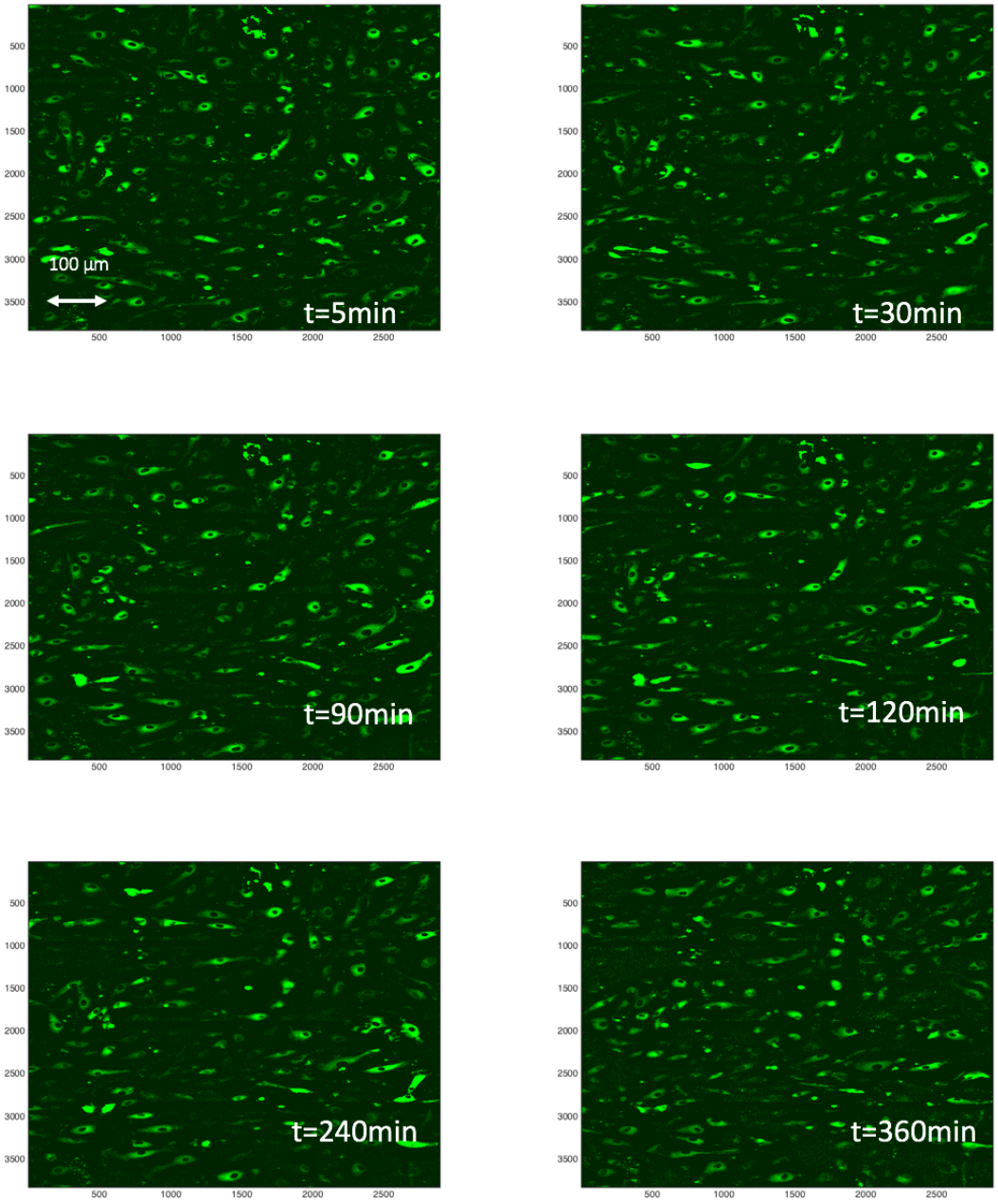

Figure 193: HUVECs expressing GFP-RelA exposed to 11 dyne/cm^2 within a shear stress gradient (2-16 dyne/cm^2)

13 dyne/cm^2 within a shear stress gradient (2 – 16 dyne/cm^2)

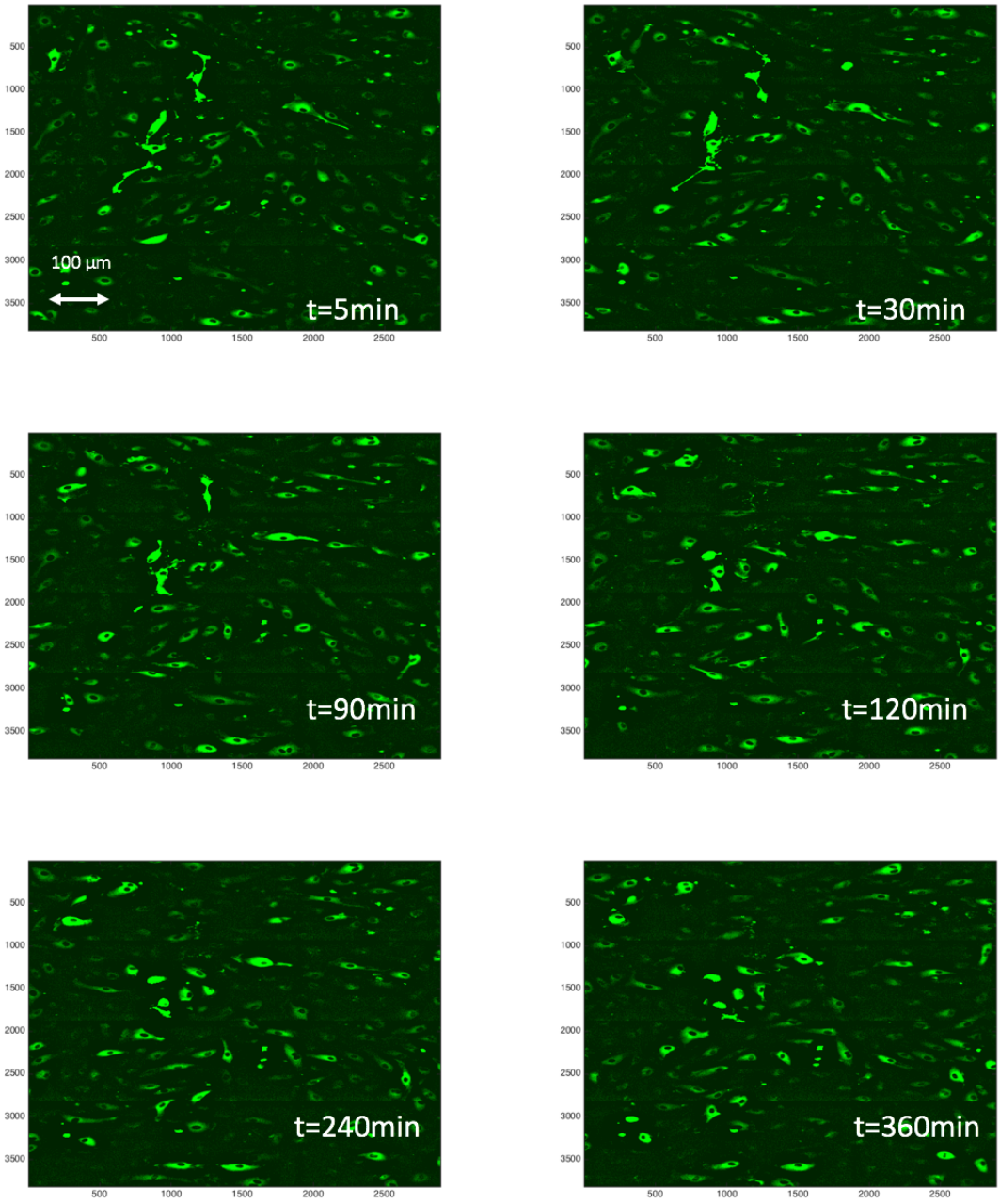

Figure 194: HUVECs expressing GFP-RelA exposed to 13 dyne/cm^2 within a shear stress gradient (2-16 dyne/cm^2)

16 dyne/cm^2 within a shear stress gradient (2 – 16 dyne/cm^2)

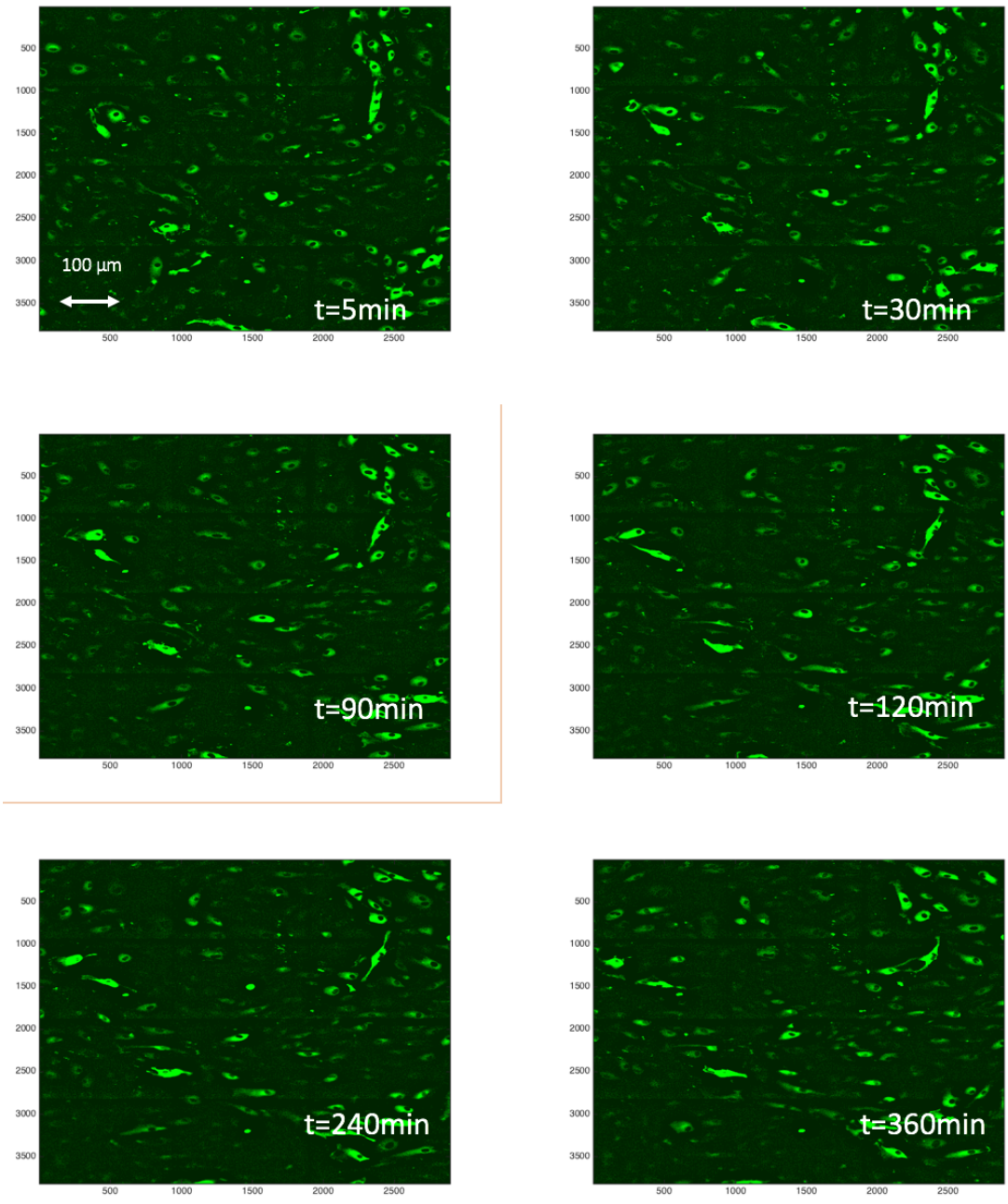

Figure 195: HUVECs expressing GFP-RelA exposed to 16 dyne/cm^2 within a shear stress gradient (2-16 dyne/cm^2)

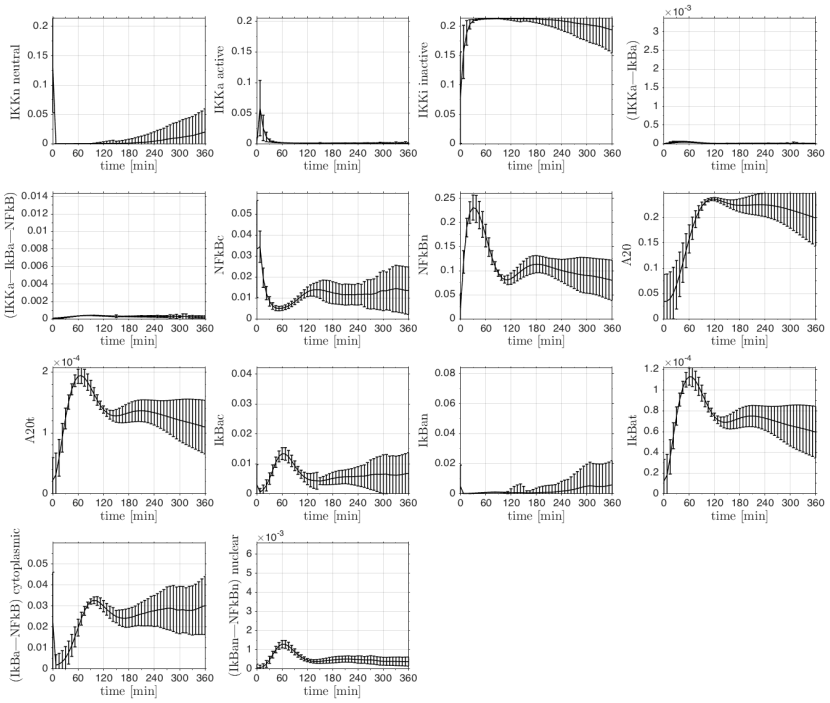

Figure 196: All molecules of the cell population model when stimulated with 100ng/mL TNF-α

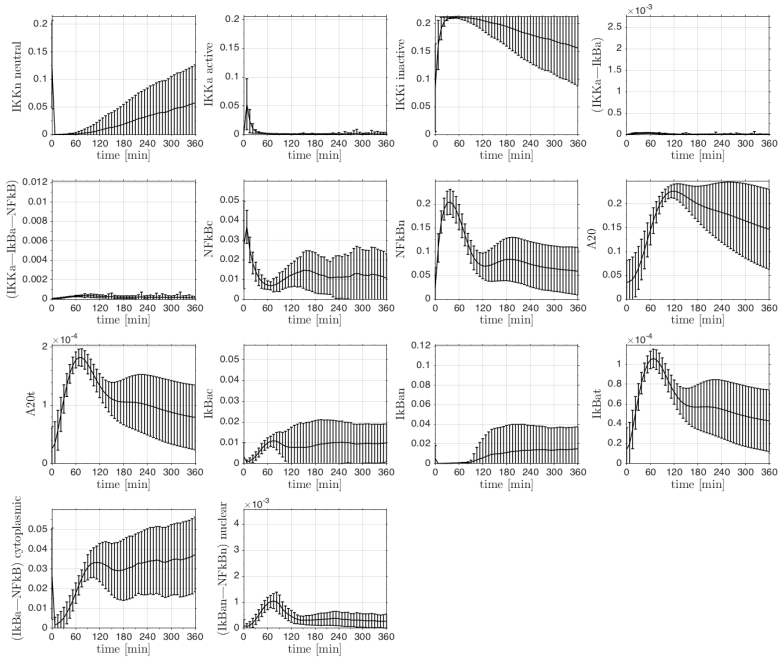

Figure 197: All molecules of the cell population model when stimulated with 10ng/mL TNF-α

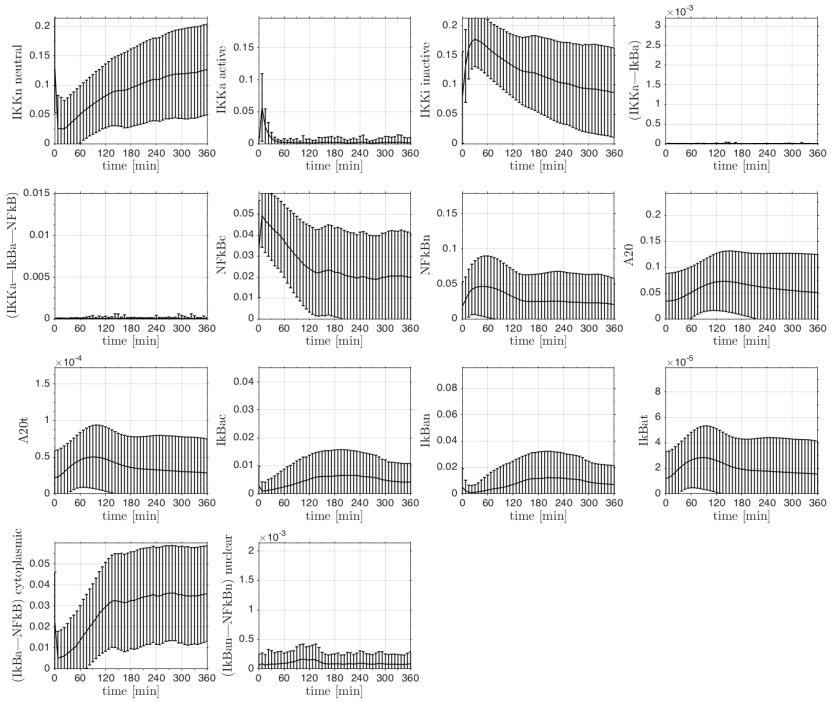

Figure 198: All molecules of the cell population model when stimulated with 1ng/mL TNF-α

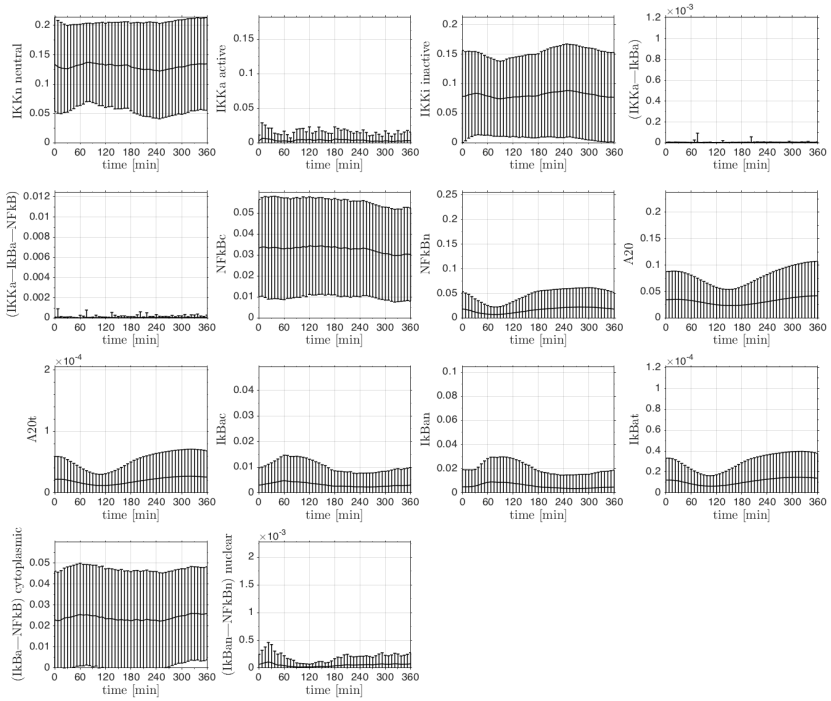

Figure 199: All molecules of the cell population model when stimulated with 100ng/mL TNF-α

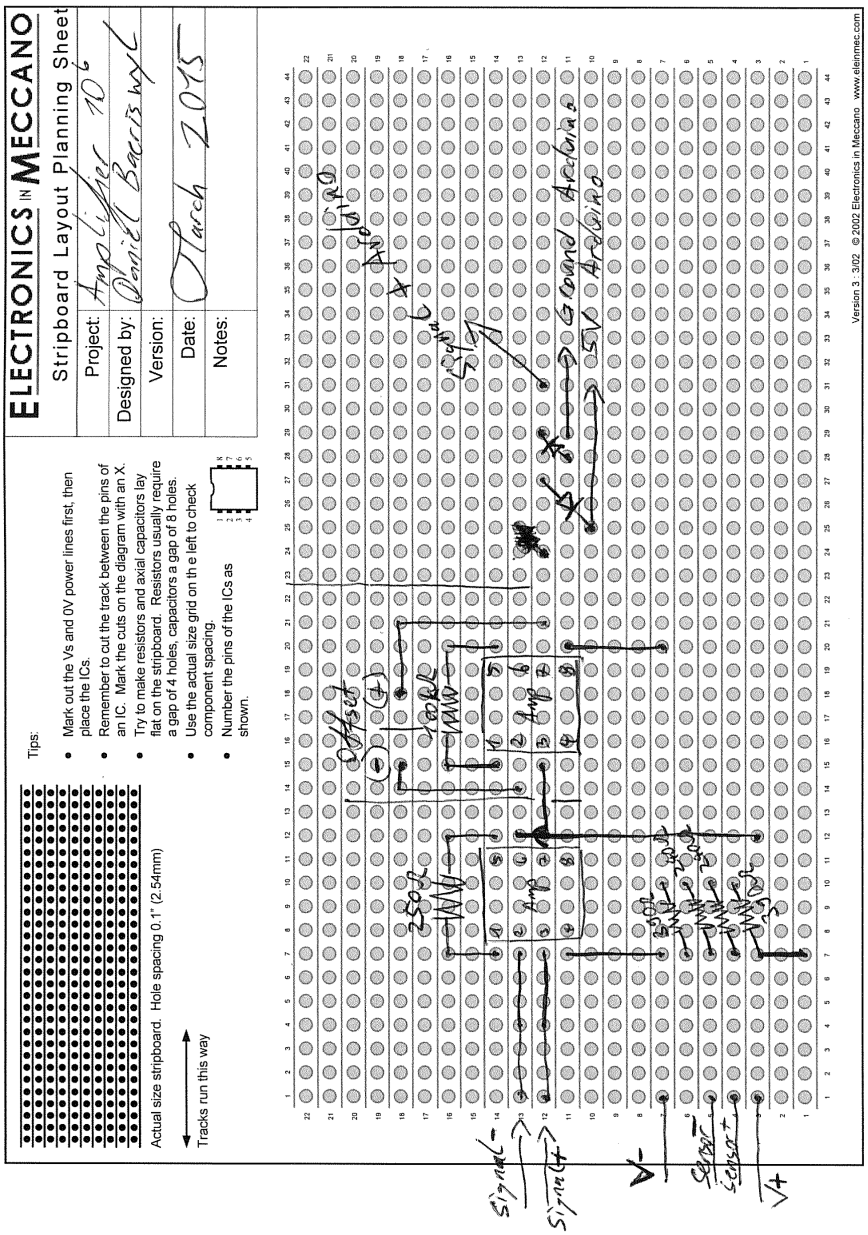

Figure 200: Amplifier from microVolts to Volts.

References

[1] Levick, J. R., 2010, An introduction to cardiovascular physiology, Hodder Arnold, London.

[2] Boron, W. F., and Boulpaep, E. L., 2009, Medical physiology : a cellular and molecular approach, Saunders, Philadelphia, Pa. ; London.

[3] Medzhitov, R., 2008, "Origin and physiological roles of inflammation," Nature, 454(7203), pp. 428-435.

[4] Hahn, C., and Schwartz, M., 2009, "Mechanotransduction in vascular physiology and atherogenesis," Nature Reviews Molecular Cell Biology, 10(1), pp. 53-62.

[5] Garipcan, B., Maenz, S., Pham, T., Settmacher, U., Jandt, K. D., Zanow, J., and Bossert, J., 2011, "Image Analysis of Endothelial Microstructure and Endothelial Cell Dimensions of Human Arteries; A Preliminary Study," 13(1-2).

[6] Chiu, J., and Chien, S., 2011, "Effects of Disturbed Flow on Vascular Endothelium: Pathophysiological Basis and Clinical Perspectives," Physiological Reviews, 91(1), pp. 327-387.

[7] Balligand, J., Feron, O., and Dessy, C., 2009, "eNOS Activation by Physical Forces: From Short-Term Regulation of Contraction to Chronic Remodeling of Cardiovascular Tissues," Physiological Reviews, 89(2), pp. 481-534.

[8] Chien, S., 2007, "Mechanotransduction and endothelial cell homeostasis: the wisdom of the cell," American Journal of Physiology-Heart and Circulatory Physiology, 292(3), pp. H1209-H1224.

[9] Alphonsus, C., and Rodseth, R., 2014, "The endothelial glycocalyx: a review of the vascular barrier," Anaesthesia, 69(7), pp. 777-784.

[10] Weinbaum, S., Tarbell, J., and Damiano, E., 2007, "The structure and function of the endothelial glycocalyx layer," Annual Review of Biomedical Engineering, 9, pp. 121-167.

[11] Becker, B., Chappell, D., and Jacob, M., 2010, "Endothelial glycocalyx and coronary vascular permeability: the fringe benefit," Basic Research in Cardiology, 105(6), pp. 687-701.

[12] Pries, A., Secomb, T., and Gaehtgens, P., 2000, "The endothelial surface layer," Pflugers Archiv-European Journal of Physiology, 440(5), pp. 653-666.

[13] Reitsma, S., Slaaf, D., Vink, H., van Zandvoort, M., and Egbrink, M., 2007, "The endothelial glycocalyx: composition, functions, and visualization," Pflugers Archiv-European Journal of Physiology, 454(3), pp. 345-359.

[14] Pahakis, M., Kosky, J., Dull, R., and Tarbell, J., 2007, "The role of endothelial glycocalyx components in mechanotransduction of fluid shear stress," Biochemical and Biophysical Research Communications, 355(1), pp. 228-233.

[15] Arnaout, M., Goodman, S., and Xiong, J., 2007, "Structure and mechanics of integrin-based cell adhesion," Current Opinion in Cell Biology, 19(5), pp. 495-507.

[16] Luo, B., Carman, C., and Springer, T., 2007, "Structural basis of integrin regulation and signaling," Annual Review of Immunology, 25, pp. 619-647.

[17] Conway, D., and Schwartz, M. A., 2012 "Lessons from the endothelial junctional mechanosensory complex," F1000 Biology Reports

[18] Tzima, E., Irani-Tehrani, M., Kiosses, W., Dejana, E., Schultz, D., Engelhardt, B., Cao, G., DeLisser, H., and Schwartz, M., 2005, "A mechanosensory complex that mediates the endothelial cell response to fluid shear stress," Nature, 437(7057), pp. 426-431.

[19] Conway, D., Breckenridge, M., Hinde, E., Gratton, E., Chen, C., and Schwartz, M., 2013, "Fluid Shear Stress on Endothelial Cells Modulates Mechanical Tension across VE-Cadherin and PECAM-1," Current Biology, 23(11), pp. 1024-1030.

[20] Collins, C., Guilluy, C., Welch, C., O'Brien, E., Hahn, K., Superfine, R., Burridge, K., and Tzima, E., 2012, "Localized Tensional Forces on PECAM-1 Elicit a Global Mechanotransduction Response via the Integrin-RhoA Pathway," Current Biology, 22(22), pp. 2087-2094.

[21] Brasch, J., Harrison, O., Ahlsen, G., Carnally, S., Henderson, R., Honig, B., and Shapiro, L., 2011, "Structure and Binding Mechanism of Vascular Endothelial Cadherin: A Divergent Classical Cadherin," Journal of Molecular Biology, 408(1), pp. 57-73.

[22] Liu, Y., Sweet, D., Irani-Tehrani, M., Maeda, N., and Tzima, E., 2008, "Shc coordinates signals from intercellular junctions and integrins to regulate flow-induced inflammation," Journal of Cell Biology, 182(1), pp. 185-196.

[23] Olsson, A., Dimberg, A., Kreuger, J., and Claesson-Welsh, L., 2006, "VEGF receptor signalling - in control of vascular function," Nature Reviews Molecular Cell Biology, 7(5), pp. 359-371.

[24] Holmes, K., Roberts, O., Thomas, A., and Cross, M., 2007, "Vascular endothelial growth factor receptor-2: Structure, function, intracellular signalling and therapeutic inhibition," Cellular Signalling, 19(10), pp. 2003-2012.

[25] Jin, Z., Ueba, H., Tanimoto, T., Lungu, A., Frame, M., and Berk, B., 2003, "Ligand-independent activation of vascular endothelial growth factor receptor 2 by fluid shear stress regulates activation of endothelial nitric oxide synthase," Circulation Research, 93(4), pp. 354-363.

[26] Shay-Salit, A., Shushy, M., Wolfovitz, E., Yahav, H., Breviario, F., Dejana, E., and Resnick, N., 2002, "VEGF receptor 2 and the adherens junction as a mechanical transducer in vascular endothelial cells," Proceedings of the National Academy of Sciences of the United States of America, 99(14), pp. 9462-9467.

[27] Chen, K., Li, Y., Kim, M., Li, S., Yuan, S., Chien, S., and Shyy, J., 1999, "Mechanotransduction in response to shear stress - Roles of receptor tyrosine kinases, integrins, and Shc," Journal of Biological Chemistry, 274(26), pp. 18393-18400.

[28] Oldham, W., and Hamm, H., 2008, "Heterotrimeric G protein activation by G-protein-coupled receptors," Nature Reviews Molecular Cell Biology, 9(1), pp. 60-71.

[29] Gudi, S., Nolan, J., and Frangos, J., 1998, "Modulation of GTPase activity of G proteins by fluid shear stress and phospholipid composition," Proceedings of the National Academy of Sciences of the United States of America, 95(5), pp. 2515-2519.

[30] Chachisvilis, M., Zhang, Y., and Frangos, J., 2006, "G protein-coupled receptors sense fluid shear stress in endothelial cells," Proceedings of the National Academy of Sciences of the United States of America, 103(42), pp. 15463-15468.

[31] Satir, P., Pedersen, L., and Christensen, S., 2010, "The primary cilium at a glance," Journal of Cell Science, 123(4), pp. 499-503.

[32] Nauli, S., Kawanabe, Y., Kaminski, J., Pearce, W., Ingber, D., and Zhou, J., 2008, "Endothelial cilia are fluid shear sensors that regulate calcium signaling and nitric oxide production through polycystin-1," Circulation, 117(9), pp. 1161-1171.

[33] Hierck, B., Van der Heiden, K., Alkemade, F., de Pas, S., Van Thienen, J., Groenendijk, B., Bax, W., Van der Laarse, A., DeRuiter, M., Horrevoets, A., and Poelmann, R., 2008, "Primary cilia sensitize endothelial cells for fluid shear stress," Developmental Dynamics, 237(3), pp. 725-735.

[34] Veland, I., Awan, A., Pedersen, L., Yoder, B., and Christensen, S., 2009, "Primary Cilia and Signaling Pathways in Mammalian Development, Health and Disease," Nephron Physiology, 111(3), pp. 39-53.

[35] Van der Heiden, K., Hierck, B., Krams, R., de Crom, R., Cheng, C., Baiker, M., Pourquie, M., Alkemade, F., DeRuiter, M., Gittenberger-de Groot, A., and Poelmann, R., 2008, "Endothelial primary cilia in areas of disturbed flow are at the base of atherosclerosis," Atherosclerosis, 196(2), pp. 542-550.

[36] Parton, R., and Simons, K., 2007, "The multiple faces of caveolae," Nature Reviews Molecular Cell Biology, 8(3), pp. 185-194.

[37] Rizzo, V., Morton, C., DePaola, N., Schnitzer, J., and Davies, P., 2003, "Recruitment of endothelial caveolae into mechanotransduction pathways by flow conditioning in vitro," American Journal of Physiology-Heart and Circulatory Physiology, 285(4), pp. H1720-H1729.

[38] Boyd, N., Park, H., Yi, H., Boo, Y., Sorescu, G., Sykes, M., and Jo, H., 2003, "Chronic shear induces caveolae formation and alters ERK and Akt responses in endothelial cells," American Journal of Physiology-Heart and Circulatory Physiology, 285(3), pp. H1113-H1122.

[39] Radel, C., and Rizzo, V., 2005, "Integrin mechanotransduction stimulates caveolin-1 phosphorylation and recruitment of Csk to mediate actin reorganization," American Journal of Physiology-Heart and Circulatory Physiology, 288(2), pp. H936-H945.

[40] Yu, J., Bergaya, S., Murata, T., Alp, I., Bauer, M., Lin, M., Drab, M., Kurzchalia, T., Stan, R., and Sessa, W., 2006, "Direct evidence for the role of caveolin-1 and caveolae in mechanotransduction and remodeling of blood vessels," Journal of Clinical Investigation, 116(5), pp. 1284-1291.

[41] Alberts, B., Wilson, J. H., and Hunt, T., 2008, Molecular biology of the cell, Garland Science, New York, N.Y. ; Abingdon.

[42] Gautam, M., Gojova, A., and Barakat, A., 2006, "Flow-activated ion channels in vascular endothelium," Cell Biochemistry and Biophysics, 46(3), pp. 277-284.

[43] Nilius, B., and Droogmans, G., 2001, "Ion channels and their functional role in vascular endothelium," Physiological Reviews, 81(4), pp. 1415-1459.

[44] Barakat, A., Lieu, D., and Gojova, A., 2006, "Secrets of the code: Do vascular endothelial cells use ion channels to decipher complex flow signals?," Biomaterials, 27(5), pp. 671-678.

[45] Chien, S., 2008, "Effects of disturbed flow on endothelial cells," Annals of Biomedical Engineering, 36(4), pp. 554-562.

[46] Chatzizisis, Y., Coskun, A., Jonas, M., Edelman, E., Feldman, C., and Stone, P., 2007, "Role of endothelial shear stress in the natural history of coronary atherosclerosis and vascular remodeling - Molecular, cellular, and vascular behavior," Journal of the American College of Cardiology, 49(25), pp. 2379-2393.

[47] Tarbell, J., Shi, Z., Dunn, J., Jo, H., Davis, S., and Moin, P., 2014, "Fluid Mechanics, Arterial Disease, and Gene Expression," Annual Review of Fluid Mechanics, Vol 46, 46, pp. 591-614.

[48] Lu, D., and Kassab, G., 2011, "Role of shear stress and stretch in vascular mechanobiology," Journal of the Royal Society Interface, 8(63), pp. 1379-1385.

[49] Tousoulis, D., Kampoli, A., Papageorgiou, C., and Stefanadis, C., 2012, "The Role of Nitric Oxide on Endothelial Function," Current Vascular Pharmacology, 10(1), pp. 4-18.

[50] Fry, D., 1969, "Certain chemorheologic considerations regarding blood vascular interface with particular reference to coronary artery disease," Circulation, 40(5S4), pp. IV38-&.

[51] Peiffer, V., Sherwin, S., and Weinberg, P., 2013, "Does low and oscillatory wall shear stress correlate spatially with early atherosclerosis? A systematic review," Cardiovascular Research, 99(2), pp. 242-250.

[52] Loudon, C., and Tordesillas, A., 1998, "The Use of the Dimensionless Womersley Number to Characterize the Unsteady Nature of Internal Flow," Journal of Theoretical Biology, 191(1), pp. 63-78.

[53] Perktold, K., and Rappitsch, G., 1995, "Computer-simulation of local blood-flow and vessel mechanics in a compliant carotid-artery bifurcation model," Journal of Biomechanics, 28(7), pp. 845-856.

[54] Mittal, R., Simmons, S., and Udaykumar, H., 2001, "Application of large-eddy simulation to the study of pulsatile flow in a modeled arterial stenosis," Journal of Biomechanical Engineering-Transactions of the Asme, 123(4), pp. 325-332.

[55] Lantz, J., Gardhagen, R., and Karlsson, M., 2012, "Quantifying turbulent wall shear stress in a subject specific human aorta using large eddy simulation," Medical Engineering & Physics, 34(8), pp. 1139-1148.

[56] Brisman, J., Song, J., and Newell, D., 2006, "Medical progress: Cerebral aneurysms," New England Journal of Medicine, 355(9), pp. 928-939.

[57] Ventikos, Y., Bowker, T. J., Watton, P. N., Kakalis, N. M. P., and Byrne, J. V., 2009, "Risk evaluation and interventional planning for cerebral aneurysms: computational models for growth, coiling and thrombosis," International Journal of Computational Fluid Dynamics, 23(8), pp. 595-607.

[58] Rincon, F., Rossenwasser, R., and Dumont, A., 2013, "The Epidemiology of Admissions of Nontraumatic Subarachnoid Hemorrhage in the United States," Neurosurgery, 73(2), pp. 217-222.

[59] Chalouhi, N., Hoh, B., and Hasan, D., 2013, "Review of Cerebral Aneurysm Formation, Growth, and Rupture," Stroke, 44(12), pp. 3613-3622.

[60] Chalouhi, N., Ali, M. S., Jabbour, P. M., Tjoumakaris, S. I., Gonzalez, L. F., Rosenwasser, R. H., Koch, W. J., and Dumont, A. S., 2012, "Biology of intracranial aneurysms: role of inflammation," J Cereb Blood Flow Metab, 32(9), pp. 1659-1676.

[61] Takemura, Y., Hirata, Y., Sakata, N., Nabeshima, K., Takeshita, M., and Inoue, T., 2010, "Histopathologic characteristics of a saccular aneurysm arising in the non-branching segment of the distal middle cerebral artery," Pathology Research and Practice, 206(6), pp. 391-396.

[62] Bashir, M., Bhatti, L., Marin, D., and Nelson, R., 2015, "Emerging Applications for Ferumoxytol as a Contrast Agent in MRI," Journal of Magnetic Resonance Imaging, 41(4), pp. 884-898.

[63] Hasan, D., Mahaney, K., Magnotta, V., Kung, D., Lawton, M., Hashimoto, T., Winn, H., Saloner, D., Martin, A., Gahramanov, S., Dosa, E., Neuwelt, E., and Young, W., 2012, "Macrophage Imaging Within Human Cerebral Aneurysms Wall Using Ferumoxytol-Enhanced MRI: A Pilot Study," Arteriosclerosis Thrombosis and Vascular Biology, 32(4), pp. 1032-1038.

[64] Richards, J. M., Semple, S. I., MacGillivray, T. J., Gray, C., Langrish, J. P., Williams, M., Dweck, M., Wallace, W., McKillop, G., Chalmers, R. T., Garden, O. J., and Newby, D. E., 2011, "Abdominal aortic aneurysm growth predicted by uptake of ultrasmall superparamagnetic particles of iron oxide: a pilot study," Circ Cardiovasc Imaging, 4(3), pp. 274-281.

[65] Sen, R., and Baltiomore, D., 1986, "Inducibility of kappa-immunoglobulin enhancer-binding protein NF-kappa-B by a posttranslational mechanism," Cell, 47(6), pp. 921-928.

[66] SEN, R., and BALTIMORE, D., 1986, "MULTIPLE NUCLEAR FACTORS INTERACT WITH THE IMMUNOGLOBULIN ENHANCER SEQUENCES," Cell, 46(5), pp. 705-716.

[67] Napetschnig, J., Wu, H., and Dill, K., 2013, "Molecular Basis of NF-kappa B Signaling," Annual Review of Biophysics, Vol 42, 42, pp. 443-468.

[68] Oeckinghaus, A., Hayden, M., and Ghosh, S., 2011, "Crosstalk in NF-kappa B signaling pathways," Nature Immunology, 12(8), pp. 695-708.

[69] Basseres, D., and Baldwin, A., 2006, "Nuclear factor-kappa B and inhibitor of kappa B kinase pathways in oncogenic initiation and progression," Oncogene, 25(51), pp. 6817-6830.

[70] Courtois, G., and Gilmore, T., 2006, "Mutations in the NF-kappa B signaling pathway: implications for human disease," Oncogene, 25(51), pp. 6831-6843.

[71] Toubi, E., and Shoenfeld, Y., 2004, "Toll-like receptors and their role in the development of autoimmune diseases," Autoimmunity, 37(3), pp. 183-188.

[72] Oeckinghaus, A., and Ghosh, S., 2009, "The NF-kappa B Family of Transcription Factors and Its Regulation," Cold Spring Harbor Perspectives in Biology, 1(4).

[73] Lawrence, T., 2009, "The Nuclear Factor NF- κ B Pathway in Inflammation," Cold Spring Harbor Perspectives in Biology, 1(6).

[74] Cheong, R., Hoffmann, A., and Levchenko, A., 2008, "Understanding NF-kappa B signaling via mathematical modeling," Molecular Systems Biology, 4.

[75] Hoffmann, A., Levchenko, A., Scott, M., and Baltimore, D., 2002, "The I kappa B-NF-kappa B signaling module: Temporal control and selective gene activation," Science, 298(5596), pp. 1241-1245.

[76] Cell-Signaling-Technology, 2012, "NFkappaB Signaling Pathway," Cell Signaling Technology, www.cellsignal.com.

[77] Häcker, H., and Karin, M., 2006, "Regulation and Function of IKK and IKK-Related Kinases,"Science Stke.

[78] Carlotti, F., Chapman, R., Dower, S., and Qwarnstrom, E., 1999, "Activation of nuclear factor kappa B in single living cells - Dependence of nuclear translocation and anti-apoptotic function on EGFPRELA concentration," Journal of Biological Chemistry, 274(53), pp. 37941-37949.

[79] Carlotti, F., Dower, S., and Qwarnstrom, E., 2000, "Dynamic shuttling of nuclear factor kappa B between the nucleus and cytoplasm as a consequence of inhibitor dissociation," Journal of Biological Chemistry, 275(52), pp. 41028-41034.

[80] Lipniacki, T., Paszek, P., Brasier, A., Luxon, B., and Kimmel, M., 2004, "Mathematical model of NF-kappa B regulatory module," Journal of Theoretical Biology, 228(2), pp. 195-215.

[81] Nelson, D., Ihekwaba, A., Elliott, M., Johnson, J., Gibney, C., Foreman, B., Nelson, G., See, V., Horton, C., Spiller, D., Edwards, S., McDowell, H., Unitt, J., Sullivan, E., Grimley, R., Benson, N., Broomhead, D., Kell, D., and White, M., 2004, "Oscillations in NF-kappa B signaling control the dynamics of gene expression," Science, 306(5696), pp. 704-708.

[82] Pogson, M., Holcombe, M., Smallwood, R., and Qwarnstrom, E., 2008, "Introducing Spatial Information into Predictive NF-kappa B Modelling - An Agent-Based Approach," Plos One, 3(6).

[83] Lipniacki, T., Paszek, P., Brasier, A., Luxon, B., and Kimmel, M., 2006, "Stochastic regulation in early immune response," Biophysical Journal, 90(3), pp. 725-742.

[84] Hayot, F., and Jayaprakash, C., 2006, "NF-kappa B oscillations and cell-to-cell variability," Journal of Theoretical Biology, 240(4), pp. 583-591.

[85] Altschuler, S., and Wu, L., 2010, "Cellular Heterogeneity: Do Differences Make a Difference?," Cell, 141(4), pp. 559-563.

[86] Cheong, R., Bergmann, A., Werner, S., Regal, J., Hoffmann, A., and Levchenko, A., 2006, "Transient I kappa B kinase activity mediates temporal NF-kappa B dynamics in response to a wide range of tumor necrosis factor-alpha doses," Journal of Biological Chemistry, 281(5), pp. 2945-2950.

[87] Basak, S., Kim, H., Kearns, J., Tergaonkar, V., O'Dea, E., Werner, S., Benedict, C., Ware, C., Ghosh, G., Verma, I., and Hoffmann, A., 2007, "A fourth I kappa B protein within the NF-kappa B signaling module," Cell, 128(2), pp. 369-381.

[88] O'Dea, E., Barken, D., Peralta, R., Tran, K., Werner, S., Kearns, J., Levchenko, A., and Hoffmann, A., 2007, "A homeostatic model of I kappa B metabolism to control constitutive NF-kappa B activity," Molecular Systems Biology, 3.

[89] Lipniacki, T., Puszynski, K., Paszek, P., Brasier, A., and Kimmel, M., 2007, "Single TNF alpha trimers mediating NF-kappa B activation: stochastic robustness of NF-kappa B signaling," Bmc Bioinformatics, 8.

[90] Lipniacki, T., and Kimmel, M., 2007, "Deterministic and stochastic models of NF kappa B pathway," Cardiovascular Toxicology, 7(4), pp. 215-234.

[91] Shih, V. F. S., Kearns, J. D., Basak, S., Savinova, O. V., Ghosh, G., and Hoffmann, A., 2009, "Kinetic control of negative feedback regulators of NF- κ B/RelA determines their pathogen- and cytokine-receptor signaling specificity," Proceedings of the National Academy of Sciences, 106(24), pp. 9619-9624.

[92] Ashall, L., Horton, C., Nelson, D., Paszek, P., Harper, C., Sillitoe, K., Ryan, S., Spiller, D., Unitt, J., Broomhead, D., Kell, D., Rand, D., See, V., and White, M., 2009, "Pulsatile Stimulation Determines Timing and Specificity of NF-kappa B-Dependent Transcription," Science, 324(5924), pp. 242-246.

[93] Lee, T., Denny, E., Sanghvi, J., Gaston, J., Maynard, N., Hughey, J., and Covert, M., 2009, "A Noisy Paracrine Signal Determines the Cellular NF-kappa B Response to Lipopolysaccharide," Science Signaling, 2(93).

[94] Gutschow, M., Hughey, J., Ruggero, N., Bajar, B., Valle, S., and Covert, M., 2013, "Single-Cell and Population NF-kappa B Dynamic Responses Depend on Lipopolysaccharide Preparation," Plos One, 8(1).

[95] Tay, S., Hughey, J., Lee, T., Lipniacki, T., Quake, S., and Covert, M., 2010, "Single-cell NF-kappa B dynamics reveal digital activation and analogue information processing," Nature, 466(7303), pp. 267-U149.

[96] Turner, D., Paszek, P., Woodcock, D., Nelson, D., Horton, C., Wang, Y., Spiller, D., Rand, D., White, M., and Harper, C., 2010, "Physiological levels of TNF alpha stimulation induce stochastic dynamics of NF-kappa B responses in single living cells," Journal of Cell Science, 123(16), pp. 2834-2843.

[97] Fallahi-Sichani, M., Kirschner, D., and Linderman, J., 2012, "NF-kappa B signaling dynamics play a key role in infection control in tuberculosis," Frontiers in Physiology, 3.

[98] Choudhary, S., Kalita, M., Fang, L., Patel, K., Tian, B., Zhao, Y., Edeh, C., and Brasier, A., 2013, "Inducible Tumor Necrosis Factor (TNF) Receptor-associated Factor-1 Expression Couples the Canonical to the Non-canonical NF-kappa B Pathway in TNF Stimulation," Journal of Biological Chemistry, 288(20), pp. 14612-14623.

[99] Zambrano, S., Bianchi, M., and Agresti, A., 2014, "High-Throughput Analysis of NF-kappa B Dynamics in Single Cells Reveals Basal Nuclear Localization of NF-kappa B and Spontaneous Activation of Oscillations," Plos One, 9(3).

[100] Zambrano, S., De Toma, I., Piffer, A., Bianchi, M., and Agresti, A., 2016, "NF-kappa B oscillations translate into functionally related patterns of gene expression," Elife, 5.

[101] Fuseler, J., Merrill, D., Rogers, J., Grisham, M., and Wolf, R., 2006, "Analysis and quantitation of NF-kappa B nuclear translocation in tumor necrosis factor alpha

(TNF-alpha) activated vascular endothelial cells," Microscopy and Microanalysis, 12(3), pp. 269-276.

[102] Ganguli, A., Persson, L., Palmer, I., Evans, I., Yang, L., Smallwood, R., Black, R., and Qwarnstrom, E., 2005, "Distinct NF-kappa B regulation by shear stress through ras-dependent I kappa B alpha oscillations - Real-time analysis of flow-mediated activation in live cells," Circulation Research, 96(6), pp. 626-634.

[103] Bhullar, I., Li, Y., Miao, H., Zandi, E., Kim, M., Shyy, J., and Chien, S., 1998, "Fluid shear stress activation of I kappa B kinase is integrin-dependent," Journal of Biological Chemistry, 273(46), pp. 30544-30549.

[104] Wang, Y., Chang, J., Li, Y. C., Li, Y. S., Shyy, J. Y., and Chien, S., 2004, "Shear stress and VEGF activate IKK via the Flk-1/Cbl/Akt signaling pathway," Am J Physiol Heart Circ Physiol, 286(2), pp. H685-692.

[105] Wang, Y., Flores, L., Lu, S., Miao, H., Li, Y., and Chien, S., 2009, "Shear Stress Regulates the Flk-1/Cbl/PI3K/NF-kappa B Pathway Via Actin and Tyrosine Kinases," Cellular and Molecular Bioengineering, 2(3), pp. 341-350.

[106] Hay, D., Beers, C., Cameron, V., Thomson, L., Flitney, F., and Hay, R., 2003, "Activation of NF-kappa B nuclear transcription factor by flow in human endothelial cells," Biochimica Et Biophysica Acta-Molecular Cell Research, 1642(1-2), pp. 33-44.

[107] Mohan, S., Koyoma, K., Thangasamy, A., Nakano, H., Glickman, R., and Mohan, N., 2007, "Low shear stress preferentially enhances IKK activity through selective sources of ROS for persistent activation of NF-kappa B in endothelial cells," American Journal of Physiology-Cell Physiology, 292(1), pp. C362-C371.

[108] Mohan, S., Mohan, N., and Sprague, E., 1997, "Differential activation of NF-kappa B in human aortic endothelial cells conditioned to specific flow environments," American Journal of Physiology-Cell Physiology, 273(2), pp. C572-C578.

[109] Khachigian, L., Resnick, N., Gimbrone, M., and Collins, T., 1995, "Nuclear factor-kappa-B interacts functionally with the platelet-derived growth-factor B-chain shear-stress response element in vascular endothelial cells exposed to fluid shear stress," Journal of Clinical Investigation, 96(2), pp. 1169-1175.

[110] Lan, Q., Mercurius, K., and Davies, P., 1994, "Stimulation of transcription factors NF-kappa-B and AP1 in endothelial cells subjected to shear stress," Biochemical and Biophysical Research Communications, 201(2), pp. 950-956.

[111] Nagel, T., Resnick, N., Dewey, C., and Gimbrone, M., 1999, "Vascular endothelial cells respond to spatial gradients in fluid shear stress by enhanced activation of transcription factors," Arteriosclerosis Thrombosis and Vascular Biology, 19(8), pp. 1825-1834.

[112] Won, D., Zhu, S., Chen, M., Teichert, A., Fish, J., Matouk, C., Bonert, M., Ojha, M., Marsden, P., and Cybulsky, M., 2007, "Relative reduction of endothelial nitric-oxide synthase expression and transcription in atherosclerosis-prone regions of the mouse aorta and in an in Vitro model of disturbed flow," American Journal of Pathology, 171(5), pp. 1691-1704.

[113] Partridge, J., Carlsen, H., Enesa, K., Chaudhury, H., Zakkar, M., Luong, L., Kinderlerer, A., Johns, M., Blomhoff, R., Mason, J., Haskard, D., and Evans, P., 2007,

"Laminar shear stress acts as a switch to regulate divergent functions of NF-kappa B in endothelial cells," Faseb Journal, 21(13), pp. 3553-3561.

[114] Feaver, R., Gelfand, B., and Blackman, B., 2013, "Human haemodynamic frequency harmonics regulate the inflammatory phenotype of vascular endothelial cells," Nature Communications, 4.

[115] Hajra, L., Evans, A., Chen, M., Hyduk, S., Collins, T., and Cybulsky, M., 2000, "The NF-kappa B signal transduction pathway in aortic endothelial cells is primed for activation in regions predisposed to atherosclerotic lesion formation," Proceedings of the National Academy of Sciences of the United States of America, 97(16), pp. 9052-9057.

[116] Dai, G., Kaazempur-Mofrad, M., Natarajan, S., Zhang, Y., Vaughn, S., Blackman, B., Kamm, R., Garcia-Cardena, G., and Gimbrone, M., 2004, "Distinct endothelial phenotypes evoked by arterial waveforms derived from atherosclerosis-susceptible and -resistant regions of human vasculature," Proceedings of the National Academy of Sciences of the United States of America, 101(41), pp. 14871-14876.

[117] Hwang, S., Ballantyne, C., Sharrett, A., Smith, L., Davis, C., Gotto, A., and Boerwinkle, E., 1997, "Circulating adhesion molecules VCAM-1, ICAM-1, and E-selectin in carotid atherosclerosis and incident coronary heart disease cases - The atherosclerosis risk in communities (ARIC) study," Circulation, 96(12), pp. 4219-4225.

[118] Binion, D., Heidemann, J., Li, M., Nelson, V., Otterson, M., and Rafiee, P., 2009, "Vascular cell adhesion molecule-1 expression in human intestinal microvascular endothelial cells is regulated by PI 3-kinase/Akt/MAPK/NF-kappa B: inhibitory role of curcumin," American Journal of Physiology-Gastrointestinal and Liver Physiology, 297(2), pp. G259-G268.

[119] Shu, H., Agranoff, A., Nabel, E., Leung, K., Duckett, C., Neish, A., Collins, T., and Nabel, G., 1993, "Differential regulation of vascular cell-adhesion molecule-1 gene-expression by specific NF-kappa-B subunits in endothelial and epithelial-cells," Molecular and Cellular Biology, 13(10), pp. 6283-6289.

[120] Morigi, M., Zoja, C., Figliuzzi, M., Foppolo, M., Micheletti, G., Bontempelli, M., Saronni, M., Remuzzi, G., and Remuzzi, A., 1995, "Fluid shear-stress modulates surface expression of adhesion molecules by endothelial-cells," Blood, 85(7), pp. 1696-1703.

[121] Chiu, J., Lee, P., Chen, C., Lee, C., Chang, S., Chen, L., Lien, S., Ko, Y., Usami, S., and Chien, S., 2004, "Shear stress increases ICAM-1 and decreases VCAM-1 and E-selectin expressions induced by tumor necrosis factor-alpha in endothelial cells," Arteriosclerosis Thrombosis and Vascular Biology, 24(1), pp. 73-79.

[122] Nagel, T., Resnick, N., Atkinson, W., Dewey, C., and Gimbrone, M., 1994, "Sheer stress selectively up-regulates intercellular-adhesion molecule-1 expression in cultured human vascular endothelial-cells," Journal of Clinical Investigation, 94(2), pp. 885-891.

[123] Martinez-Lemus, L. A., and Galinanes, E. L., 2011, "Matrix metalloproteinases and small artery remodeling,"Drug Discovery Today: Disease ModelsDrug Discovery Today: Disease Models.

[124] Sun, H., Li, C., Chen, H., Lin, H., Lv, H., Zhang, Y., and Zhang, M., 2007, "Involvement of integrins, MAPK, and NF-kappa B in regulation of the shear stress-induced MMP-9 expression in endothelial cells," Biochemical and Biophysical Research Communications, 353(1), pp. 152-158.

[125] Magid, R., Murphy, T., and Galis, Z., 2003, "Expression of matrix metalloproteinase-9 in endothelial cells is differentially regulated by shear stress - role of c-Myc," Journal of Biological Chemistry, 278(35), pp. 32994-32999.

[126] Chen, Q., Jin, M., Yang, F., Zhu, J., Xiao, Q., and Zhang, L., 2013, "Matrix Metalloproteinases: Inflammatory Regulators of Cell Behaviors in Vascular Formation and Remodeling," Mediators of Inflammation.

[127] Chalouhi, N., Ali, M., Jabbour, P., Tjoumakaris, S., Gonzalez, L., Rosenwasser, R., Koch, W., and Dumont, A., 2012, "Biology of intracranial aneurysms: role of inflammation," Journal of Cerebral Blood Flow and Metabolism, 32(9), pp. 1659-1676.

[128] Aoki, T., Kataoka, H., Moriwaki, T., Nozaki, K., and Hashimoto, N., 2007, "Role of TIMP-1 and TIMP-2 in the Progression of Cerebral Aneurysms," Stroke, 38(8), pp. 2337-2345.

[129] Specht, E., Braselmann, E., Palmer, A., and Julius, D., 2017, "A Critical and Comparative Review of Fluorescent Tools for Live-Cell Imaging," Annual Review of Physiology, Vol 79, 79, pp. 93-117.

[130] Sander, J., and Joung, J., 2014, "CRISPR-Cas systems for editing, regulating and targeting genomes," Nature Biotechnology, 32(4), pp. 347-355.

[131] Kim, T., and Eberwine, J., 2010, "Mammalian cell transfection: the present and the future," Analytical and Bioanalytical Chemistry, 397(8), pp. 3173-3178.

[132] Liu, Z., Lavis, L., and Betzig, E., 2015, "Imaging Live-Cell Dynamics and Structure at the Single-Molecule Level," Molecular Cell, 58(4), pp. 644-659.

[133] Hilsenbeck, O., Schwarzfischer, M., Skylaki, S., Schauberger, B., Hoppe, P., Loeffler, D., Kokkaliaris, K., Hastreiter, S., Skylaki, E., Filipczyk, A., Strasser, M., Buggenthin, F., Feigelman, J., Krumsiek, J., van den Berg, A., Endele, M., Etzrodt, M., Marr, C., Theis, F., and Schroeder, T., 2016, "Software tools for single-cell tracking and quantification of cellular and molecular properties," Nature Biotechnology, 34(7), pp. 703-+.

[134] Schwarzfischer, M., Marr, C., Krumsiek, J., and Theis, F. J., 2011, "Efficient fluorescence image normalization for time lapse movies,"Proc. Microscopic Image Analysis with Applications in Biology.

[135] Grant, I., 1997, "Particle image velocimetry: A review," Proceedings of the Institution of Mechanical Engineers Part C-Journal of Mechanical Engineering Science, 211(1), pp. 55-76.

[136] Davis, C., Zambrano, S., Anumolu, P., Allen, A., Sonoqui, L., and Moreno, M., 2015, "Device-Based In Vitro Techniques for Mechanical Stimulation of Vascular Cells: A Review," Journal of Biomechanical Engineering-Transactions of the Asme, 137(4).

[137] FRANGOS, J., MCINTIRE, L., and ESKIN, S., 1988, "SHEAR-STRESS INDUCED STIMULATION OF MAMMALIAN-CELL METABOLISM," Biotechnology and Bioengineering, 32(8), pp. 1053-1060.

[138] Bacabac, R., Smit, T., Cowin, S., Van Loon, J., Nieuwstadt, F., Heethaar, R., and Klein-Nulend, J., 2005, "Dynamic shear stress in parallel-plate flow chambers," Journal of Biomechanics, 38(1), pp. 159-167.

[139] Usami, S., Chen, H.-H., Zhao, Y., Chien, S., and Skalak, R., 1993, "Design and construction of a linear shear stress flow chamber," Annals of biomedical engineering, 21(1), pp. 77-83.

[140] Dolan, J., Meng, H., Singh, S., Paluch, R., and Kolega, J., 2011, "High Fluid Shear Stress and Spatial Shear Stress Gradients Affect Endothelial Proliferation, Survival, and Alignment," Annals of Biomedical Engineering, 39(6), pp. 1620-1631.

[141] Wang, C., Lu, H., and Schwartz, M., 2012, "A novel in vitro flow system for changing flow direction on endothelial cells," Journal of Biomechanics, 45(7), pp. 1212-1218.

[142] DEWEY, C., BUSSOLARI, S., and SDOUGOS, H., 1978, "CHARACTERISTICS OF SECONDARY FLOW AND TURBULENCE IN A CONE-PLATE APPARATUS," Biorheology, 15(5-6), pp. 488-488.

[143] Warboys, C., de Luca, A., Amini, N., Luong, L., Duckles, H., Hsiao, S., White, A., Biswas, S., Khamis, R., Chong, C., Cheung, W., Sherwin, S., Bennett, M., Gil, J., Mason, J., Haskard, D., and Evans, P., 2014, "Disturbed Flow Promotes Endothelial Senescence via a p53-Dependent Pathway," Arteriosclerosis Thrombosis and Vascular Biology, 34(5), pp. 985-995.

[144] Warboys, C. M., Eric Berson, R., Mann, G. E., Pearson, J. D., and Weinberg, P. D., 2010, "Acute and chronic exposure to shear stress have opposite effects on endothelial permeability to macromolecules," American Journal of Physiology - Heart and Circulatory Physiology, 298(6), p. H1850.

[145] Thomas, J. M. D., Chakraborty, A., Berson, R. E., Shakeri, M., and Sharp, M. K., 2017, "Validation of a CFD model of an orbiting culture dish with PIV and analytical solutions," pp. n/a-n/a.

[146] Tucker, R., Henningsson, P., Franklin, S., Chen, D., Ventikos, Y., Bomphrey, R., and Thompson, M., 2014, "See-saw rocking: an in vitro model for mechanotransduction research," Journal of the Royal Society Interface, 11(97).

[147] Neuhaus, W., Lauer, R., Oelzant, S., Fringeli, U., Ecker, G., and Noe, C., 2006, "A novel flow based hollow-fiber blood-brain barrier in vitro model with immortalised cell line PBMEC/C1-2," Journal of Biotechnology, 125(1), pp. 127-141.

[148] Wang, J., Khafagy, E., Khanafer, K., Takayama, S., and Elsayed, M., 2016, "Organization of Endothelial Cells, Pericytes, and Astrocytes into a 3D Microfluidic in Vitro Model of the Blood-Brain Barrier," Molecular Pharmaceutics, 13(3), pp. 895-906.

[149] van der Meer, A., Poot, A., Duits, M., Feijen, J., and Vermes, I., 2009, "Microfluidic Technology in Vascular Research," Journal of Biomedicine and Biotechnology.

[150] D'Acquisto, F., May, M. J., Ghosh, S., 2002, "Inhibition of nuclear factor kappa B (NF-B): an emerging theme in anti-inflammatory therapies. Molecular interventions, p.p1 422-435.

[151] http://www.addgene.org/, "AddGene."

[152] Semrock, "Semrock Searchligh."

[153] Openmicroscopy, "BioFormats,"http://www.openmicroscopy.org/.

[154] Orfanidis, S., 1996, "*Introduction to Signal Processing* ."Englewood Cliffs, NJ.

[155] 1987, Kendall's advanced theory of statistics, Oxford University Press, Inc.

[156] MathWorks, I., 2014, "Matlab R2014b,"Natick, Massachusetts.

[157] Arthur, D., 2007, "K-means++: The Advantages of Careful Seeding.," V. Sergi, ed.*SODA '07: Proceedings of the Eighteenth Annual ACM-SIAM Symposium on Discrete Algorithms*, pp. pp. 1027–1035.

[158] Tibshirani, R., Walther, G., and Hastie, T., 2001, "Estimating the number of clusters in a data set via the gap statistic," Journal of the Royal Statistical Society Series B-Statistical Methodology, 63, pp. 411-423.

[159] Eisen, M., Spellman, P., Brown, P., and Botstein, D., 1998, "Cluster analysis and display of genome-wide expression patterns," Proceedings of the National Academy of Sciences of the United States of America, 95(25), pp. 14863-14868.

[160] ESI-Group, 2013, "CFD-ACE+ Manual."

[161] Versteeg, H., and Malalasekera, W., 1995, An Introduction to Computational Fluid Dynamics. The Finite Volume Method, Longman Group Ltd., London.

[162] Vogel, M., Franke, J., Frank, W., and Schroten, H., 2007, "Flow in the well: computational fluid dynamics is essential in flow chamber construction," Cytotechnology, 55(1), pp. 41-54.

[163] ARMALY, B., DURST, F., PEREIRA, J., and SCHONUNG, B., 1983, "EXPERIMENTAL AND THEORETICAL INVESTIGATION OF BACKWARD-FACING STEP FLOW," Journal of Fluid Mechanics, 127(FEB), pp. 473-496.

[164] Kaiktsis, L., Karniadakis, G., and Orszag, S., 1991, "Onset of 3-dimensionality, equilibria, and early transition in flow over a backward-facing step," Journal of Fluid Mechanics, 231, pp. 501-528.

[165] Scheider, M. V., 2013, "In Silico Systems Biology," Springer, p. 313.

[166] Michaelis, L., and Menten, M., 1913, "The kenetics of the inversion effect.," Biochemische Zeitschrift, 49, pp. 333-369.

[167] Huang, S., 2009, "Non-genetic heterogeneity of cells in development: more than just noise," Development, 136(23), pp. 3853-3862.

[168] Filippi, S., Barnes, C., Kirk, P., Kudo, T., Kunida, K., McMahon, S., Tsuchiya, T., Wada, T., Kuroda, S., and Stumpf, M., 2016, "Robustness of MEK-ERK Dynamics and Origins of Cell-to-Cell Variability in MAPK Signaling," Cell Reports, 15(11), pp. 2524-2535.

[169] Fagerlund, R., Kinnunen, L., Kohler, M., Julkunen, I., and Melen, K., 2005, "NF-kappa B is transported into the nucleus by importin alpha 3 and importin alpha 4," Journal of Biological Chemistry, 280(16), pp. 15942-15951.

[170] Fagerlund, R., Melen, K., Kinnunen, L., and Julkunen, I., 2007, "NF-kappa B is transported into the nucleus by a subset of importin a molecules," Journal of Immunology, 178.

[171] Lagarias, J., Reeds, J., Wright, M., and Wright, P., 1998, "Convergence properties of the Nelder-Mead simplex method in low dimensions," Siam Journal on Optimization, 9(1), pp. 112-147.

[172] Butcher, J. C., 2008, Numerical methods for ordinary differential equations, Wiley ; Chichester : John Wiley [distributor], Hoboken, N.J.

[173] Chapra, S. C., and Canale, R. P., 2010, Numerical methods for engineers, McGraw-Hill Higher Education, Boston, [Mass.] ; London.

[174] Hairer, E., and Wanner, G., 1996, Solving ordinary differential equations II : stiff and differential-algebraic problems, Springer, Berlin ; London.

[175] Shampine, L., and Reichelt, M., 1997, "The MATLAB ODE suite," Siam Journal on Scientific Computing, 18(1), pp. 1-22.

[176] Hosea, M., and Shampine, L., 1996, "Analysis and implementation of TR-BDF2," Applied Numerical Mathematics, 20(1-2), pp. 21-37.

[177] Stefanini, M., Wu, F., Mac Gabhann, F., and Popel, A., 2008, "A compartment model of VEGF distribution in blood, healthy and diseased tissues," Bmc Systems Biology, 2.

[178] Koh, G., Teong, H., Clement, M., Hsu, D., and Thiagarajan, P., 2006, "A decompositional approach to parameter estimation in pathway modeling: a case study of the Akt and MAPK pathways and their crosstalk," Bioinformatics, 22(14), pp. E271-E280.

[179] Koo, A., Nordsletten, D., Umeton, R., Yankama, B., Ayyadurai, S., Garcia-Cardena, G., and Dewey, C. F., Jr., 2013, "In silico modeling of shear-stress-induced nitric oxide production in endothelial cells through systems biology," Biophys J, 104(10), pp. 2295-2306.

[180] Go, Y., Park, H., Maland, M., Darley-Usmar, V., Stoyanov, B., Wetzker, R., and Jo, H., 1998, "Phosphatidylinositol 3-kinase gamma mediates shear stress-dependent activation of JNK in endothelial cells," American Journal of Physiology-Heart and Circulatory Physiology, 275(5), pp. H1898-H1904.

[181] Bartfeld, S., Hess, S., Bauer, B., Machuy, N., Ogilvie, L., Schuchhardt, J., and Meyer, T., 2010, "High-throughput and single-cell imaging of NF-kappa B oscillations using monoclonal cell lines," Bmc Cell Biology, 11.

[182] Shaik, S., Soltau, T., Chaturvedi, G., Totapally, B., Hagood, J., Andrews, W., Athar, M., Voitenok, N., Killingsworth, C., Patel, R., Fallon, M., and Maheshwari, A., 2009, "Low Intensity Shear Stress Increases Endothelial ELR+ CXC Chemokine Production via a Focal Adhesion Kinase-p38 beta MAPK-NF-kappa B Pathway," Journal of Biological Chemistry, 284(9), pp. 5945-5955.

[183] Tsou, J., Gower, R., Ting, H., Schaff, U., Insana, M., Passerini, A., and Simon, S., 2008, "Spatial regulation of inflammation by human aortic endothelial cells in a linear gradient of shear stress," Microcirculation, 15(4), pp. 311-323.

[184] Depaola, N., Gimbrone, M., Davies, P., And Dewey, C., 1992, "Vascular Endothelium Responds To Fluid Shear-Stress Gradients," Arteriosclerosis and Thrombosis, 12(11), pp. 1254-1257.

[185] Tardy, Y., Resnick, N., Nagel, T., Gimbrone, M., and Dewey, C., 1997, "Shear stress gradients remodel endothelial monolayers in vitro via a cell proliferation-migration-loss cycle," Arteriosclerosis Thrombosis and Vascular Biology, 17(11), pp. 3102-3106.

[186] Remuzzi, A., Dewey, C., Davies, P., And Gimbrone, M., 1984, "Orientation Of Endothelial-Cells In Shear Fields Invitro," Biorheology, 21(4), pp. 617-630.

[187] White, C., Stevens, H., Haidekker, M., and Frangos, J., 2005, "Temporal gradients in shear, but not spatial gradients, stimulate ERK1/2 activation in human endothelial cells," American Journal of Physiology-Heart and Circulatory Physiology, 289(6), pp. H2350-H2355.

[188] White, C., Haidekker, M., Bao, X., and Frangos, J., 2001, "Temporal gradients in shear, but not spatial gradients, stimulate endothelial cell proliferation," Circulation, 103(20), pp. 2508-2513.

[189] Rouleau, L., Farcas, M., Tardif, J., Mongrain, R., and Leask, R., 2010, "Endothelial Cell Morphologic Response to Asymmetric Stenosis Hemodynamics: Effects of Spatial Wall Shear Stress Gradients," Journal of Biomechanical Engineering-Transactions of the Asme, 132(8).

[190] Szymanski, M., Metaxa, E., Meng, H., and Kolega, J., 2008, "Endothelial cell layer subjected to impinging flow mimicking the apex of an arterial bifurcation," Annals of Biomedical Engineering, 36(10), pp. 1681-1689.

[191] Sakamoto, N., Saito, N., Han, X., Ohashi, T., and Sato, M., 2010, "Effect of spatial gradient in fluid shear stress on morphological changes in endothelial cells in response to flow," Biochemical and Biophysical Research Communications, 395(2), pp. 264-269.

[192] Ostrowski, M., Huang, N., Walker, T., Verwijlen, T., Poplawski, C., Khoo, A., Cooke, J., Fuller, G., and Dunn, A., 2014, "Microvascular Endothelial Cells Migrate Upstream and Align Against the Shear Stress Field Created by Impinging Flow," Biophysical Journal, 106(2), pp. 366-374.

[193] Kiosses, W. B., McKee, N. H., and Kalnins, V. I., 1997, "Evidence for the Migration of Rat Aortic Endothelial Cells Toward the Heart," Arteriosclerosis, Thrombosis, and Vascular Biology, 17(11), p. 2891.

[194] McCue, S., Dajnowiec, D., Xu, F., Zhang, M., Jackson, M. R., and Langille, B. L., 2006, "Shear Stress Regulates Forward and Reverse Planar Cell Polarity of Vascular Endothelium In Vivo and In Vitro," Circulation Research, 98(7), p. 939.

[195] Polacheck, W. J., Charest, J. L., and Kamm, R. D., 2011, "Interstitial flow influences direction of tumor cell migration through competing mechanisms," Proceedings of the National Academy of Sciences, 108(27), pp. 11115-11120.

[196] Lipowsky, H. H., Kovalcheck, S., and Zweifach, B. W., 1978, "The distribution of blood rheological parameters in the microvasculature of cat mesentery," Circulation Research, 43(5), p. 738.

[197] R. Gorelik and A. Gautreau, "Quantitative and unbiased analysis of directional persistence in cell migration," *Nature Protocols,* vol. 9, p. 1931, 07/17/online 2014.